



Investigation of Magnetically Geared Stator Permanent Magnet Machines

Zhongze Wu

A thesis submitted for the degree of Doctor of Philosophy

Department of Electronic and Electrical Engineering

The University of Sheffield

Mapping Building, Sheffield, S1 3JD, UK

January 2017

Abstract

Stator-permanent magnet (PM) (Stator-PM) machines include doubly salient PM, flux reversal PM (FRPM), and switched flux PM (SFPM) machines, in which both the PMs and armature windings are placed in the stator, whilst there is neither PM nor coil in the rotor. They have been the subject of much interest over the last 20 years. The operation and interaction mechanisms between the open-circuit and armature excitation magnetomotive forces (MMFs) in stator-PM machines have not been well described, however, which will be explained by the magnetic gearing effect in the first part of this thesis. It is found that similar to magnetic gears and magnetically geared (MG) machines, conventional single-stator-PM machines operate based on the modulation effect of the rotor to the open-circuit and armature excitation MMFs. It is also found that more than 95% of the average electromagnetic torque in SFPM machines is contributed by several dominant open-circuit and armature excitation air-gap field harmonics. The magnetic gearing effect in the partitioned stator SFPM (PS-SFPM) machines, which was proposed recently based on the magnetic gearing effect in the conventional single stator SFPM machines, is also investigated in this thesis. The partitioned-stator-PM machines also operate based on the magnetic gearing effect. Furthermore, over 93% of the electromagnetic torque generated in both the outer and inner air-gaps in the PS-SFPM machines is contributed by the dominant air-gap field harmonics.

Consequent-pole PM topology and overlapping armature winding topology for the partitioned stator FRPM (PS-FRPM) machines, based on the magnetic gearing effect in the partitioned-stator-PM machines, are investigated in this thesis. By applying consequent-pole PM topology, about a third of the PM volume can be saved, but the torque density and efficiency are similar. For the overlapping armature winding topology, higher torque density, smaller loss, and hence larger efficiency etc. can be achieved when the machine stack length is relatively long.

Finally, the PS-FRPM machines and the conventional MG machines, both of which have surface-mounted PMs, are compared in terms of electromagnetic performance. Compared with conventional MG machines, PS-FRPM machines have a smaller flux-leakage and hence a higher torque density and a larger power factor due to their smaller PM pole-pair number and iron piece number.

Acknowledgements

Great gratitude and thanks are due to my supervisor, Prof. Zi-Qiang Zhu, for his very strong and continued help, support, advice and encouragement all the time, which have been invaluable during my PhD study and in the completion of this thesis.

I would like to thank Prof. Ming Cheng and Prof. Wei Hua at Southeast University, China, to recommend me to pursue the PhD degree supervised by Prof. Zhu at The University of Sheffield. Without their recommendation, I would not have this chance to study in the Electrical Machines and Drives Research Group, The University of Sheffield. Thanks are also due to all members of the Electrical Machines and Drives Research Group at the University of Sheffield, especially Mr Hanlin Zhan for his help in testing the prototypes, Dr Kai Wang who is now a full professor at Nanjing University of Aeronautics and Astronautics for his help in electrical machine analysis, and Mr John Wilkinson for his help in building the prototypes.

I also would like to thank VALEO Powertrain Electrical Systems for the financial support, particularly Dr Philippe Farah and Dr Jean-Claude Mipo for their very helpful supervision and advices.

Finally, I warmly thank my wife Lingyun Shao and my parents for their endless love, care and encouragement.

Content

Abstract.....	2
Acknowledgements	3
Nomenclatures.....	9
Abbreviation.....	17
1 General Introduction	18
1.1 Introduction	18
1.2 Conventional Single-Stator-PM Machines	18
1.2.1 DSPM machines.....	18
1.2.2 FRPM machines.....	21
1.2.3 SFPM machines	22
1.3 Magnetic Gears and Magnetically Geared Machines.....	26
1.3.1 Magnetic gears	26
1.3.2 Magnetically geared machines.....	28
1.4 PhD Research Scope and Contributions	31
1.4.1 Scope.....	31
1.4.2 Contributions.....	34
2 Analysis of Magnetic Gearing Effects in Switched Flux Permanent Magnet Machines	36
2.1 Introduction	36
2.2 Magnetic Gearing Effect in Conventional 12/10-Pole SFPM Machine.....	37

2.2.1	Open-circuit air-gap flux density	41
2.2.2	Armature excitation air-gap flux density	43
2.2.3	Magnetic gearing effect	47
2.3	Magnetic Gearing Effect in Various SFPM Machine Topologies	53
2.3.1	All poles wound SFPM machines having different rotor pole numbers.....	53
2.3.2	Alternate poles wound SFPM machines	55
2.3.3	E- and C-core SFPM machines	56
2.4	Torque Contribution of Dominant Field Harmonics.....	59
2.5	Experimental Validation	67
2.6	Conclusions	69
3	Analysis of Magnetic Gearing Effects in Partitioned Stator Switched Flux Permanent Magnet Machines	71
3.1	Introduction	71
3.2	Analysis of 12/10-Pole PS-SFPM Machine.....	73
3.2.1	Inner air-gap open-circuit PM MMF	74
3.2.2	Outer air-gap armature excitation MMF	76
3.2.3	Magnetic gearing effect	78
3.3	Further Analysis of Developed PS-SFPM Machines	86
3.3.1	All poles wound PS-SFPM machines having different rotor pole numbers.....	86
3.3.2	Alternate poles wound PS-SFPM machines	89
3.3.3	E-core and C-core PS-SFPM machines	90
3.4	Torque Contributions of Dominant Field Harmonics	93
3.5	Experimental Validation	100
3.6	Conclusions	104
4	Partitioned Stator Flux Reversal Permanent Magnet Machine with Consequent Pole Permanent Magnets	105

4.1	Introduction	105
4.2	12/11-Pole PS-FRPM Machine with CPM Inner Stator	106
4.3	Stator and Rotor Pole Combinations	112
4.4	Electromagnetic Performance.....	119
4.4.1	Open-circuit flux-linkage and back-EMF	119
4.4.2	Torque characteristics	121
4.4.3	Loss and efficiency	125
4.4.4	Winding inductance	129
4.4.5	Unbalanced magnetic force.....	129
4.5	Experimental Validation	131
4.6	Conclusions	137
5	Partitioned Stator Flux Reversal Permanent Magnet Machine Having Overlapping Windings.....	138
5.1	Introduction	138
5.2	PS-FRPM Machine with Non-Overlapping and Overlapping Windings	140
5.2.1	Fractional-slot non-overlapping winding with $q=0.5$	140
5.2.2	Integer-slot overlapping winding with $q=1$	143
5.3	Electromagnetic Performance.....	147
5.3.1	Open-circuit flux-Linkage and back-EMF.....	150
5.3.2	Torque characteristics	152
5.3.3	Loss and efficiency	156
5.3.4	Winding inductances.....	157
5.3.5	Influence of end winding	159
5.4	Experimental Validation	162
5.5	Conclusions	173

6	Comparison of Partitioned Stator Flux Reversal PM Machine and Magnetically Geared Machine Operating in Static-PM and Rotating-PM Modes.....	175
6.1	Introduction	175
6.2	Operation Principle.....	177
6.3	Electromagnetic Performance.....	185
6.3.1	Open-circuit flux-linkage and back-EMF	187
6.3.2	Torque characteristics	190
6.3.3	Loss and efficiency	193
6.3.4	Winding inductances.....	196
6.4	Experimental Validation	197
6.5	Conclusions	204
7	General Conclusions and Future Work.....	205
7.1	Summary	205
7.2	Magnetic Gearing Effect in Single- and Partitioned-Stator-PM Machines.....	205
7.3	Partitioned Stator Flux Reversal PM Machines.....	206
7.3.1	Basic topology having surface-mounted PMs and non-overlapping armature windings.....	207
7.3.2	Developed topology having consequent-pole PMs and non-overlapping armature windings.....	207
7.3.3	Developed topology having surface-mounted PMs and overlapping armature windings.....	207
7.3.4	Comparison of conventional FRPM machine and PS-FRPM machines with basic topology and developed topologies	208
7.4	Future Work	210
	References.....	211

Appendix A	Air-Gap MMF and Field Harmonics of Armature Excitation in 12-Stator-Pole SFPM Machines Having 11-, 13- And 14-Rotor-Pole Rotors	233
Appendix B	Partitioned Stator Flux Reversal Permanent Magnet Machine	238
B.1	Introduction	238
B.2	Operation Principle.....	238
B.3	Stator and Rotor Pole Combinations	242
B.4	Electromagnetic Performance.....	246
B.5	Influence of Leading Design Parameters	252
B.6	Experimental Validation	259
B.7	Conclusions	266
Appendix C	Comparative Analysis of End Effect in Partitioned Stator Flux Reversal Machines Having Surface-Mounted and Consequent Pole Permanent Magnets	267
C.1	Introduction	267
C.2	Machine Topology and Operation Principle	267
C.3	End Effect.....	268
C.3.1	Open-circuit	268
C.3.2	On-load	272
C.3.3	Influence of aspect ratio	276
C.3.4	Influence of PM arc in CPM machine	278
C.4	Experimental Validation	279
C.5	Conclusions	281
Publications	283

Nomenclatures

B_{ABC}	Armature excitation air-gap flux density	T
B_{ABCin}	Armature excitation inner air-gap flux density	T
B_{PM}	PM air-gap flux density	T
B_{PMout}	PM outer air-gap flux density	T
B_r	Air-gap flux density, radial component	T
B_{rin}	Inner air-gap flux density, radial component	T
B_{rinn}	n^{th} Fourier coefficient of inner air-gap flux density, radial component B_{rin}	T
B_{rn}	n^{th} Fourier coefficient of air-gap flux density, radial component B_r	T
B_{rout}	Outer air-gap flux density, radial component	T
B_{routn}	n^{th} Fourier coefficient of outer air-gap flux density, radial component B_{rout}	T
B_{rPM}	PM remanence	T
B_t	Air-gap flux density, tangential component	T
B_{tin}	Inner air-gap flux density, tangential component	T
B_{tinn}	n^{th} Fourier coefficient of inner air-gap flux density, tangential component B_{tin}	T
B_{tn}	n^{th} Fourier coefficient of air-gap flux density, tangential component B_t	T
B_{tout}	Outer air-gap flux density, tangential component	T
B_{toutn}	n^{th} Fourier coefficient of outer air-gap flux density, tangential component B_{tout}	T
C_{l31}	Distance between coils A1 and A3 in stator slot number	-
E_{2D}	2D FE predicted phase fundamental back-EMF	V
E_{3D}	3D FE predicted phase fundamental back-EMF	V
E_{eload}	On-load end effect coefficient	-
E_{eopen}	Open-circuit end effect coefficient	-

F_A	Phase A armature excitation MMF	A
F_{ABC}	Armature excitation MMFs	A
F_B	Phase B armature excitation MMF	A
F_C	Phase C armature excitation MMF	A
F_{PM}	PM MMF	A
F_{PMs}	PM MMF square waveform peak value	A
g	Air-gap length	m
g_i	Inner air-gap length	m
g_o	Outer air-gap length	m
G_r	Gear ratio	-
i_A	Phase A current	A
i_B	Phase B current	A
i_C	Phase C current	A
i_d	D -axis current	A
I_{dc}	DC bus current of inverter	A
I_{max}	Maximum phase current	A
i_q	Q -axis current	A
I_{rms}	Phase current RMS current	A
k_{cfe}	Iron eddy current loss coefficient	W/m^3
k_{efe}	Iron excess loss coefficient	W/m^3
k_{fw}	Flux-weakening coefficient	-
k_{hfe}	Iron hysteresis loss coefficient	W/m^3
k_{pv}	v^{th} winding pitch factor	-
K_s	End winding empirical coefficient	-
K_{Tr}	Torque ripple coefficient	%
U_{dc}	DC bus voltage of inverter	V

L_{A+B}	Self-inductance of serially connected phase A and phase B	H
L_{AA}	Phase A self-inductance	H
L_{BB}	Phase B self-inductance	H
L_d	D -axis inductance	H
L_e	Half turn coil end length	m
L_{half}	Half turn coil total length	m
l_{otb}	Outer stator tip bottom length	m
l_{ott}	Outer stator tip top length	m
L_q	Q -axis inductance	H
L_s	Stack length	m
m	Phase number	-
M_{2k}	Fourier coefficient of air-gap permeance determined by k	H
M_{ABCq}	Fourier coefficient of armature excitation MMF determined by q	A
M_{BA}	Mutual inductance between Phase A and Phase B	H
M_{CA}	Mutual inductance between Phase A and Phase C	H
M_{ipk}	Fourier coefficient of iron piece permeance determined by k	H
M_{PMi}	Fourier coefficient of PM MMF determined by i	A
N_{ac}	Number of turns per armature coil	-
N_c	Number of turns per coil	-
n_{ce}	Cogging torque cycles per electric period	-
N_{fc}	Number of turns per field coil	-
N_{ip}	Iron piece number	-
N_{os}	Outer stator pole number	-
N_r	Rotor pole number	-
N_s	Stator pole number	-
P_0	DC component value of air-gap permeance waveform	H

P_2	Peak-to-peak value of air-gap permeance waveform	H
p_{cfe}	Iron eddy current loss	W
p_{cu}	Copper loss	W
p_{cue}	End winding copper loss	W
p_{cus}	Copper loss excluding end winding copper loss	W
p_{ea}	Armature excitation pole-pair number	-
p_{efe}	Iron excess loss	W
P_{EM}	Electromagnetic power	W
p_{fe}	Iron loss	W
p_{feis}	Inner stator iron loss	W
p_{feos}	Outer stator iron loss	W
p_{fer}	Rotor iron loss	W
p_{fes}	Stator iron loss	W
p_{hfe}	Iron hysteresis loss	W
p_i	Inner PM pole-pair number	-
P_{in}	Input power	W
P_{ip}	Peak-to-peak value of air-gap permeance waveform	H
p_o	Outer PM pole-pair number	-
P_{out}	Output power	W
p_{PM}	PM pole-pair number	-
p_{PMe}	PM eddy current loss	W
q	Slot number per pole per phase	-
R_g	Air-gap radius	m
R_{gi}	Inner air-gap radius	m
R_{go}	Outer air-gap radius	m
R_{ii}	PM body inner radius	m

R_{in}	Inner air-gap radius	m
R_{ipi}	Iron piece inner edge radius	m
R_{isi}	Inner stator inner radius	m
R_{oi}	Winding body inner radius	m
R_{oo}	Winding body outer radius	m
R_{osi}	Outer stator inner radius	m
R_{oso}	Outer stator outer radius	m
R_{osy}	Outer stator yoke radius	m
R_{out}	Outer air-gap radius	m
R_{oy}	Winding body yoke radius	m
R_{ri}	Rotor inner radius	m
R_{ro}	Rotor outer radius	m
R_{ry}	Rotor yoke radius	m
R_{si}	Stator inner radius	m
R_{so}	Stator outer radius	m
R_{sy}	Stator yoke radius	m
S_2	Constant in air-gap permeance	-
S_{ABC}	Constant in armature excitation MMF	-
S_{ip}	Constant in iron piece permeance	-
S_{PM}	Constant in PM MMF	-
T_{avg}	Average electromagnetic torque	Nm
T_{avg2D}	2D FE predicted average electromagnetic torque	Nm
T_{avg3D}	3D FE predicted average electromagnetic torque	Nm
T_{bri}	Flux iron bridge thickness	m
T_{em}	Air-gap electromagnetic torque	Nm

T_{emn}	Air-gap electromagnetic torque component generated by the n^{th} radial and tangential field harmonics	Nm
T_{emnavg}	Average value of air-gap electromagnetic torque component generated by the n^{th} radial and tangential field harmonics T_{emn}	Nm
T_{emout}	Outer air-gap electromagnetic torque	Nm
T_{emoutn}	Outer air-gap electromagnetic torque component generated by the n^{th} radial and tangential field harmonics	Nm
$T_{emoutnavg}$	Average value of outer air-gap electromagnetic torque component generated by the n^{th} radial and tangential field harmonics	Nm
T_L	Load torque	Nm
T_{max}	Maximum electromagnetic torque	Nm
T_{min}	Minimum electromagnetic torque	Nm
T_{outavg}	Outer air-gap average electromagnetic torque	Nm
T_r	Torque ripple	%
U_{max}	Maximum phase voltage	V
$V_{machine}$	Machine volume	m ³
V_{PM}	PM volume	m ³
γ_{sp}	Split ratio	-
η	Efficiency	%
θ_0	Angle between initial rotor pole position and horizon line	rad
θ_1	Half of PM arc	rad
θ_2	Half of rotor pole arc	rad
θ_3	Half of PM arc plus stator tooth arc	rad
θ_4	Half of stator tooth arc	rad
θ_{ad31}	Additional phase angle resulted from the polarity of the coil A3 and its corresponding PM	rad
θ_{coil}	Coil pitch arc	rad
θ_{ipi}	Iron piece inner arc	rad

θ_{ipo}	Iron piece outer arc	rad
θ_{osp}	Outer stator slot pitch arc	rad
θ_{ost}	Outer stator tooth arc	rad
θ_{ot}	Outer stator tooth tip arc	rad
θ_{PM}	PM arc	rad
θ_{ri}	Rotor pole inner arc	rad
θ_{rinn}	n^{th} phase angle of inner air-gap flux density, radial component B_{rin}	rad
θ_{rn}	n^{th} phase angle of air-gap flux density, radial component B_r	rad
θ_{ro}	Rotor pole outer arc	rad
θ_{routn}	n^{th} phase angle of outer air-gap flux density, radial component B_{rout}	rad
θ_{rp}	Rotor pole arc	rad
θ_{ry}	Rotor yoke arc	rad
θ_{st}	Stator tooth arc	rad
θ_{tinn}	n^{th} phase angle of inner air-gap flux density, tangential component B_{tin}	rad
θ_{tn}	n^{th} phase angle of air-gap flux density, tangential component B_t	rad
θ_{toutn}	n^{th} phase angle of outer air-gap flux density, tangential component B_{tout}	rad
κ_{PM}	PM bulk conductivity	S/m
μ_0	Vacuum permeability	H/m
μ_{rPM}	PM relative permeability	-
τ_y	Coil pitch in terms of circumferential length	m
Φ_A	Open-circuit phase A flux-linkage	Wb
Φ_{A1}	Open-circuit coil A1 flux-linkage	Wb
Φ_{A1v}	v^{th} harmonic of open-circuit coil A1 flux-linkage Φ_{A1}	Wb
Φ_{A2}	Open-circuit coil A2 flux-linkage	Wb
Φ_{A2v}	v^{th} harmonic of open-circuit coil A2 flux-linkage Φ_{A2}	Wb

Φ_{A3}	Open-circuit coil A3 flux-linkage	Wb
$\Phi_{A3\nu}$	ν^{th} harmonic of open-circuit coil A3 flux-linkage Φ_{A3}	Wb
Φ_{A4}	Open-circuit coil A4 flux-linkage	Wb
$\Phi_{A4\nu}$	ν^{th} harmonic of open-circuit coil A4 flux-linkage Φ_{A4}	Wb
ψ_{AA}	Average flux-linkage of phase A under constant phase A current I_A	Wb
ψ_{APM}	Average flux-linkage of phase A due to only PM	Wb
ψ_{BA}	Average flux-linkage of phase B under constant phase A current I_A	Wb
ψ_{BPM}	Average flux-linkage of phase B due to only PM	Wb
ψ_{CA}	Average flux-linkage of phase C under constant phase A current I_A	Wb
ψ_{CPM}	Average flux-linkage of phase C due to only PM	Wb
ψ_{PM}	D -axis PM flux-linkage	Wb
ω_e	Rotor electric angular speed	rad/s
Ω_{ip}	Iron piece mechanical angular speed	rad/s
Ω_{PM}	PM mechanical angular speed	rad/s
Ω_r	Rotor mechanical angular speed	rad/s
Ω_{rmax}	Maximum mechanical angular speed	rad/s
$\beta_{31\nu}$	Lag angle between open-circuit coil A3 flux-linkage $\Phi_{A3\nu}$ and open-circuit coil A1 flux-linkage $\Phi_{A1\nu}$	rad

Abbreviation

AC	Alternating current
BLAC	Brushless alternating current
BLDC	Brushless direct current
CPM	Consequent-pole permanent magnet
DC	Direct current
DS	Double salient
DSPM	Double salient permanent magnet
EMF	Electromotive force
FE	Finite element
FR	Flux reversal
FRPM	Flux reversal permanent magnet
MG	Magnetically geared
MMF	Magnetomotive force
PM	Permanent magnet
PS	Partitioned stator
PS-DSPM	Partitioned stator double salient permanent magnet
PS-FRPM	Partitioned stator flux reversal permanent magnet
PS-SFPM	Partitioned stator switched flux permanent magnet
RTPM	Rotating permanent magnet
SF	Switched flux
SFPM	Switched flux permanent magnet
SPM	Surface-mounted permanent magnet
SRM	Switched reluctance machine
STPM	Static permanent magnet

1 General Introduction

1.1 Introduction

By introducing permanent magnets (PMs) into the stator of a switched reluctance machine (SRM), higher torque density and higher efficiency stator-PM machines can be achieved when they have both PMs and armature windings in the stator [ZHU07a]. It is easier to manage the PM temperature in stator-PM machines compared with conventional rotor-PM machines, in which the PMs are accommodated in the rotor [ZHU11b] [CHE11a].

Stator-PM machines can be classified into three categories according to the different PM positions therein, i.e.:

- Doubly salient PM (DSPM) machine with yoke-inserted PMs
- Flux reversal PM (FRPM) machine with tooth-surface-mounted PMs
- Switched flux PM (SFPM) machine with tooth-sandwiched PMs

Based on these three main types of stator-PM machines named above, various topologies have been proposed and analysed over the last 20 years [ZHU11b] [CHE11a] [ZHU14a]. The operation and interaction mechanisms between the open-circuit and armature excitation magnetomotive forces (MMFs) in stator-PM machines have not been well explained, however, this thesis will clarify this using the magnetic gearing effect, which is similar to magnetic gears [ATA01a] [ATA04a] and magnetically geared (MG) machines [ATA08a] [JIA09b] [WAN11c] [BAI15a] [WAN08a] [QU11a]. Some novel topologies of partitioned-stator-PM machines having separated PMs and armature windings will be explored in this thesis based on the magnetic gearing effect, in order to further improve the electromagnetic performance of existing stator-PM machines in terms of torque density and efficiency.

1.2 Conventional Single-Stator-PM Machines

1.2.1 DSPM machines

The SRM has a robust rotor without any PM or coil, as well as non-overlapping concentrated windings [SPO87a], as shown in Fig. 1.1 for a 12/8-stator/rotor-pole counterpart. The coil connection of the 12/8-stator/rotor-pole SRM is shown in Fig. 1.2. Theoretically, the rectangular current waveform in the SRM can be regarded as a sum of the DC component, the

fundamental sinusoidal component, and other higher order harmonics in the Fourier series [LIU12a]. By neglecting the current harmonics, a SRM with only a DC current and a fundamental sinusoidal current could be regarded as a stator-wound field machine [LIU12a].

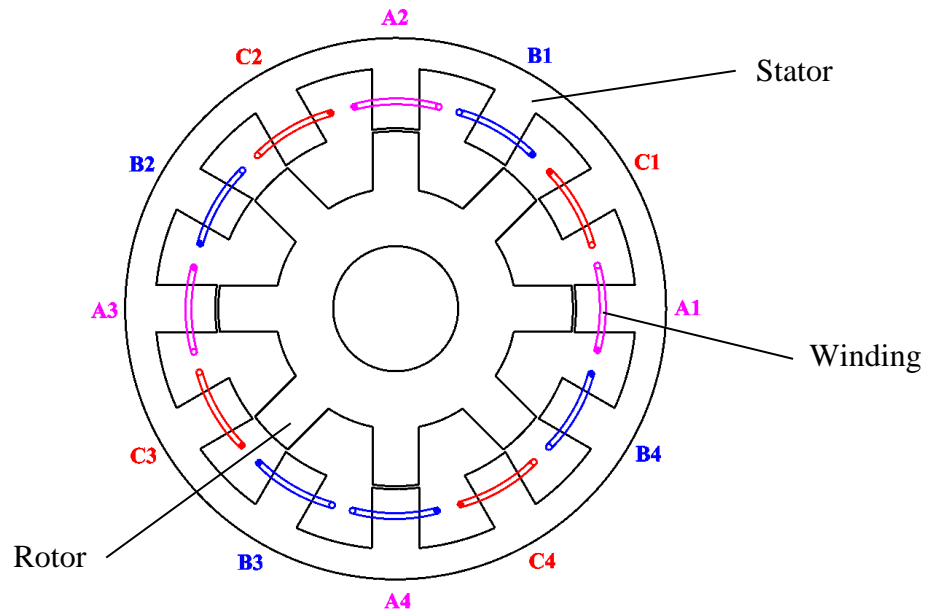


Fig. 1.1 Cross-section of a 3-phase 12/8-stator/rotor-pole SRM.

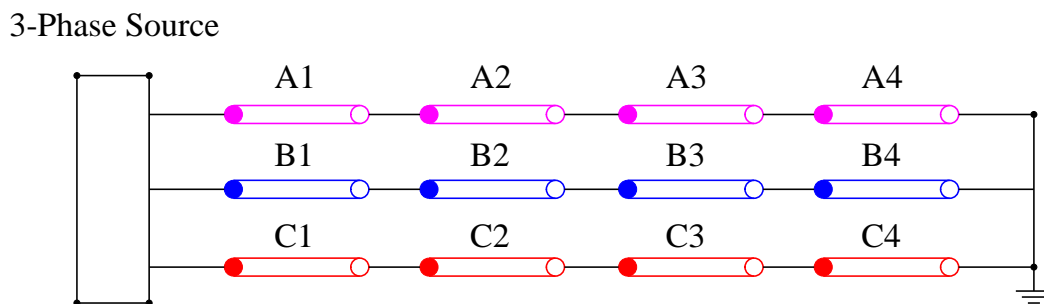


Fig. 1.2 Coil connection of the 3-phase 12/8-stator/rotor-pole SRM.

To enlarge the torque density in a SRM by introducing PM excitation, the DSPM machine was developed in [LIA95a]. As for the typical 12/8-stator/rotor-pole SRM shown in Fig. 1.1, the corresponding DSPM machine [CHE00a] is illustrated in Fig. 1.3. As shown in Fig. 1.3, the rotor of the DSPM machine is similar to that of the SRM, i.e. there is neither PM nor coil. However, both the armature coils and PMs are placed in the stator, with non-overlapping concentrated armature windings, similar to the SRM, and yoke-inserted PMs obtained. The open-circuit phase flux-linkage varies linearly versus the rotor position, and the phase back-EMF is theoretically trapezoidal [CHE11a]. Consequently, the DSPM machine can operate in

brushless DC (BLDC) mode [LI07a]. By skewing the rotor, however, a more sinusoidal phase back-EMF with fewer harmonics can be achieved and hence a brushless AC (BLAC) mode can also be employed [CHE03a].

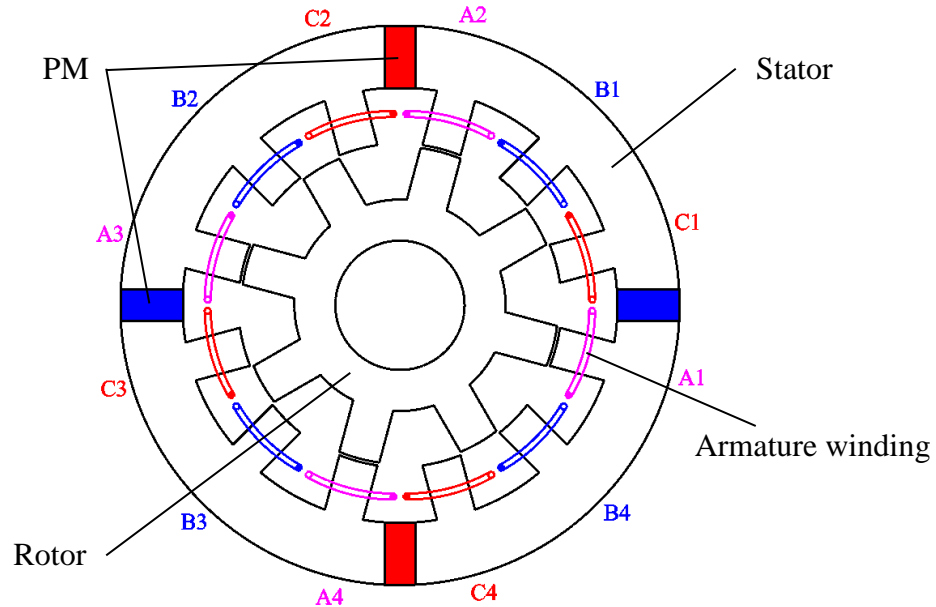


Fig. 1.3 Cross-section of a 3-phase 12/8-stator/rotor-pole DSPM machine.

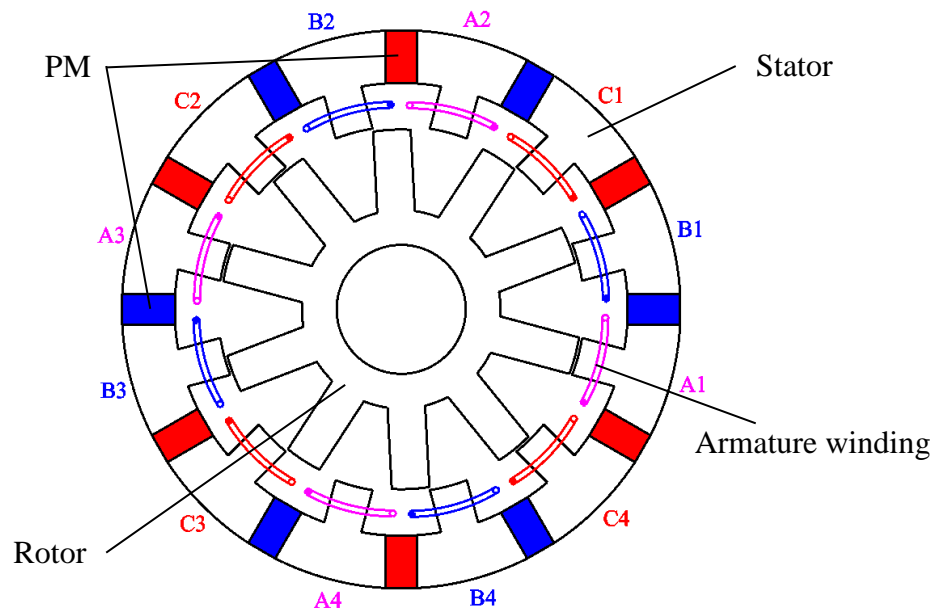


Fig. 1.4 Cross-section of a 3-phase new type 12/10-stator/rotor-pole DSPM machine.

The 12/8-stator/rotor-pole DSPM machine shown in Fig. 1.3 suffers from an asymmetric magnetic path, and hence the asymmetric phase back-EMF as well as a large torque ripple. In the 3-phase 12/8-stator/rotor-pole DSPM machine shown in Fig. 1.3, the PM number is one-

third of the stator pole number. A new type of DSPM machine with equal numbers of stator poles and PMs is proposed and analysed in [WU14a], as shown in Fig. 1.4. In the new type of DSPM machines, the magnetic path is symmetrical, and the even harmonics in coil back-EMF can be eliminated in the phase winding by appropriately connecting the coils. Consequently, the torque ripple is much smaller than the conventional type of DSPM machine shown in Fig. 1.3. This new type of DSPM machine has a much higher PM volume and hence cost, as well as a slightly lower torque [WU15b].

1.2.2 FRPM machines

When the PMs are surface-mounted on the stator teeth, a FRPM machine can be achieved, as firstly proposed and analysed in [DEO97a] and [WAN01a] for the single phase 3/2-stator/rotor-pole and three-phase 12/8-stator/rotor-pole counterparts, respectively. In [HUA10a], the 12/10-stator/rotor-pole FRPM machine is developed, which has a more sinusoidal open-circuit phase flux-linkage, hence also the back-EMF, since the coil even harmonics can be cancelled in the phase winding by appropriately connecting the coils.

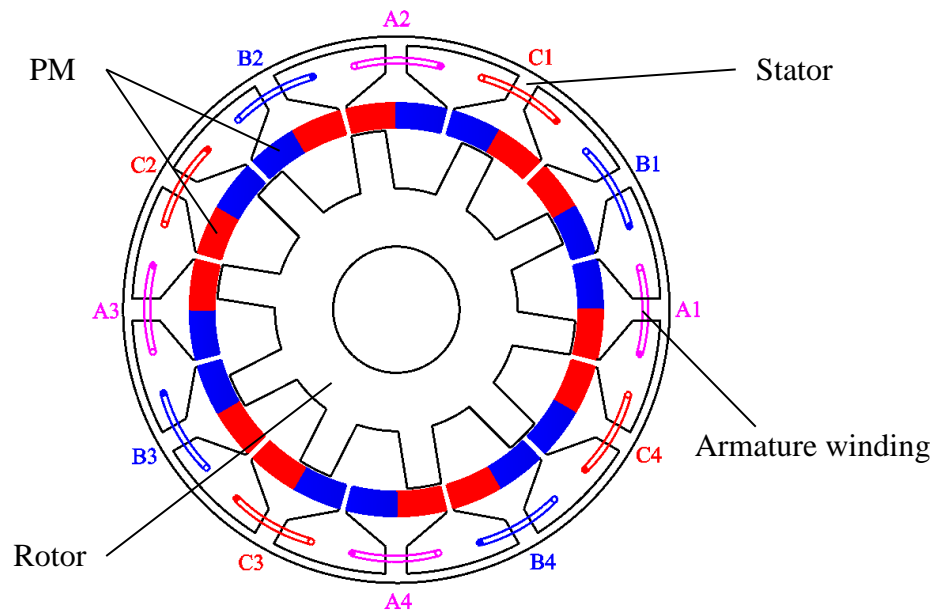


Fig. 1.5 Cross-section of a 3-phase 12/10-stator/rotor-pole FRPM machine.

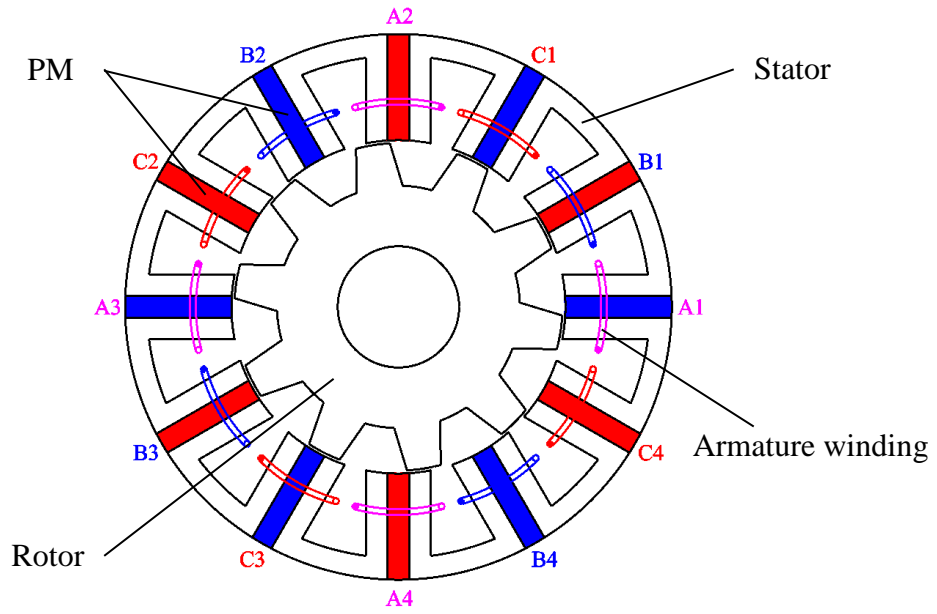
As for the 12/10-stator/rotor-pole FRPM machine [HUA10a], as shown in Fig. 1.5, when the rotor position changes, various open-circuit coil flux-linkages, hence also the back-EMF, can be obtained. By injecting currents into coils, electromagnetic torque can be generated in the air-gap. Compared with the conventional DSPM machine, the FRPM machine has a symmetrical magnetic path and more a sinusoidal phase back-EMF, therefore also a smaller

torque ripple. More importantly, unlike the unipolar coil open-circuit flux-linkage in the DSPM machine, the open-circuit coil flux-linkage is bipolar due to the alternately reversed PM magnetisation directions, which is beneficial to torque density. Due to the stator surface-mounted PMs, however, the FRPM machines suffer from a larger equivalent air-gap width, hence a higher magnetic reluctance and a poorer torque density, as well as a poorer demagnetisation withstand capability, since the PM flux and the armature excitation flux are in series.

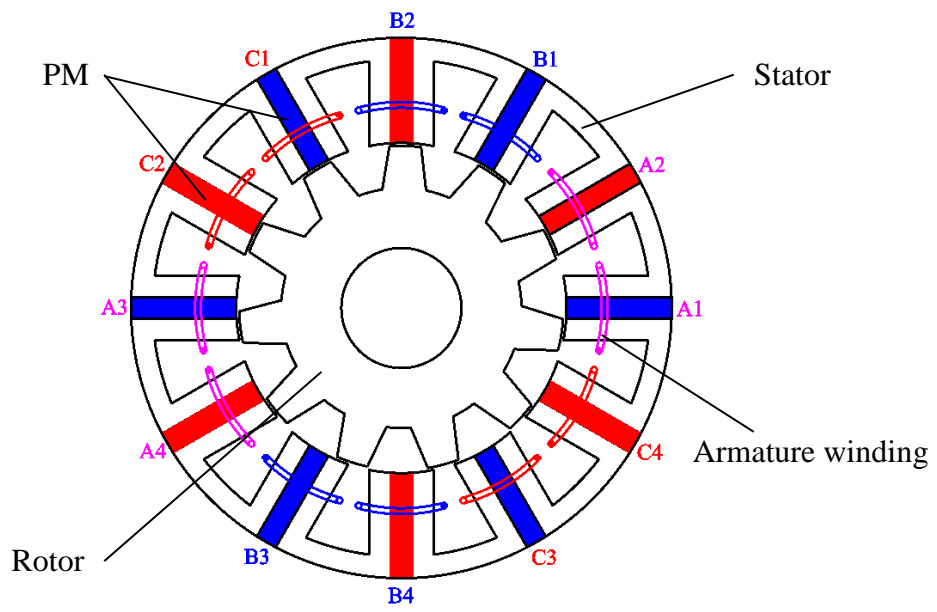
1.2.3 SFPM machines

Another typical stator-PM machine is the SFPM machine, in which PMs are tooth sandwiched, as shown in Fig. 1.6(a) for a 12/10-stator/rotor-pole SFPM machine [HOA97a] [ZHU05a]. The rotor in the SFPM machine is similar to the one in the SRM, DSPM machine, and FRPM machine, i.e. without any coil or PM. The PMs are, however, inserted in the stator teeth, which is different from the DSPM machines that have yoke-inserted PMs and the FRPM machines with tooth-surface-mounted PMs. In SFPM machines, due to their alternately reversed PM magnetisation directions, by appropriately connecting the coils belonging to the same phase, even harmonics can also be eliminated in the phase flux-linkage, hence also the back-EMF. Consequently, the phase back-EMF waveforms of SFPM machines are very sinusoidal [HUA08a], thus the BLAC mode operation is preferred.

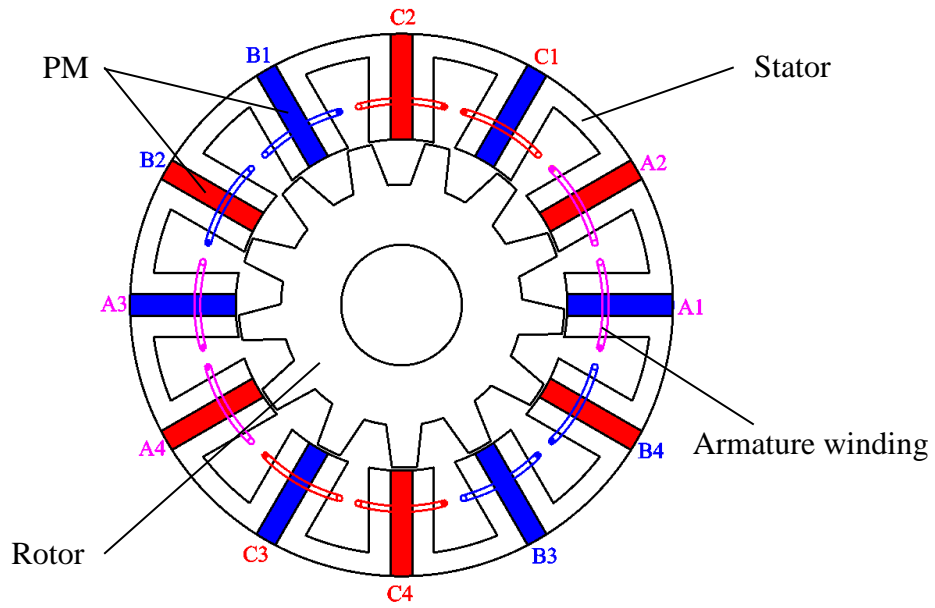
Compared with DSPM machines and FRPM machines, SFPM machines exhibit higher torque density due to the flux focusing effect caused by the spoke type PMs [ZHU05a] [ZHA09a] [ZHU11b]. Also, SFPM machines have a better PM demagnetisation withstand capability, since the PM flux and armature excitation flux are parallel [ZHU05a] [MCF14b]. SFPM machines have therefore drawn a lot of attention in recent years [ZHU11b] [ZHU14a]. Besides the 12/10-stator/rotor-pole SFPM machine shown in Fig. 1.6(a), different stator/rotor-pole combinations are also investigated for SFPM machines. In [CHE10a], electromagnetic performance of the 12-stator-pole SFPM machines having 10-, 11-, 13- and 14-rotor-pole rotors shown in Fig. 1.6(a)-Fig. 1.6(d) were comparatively analysed using finite element (FE) analysis. It shows that the 12/11- and 12/13-stator/rotor-pole SFPM machines have higher torque density due to a larger pitch factor but a lower cogging torque, hence also a lower torque ripple due to having closer stator and rotor pole numbers. For the 6/5- and 6/7-stator/rotor-pole SFPM machines, a similar comparative analysis is conducted in [CHE10d].



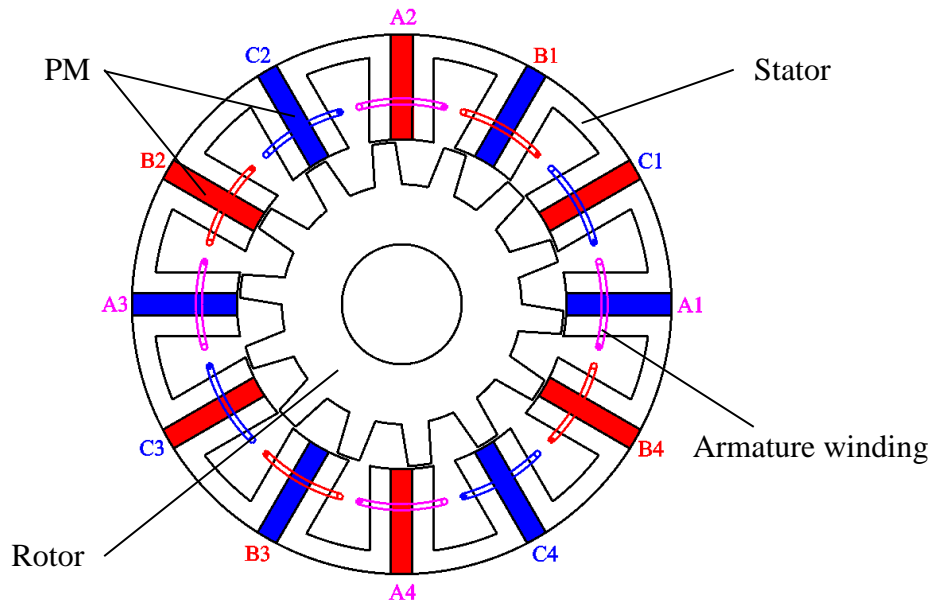
(a) 10-rotor-pole rotor



(b) 11-rotor-pole rotor



(c) 13-rotor-pole rotor



(d) 14-rotor-pole rotor

Fig. 1.6 Cross-sections of 3-phase 12-stator-pole SFPM machines with 10-, 11-, 13- and 14-rotor-pole rotors.

Besides the all poles wound windings shown in Fig. 1.6, alternate poles wound windings can be adopted in SFPM machines, as shown in Fig. 1.7 for a 3-phase 12/10-stator-pole alternate poles wound counterpart [OWE10a] [CHE10d]. It shows that the phase back-EMF in 12/11- and 12/13-stator/rotor-pole alternate poles wound SFPM machines are higher than their all

poles wound counterparts, respectively, due to the enhanced winding factor, whilst in the 12/10- and 12/14-stator/rotor-pole machines respectively they are similar. By further removing the PMs without coils wound, the E-core SFPM machine can be achieved, with a higher slot area and hence torque density for the same copper loss, e.g. a 6/5-stator/rotor-pole SFPM machine as shown in Fig. 1.8(a). Compared with the U-core SFPM machines shown in Fig. 1.6, E-core SFPM machine also has a higher fault tolerance capability due to the additional teeth between the coils. However, these teeth can be further removed to enlarge the slot area and torque density to form a C-core SFPM machine, as shown in Fig. 1.8(b) for a 6/5-stator/rotor-pole C-core SFPM machine. Other modified stator/rotor topologies can be applied to SFPM machines to improve the electromagnetic performance, such as applying a modular stator in [TAR15a] to enhance the fault tolerance capability, a modular rotor in [THO12a] to reduce the iron loss, and additional PMs outside the stator in [DEO14a] to improve the mechanical flux-weakening capability.

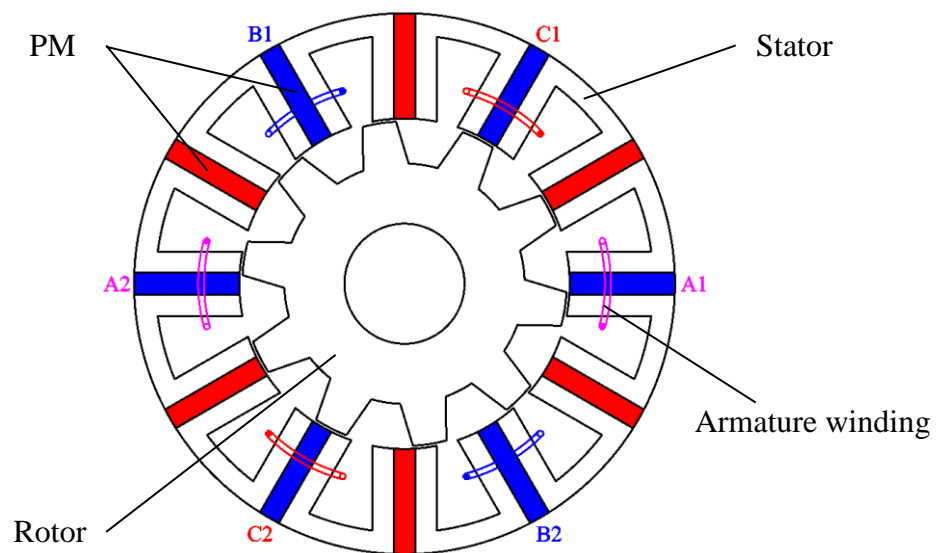
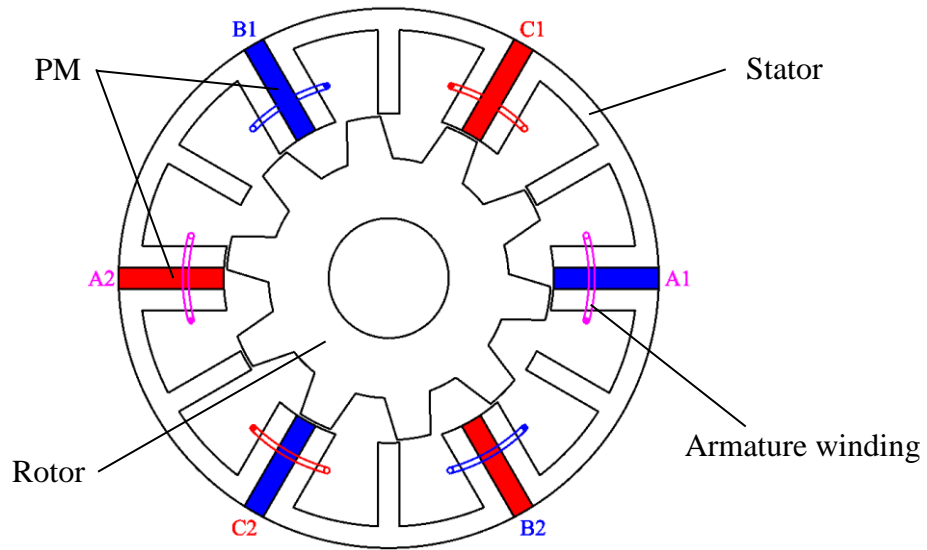
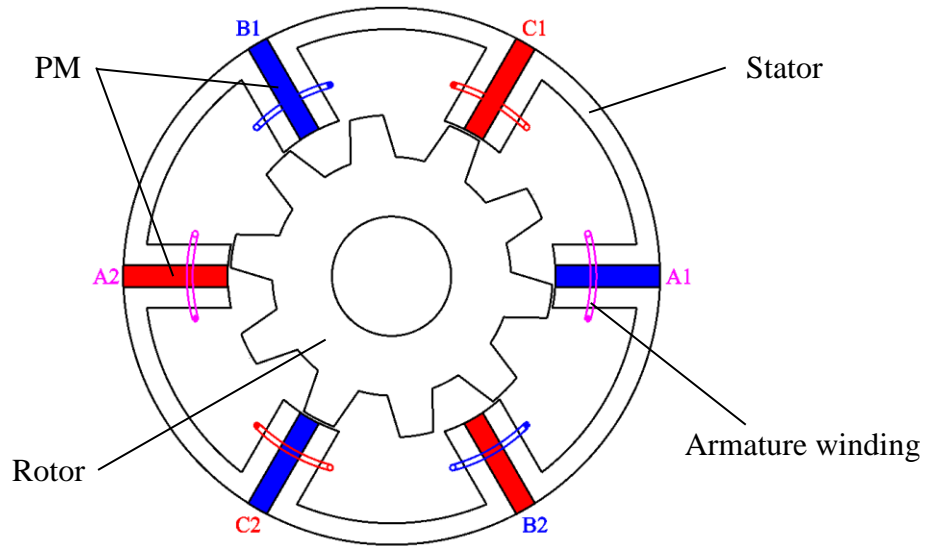


Fig. 1.7 Cross-sections of a 3-phase 12/10-stator-pole alternate poles wound SFPM machine.



(a) E-core



(b) C-core

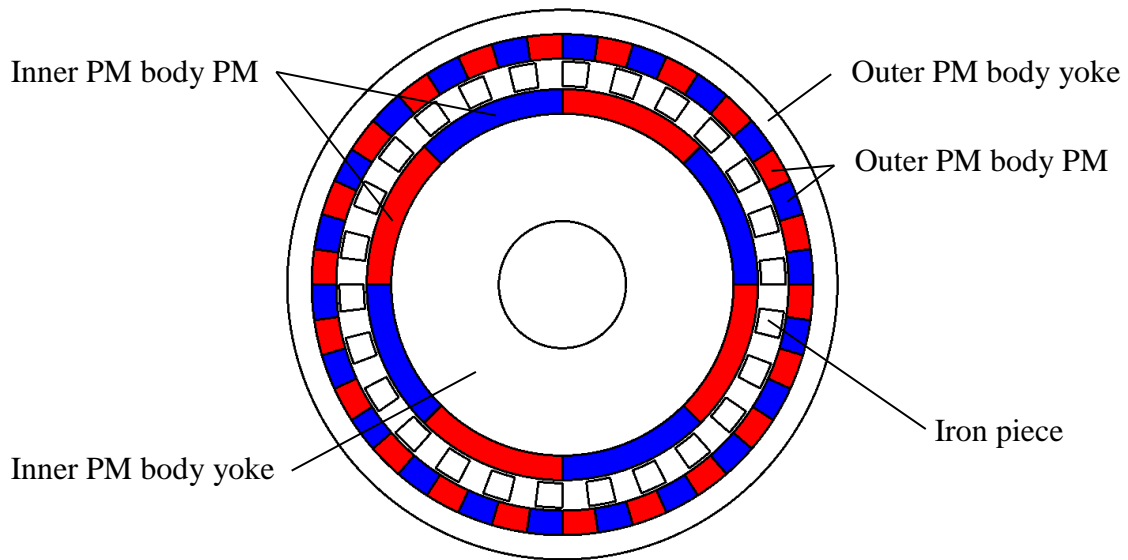
Fig. 1.8 Cross-sections of 3-phase 6/5-stator/rotor-pole E-core and C-core SFPM machines.

1.3 Magnetic Gears and Magnetically Geared Machines

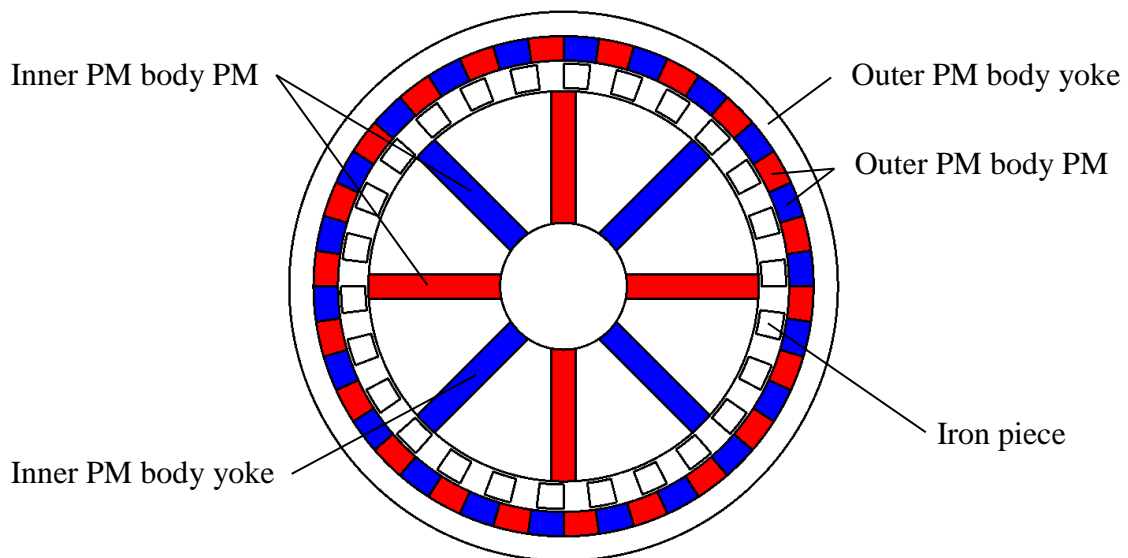
1.3.1 Magnetic gears

A magnetic gear is a torque transmission device, which consists of two PM bodies and iron pieces modulating the PM MMFs, as shown in Fig. 1.9(a) for a 4-inner-pole-pair/26-pole/22-outer-pole-pair magnetic gear with surface-mounted PMs [ATA01a]. Torque can be transmitted between each pair of gears, with various gearing ratios being obtained [ATA04a].

In a magnetic gear, however, the torque transmission between the high- and low-speed gears is conducted electromagnetically, whilst this is completed by direct contact with a mechanical gear. Unlike mechanical gears, magnetic gears do not require lubrication, hence noise, vibration, and reliability can be improved [ATA01a] [ATA04a].



(a) Surface-mounted PMs



(b) Spoke type PMs

Fig. 1.9 Cross-sections of a 4-inner-pole-pair/26-pole/22-outer-pole-pair magnetic gear having surface-mounted and spoke type PMs.

In [RAS05a], a new type of magnetic gear with spoke-type PMs which has a flux focusing effect, hence higher torque density is proposed and analysed, as shown in Fig. 1.9(b). This is

similar to the higher torque density found in the SFPM machines compared to the FRPM machines. An interior PM type magnetic gear is proposed and analysed in [FRA11a].

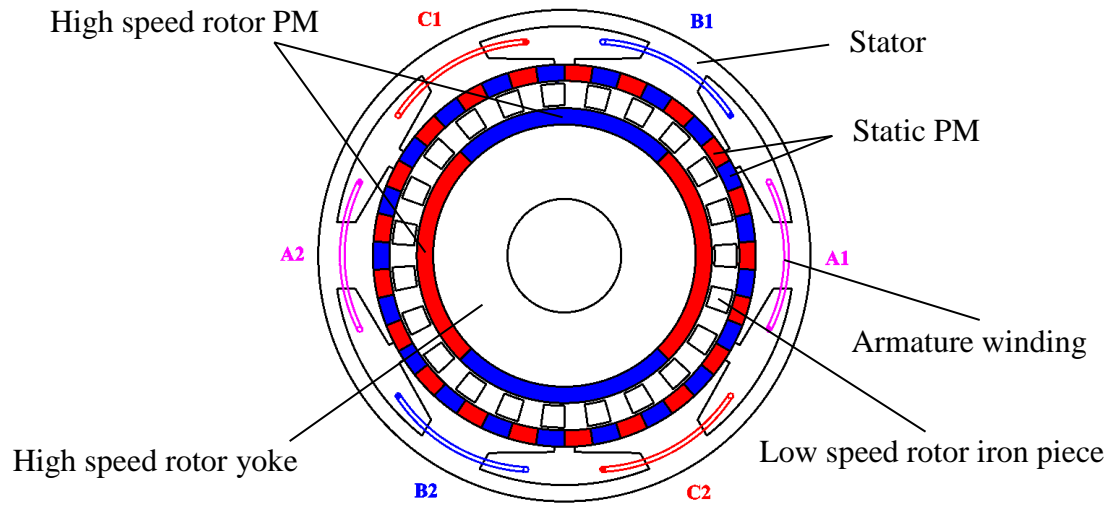
Another type of magnetic gear having surface-mounted PMs with Halbach magnetisation arrays is proposed in [JIA10a]. Compared to the counterpart with parallel magnetisation arrays in [ATA01a], the proposed magnetic gear with Halbach PMs in [JIA10a] exhibits a higher torque density, a lower cogging torque, and a lower iron loss due to less harmonics [JIA09a].

An axial flux magnetic gear with surface-mounted PMs is proposed and analysed in [MEZ06a]. Compared with the conventional radial flux magnetic gear in [ATA01a], the proposed axial flux magnetic gear proposed in [MEZ06a] has a larger torque density due to the higher effective area with a smaller end effect. Nevertheless, the axial flux magnetic gear can offer hermetic isolation between the two rotor shafts. The axial flux magnetic gear adopted with spoke type PMs exhibiting higher torque density is proposed and analysed [ACH13a]. Transverse flux magnetic gears are proposed and analysed in [LI11a] [BOM14a]. To further enhance the torque density, axial flux and transverse flux concepts are combined together in the magnetic gears [YIN15a].

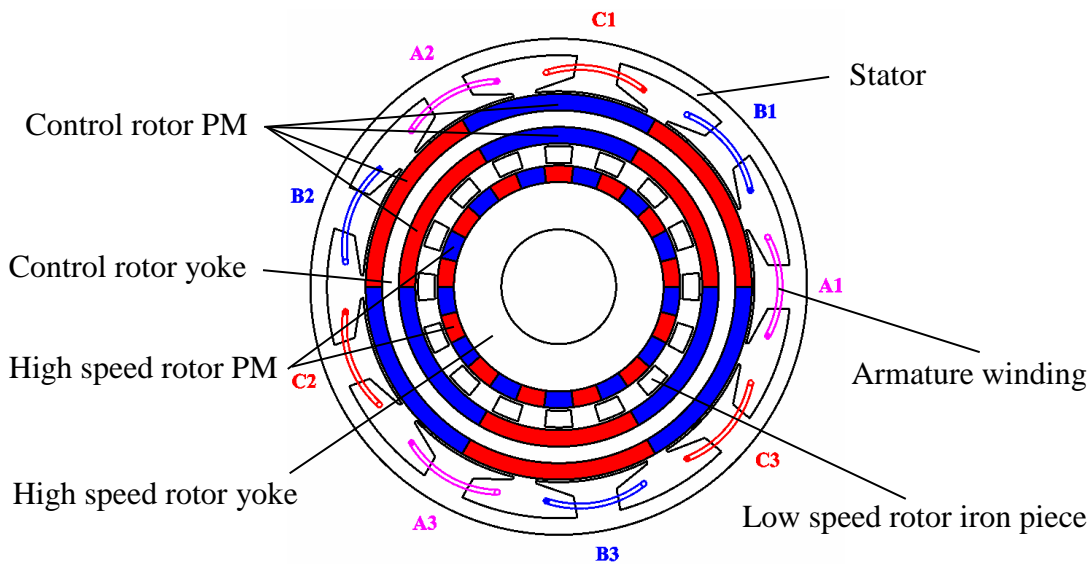
1.3.2 Magnetically geared machines

Due to the merits of magnetic gears and electromagnetic torque transmission, MG machines which integrate electrical machines and magnetic gears together have received much attention [ATA08a] [JIA09b] [WAN11c] [BAI15a], due to their low speed and high torque capabilities.

In terms of the magnetic gear with rotating inner PM body and rotating iron pieces, a MG machine can be obtained by attaching an armature winding stator with the same pole-pair number as the inner PM body to the static outer PM body, as demonstrated in Fig. 1.10(a) for a 2-armature excitation-pole-pair/23-pole/21-PM-pole-pair MG machine proposed and analysed in [ATA08a]. Another typical MG machine with 3 air-gaps is shown in Fig. 1.10(b), which has three rotors, i.e. a control rotor, an output rotor and an inner rotor. By controlling the armature winding currents, a gear ratio between the rotors can be achieved in these types of MG machines [ATA08a] [JIA09b] [WAN11c] [BAI15a], thus obtaining low speed/high torque output for the whole machine.



(a) 2-armature excitation-pole-pair/23-pole/21-PM-pole-pair



(b) 3-armature excitation-pole-air/16-pole/13-PM-pole-pair

Fig. 1.10 Cross-section of a 2-armature excitation-pole-pair/23-pole/21-PM-pole-pair and a 3-armature excitation-pole-air/16-pole/13-PM-pole-pair.

For magnetic gears with two rotating PM bodies whilst the iron pieces are static, as analysed in [ATA01a] and [ATA04a], the MG machine analysed in [WAN08a] can be obtained by displacing the outer rotating PM body using an equivalent 4-pole-pair armature winding stator, as shown in Fig. 1.11. Compared with other types of MG machines, such as those analysed in [ATA08a] [JIA09b] [WAN11c] [BAI15a], the MG machine shown in Fig. 1.11 has only one rotor, which is easier to manufacturing.

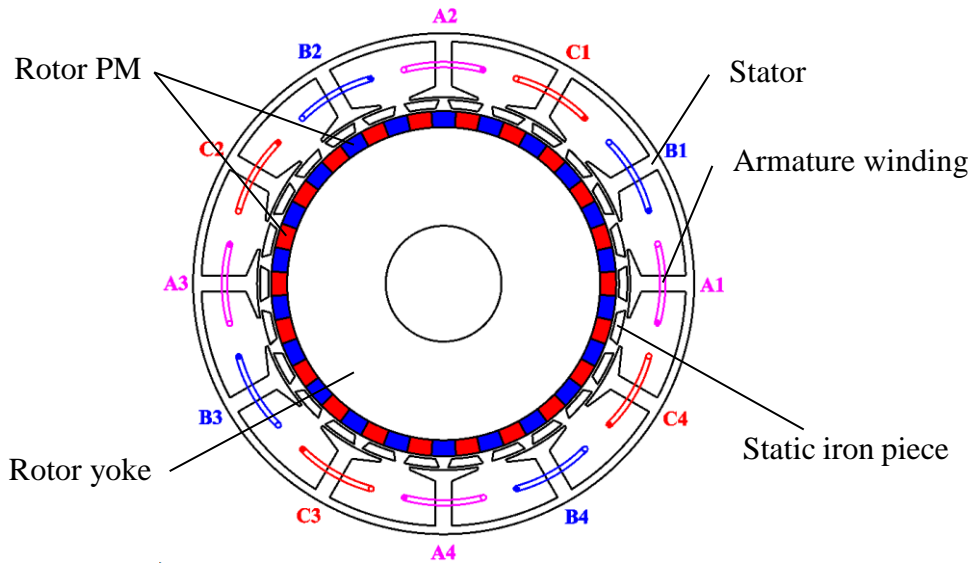


Fig. 1.11 Cross-section of a 4-armature excitation-pole-pair/26-pole/22-PM-pole-pair MG machine.

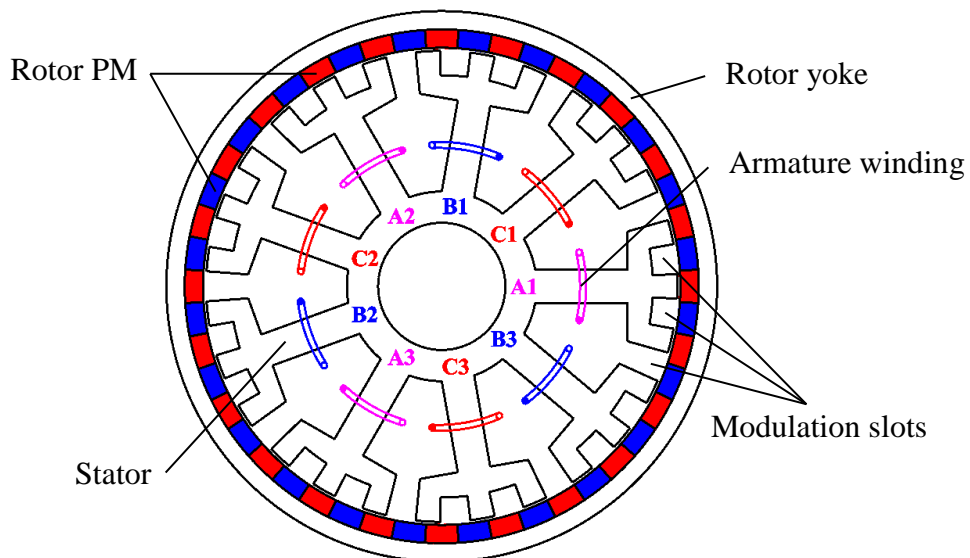


Fig. 1.12 Cross-section of a 3-armature excitation-pole-pair/27-pole/24-PM-pole-pair vernier machine.

Obviously, in the MG machines shown in Fig. 1.11, the static iron pieces and the outer armature winding stator can be integrated to eliminate the air-gap between them, e.g. the 3-armature excitation-pole-pair/27-pole/24-PM-pole-pair vernier machine [LI10a] shown in Fig. 1.12. Compared with the MG machines, the vernier machine shown in Fig. 1.12 has only one air-gap, which means it is much easier to build. Furthermore, if the armature winding stator pole number is the same as the static iron piece number, a flux modulated machine can be achieved, as shown in Fig. 1.13 for a 2-armature excitation-pole-pair/24-pole/22-PM-pole-pair

counterpart [QU11a]. The flux modulated machine shown in Fig. 1.13 has a similar topology to the conventional surface-mounted PM synchronous machine. However, the flux modulated machine operates based on the modulation of the stator slots to the open-circuit and armature excitation MMFs.

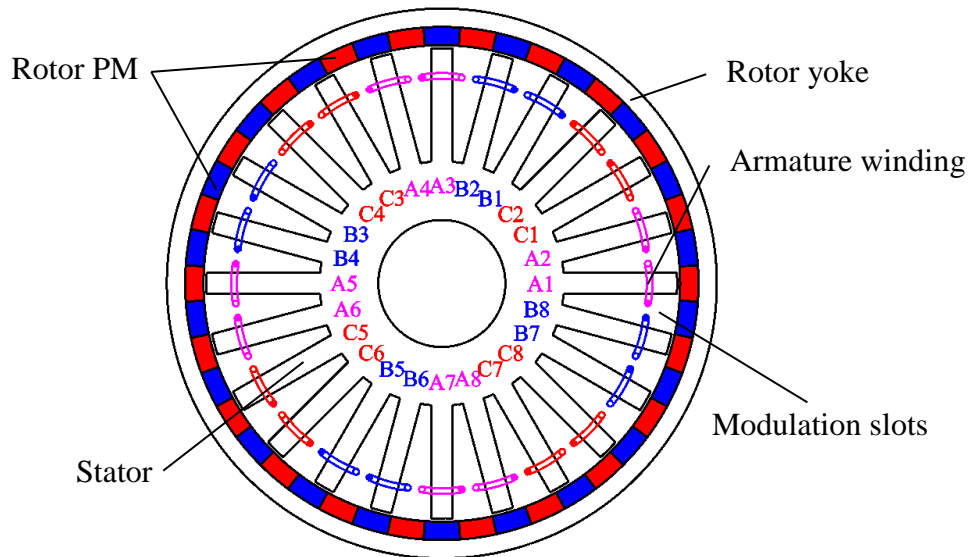


Fig. 1.13 Cross-section of a 2-armature excitation-pole-pair/24-pole/22-PM-pole-pair flux modulated machine.

1.4 PhD Research Scope and Contributions

1.4.1 Scope

The research during the PhD study and in this thesis is mainly divided into the following steps:

- Step 1: Investigation of the operation and interaction mechanisms between the open-circuit and armature excitation MMFs in conventional single-stator-PM machines;
- Step 2: Investigation of the operation and interaction mechanisms between the open-circuit and armature excitation MMFs in the recently proposed and analysed partitioned-stator-PM machines;
- Step 3: Based on the magnetic gearing effect in the partitioned-stator-PM machines investigated in step 2, advanced consequent-pole PM topology and overlapping armature winding topology are applied to the partitioned-stator-PM machines and the resulting electromagnetic performances are investigated.

- Step 4: The PS-FRPM machines and the conventional MG machines, both of which have surface-mounted PMs, are compared in terms of electromagnetic performance.

All of the above theoretical analysis are experimentally validated based on the prototypes.

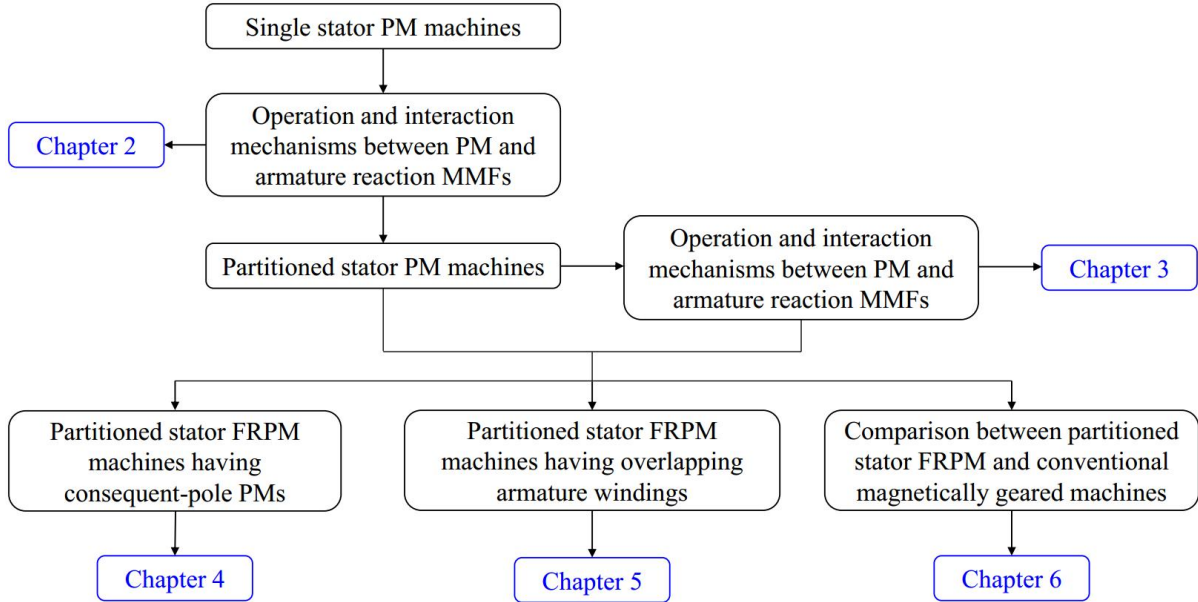


Fig. 1.14 Illustration of research scope and contributions.

The contents of subsequent chapters are summarised as follows:

Chapter 2

In this chapter, the operation and interaction mechanisms between the open-circuit and the armature excitation MMFs in SFPM machines with various topologies and armature winding connections are analysed based on a simple MMF-permeance model. It is found that similar to magnetic gears and MG machines, SFPM machines operate based on the modulation effect of the rotor to the open-circuit and armature excitation MMFs. After modulation, the open-circuit and armature excitation air-gap field harmonics are multi-synchronised, generating an average electromagnetic torque in the air-gap. It is found that more than 95% of the average electromagnetic torque in SFPM machines with N_r -pole rotor and p_{PM} -pole-pair PMs is contributed by the dominant rotating field harmonics in open-circuit and armature excitation fields with the same pole-pair number of $|kN_r \pm (2i-1)p_{PM}|$ ($k=1, i=1, 2, 3$) and static field harmonics with the same pole-pair number of $(2i-1)p_{PM}$ ($i=1, 2, 3$). This analysis is also applicable to other types of stator-excitation machines.

Chapter 3

In this chapter, the operation and interaction mechanisms between the open-circuit and the armature excitation MMFs of the partitioned-stator-PM machines is analysed based on both the outer and inner air-gap open-circuit and armature excitation field harmonics. It is found that the partitioned-stator-PM machines also operate based on the magnetic gearing effect. The modulation of the rotor iron pieces to the open-circuit and armature excitation MMFs is similar to that in magnetic gears and MG machines, as well as conventional single-stator SFPM machines. It is also found that in PS-SFPM machines with N_r -pole rotor and p_{PM} -pole-pair PMs, more than 93% of the electromagnetic torque generated in both the outer and inner air-gaps is contributed by the dominant rotating field harmonics in open-circuit and armature excitation fields with the same pole-pair number of $|kN_r \pm (2i-1)p_{PM}|$ ($k=1, i=1, 2, 3$) and static field harmonics with the same pole-pair number of $(2i-1)p_{PM}$ ($i=1, 2, 3$).

Chapter 4

In this chapter, consequent-pole PMs are applied to the PS-FRPM machines to reduce the PM volume, based on the magnetic gearing effect in the partitioned-stator-PM machines. It is found that the 12-stator-pole PS-FRPM machine having 10-, 11-, 13- and 14-rotor-pole with consequent-pole PMs can generate 98.59%, 96.69%, 95.50% and 97.15% torque density of their corresponding surface-mounted PM counterparts respectively, whilst 28.33%, 30%, 30% and 33.33% of the PM volume can be saved. PS-FRPM machines with consequent-pole PMs can exhibit less than a 1% reduction in efficiency than their surface-mounted PM counterparts.

Chapter 5

In this chapter, based on the magnetic gearing effect, overlapping armature winding topology with the same armature excitation pole-pair numbers is applied to the 12/10-stator/rotor-pole PS-FRPM machines and the electromagnetic performance is comparatively investigated, with the counterpart having non-overlapping windings. It is found that compared with the existing 12/10/12-pole PS-FRPM machine with non-overlapping armature windings, the proposed 24/10/12-pole PS-FRPM machine with overlapping armature windings exhibit less iron loss and PM eddy current loss, larger open-circuit fundamental phase flux-linkage and back-EMF, hence higher torque density but smaller torque ripple, higher efficiency, higher self-inductance and lower mutual inductance, and hence a higher self/mutual-inductance ratio, and better capability to restrict the short-circuit current, as well as much higher flux-weakening capability

when the machine stack length is relatively long. The proposed 24/10/12-pole PS-FRPM machine does, however, suffer from larger end-winding axial length, hence larger total copper loss when the machine stack length is short.

Chapter 6

In this chapter, PS-FRPM machines and conventional MG machines, both of which have surface-mounted PMs operating in both static-PM (STPM) type and rotating-PM (RTPM) types are comparatively analysed in terms of electromagnetic performance. It is found that in both the PS-FRPM and MG machines, the STPM machine has higher phase back-EMF, hence also torque density than its RTPM counterpart, due to its higher electric frequency. The higher iron piece number and PM pole-pair number cause higher synchronous reactance and lower power factor in the MG-STPM and MG-RTPM machines, however, as well as more iron loss, therefore lower efficiency. Overall, the PS-FRPM machine operating in STPM mode has the highest torque density within the whole copper loss range, the highest efficiency, and also the largest power factor. It is also found that to reduce the flux-leakage in a MG machine to obtain a larger electromagnetic torque and a higher power factor, smaller iron piece and PM numbers are preferred. Furthermore, a STPM type machine is recommended to enhance the electric frequency, hence also the phase back-EMF and electromagnetic torque.

Chapter 7

This chapter contains the general conclusions of this thesis and potential future work in this area.

1.4.2 Contributions

The contributions of this thesis are summarised as follows:

- The operation and interaction mechanisms between open-circuit and armature excitation MMFs, i.e. magnetic gearing effect, in both the conventional single-stator-PM machines and the partitioned-stator-PM machines.
- Applying consequent-pole PM topology to the PS-FRPM machines to reduce the PM volume and cost but keep similar torque density and efficiency.
- Applying overlapping armature winding topology to the PS-FRPM machines to achieve higher torque density, higher efficiency, higher fault-tolerance capability, and higher flux-weakening capability etc. when the machine stack length is relatively long.

- The comparative study of the PS-FRPM machines and the conventional MG machines operate in both STPM and RTPM modes will provide a design guide for MG machines.

2 Analysis of Magnetic Gearing Effects in Switched Flux Permanent Magnet Machines

Many topologies were proposed for the conventional stator-permanent magnet (PM) (stator-PM) machines including doubly salient PM, flux reversal PM, and switched flux (SF) PM (SFPM) machines over the last 20 years. However, the operation and interaction mechanisms between the open-circuit and the armature excitation magnetomotive forces (MMFs) have not been investigated yet. In this chapter, this is analysed based on a simple MMF-permeance model for SFPM machines having various topologies and armature winding connections. It is found that similar to magnetic gears and magnetically geared (MG) machines, SFPM machines operate based on the modulation effect of the rotor to the open-circuit and armature excitation MMFs. After modulation, the open-circuit and armature excitation air-gap field harmonics are multi-synchronised, generating average electromagnetic torque in the air-gap. It is found that more than 95% of the average electromagnetic torque in SFPM machines having N_r -pole rotor and p_{PM} -pole-pair PMs are contributed by the dominant rotating field harmonics in open-circuit and armature excitation fields with the same pole-pair number of $|kN_r \pm (2i-1)p_{PM}|$ ($k=1, i=1, 2, 3$) and static field harmonics with the same pole-pair number of $(2i-1)p_{PM}$ ($i=1, 2, 3$). The analysis is also applicable to other types of stator-excitation machines.

This part has been published in IEEE Transactions on Magnetics.

2.1 Introduction

SF machines were firstly proposed in 1955 as a single phase PM generator [RAU55a] and re-emerged as three-phase SFPM machines [ZHU05a] [HOA97a] [HUA08a] [ZHA11a] due to their simple and robust rotor without neither PM nor coil. Different from the conventional interior PM and surface-mounted PM (SPM) machines, a doubly salient structure and stator-PM cause abundant air-gap field harmonics in a SFPM machine. The air-gap field harmonics in SFPM machine are caused by the modulation of the salient rotor to PM and armature excitation fields, similar to the iron pieces to those fields in MG machine [WAN08a] [WAN09a]. In [MCF14a], the torque production mechanism in SFPM machines was recently investigated based on the analysis of air-gap field harmonics. It shows that torque in SFPM machines is produced by air-gap field harmonics due to a pair of heterodyned harmonics of the MMF of the stator magnets and the rotor air-gap permeance, and thus, their torque production

mechanism exhibits similarities to vernier machines [QU11a] and magnetic gears [ATA01a] [ATA04a]. In addition, it is shown in [MCF14a] that in idealized case, increasing the fraction of air-gap that is occupied by rotor teeth, together with the winding factor, is important to increase the produced torque. Indeed, references [ZHU05a] [CHE10a] [CHE11b] show that optimal rotor pole width exists and is found to be around 1/3 for the ratio of rotor pole width to rotor pole pitch for many SFPM machines. In [MOR10a] and [MOR13a], another typical stator-PM machine flux reversal (FR) PM (FRPM) machine with doubly salient topology is analysed from the perspective of the fictitious electrical gear. It is pointed out in [MOR10a] [MOR13a] that the FRPM machine can be regarded as a rotor-PM synchronous machine with a built-in fictitious electrical gear. In [EVA15a] [ZHU15a] [ZHU14a], the similarities between SFPM and FRPM machines and MG machines have been revealed by directly converting them into two partitioned stators and one rotating modulating iron rotor.

In this chapter, modulation of salient rotor and magnetic gearing effect in SFPM machines with different stator/rotor pole combinations, winding configurations and stator lamination segment types are comprehensively investigated based on the air-gap field harmonics by a simple MMF-permeance model. Not only harmonic orders but also rotating speeds of the air-gap field harmonics, and more importantly, many synchronised pairs of open-circuit and armature excitation air-gap field harmonics with same orders and same rotating speeds, can be analytically predicted. The contribution of the dominant pairs of open-circuit and armature excitation air-gap field harmonics to the average electromagnetic torque in SFPM machines will be investigated in this chapter.

This chapter is organized as follows. In section II, modulation of salient rotor and magnetic gearing effect of the conventional 12/10-pole, U-core, all poles wound SFPM machine are evaluated. In section III, the influence of rotor pole number on air-gap field harmonics and magnetic gearing effect is investigated, together with that in alternate poles wound, E- and C-core SFPM machines. Then, in section IV, the contribution of the main field harmonics to the average electromagnetic torque is analysed. Finally, in section V, prototype machines are built and measured in order to verify the FE predicted average static torques in 12-stator-pole U-core all poles wound SFPM machines having 10-, 11-, 13- and 14-rotor-poles.

2.2 Magnetic Gearing Effect in Conventional 12/10-Pole SFPM Machine

The main design parameters of the 12-stator-pole SFPM machines with different rotor pole

numbers shown in Fig. 2.1 are listed in Table 2.1. The coil connection of the SFPM machines can be referred to Fig. 1.2. These dimensional parameters can be referred in the linear illustration shown in Fig. 2.2. In this sub-section, the magnetic gearing effect in the 12/10-pole SFPM machine Fig. 2.1(a) is investigated by a simple MMF-permeance model. In next sub-section 2.3, the contribution of the main air-gap field harmonics will be investigated by FE analysis.

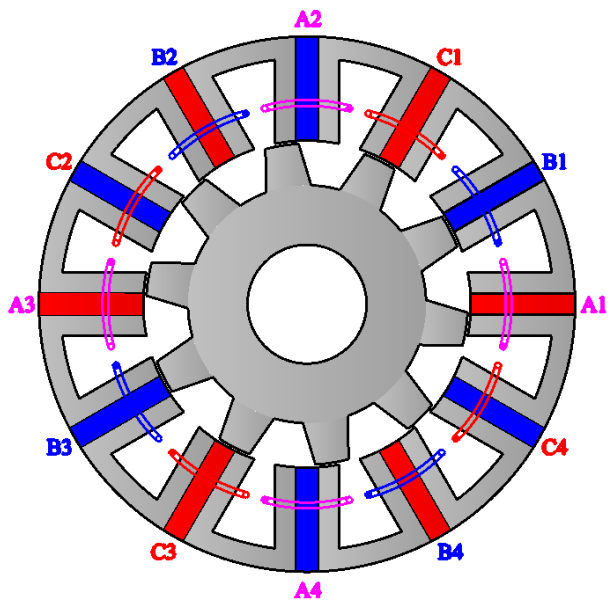
In order to obtain an analytical model for the air-gap flux density, the following assumptions are made:

(1) The permeance of the steel lamination is infinite and hence not saturated, and the flux lines are perpendicular to the steel lamination surface and no tangential component of air-gap flux exists. It should be noted that in practice the steel lamination suffers from saturation. Especially, it is relatively highly saturated in SFPM machine. However, the analytical model adopted here is for clearly showing the air-gap field harmonic orders and rotating speeds, and reveal the modulation of the salient rotor, not for predicting the air-gap field amplitude and hence electromagnetic torque precisely. The accurate air-gap flux density and electromagnetic torque will be calculated by finite element (FE) analyses later.

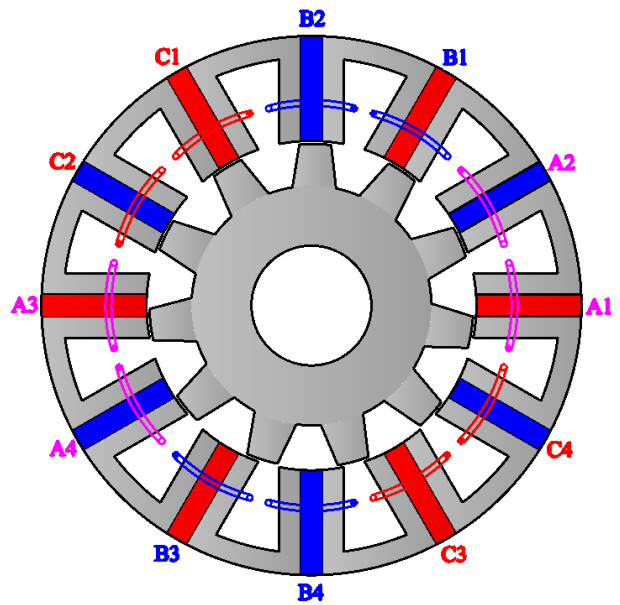
(2) The relative recoil permeability of PM is unit, *i.e.* the same as that of air.

(3) The flux leakage and the effect of finite axial length are neglected.

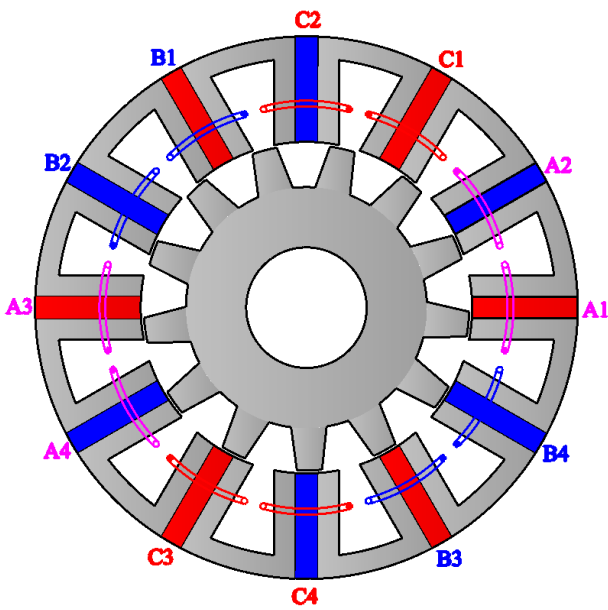
For taking both the rotor and stator saliency into consideration in the MMF-permeance model for clearly showing the modulation effect of rotor poles to the PM open-circuit and armature excitation fields, the rotor saliency is accounted in the air-gap permeance, whilst that of the stator including both slots and PMs is taken into account in PM open-circuit and armature excitation MMFs, as given as follows.



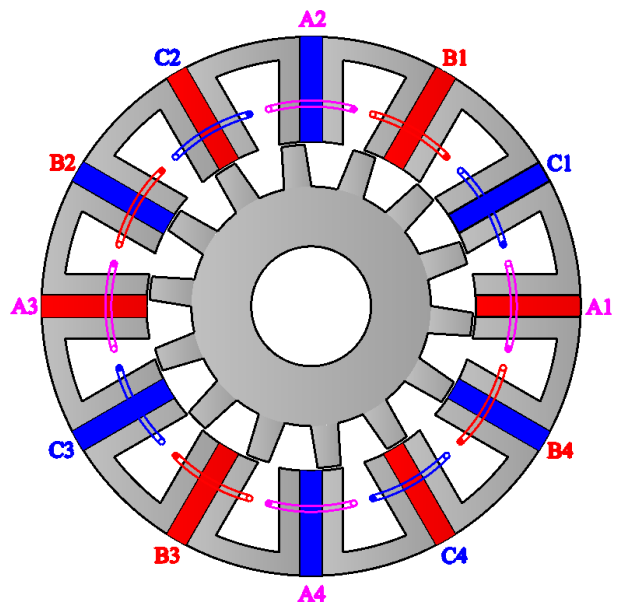
(a) 10-rotor-pole rotor



(b) 11-rotor-pole rotor



(c) 13-rotor-pole rotor



(d) 14-rotor-pole rotor

Fig. 2.1. Cross-section of 3-phase 12-stator-pole SFPM machines with 10-, 11-, 13- and 14-rotor-pole rotors.

Table 2.1 Main Design Parameters of SFPM Machines

Items/stator/rotor pole numbers	Unit	12/10	12/11	12/13	12/14
Stator pole number, N_s	-	12			
PM pole-pair number, p_{PM}	-	6			
Rotor pole number, N_r	-	10	11	13	14
Number of turns per coil, N_c	-	18			
Rotor mechanical angular speed, Ω_r	rpm	400			
Stack length, L_s	mm	25			
Stator outer radius, R_{so}	mm	45			
Stator yoke radius, R_{sy}	mm	41.5			
Stator inner radius, R_{si}	mm	27.5			
Air-gap width, g	mm	0.5			
Rotor outer radius, R_{ro}	mm	27			
Rotor yoke radius, R_{ry}	mm	20			
Rotor inner radius, R_{ri}	mm	10			
PM arc, θ_{PM}	°	7.5			
Stator tooth arc, θ_{st}	°	7.5			
Rotor pole arc, θ_{rp}	°	12	11.25	9	8.25
Rotor yoke arc, θ_{ry}	°	22	21	17	13.2
Angle between initial rotor pole position and horizon line, θ_0	°	-9	-9.55	-5.77	-6.43
Half of PM arc, θ_1	°	3.75			
Half of rotor pole arc, θ_2	°	6	5.625	4.5	4.125
θ_1 +arc of stator tooth, θ_3	°	11.25			
Half of stator tooth arc, θ_4	°	3.75			

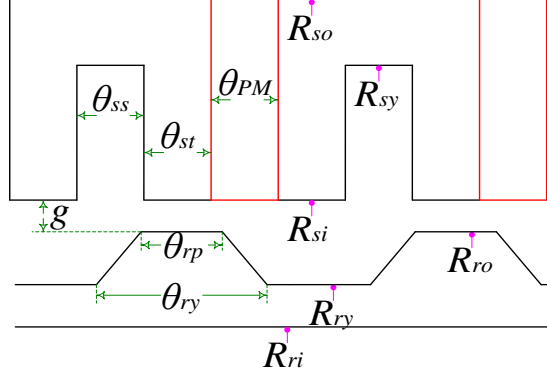


Fig. 2.2. Linear illustration of SFPM machines.

2.2.1 Open-circuit air-gap flux density

The air-gap PM MMF generated by sandwiched PMs in the stator teeth accounting for the stator saliency including both slots and PMs is assumed to be square wave with air-gap circumferential position θ , as shown in Fig. 2.3, and its Fourier series expansion $F_{PM}(\theta)$ is given by (2.1), in which M_{PMi} and S_{PM} are the Fourier coefficients.

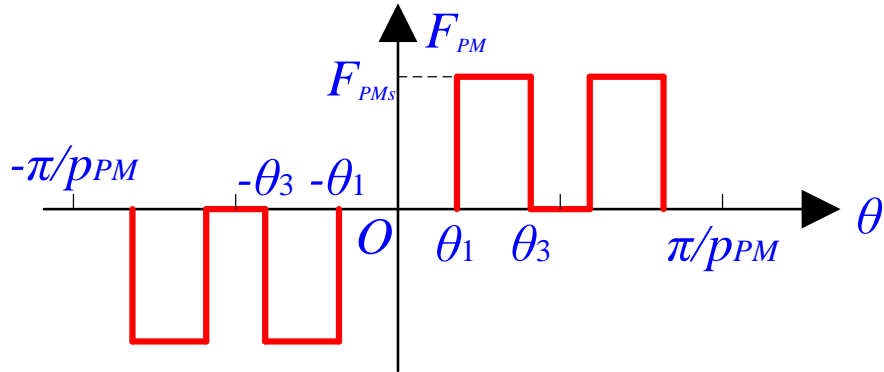


Fig. 2.3. Air-gap PM MMF in SFPM machines accounting for the stator saliency.

$$\begin{cases} F_{PM}(\theta) = S_{PM} \sum_{i=1}^{\infty} \{M_{PMi} \sin[(2i-1)p_{PM}\theta]\} \\ S_{PM} = \frac{4F_{PMs}}{\pi} \\ M_{PMi} = \frac{\cos[(2i-1)p_{PM}\theta_1] - \cos[(2i-1)p_{PM}\theta_3]}{2i-1} \end{cases} \quad (2.1)$$

where p_{PM} , N_r , θ_1 and θ_3 are PM pole-pair number, rotor pole number, the half arc of PM and the half arc of PM plus the arc of stator tooth given in Table 2.1, and F_{PMs} is the PM MMF square waveform peak value.

The air-gap permeance model accounting for rotor slots is presented in Fig. 2.4. For a simple model, the influence of the stator slots and PMs on the air-gap permeance is neglected here, as they do not influence the interaction mechanism between the PMs and the armature excitations. The Fourier series of the air-gap permeance presented in Fig. 2.4 can be obtained as (2.2), in which M_{2k} and S_2 are the Fourier coefficients.

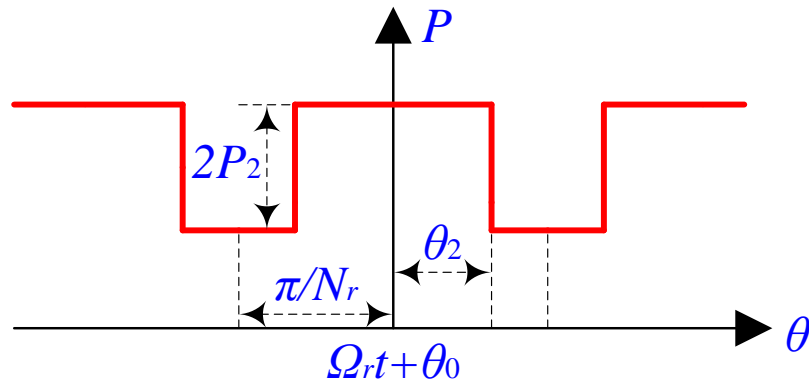


Fig. 2.4. Air-gap permeance model accounting for rotor slots.

$$\begin{cases} P(\theta, t) = P_0 + S_2 \sum_{k=1}^{\infty} \{M_{2k} \cos[kN_r(\theta - \Omega_r t - \theta_0)]\} \\ S_2 = \frac{4P_2}{\pi} \\ M_{2k} = \frac{\sin(kN_r\theta_2)}{k} \end{cases} \quad (2.2)$$

where Ω_r , θ_0 and θ_2 are the rotor speed in rad/s, the angle between initial rotor pole position and horizon line, and the half arc of rotor pole given in Table 2.1, whilst P_0 and P_2 are the DC component and peak-to-peak value of permeance waveform in Fig. 2.4.

Therefore, the open-circuit PM air-gap flux density distribution $B_{PM}(\theta, t)$ can be deduced by multiplying $F(\theta)$ and $P(\theta, t)$ from (2.1) and (2.2),

$$\left\{ \begin{aligned}
B(\theta, t) &= F_{PM}(\theta)P(\theta, t) = P_0 S_{PM} \sum_{i=1}^{\infty} \{M_{PMi} \sin[(2i-1)p_{PM}\theta]\} \\
&\quad + \frac{S_{PM}S_2}{2} \sum_{i=1}^{\infty} \sum_{k=1}^{\infty} [M_{PMi}M_{2k}(\cos \alpha_1 + \cos \alpha_2)] \\
\alpha_1 &= [kN_r + (2i-1)p_{PM}] \left[\theta - \frac{kN_r(\Omega_r t + \theta_0) + \frac{\pi}{2}}{kN_r + (2i-1)p_{PM}} \right] \\
\alpha_2 &= [kN_r - (2i-1)p_{PM}] \left[\theta - \frac{kN_r(\Omega_r t + \theta_0) - \frac{\pi}{2}}{kN_r - (2i-1)p_{PM}} \right]
\end{aligned} \right. \quad (2.3)$$

Table 2.2 Characteristics of PM Open-Circuit Air-Gap Field Harmonics in SFPM Machines

No.	Pole-Pairs	Rotating Speed, $N_r\Omega_r$
1	$(2i-1)p_{PM}$	0 (static)
2	$kN_r + (2i-1)p_{PM}$	$\frac{k}{kN_r + (2i-1)p_{PM}}$
3	$ kN_r - (2i-1)p_{PM} $	$\frac{k}{kN_r - (2i-1)p_{PM}}$

The characteristics of open-circuit air-gap flux density spatial harmonics accounting for rotor slots are listed in Table 2.2. Since the PMs and hence PM MMFs in SFPM machines are static, static air-gap field harmonics having $(2i-1)p_{PM}$ -pole-pair ($i=1, 2, 3\dots$) exist under open-circuit operation condition as No.1 in Table 2.2. More importantly, due to the modulation of the N_r -pole salient rotor to the p_{PM} -pole-pair PM magnetic field, air-gap rotating field harmonics having pole-pairs of $|kN_r \pm (2i-1)p_{PM}|$ ($k, i=1, 2, 3\dots$) are generated as No.2 and No.3 in Table 2.2, respectively. It should be noted that the positive or negative rotating speeds mean that the corresponding field harmonic rotates forward or backward to the rotor, respectively.

2.2.2 Armature excitation air-gap flux density

Fig. 2.5 shows the air-gap MMF of armature excitation in the 12/10-pole SFPM machine accounting for the stator saliency including both slots and PMs, where i_A, i_B, i_C are the phase currents respectively and given as,

$$\begin{cases} i_A = \sqrt{2}I_{rms} \sin(\omega_e t) \\ i_B = \sqrt{2}I_{rms} \sin\left(\omega_e t - \frac{2\pi}{3}\right) \\ i_C = \sqrt{2}I_{rms} \sin\left(\omega_e t + \frac{2\pi}{3}\right) \end{cases} \quad (2.4)$$

where I_{rms} and N_c are phase current RMS current and number of coil turns, respectively. The relationship between ω_e and Ω_r is given as,

$$\omega_e = N_r \Omega_r \quad (2.5)$$

The Fourier series expansion of the air-gap MMF shown in Fig. 2.5 can be derived as,

$$\begin{cases} F_{ABC}(\theta, t) = \frac{3S_{ABC}}{2} \sum_{q=1}^{\infty} [M_{ABCq} \sin(\xi)] \\ S_{ABC} = \frac{2\sqrt{2}N_c I_{rms}}{\pi} \\ M_{ABCq} = \frac{1}{q} [\sin(4q\theta_3) - \sin(4q\theta_1)] \\ \xi = \begin{cases} -4q\theta + N_r \Omega_r t, q = 3r - 2 \\ 4q\theta + N_r \Omega_r t, q = 3r - 1 \\ 0, q = 3r \end{cases} \end{cases} \quad (2.6)$$

where S_{ABC} and M_{ABCq} are the Fourier series coefficients, and r is a positive integer.

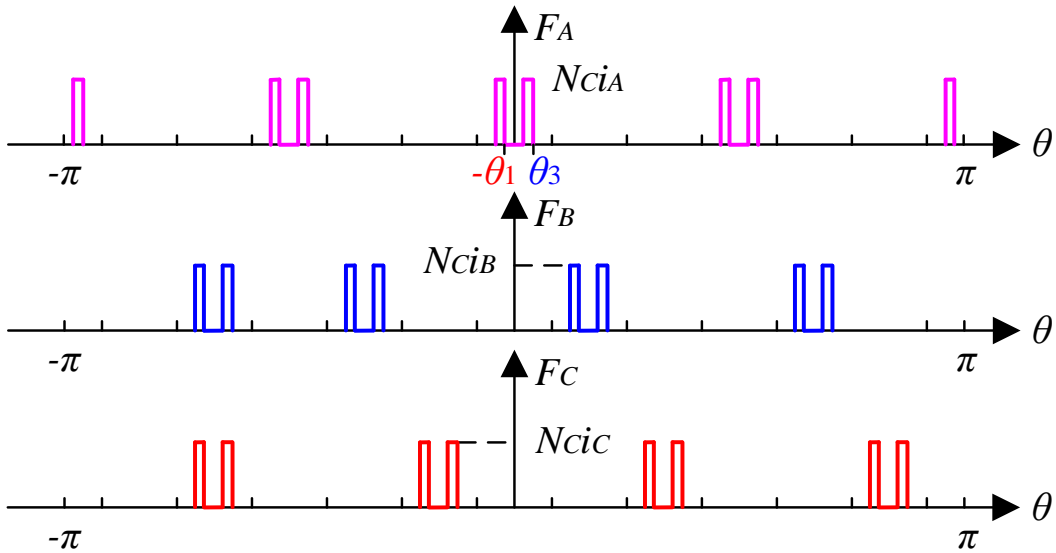


Fig. 2.5. Air-gap MMF of armature excitation in 12/10-pole SFPM machine accounting for the stator saliency ($i_A=i_B=i_C$).

In [MCF14a], the modulation of rotor poles to the armature excitation MMF is not given.

Here, it is conducted as follows.

The armature excitation air-gap flux density distribution $B_{ABC}(\theta, t)$ can be deduced by multiplying $F_{ABC}(\theta)$ and $P(\theta, t)$ from (2.6) and (2.2),

$$B_{ABC}(\theta, t) = F_{ABC}(\theta, t)P(\theta, t) \quad (2.7)$$

When $q=3r-2$ ($q=1, 4, 7, \dots$), B_{ABC} is given by (2.8) and (2.9). When $q=3r-1$ ($q=2, 5, 8, \dots$), B_{ABC} can also be expressed by (2.8) and (2.9) with the coefficient of q multiplied by “-1”.

$$B_{ABC}(\theta, t) = \frac{3P_0 S_{ABC}}{2} \sum_{q=1}^{\infty} \left\{ M_{ABCq} \cos \left[4q\theta - N_r \Omega_r t + \frac{\pi}{2} \right] \right\} \\ + \frac{3S_{ABC} S_2}{4} \sum_{q=1}^{\infty} \sum_{k=1}^{\infty} [M_{ABCq} M_{2k} (\cos \beta_1 + \cos \beta_2)] \quad (2.8)$$

$$\begin{cases} \beta_1 = (kN_r - 4q) \left[\theta - \frac{(k-1)N_r \Omega_r t + kN_r \theta_0 + \frac{\pi}{2}}{kN_r - 4q} \right] \\ \beta_2 = (kN_r + 4q) \left[\theta - \frac{(k+1)N_r \Omega_r t + kN_r \theta_0 - \frac{\pi}{2}}{kN_r + 4q} \right] \end{cases} \quad (2.9)$$

The characteristics of armature excitation air-gap flux density spatial harmonics accounting for rotor slots are listed in Table 2.3 and Table 2.4 for $q=3r-2$ and $q=3r-1$, respectively. Due to the modulation of fundamental rotor permeance ($k=1$) to the armature excitation MMF, static field harmonics can be obtained with pole-pair numbers $|N_r-4q|$ for $q=3r-2$ and N_r+4q for $q=3r-1$. When $q=3r-2$, the pole-pair numbers of armature excitation air-gap static field harmonics are given in (2.10). Obviously, the field harmonics of pole-pair numbers shown in (2.10) are exactly synchronous to those of $(2i-1)p_{PM}$ ($i=1, 2, 3, \dots$) given in Table 2.2. As for the pole-pair numbers of armature excitation air-gap static field harmonics with $q=3r-1$, it is shown in (2.11). Again, they are completely synchronous to those of $(2i-1)p_{PM}$ ($i=2, 3, \dots$) given in Table 2.2.

$$|N_r - 4q| = |18 - 12r| = \begin{cases} p_{PM}, \text{ when } r = 1 \\ [2(r-1) - 1]p_{PM}, \text{ when } r \geq 2 \end{cases} \quad (2.10)$$

$$N_r + 4q = 12r + 6 = [2(r+1) - 1]p_{PM} \quad (2.11)$$

Besides the static field harmonics, rotating ones are also generated in the air-gap. They are

also synchronous to their PM open-circuit counterparts given in Table 2.2. This is explained as follows.

For No.1~No.3 in Table 2.3, the pole-pair numbers of rotating field harmonics can be rewritten as (2.12)-(2.14). (2.12) and (2.14) are identical to No.2 in Table 2.2, whilst (2.13) is equal to No.3 in Table 2.2, respectively.

$$4q = 12r - 8 = N_r + [2(r - 1) - 1]p_{PM} \quad (2.12)$$

$$|kN_r - 4q| = |10k - 12r + 8| = |(k - 1)N_r - [2(r - 1) - 1]p_{PM}| \quad (2.13)$$

$$kN_r + 4q = 10k + 12r - 8 = (k + 1)N_r + [2(r - 1) - 1]p_{PM} \quad (2.14)$$

As for No.1~No.3 in Table 2.4, the pole-pair numbers of rotating field harmonics are given in (2.15)-(2.17). (2.15) and (2.17) are the same with No.3 in Table 2.2, whilst (2.16) is equal to No.2 in Table 2.2.

$$4q = 12r - 4 = -\{N_r - [2(r + 1) - 1]p_{PM}\} \quad (2.15)$$

$$kN_r + 4q = 10k + 12r - 4 = (k - 1)N_r + [2(r + 1) - 1]p_{PM} \quad (2.16)$$

$$|kN_r - 4q| = |10k + 12r - 8| = |(k + 1)N_r - [2(r + 1) - 1]p_{PM}| \quad (2.17)$$

Table 2.3 Characteristics of Armature Excitation Air-Gap Flux Density Elements in 12/10-Pole SFPM Machines, $q=3r-2$

No.	Pole-Pairs	Rotating Speed, $N_r\Omega_r$
1	$4q$	$\frac{1}{4q}$
2	$ kN_r - 4q $	$\frac{k - 1}{kN_r - 4q}$
3	$kN_r + 4q$	$\frac{k + 1}{kN_r + 4q}$

Table 2.4 Characteristics of Armature Excitation Air-Gap Flux Density Elements in 12/10-Pole U-Core SFPM Machines, $q=3r-1$

No.	Pole-Pairs	Rotating Speed, $N_r\Omega_r$
1	$4q$	$-\frac{1}{4q}$
2	$kN_r + 4q$	$\frac{k-1}{kN_r + 4q}$
3	$ kN_r - 4q $	$\frac{k+1}{kN_r - 4q}$

2.2.3 Magnetic gearing effect

As foregoing analysed, after being modulated by rotor permeance, PM open-circuit and armature excitation air-gap field harmonics synchronous to each other, including both rotating and static ones, with both the same rotor pole-pair number and rotating speed.

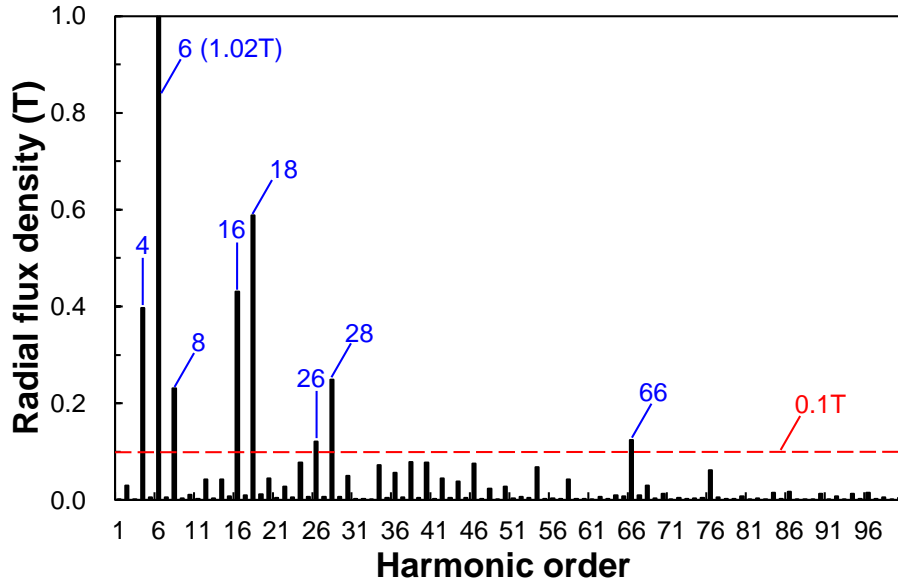
PMs with $p_{PM}=6$ pole-pairs are static in 12-stator-pole SFPM machine, which leads to static air-gap PM MMF. However, due to the modulation of the rotor permeance to the static PM MMF, rotating field harmonics with pole-pair number $|kN_r \pm (2i-1)p_{PM}|$ ($k, i=1, 2, 3\dots$) can be generated in the air-gap. More importantly, they are synchronous to those rotating field harmonics caused by armature excitation as foregoing analysed.

Although armature excitation MMFs of three-phase armature windings injected by symmetrical sinusoidal time-variant currents are rotating, air-gap static field harmonics can be obtained due to the modulation of the fundamental rotor permeance. The pole-pairs of these air-gap static field harmonics are the same with those generated by static PM MMF, *i.e.* $(2i-1)p_{PM}$ ($i=1, 2, 3\dots$).

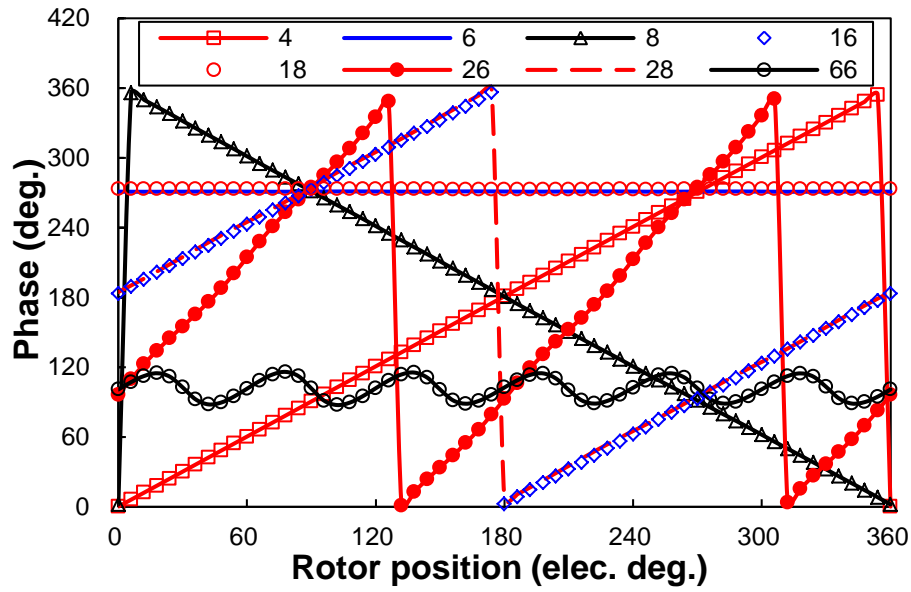
Consequently, it can be concluded that the 12/10-pole SFPM machine is a multi-harmonic synchronous machine, with many pairs of synchronised PM open-circuit and armature excitation fields harmonics. This can be verified by FE analysis as shown from Fig. 2.6 to Fig. 2.9 for open-circuit and armature excitation in the machines with and without consideration of saturation in the lamination steel. The armature excitation air-gap field harmonics in machine with saturated and non-saturated lamination steel shown in Fig. 2.8 and Fig. 2.9 are very similar, in terms of both amplitudes and rotating speeds. This can be explained by the low saturation in the lamination steel under armature excitation. As may be expected, the saturation degree will

be higher with larger armature winding current and hence MMF. As shown in Fig. 2.6 and Fig. 2.7, those for PM open-circuit are different. The air-gap field harmonics in the machine with non-saturated lamination steel have higher amplitudes generally, due to the high PM open-circuit saturation practically as aforementioned. However, the rotating speeds are the same. Therefore, it can be observed that the saturation which is not taken into consideration in the previous analytical MMF-permeance model only influence the air-gap field harmonics amplitudes, not the rotating speed. More importantly, the machines with and without consideration of saturation in the lamination steel have similar dominant air-gap field harmonics.

The modulation of rotor to the PM open-circuit and armature excitation fields in SFPM machine is similar to that of iron pieces to those fields in MG machine [WAN08a] [WAN09a]. The interaction of these synchronised harmonics pairs will generate electromagnetic torque. As shown in Fig. 2.6(a) and Fig. 2.7(a), the dominant air-gap field harmonics are with pole-pair numbers 4, 8, 16 and 28 ($|kN_r \pm (2i-1)p_{PM}|$ when $(k=1, i=1, 2)$) due to modulation of the fundamental rotor permeance and 6, 18 ($(2i-1)p_{PM}$ when $(i=1, 2)$) without modulation for rotating and static ones, as derived in (2.3). The higher armature excitation air-gap field harmonics are with pole-pairs of 4, 6, 8, 14, 16 and 20 as illustrated in Fig. 2.8(a) and Fig. 2.9(a). The dominant air-gap field harmonic orders for armature excitation are $4q$ ($r=1, 2$ and $q=1, 2, 4, 5$), *i.e.* 1, 4, 16, 20, without modulation of the salient rotor, and kN_r+4q ($k=1, q=1$) resulted from the modulation of the fundamental rotor permeance and the fundamental armature excitation MMF, as derived in (2.8) and (2.9). This implies that those dominant air-gap field harmonics may contribute to most of the average electromagnetic torque, as will be shown later. It is worth noting that the number of elements in the air-gap for finite element analysis is 1200 in this chapter.

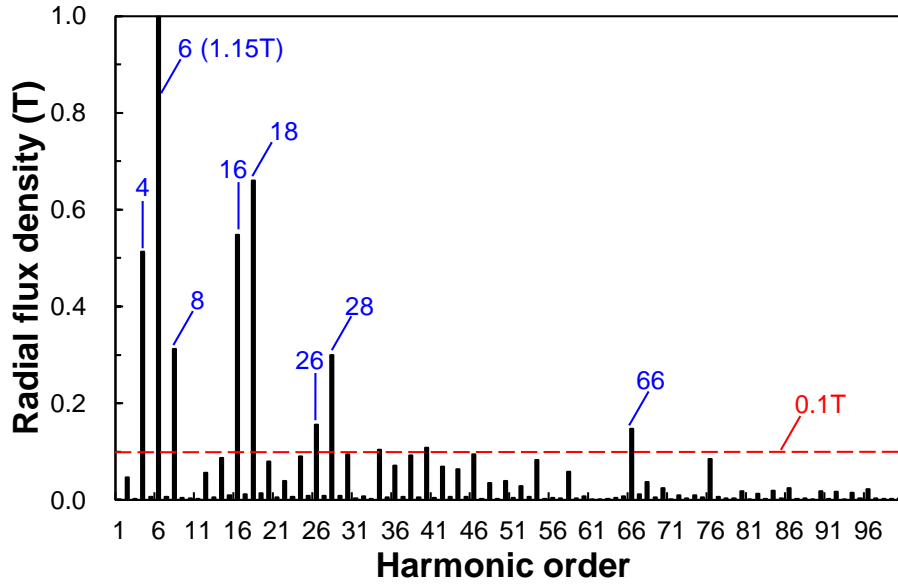


(a) Amplitude (rotor position $\delta=0$)

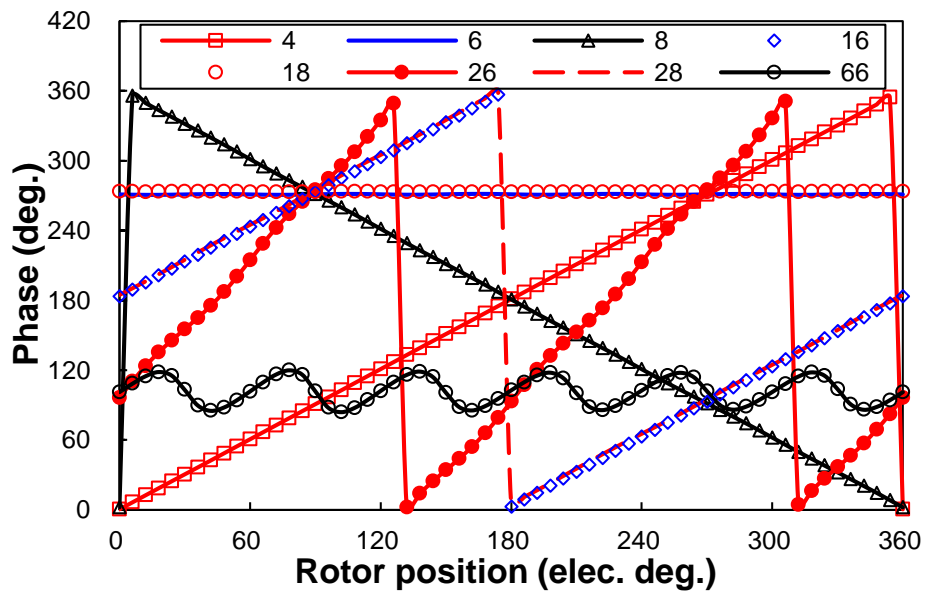


(b) Phases of harmonics larger than 0.1T

Fig. 2.6. FE predicted open-circuit air-gap radial field harmonics of 12/10-pole SFPM machine with saturated lamination steel.

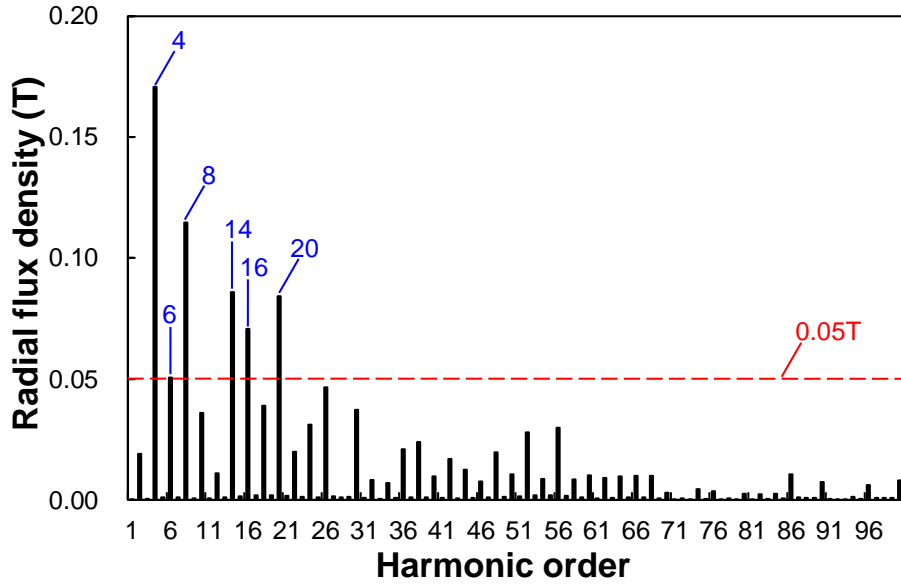


(a) Amplitude (rotor position $\delta=0$)

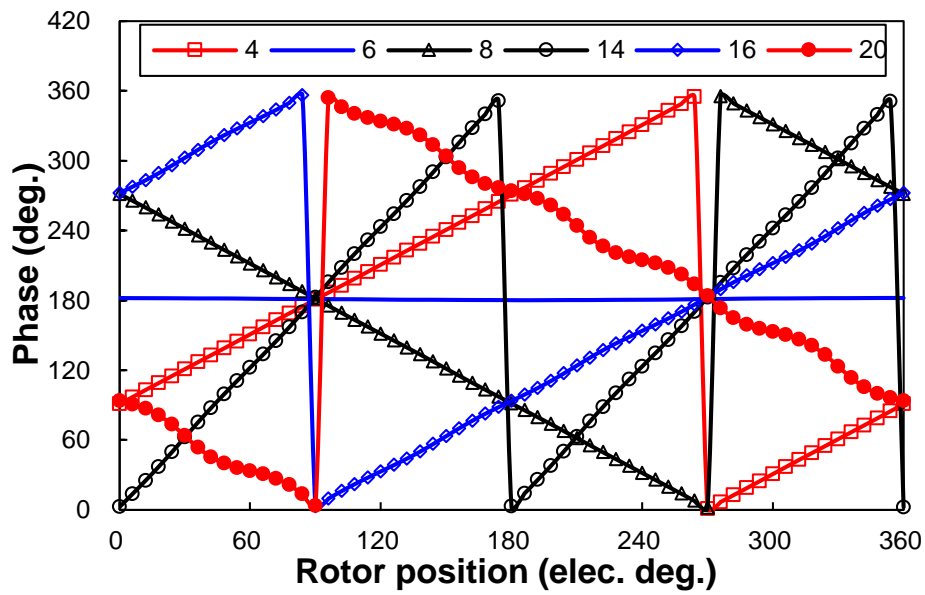


(b) Phases of harmonics shown in Fig. 2.6(b)

Fig. 2.7. FE predicted open-circuit air-gap radial field harmonics of 12/10-pole SFPM machine with non-saturated lamination steel.

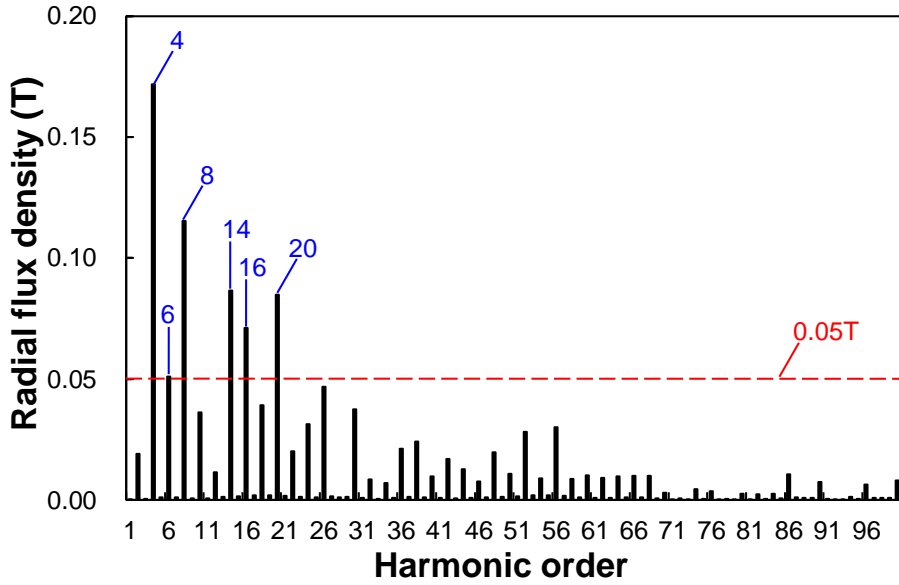


(a) Amplitude (rotor position $\delta=0$)

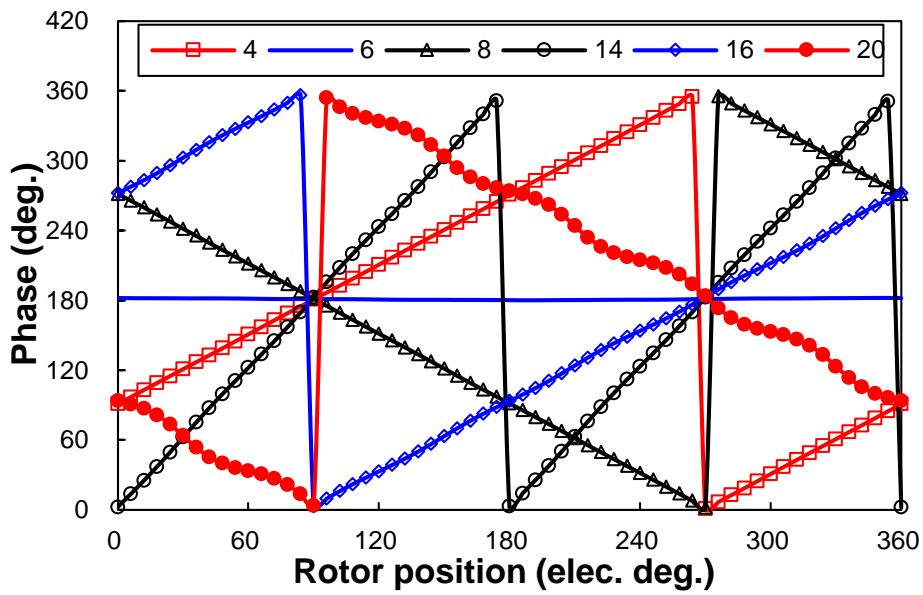


(b) Phases of harmonics larger than 0.05T

Fig. 2.8. FE predicted armature excitation air-gap radial field harmonics of 12/10-pole SFPM machine with saturated lamination steel ($p_{cu}=20W$, phase current and phase back-EMF have the same phase angle).



(a) Amplitude (rotor position $\delta=0$)



(b) Phases of harmonics shown in Fig. 2.8(b)

Fig. 2.9. FE predicted armature excitation air-gap radial field harmonics of 12/10-pole SFPM machine with non-saturated lamination steel ($p_{cu}=20W$, phase current and phase back-EMF have the same phase angle).

2.3 Magnetic Gearing Effect in Various SFPM Machine Topologies

2.3.1 All poles wound SFPM machines having different rotor pole numbers

In [CHE10a], the rotor pole number in 12-stator-pole SFPM machine is expanded from 10 to 11, 13 and 14. The electromagnetic performance of 12-stator-pole SFPM machines with different rotor pole numbers is investigated by a lumped circuit model in [CHE10b]. In this section, the magnetic gearing effect in 12-stator-pole SFPM machines having 11-, 13- and 14-rotor-poles is analysed. The dominant open-circuit air-gap field harmonics in 12-stator-pole SFPM machines having 11-, 13- and 14-rotor-poles with $|aN_r \pm (2b-1)p_{PM}|$ ($a=1, b=1, 2$) and $(2b-1)p_{PM}$ ($b=1, 2$) for rotating and static ones have been synthesised in Table 2.5. Although the field harmonics in the air-gap for armature excitation are complicated, they can be analytically predicted by the MMF-permeance model as listed in Appendix A for 12/11-, 12/13- and 12/14-pole SFPM machines, respectively.

Table 2.5 Characteristics of Dominant PM Open-Circuit Air-Gap Field Harmonics in SFPM Machines

Rotating direction	Formula	k	i	10	11	13	14
Static	$(2i - 1)p_{PM}$	-	1	6			
		-	2	18			
Forward	$kN_r + (2i - 1)p_{PM}$	1	1	16	17	19	20
		1	2	28	29	31	32
Forward	$ kN_r - (2i - 1)p_{PM} $	1	1	4	5	7	8
Backward		1	2	8	7	5	4

As shown in Appendix A, similar to the 12/10-pole SFPM machine, there are armature excitation static field harmonics also with $(2i-1)p_{PM}$ -pole-pair ($i=1, 2, 3\dots$) existing in the air-gap of 12/11-, 12/13- and 12/14-pole SFPM machines due to the modulation of the rotor permeance fundamental component to the p_{ea} -pole-pair rotating armature MMF with same rotating speed.

More importantly, the equivalent pole-pair number p_{ea} of the uppermost forward rotating harmonic corresponding to different coil connections are 4, 5, 7, and 8 for 12-stator-pole SFPM

machines having 10-, 11-, 13- and 14-rotor-poles respectively as given in Fig. 2.10 by FE analysis. In Fig. 2.10, 5th and 4th harmonics for 13- and 14-rotor-pole SFPM machines are backward rotating.

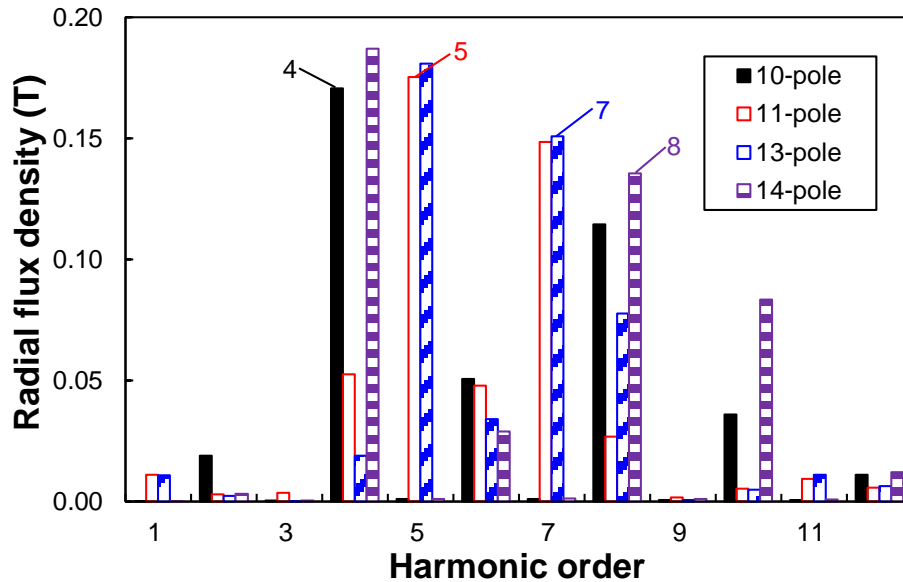


Fig. 2.10. FE predicted armature excitation air-gap radial field harmonics spectra of 12-stator-pole SFPM machine ($p_{cu}=20W$, phase current and phase back-EMF have the same phase angle).

It can be shown that the harmonic with pole-pair number p_{ea} is exactly synchronous to that modulated by fundamental rotor permeance to static PM MMF having $(N_r - p_{PM})$ -pole-pair as given in Table 2.5, as well as other dominant field harmonics. Therefore, this phenomenon that the modulation of the rotor to the static PM and rotating armature magnetic fields is designated here as ‘magnetic gearing effect’ in SFPM machines. The relationship between p_{ea} , N_r and p_{PM} is governed by,

$$N_r = p_{PM} + p_{ea} \quad (2.18)$$

This is similar to (2.19) and (2.20) for the magnetic gears [ATA01a] [ATA04a] and MG machines [WAN08a] [WAN09a], respectively.

$$N_{ip} = p_o + p_i \quad (2.19)$$

where p_o and p_i are the outer and inner PM pole-pair numbers and N_{ip} is the iron piece number in a magnetic gear.

$$N_{ip} = p_{PM} + p_{ea} \quad (2.20)$$

where p_{PM} and p_{ea} are the PM pole-pair number and equivalent pole-pair number of armature windings whilst N_{ip} is also the iron piece number in a MG machine.

Similar to a magnetic gear with rotating iron pieces and outer PMs [ATA04a], the magnetic gearing ratio in SFPM machines and substituting rotating armature excitation field is defined as,

$$G_r = \frac{N_r}{p_{ea}} = \frac{p_{PM} + p_{ea}}{p_{ea}} \quad (2.21)$$

The magnetic gearing characteristics of 12-stator-pole SFPM machines with different rotor pole number are given in Table 2.6. p_{ea} of armature windings increases with rotor pole number, and consequently the gearing ratio G_r decreases from 2.5 to 1.75.

Table 2.6 Magnetic Gearing Characteristics in 12-Stator-Pole SFPM Machines with Different Rotor Pole Numbers

N_s	p_{PM}	N_r	p_{ea}	G_r
12	6
		10	4	2.5
		11	5	2.2
		12	6	2
		13	7	1.86
		14	8	1.75
	

2.3.2 Alternate poles wound SFPM machines

In the previous section, SFPM machines have all poles wound with armature windings. In this section, magnetic gearing effect in SFPM machines with alternate poles wound windings is investigated, e.g. 12/10-pole one as shown in Fig. 2.11(b). It should be noted that the dimensional parameters of the 12/10-pole SFPM machine with all and alternate poles wound windings are the same, except the different winding configurations.

The winding type is A1-C1-B1-A2-C2-B2 anti-clockwise in 12/10-pole SFPM machine with alternate armature windings Fig. 2.11(b), whilst the 12/14-pole all poles wound SFPM machine with all poles wound has a double winding type Fig. 2.1(d), *i.e.* A1-C1-B1-A2-C2-B2-A3-C3-B3-A4-C4-B4 anti-clockwise. p_{ea} in the 12/14-pole SFPM machine with all poles wound is 8 as foregoing analysed. However, p_{ea} in 12/10-pole SFPM machine with alternate armature windings is half of that of 12/14-pole all poles wound SFPM machine, *i.e.* 4. This is the same with the 12/10-pole SFPM machine with all poles wound, Fig. 2.11(a). Consequently, p_{ea} , p_{PM} , N_r also match the equation (2.18). More importantly, the gearing ratios are the same in SFPM machines with all and alternate poles wound.

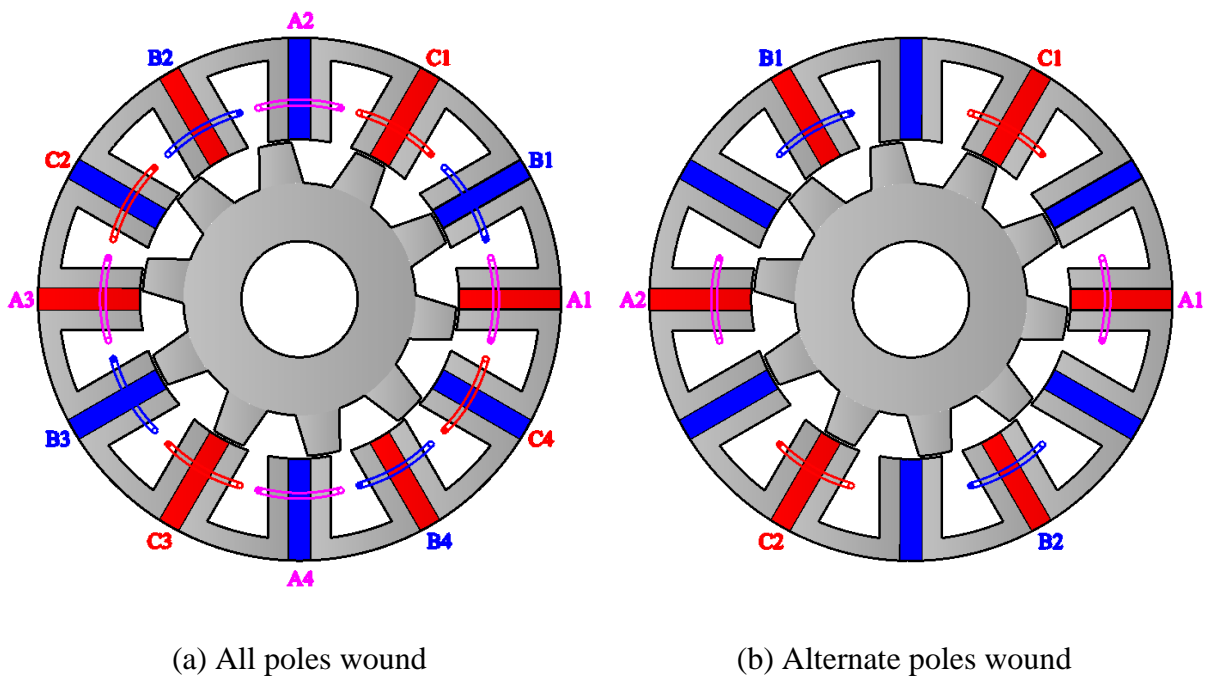


Fig. 2.11. Cross-section of 12/10-pole SFPM machine with all and alternate poles wound armature windings.

2.3.3 E- and C-core SFPM machines

In the previous analysis, the magnetic gearing effect in the SFPM machines with conventional U-core lamination segments is investigated. In [CHE11b] [CHE11c], developed SFPM machines with E- and C-core lamination segments exhibiting higher torque density due to larger slot area are proposed and analysed, respectively. For 12/10-pole SFPM machine with U-core stator lamination segment, Fig. 2.1(a), its 6/10-pole E- and C-core counterparts with same dimensional parameters are shown in Fig. 2.12(a) and Fig. 2.12(b), respectively. Coil numbers in 6/10-pole E- and C-core SFPM machines are the same with that of 12/10-pole

SFPM machine with alternate armature windings, Fig. 2.11(b), *i.e.* 6. However, p_{ea} is variant due to different coil polarities. p_{ea} in 6/10-pole SFPM machine having E- and C-core can be obtained as follows.

Fig. 2.13 illustrates the air-gap armature excitation MMF of 6/10-pole SFPM machine with E- and C-core accounting for the stator saliency. The Fourier series expansion of the air-gap MMF shown in Fig. 2.13 is given by,

$$\begin{cases} F_{ABC}(\theta, t) = \sum_{q=1}^{\infty} \left[\frac{3S_{ABC}}{2} M_{ABCq} \sin(\xi) \right] \\ S_{ABC} = \frac{4\sqrt{2}N_c I_{rms}}{\pi} \\ \xi = \begin{cases} -q\theta + N_r \Omega_r t, q = 6r - 5 \\ q\theta + N_r \Omega_r t, q = 6r - 1 \\ 0, q = \text{else} \end{cases} \end{cases} \quad (2.22)$$

where M_{ABCq} for E-core machine is,

$$M_{ABCq} = \frac{1}{q} [\sin(q\theta_3) - \sin(q\theta_1) + 2\sin(q\theta_4)\cos(\frac{q\pi}{6})] \quad (2.23)$$

and for C-core machine M_{ABCq} is,

$$M_{ABCq} = \frac{1}{q} [\sin(q\theta_3) - \sin(q\theta_1)] \quad (2.24)$$

where θ_4 is the half arc of stator tooth given in Table 2.1.

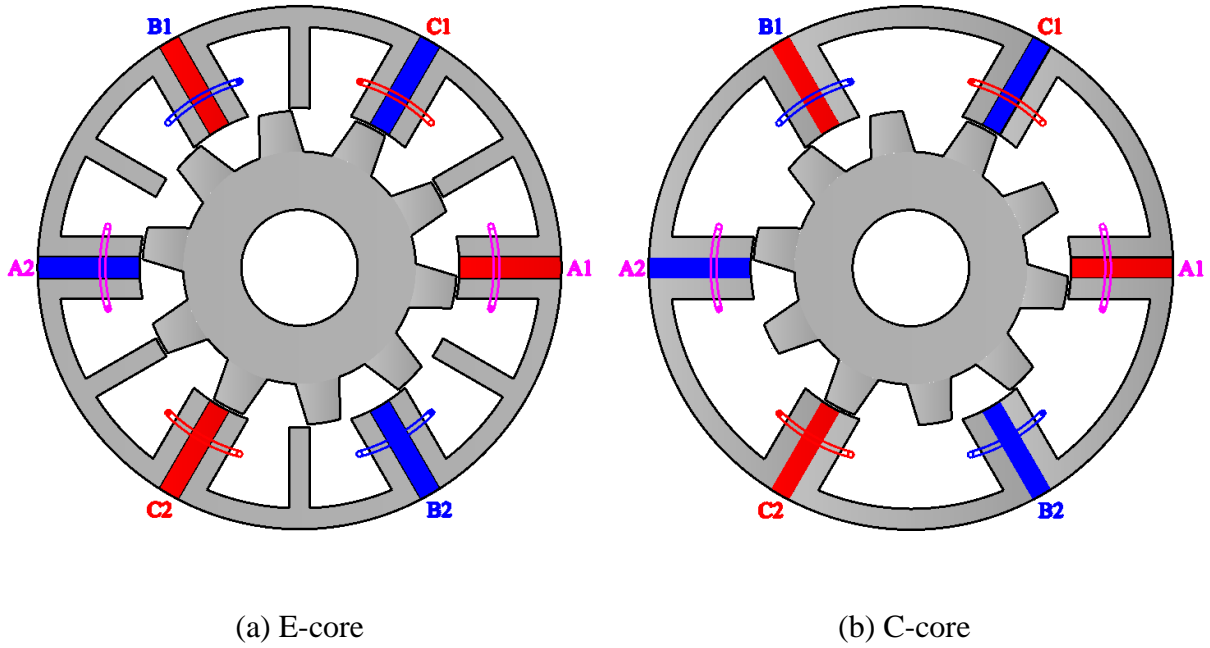
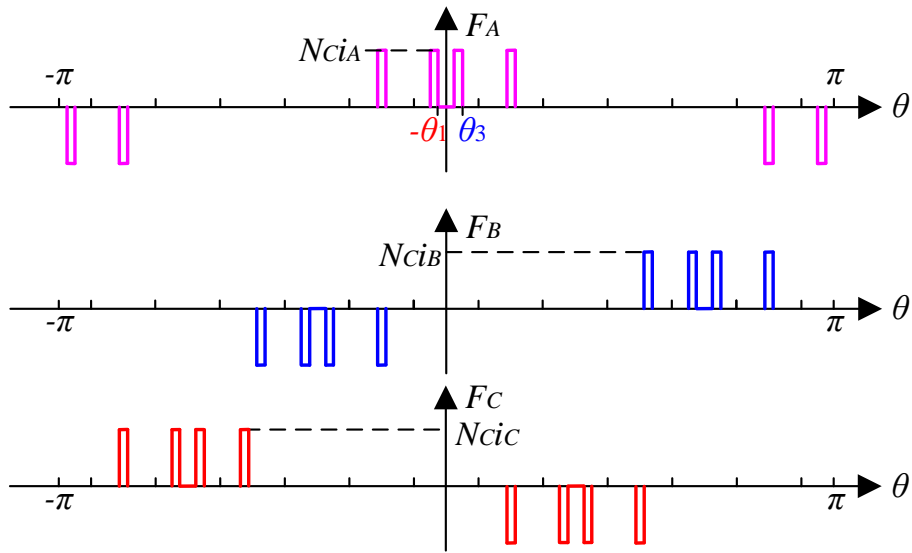
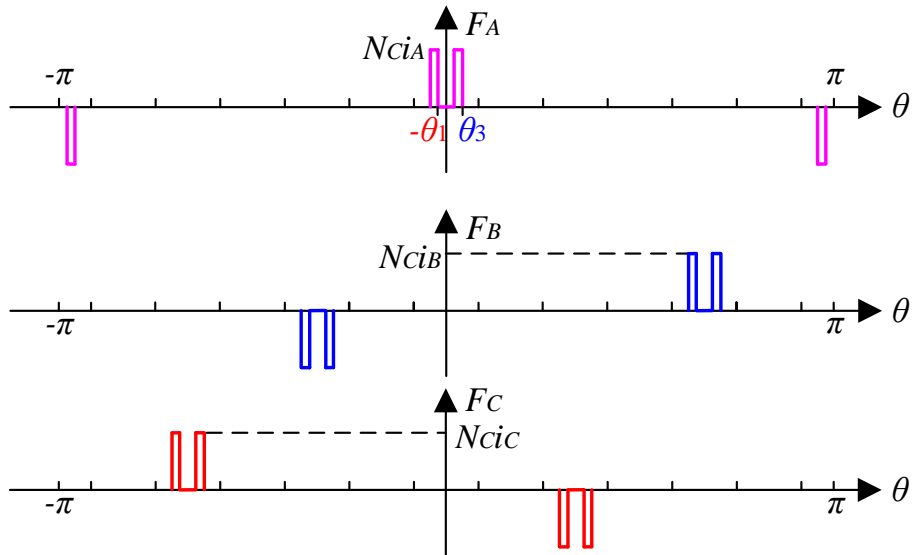


Fig. 2.12. Cross-section of 6/10-pole SFPM machine with E-core and C-core stator lamination segments.

As shown in (2.22), the equation is similar to 12/13-pole SFPM machine shown in Appendix A except the amplitudes of harmonics. Consequently, characteristics of armature excitation air-gap field harmonics in 6/10-pole E- and C-core SFPM machines can also be synthesised as similar to the 12/13-pole SFPM machine in Appendix A. Therefore, the equivalent pole-pair number of armature excitation in 6/10-pole E- and C-core SFPM machines is the same with that of 12/13-pole SFPM machine, *i.e.* $p_{ea}=7$. With $N_r=10$ and $p_{PM}=3$, these three parameters match the equation (2.18) again. This implies that the E- and C-core SFPM machines also operate on magnetic gearing principle. More importantly, the gearing ratio is 1.43 in 6/10-pole E- and C-core SFPM machines, whilst that in 12/10-pole U-core SFPM machines it is 2.5 due to the different p_{ea} as shown in (2.21).



(a) E-core



(b) C-core

Fig. 2.13. Air-gap MMF of armature excitation in 6/10-pole E- and C-core SFPM machines accounting for the stator saliency.

2.4 Torque Contribution of Dominant Field Harmonics

In the foregoing sections, the magnetic gearing effect of SFPM machines with different stator/rotor pole combinations, winding configurations, and stator lamination segment types are analysed. It is found that all the SFPM machines operates on magnetic gearing principle, with abundant field harmonics due to the modulation of rotor permeance harmonics. In this

section, the torque contribution of the dominant field harmonics will be investigated by the Maxwell stress tensor. In [MCF14a], it is concluded that only open-circuit air-gap field harmonics and armature excitation MMF with same pole-pairs $|N_r - p_{PM}|$ and $N_r + p_{PM}$ generate non-zero electromagnetic torques in SFPM machine having p_{PM} stator pole-pairs and N_r rotor poles, and the torque proportions of the field harmonics to the average electromagnetic torque are not considered. In this section, it is found that >95% of the average electromagnetic torque in SFPM machines are contributed by several dominant field harmonics.

Under on-load operation condition, the air-gap flux density radial component B_r and tangential component B_t can be expanded by Fourier series,

$$\begin{cases} B_r(t, \theta) = \sum_k B_{rn} \cos[n\theta - \theta_{rn}(t)] \\ B_t(t, \theta) = \sum_k B_{tn} \cos[n\theta - \theta_{tn}(t)] \end{cases} \quad (2.25)$$

where B_{rn} and B_{tn} are the n^{th} Fourier coefficients of B_r and B_t whilst θ_{rn} and θ_{tn} are the corresponding phases.

The electromagnetic torque T_{em} calculated by the Maxwell stress tensor based on the obtained air-gap flux density can be given by,

$$T_{em}(t) = \frac{R_g^2 L_s}{\mu_0} \int_0^{2\pi} B_r B_t d\theta = \sum_n T_{emn}(t) \quad (2.26)$$

where R_g is the air-gap radius, μ_0 is the vacuum permeability, L_s is the stack length, and $T_{em}(t)$ is the instantaneous electromagnetic torque generated by the n^{th} radial and tangential field harmonics expressed as,

$$T_{emn}(t) = \frac{\pi R_g^2 L_s}{\mu_0} B_{rn} B_{tn} \cos[\theta_{rn}(t) - \theta_{tn}(t)] \quad (2.27)$$

As can be seen from (2.26) and (2.27), only the interaction between the radial and tangential air-gap flux densities of the same spatial order can produce electromagnetic torque. For the previously analysed 12-stator-pole SFPM machines, Fig. 2.14 and Fig. 2.15 give the FE predicted electromagnetic torque waveforms and the torque proportion contributed by the dominant field harmonics, under brushless AC (BLAC) mode, copper loss $p_{cu}=20W$ and d -axis zero current control, *i.e.* phase current and phase back-EMF have the same phase angle. In Fig.

2.15, the torque proportion contributed by the n^{th} field harmonic with reference to the average electromagnetic torque is obtained by 3 steps:

Step 1: At a certain time t , FE predicted $B_r(t, \theta)$ and $B_t(t, \theta)$ are expanded to Fourier series based on (2.25). Consequently, B_{rn} , B_{tn} , $\theta_{rn}(t)$ and $\theta_{tn}(t)$ can be obtained.

Step 2: Instantaneous electromagnetic torque $T_{emn}(t)$ generated by the n^{th} radial and tangential field harmonics $B_r(t, \theta)$ and $B_t(t, \theta)$ can be obtained from (2.27).

Step 3: The average electromagnetic torque component of the n^{th} field harmonic T_{emnavg} within the full electric period can be obtained, as well as its torque proportion.

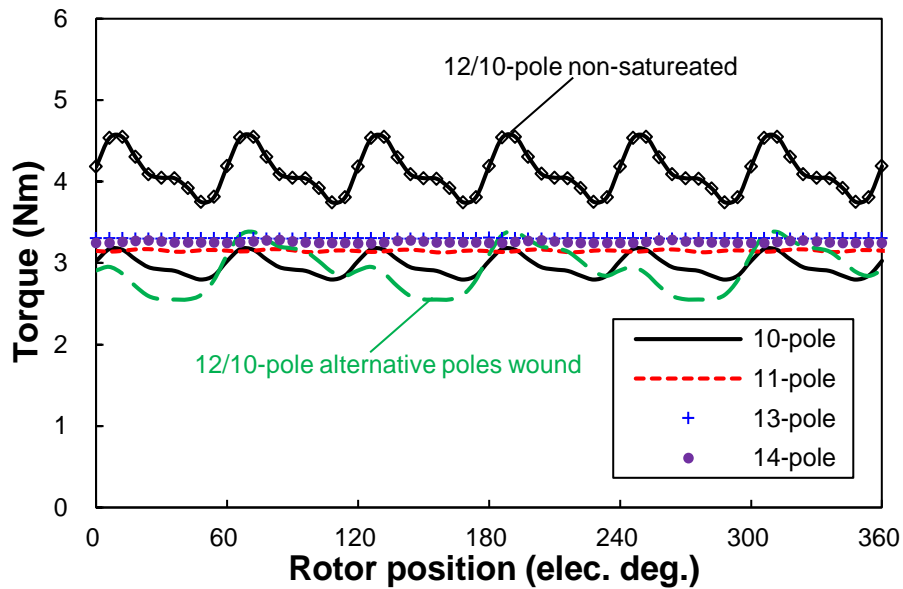


Fig. 2.14. FE predicted electromagnetic torque in 12-stator-pole SFPM machines (BLAC, $p_{cu}=20W$, phase current and phase back-EMF have the same phase angle).

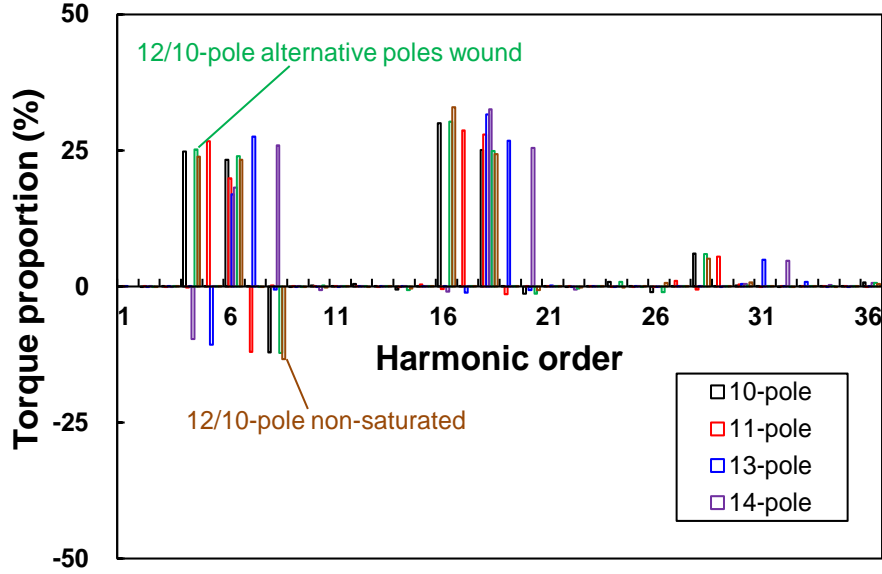


Fig. 2.15. Torque proportion contributed by field harmonics in 12-stator-pole SFPM machines (BLAC, $p_{cu}=20W$, phase current and phase back-EMF have the same phase angle).

As listed in Table 2.7 and Table 2.8, more than 96% of electromagnetic torques in SFPM machines are contributed by the dominant air-gap field harmonics, *i.e.* rotating ones in open-circuit and armature excitation fields with the same pole-pair number of $|kN_r \pm (2i-1)p_{PM}|$ ($k=1, i=1, 2$) and static ones with the same pole-pair number of $(2i-1)p_{PM}$ ($i=1, 2$). Among these field harmonics, harmonics with pole-pair number $-N_r + 3p_{PM}$ are rotating backward on both open-circuit and armature excitation operation conditions, generating negative electromagnetic torque.

As aforementioned, the analytical MMF-permeance model without consideration of the lamination steel saturation can clearly predict the dominant air-gap field harmonics for both open-circuit and armature excitation, verified by FE analysis with both non-saturated and saturated lamination steel. As shown in Fig. 2.15 and listed in Table 2.7, for 12/10-pole SFPM machines with saturated and non-saturated lamination steel, in both of them >96% the electromagnetic torques are generated by several same dominant harmonics although the average torque in the non-saturated machine is higher, Fig. 2.14, as may be expected. Although the saturation in the lamination steel slightly influence the torque proportions of the dominant air-gap field harmonics, they contribute more than 96% of the electromagnetic torques in both SFPM machines with non-saturated and saturated lamination steel.

Table 2.7 Torque Proportion of Field Harmonics in 12-Stator-Pole SFPM Machines with Different Rotor Pole Numbers

Lamination steel	N_r	Item	Harmonic order						
			N_r-p_{PM}	p_{PM}	$-N_r+3p_{PM}$	N_r+p_{PM}	$3p_{PM}$	N_r+3p_{PM}	
Non-Saturated	10	Harmonic order	4	6	8	16	18	28	Sum
		Torque proportion (%)	23.88	23.26	-13.40	32.89	24.29	5.12	96.03
Saturated	10	Harmonic order	4	6	8	16	18	28	Sum
		Torque proportion (%)	24.86	23.35	-12.19	29.99	25.11	6.06	97.19
	11	Harmonic order	5	6	7	17	18	29	Sum
		Torque proportion (%)	26.64	19.85	-12.09	28.68	27.92	5.43	96.43
	13	Harmonic order	7	6	5	19	18	31	Sum
		Torque proportion (%)	27.54	16.96	-10.72	26.75	31.58	4.86	96.98
	14	Harmonic order	8	6	4	20	18	32	Sum
		Torque proportion (%)	25.88	18.15	-9.67	25.43	32.51	4.73	97.02

Table 2.8 Torque Proportion of Field Harmonics in 12/10-Pole SFPM Machines with Alternate Wound Windings

Item	Harmonic order						
	N_r-p_{PM}	p_{PM}	$-N_r+3p_{PM}$	N_r+p_{PM}	$3p_{PM}$	N_r+3p_{PM}	
Harmonic order	4	6	8	16	18	28	Sum
Torque proportion (%)	25.17	23.96	-12.24	30.31	24.89	5.90	97.99

The electromagnetic torque waveforms in 6/10-pole E- and C-core SFPM machines predicted by FE are given in Fig. 2.16. The torque proportion of the dominant air-gap harmonics are given in Fig. 2.17. As listed in Table 2.9, more than 95% of the average electromagnetic torques in E- and C-core SFPM machines are contributed by harmonics with pole-pair number numbers $|kN_r \pm (2i-1)p_{PM}|$ ($k=1$, and $i=1, 2, 3$) and $(2i-1)p_{PM}$ ($i=1, 2$) for rotating and static field harmonics, respectively. It should be noted that the 6/10-pole E- and C-core SFPM machines suffers from higher torque ripple as shown in Fig. 2.16. This is caused by the larger back-EMF harmonics and cogging torque, as pointed out in [CHE11c].

As well known, in fractional-slot SPM machine there are many air-gap field harmonics mainly caused by the slot effect [ZHU93c] and non-sinusoidal armature MMF distribution determined by non-overlapping concentrated winding layout [ELR10a] [CRO02a] [ZHU11a], resulting in severe parasitic effect such as eddy current loss and torque ripple [BIA06a] [ISh05a] [FRE07a] [BIA08a]. More importantly, these field harmonics contribute little to the average electromagnetic torque, as shown in Fig. 2.18 for 12-slot/8-pole fractional-slot SPM machine. The main design parameters of the 12-slot/8-pole fractional-slot SPM machine are the same with [ZHU13a]. In Fig. 2.18 and Table 2.10, it can be observed that the average electromagnetic torque is mainly generated by the working harmonic with PM pole-pair number p_r , *i.e.* >95%.

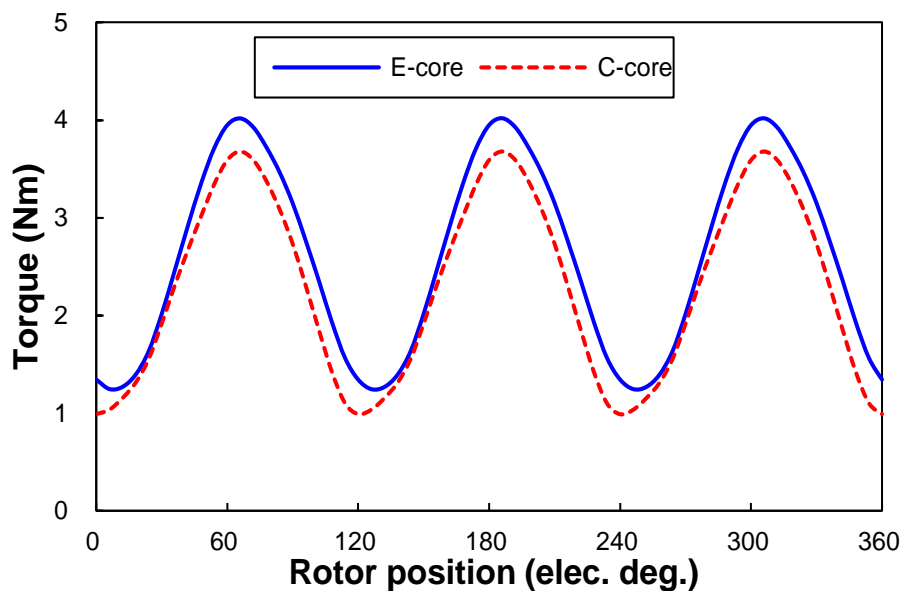


Fig. 2.16. FE predicted electromagnetic torque in 6/10-pole E- and C-core SFPM machines. (BLAC, $p_{cu}=20W$, phase current and phase back-EMF have the same phase angle).

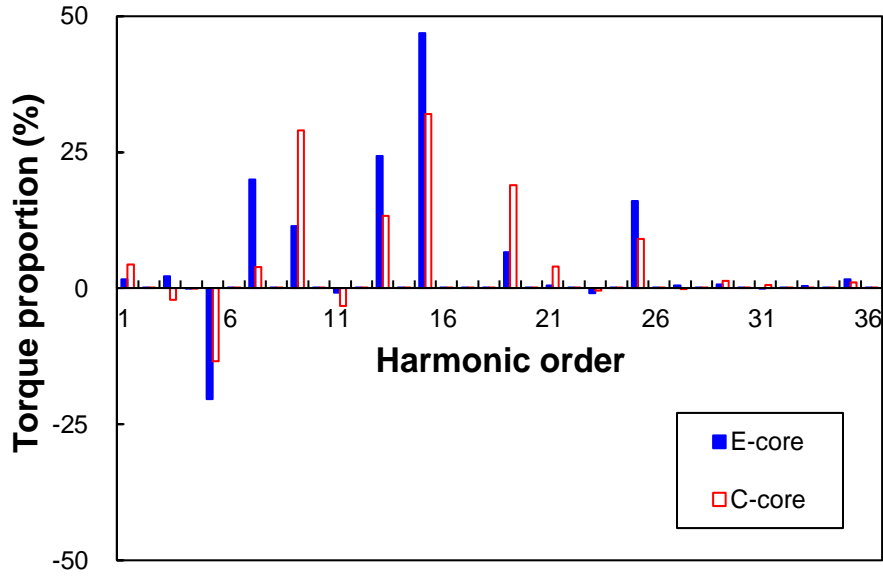


Fig. 2.17. Torque proportion of field harmonics in 6/10-pole E- and C-core SFPM machines (brushless AC, $p_{cu}=20W$, phase current and phase back-EMF have the same phase angle).

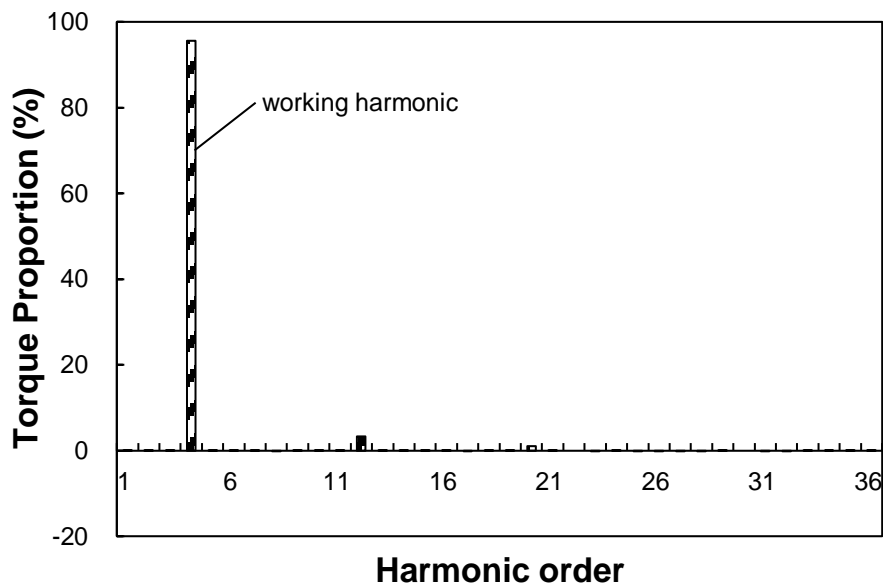


Fig. 2.18. Torque proportion of field harmonics in 12-slot/8-pole fractional-slot SPM machine (BLAC, $p_{cu}=20W$, phase current and phase back-EMF have the same phase angle).

Table 2.9 Torque Proportion of Field Harmonics in 6/10-Pole E- and C-Core SFPM Machines (%)

Harmonic order		E-core	C-core
N_r-3p_{PM}	1	1.46	4.36
p_{PM}	3	1.95	-2.09
N_r-5p_{PM}	5	-17.87	-13.42
N_r-p_{PM}	7	17.47	3.87
$3p_{PM}$	9	10.02	29.01
N_r+p_{PM}	13	21.31	13.35
$5p_{PM}$	15	41.00	32.01
N_r+3p_{PM}	19	5.80	18.91
N_r+5p_{PM}	25	14.07	9.09
Sum		95.20	95.08

Table 2.10 Torque Proportion of Field Harmonics in 12-Slot/8-pole Fractional-slot SPM Machine

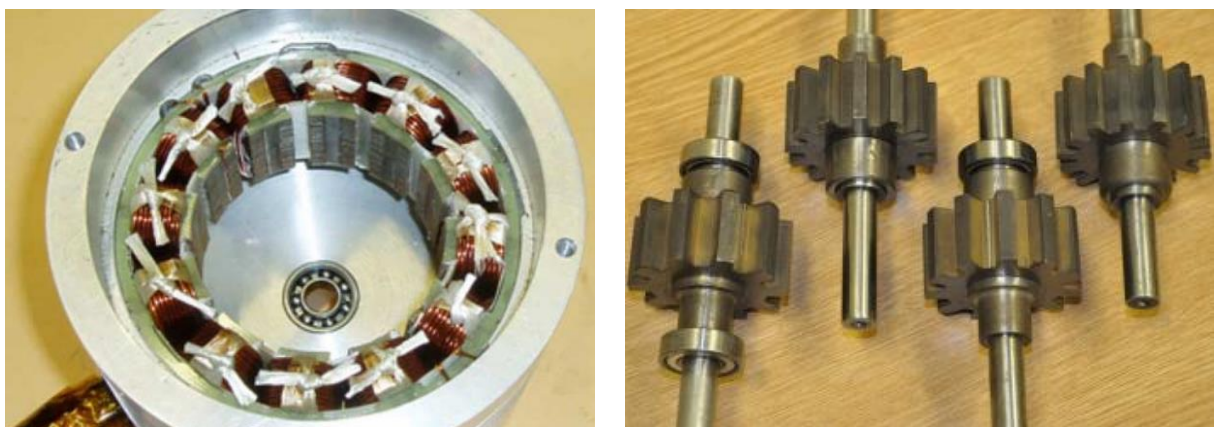
Item	Harmonic order			
	p_{PM}	$3p_{PM}$	$5p_{PM}$	
Harmonic order	4	12	20	Sum
Torque proportion (%)	95.59	3.35	1.08	~100

Although both SFPM and fractional-slot SPM machines suffer from abundant air-gap field harmonics which results in parasitic loss, their contribution to the average electromagnetic torque in these two types of machines are different. In a fractional-slot SPM machine, the working harmonic generates >95% of the average electromagnetic torque, Fig. 2.18. However, in SFPM machines, it is mainly contributed by several dominant air-gap field harmonics, as

shown in Fig. 2.15 and Fig. 2.17. Although in the fractional-slot SPM machine $3p_r^{\text{th}}$ and $5p_r^{\text{th}}$ harmonics can produce small average electromagnetic torque, their parasitic effect on losses may be dramatic due to the triple and quintuple electric frequencies, respectively. However, all the rotating dominant air-gap field harmonics in SFPM machines are of the same electric frequency due to $k=1$ and static ones give no rise to losses, as listed in Table 2.2.

2.5 Experimental Validation

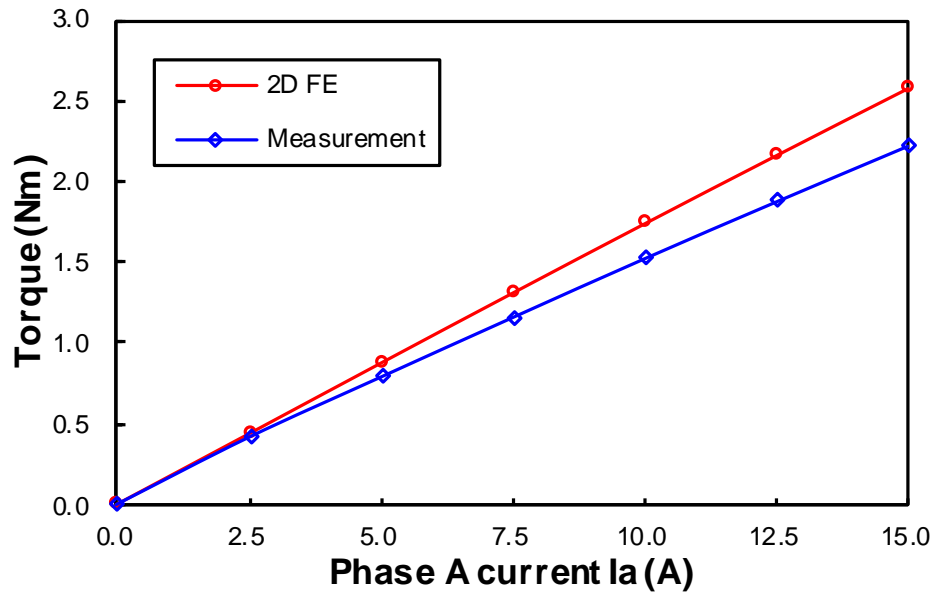
To validate the previous analyses, 12-stator-pole U-core all poles wound SFPM prototype machines with 10-, 11-, 13- and 14-rotor-pole are prototyped. Fig. 2.19 shows the photos of the stator and rotors. The four rotors Fig. 2.19(b) share the common stator, as shown in Fig. 2.19(a). In the foregoing sections, the magnetic gearing effect in SFPM machines is analysed based on the air-gap field harmonics and the torque proportion of the dominant harmonics is investigated. The air-gap field harmonics and their contributions to the average electromagnetic torque cannot be measured on the prototype machines due to the limited experimental conditions. However, the FE predicted electromagnetic torques can be verified by measurements. Average static torques within 0~180 electric degrees of the prototype machines are calculated by 2D FE and compared with measurements, as shown in Fig. 2.20(a) and Fig. 2.20(b) respectively. Although 2D FE predicted average static torques are slightly lower than those of measurements due to end effect, good agreements are obtained. As for the dynamic performances of these 4 prototypes, they are measured and analysed in [ZHU14b] [ZHU15e].



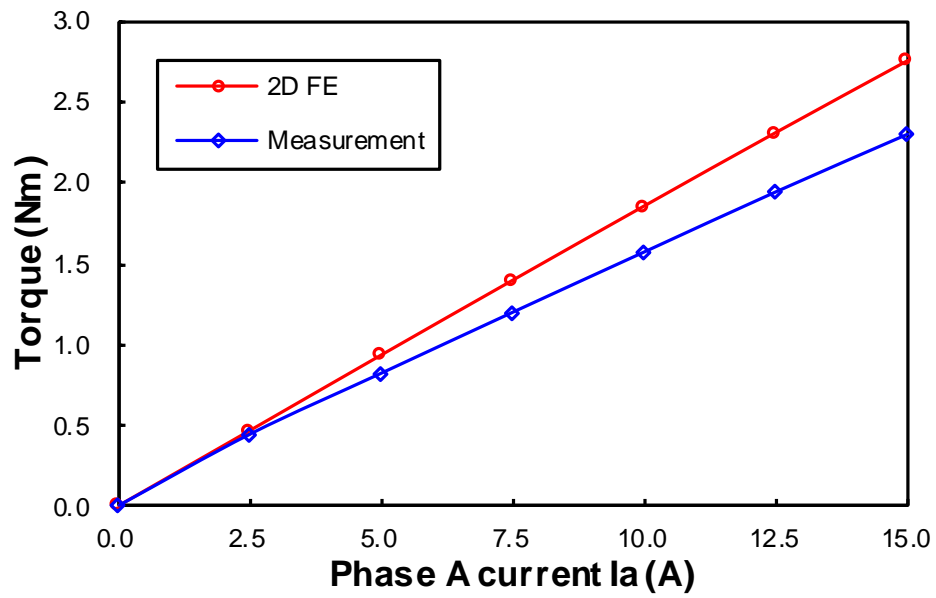
(a) 12-pole stator

(b) Rotors

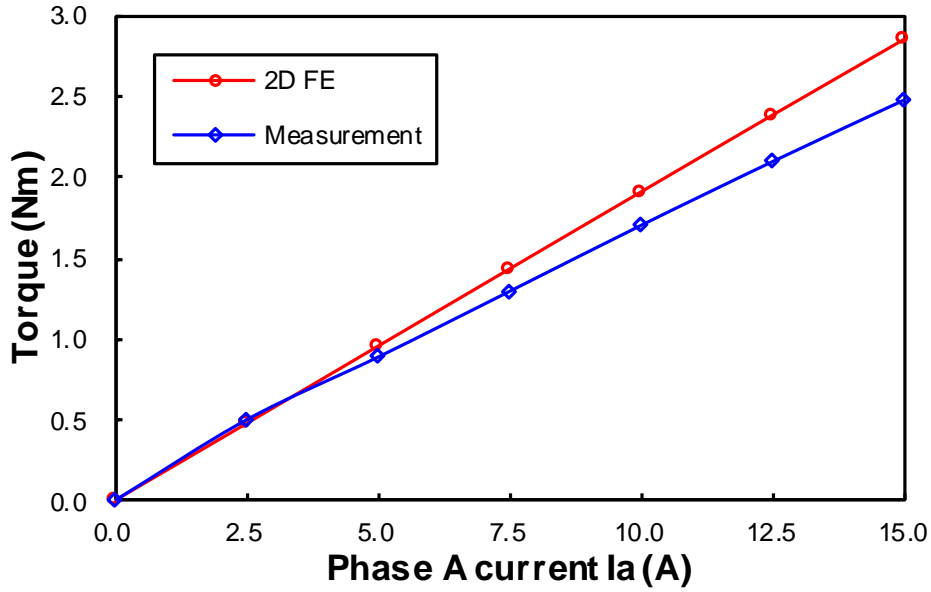
Fig. 2.19. Pictures of U-core SFPM machines.



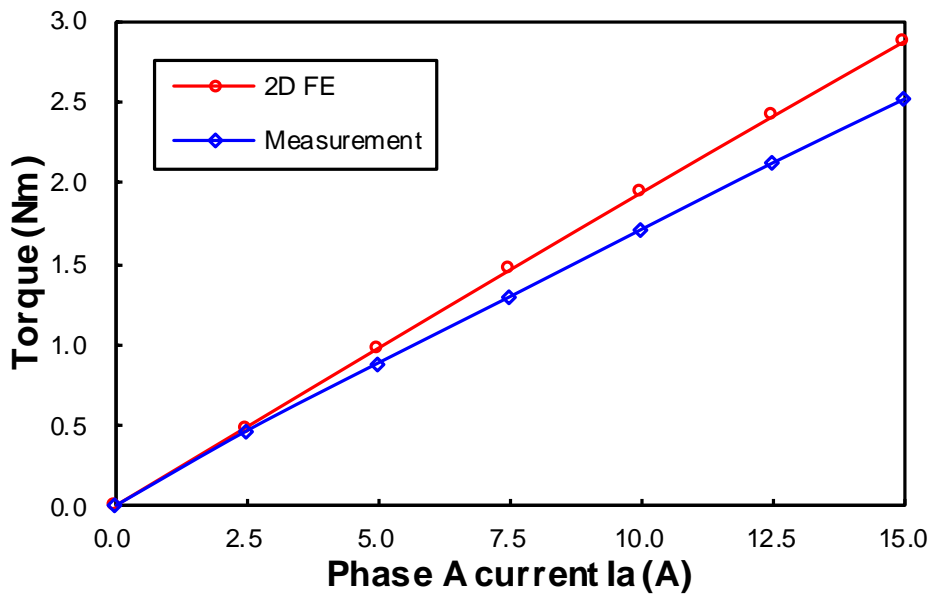
(a) 10-rotor-pole



(b) 11-rotor-pole



(c) 13-rotor-pole



(d) 14-rotor-pole

Fig. 2.20. Comparison of 2D FE predicted and measured average static torque with phase A current I_a ($I_a = -2I_b = -2I_c$).

2.6 Conclusions

In this chapter, the modulation of salient rotor and magnetic gearing effect in SFPM machines are analysed by a simple MMF-permeance model, with due accounting for different stator/rotor-pole combinations, winding configurations and stator lamination segment types. FE predicted results show that >95% of the average electromagnetic torque in SFPM machines

are contributed by the dominant rotating field harmonics in open-circuit and armature excitation fields with the same pole-pair number of $|kN_r \pm (2i-1)p_{PM}|$ ($k=1, i=1, 2, 3$) and static field harmonics with the same pole-pair number of $(2i-1)p_{PM}$ ($i=1, 2, 3$). In essence, it has numerically proved that the SFPM machine is equivalent to a MG machine and operates on magnetic gearing effect. The modulation of the salient rotor to PM and armature excitation fields in SFPM machines is similar to that of the iron pieces to those fields in magnetic gears and MG machines.

3 Analysis of Magnetic Gearing Effects in Partitioned Stator Switched Flux Permanent Magnet Machines

Based on the magnetic gearing effect in the conventional single stator switched flux permanent magnet (PM) (SFPM) machines which has been presented in Chapter 2, novel partitioned stator SFPM (PS-SFPM) machines with PMs and armature windings in two separated stators exhibiting higher torque density were proposed and analysed recently. In this chapter, the operation and interaction mechanisms between the open-circuit and the armature excitation magnetomotive forces (MMFs) in the PS-SFPM machines having various topologies and armature winding connections is analysed based on both the outer and inner air-gap open-circuit and armature excitation field harmonics. It is found that the PS-SFPM machines also operate based on the magnetic gearing effect. The modulation of the rotor iron pieces to the open-circuit and armature excitation MMFs is similar to that in magnetic gears and magnetically geared (MG) machines, as well as the conventional single stator SFPM machines. It is also found that for the PS-SFPM machines having N_r -pole rotor and p_{PM} -pole-pair PMs, more than 93% of the electromagnetic torques generated in both the outer and inner air-gaps is contributed by the dominant rotating field harmonics in open-circuit and armature excitation fields with the same pole-pair number of $|kN_r \pm (2i-1)p_{PM}|$ ($k=1, i=1, 2, 3$) and static field harmonics with the same pole-pair number of $(2i-1)p_{PM}$ ($i=1, 2, 3$).

This part has been published by IEEE Transactions on Energy Conversion.

3.1 Introduction

In order to further enhance the torque density of the SFPM machine, a partitioned stator SFPM (PS-SFPM) machine has been developed [EVA15a] in which the inner space is utilized by separating PMs and armature windings in two different stators, *i.e.* the outer one and the inner one. Due to the higher utilization of the inner space and the increased slot area for the armature windings, the novel PS-SFPM machine can produce larger torque than the conventional SFPM machine with a single stator. The cross-sections of 12-stator-pole PS-SFPM machines having 10-, 11-, 13- and 14-rotor-pole rotors are shown in Fig. 3.1(a)-(d), respectively. As shown in Fig. 3.1, armature windings and PMs are separately accommodated in the outer and inner stators, between which a rotor made up of several segmented iron pieces is sandwiched. Although the inner stator of the 12-stator-pole PS-SFPM machines having 10-,

11-, 13- and 14-rotor-pole rotors are exactly the same with 12-pole PMs and all the outer stators have 12 poles, as shown in Fig. 3.1(a)-(d), the outer stator armature winding distributions are different, besides the various rotor iron piece number. Different from the double stator PM machines [TOB99a] [CHA09a] [NIU09a] [WAN11b], in which both the outer and inner stators have the same field function and identical topology, the outer and inner stators in the PS-SFPM machines perform different field functions, *i.e.* open-circuit PM and armature excitation, respectively. It is worth noting that the coil connection of the PS-SFPM machines can be referred to Fig. 1.2.

However, as shown in Fig. 3.1, the topologies of the PS-SFPM machines are similar to those of the magnetic gear [ATA01a] [ATA04] [RAS05a] [JIA10a] and the conventional MG machines [WAN08a] [WAN09a], both of which contain two air-gaps. Magnetic gear is a non-contact physically torque transmit device. A magnetic gear consists of three parts, including two PM bodies and one iron piece ring. Torque can be transferred from one part to another, along with variable gear ratios [ATA04]. By substituting one rotating PM field by armature windings stator, the magnetic gear can be developed to a MG PM machine [WAN08a] [WAN09a].

The PS-SFPM machines shown in Fig. 3.1 can also be regarded as MG machines, having a rotating armature field and an iron piece rotor but a static PM body, which will be studied and investigated in this chapter. In addition, from the perspective of the air-gap field harmonics, the magnetic gearing effect in the PS-SFPM machines will be comprehensively analysed via a simple magnetomotive force (MMF)-permeance model, including different stator/rotor-pole combinations, all and alternate poles wound, E-core and C-core machines. More importantly, the average electromagnetic torque contribution of the main air-gap field harmonics will be investigated by finite element (FE) analysis.

This chapter is organized as follows. In section II, the magnetic gearing effect of a 12/10-pole PS-SFPM machine is firstly investigated. Then, in section III, various developed PS-SFPM machine topologies are analysed in terms of magnetic gearing effect. In section IV, the contributions of the main air-gap field harmonics to the average electromagnetic torque are obtained by the FE analysis. In section V, test results on a fabricated 12/10-pole PS-SFPM prototype machine are provided to validate the FE analysis, followed by conclusions in section VI.

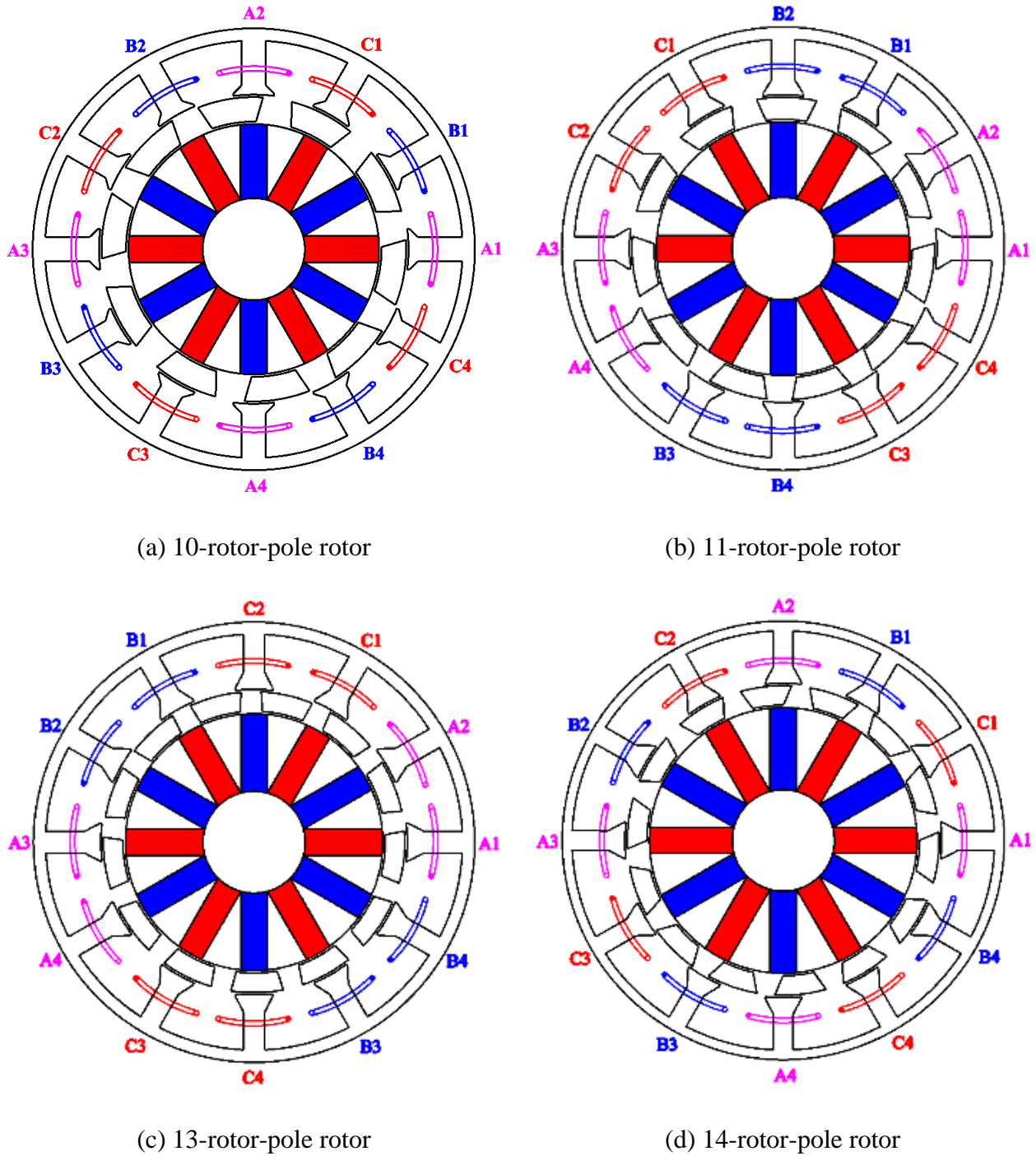


Fig. 3.1. Cross-sections of 12-stator-pole PS-SFPM machines with 10-, 11-, 13- and 14-rotor-pole rotors.

3.2 Analysis of 12/10-Pole PS-SFPM Machine

As shown in Fig. 3.1, armature windings and PMs are separately placed in the outer and the inner stators, whilst the segmented iron piece rotor is sandwiched between the two stators. This is similar to the conventional MG machine [WAN08a] [WAN09a]. However, it is different

from the conventional MG machine which has stationary iron pieces and a rotating PM field, instead the iron pieces in PS-SFPM machines are rotating whilst the PM field is stationary. In this section, the magnetic gearing effect in the 12/10-pole all poles wound (U-core) PS-SFPM machine will be investigated in terms of the air-gap field harmonics.

As is well known, the accurate prediction of the air-gap field of electrical machines is important. Although the saturation is neglected, the subdomain method is preferred to analytically calculate the air-gap field for saving computing time, such as [ZHU10b] for the surface-mounted PM machine, [BOU13a] the conventional SFPM machine with single stator, [LUB10a] the magnetic gear, [ZHA15a] and the MG machine. Both the open-circuit air-gap field and that generated by armature excitation can be accurately predicted by the subdomain method. However, the interaction between the open-circuit and armature excitation air-gap fields cannot be observed by harmonics analysis in detail via the subdomain method. This can be tackled by using the MMF-permeance model, as studied in [DAJ12a] for the salient pole PM machine, and [GAS12a] and [LI16a] for the conventional SFPM machine with single stator. A simple MMF-permeance model is adopted in this chapter for analytically predicting the air-gap field harmonic orders and rotating speeds, via which the modulation effect of the rotor iron pieces is revealed and hence the magnetic gearing effect in the PS-SFPM machine. Both the inner and outer air-gap field harmonics will be derived by the simple MMF-permeance model. It should be noted that this chapter is not aiming to analytically predict the air-gaps field distributions, but aiming to investigate the magnetic gearing effect in the PS-SFPM machine via air-gap field harmonic orders and rotating speeds. Therefore, in the adopted simple MMF-permeance model, the air-gap permeance is modelled as rectangular, although it can be precisely modelled by flux tubes [GAS12a] or the conformal mapping method [LI16a].

In the MMF-permeance model, the permeance of the steel and the PM are assumed to be infinite and unit (same with air), respectively. The flux-leakage and the axial end effect are neglected. To ease the evaluation of the magnetic gearing effect, only the influence of the rotor iron pieces on the air-gap permeance is taken into consideration, whilst those of the outer stator slot and the inner stator PM are reflected in the MMF distributions. The MMF-permeance model predicted air-gap field harmonics orders and rotating speeds will be validated by FE analysis without and with consideration of saturation in steel.

3.2.1 Inner air-gap open-circuit PM MMF

The inner air-gap open-circuit PM MMF in the PS-SFPM machines is illustrated in Fig. 3.2.

Table 3.1 Dimensions of 12-stator-pole all poles wound (U-core) PS-SFPM machines

Parameters	Unit	Value			
		10	11	13	14
Rotor pole number, N_r	-	10	11	13	14
Stack length, L_s	mm	25			
Outer stator outer radius, R_{oso}	mm	45			
Inner stator inner radius, R_{isi}	mm	10.4			
Outer air-gap length, g_o	mm	0.5			
Inner air-gap length, g_i	mm	0.5			
Outer stator tip top length, l_{ott}	mm	0.5			
Outer stator tip bottom length, l_{otb}	mm	2	3	3.5	3.5
Outer stator yoke radius, R_{osy}	mm	42.5	42.5	42.5	43
Outer stator inner radius, R_{osi}	mm	31.5	31.25	31.25	32.25
Rotor inner radius, R_{ri}	mm	26	26.25	26.75	27.75
Outer stator tooth arc, θ_{ost}	°	9	9	8	7
Outer stator tooth tip arc, θ_{ot}	°	3	3	3	3
Rotor pole outer arc, θ_{ro}	°	25	23	20	19
Rotor pole inner arc, θ_{ri}	°	20	18	18	13

3.2.2 Outer air-gap armature excitation MMF

In the 12/10-pole all poles wound PS-SFPM machine, which has non-overlapping concentrated armature windings, Fig. 3.1(a), the outer air-gap armature excitation MMF waveform of the three-phase windings can be shown in Fig. 3.4. The injected three-phase sinusoidal symmetric currents are given by (2.4).

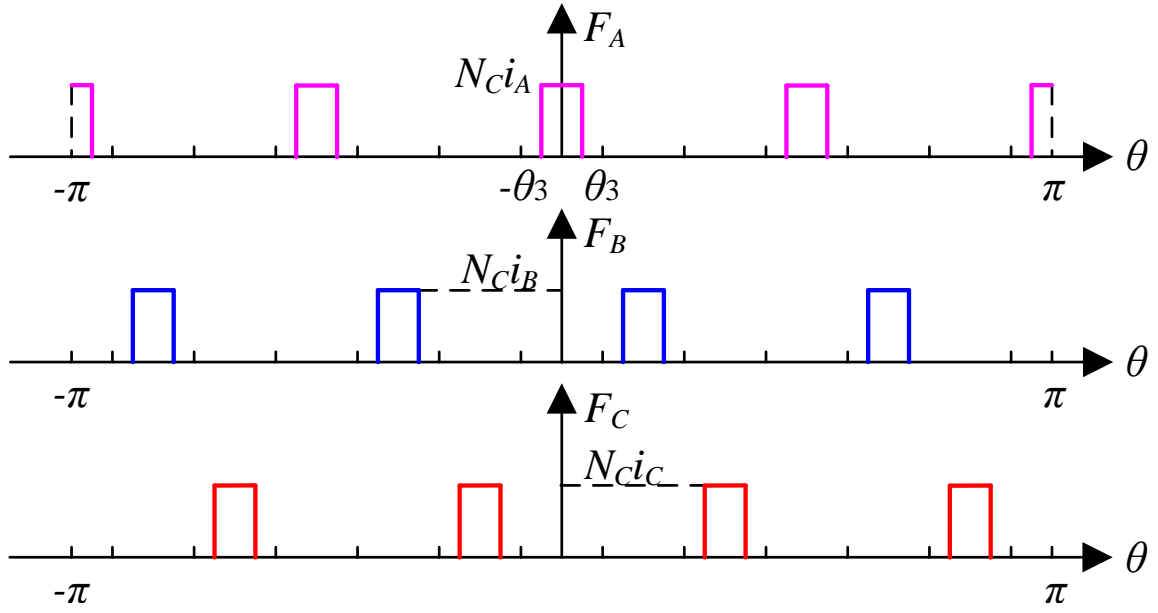


Fig. 3.4. Outer air-gap armature excitation MMF in 12/10-pole PS-SFPM machine ($i_A=i_B=i_C$).

The outer air-gap armature excitation MMF waveform, Fig. 3.4, can be expressed in Fourier series,

$$\begin{cases} F_{ABC}(\theta, t) = \frac{3S_{ABC}}{2} \sum_{q=1}^{\infty} [M_{ABCq} \sin(\xi)] \\ S_{ABC} = \frac{2\sqrt{2}N_c I_{rms}}{\pi} \\ M_{ABCq} = \frac{1}{q} \sin(4q\theta_3) \\ \xi = \begin{cases} -4jq\theta + N_r\Omega_r t, & q = 3r - 2 \\ 4jq\theta + N_r\Omega_r t, & q = 3r - 1 \\ 0, & q = 3r \end{cases} \end{cases} \quad (3.2)$$

where F_{ABC} is the three-phase armature excitation MMF. F_A , F_B , and F_C are the A-, B-, and C-phase armature excitation MMFs respectively. S_{ABC} is a constant in armature excitation MMF. M_{ABCq} is the Fourier coefficient of armature excitation MMF waveform determined by q . N_c is the number of coil turns. θ_3 is half of θ_{ost} plus θ_{ot} given in Table 3.1. Ω_r is the rotor mechanical angular speed in rad/s. r is a positive integer mathematically. j is a constant 1 here for 12/10-pole PS-SFPM machine, as well as in (3.5) and (3.6).

3.2.3 Magnetic gearing effect

The air-gap permeance waveform with consideration of slots between rotor iron pieces is shown in Fig. 3.5. Here, it is worth noting that the influence of the stator slots and PMs on the air-gap permeance is not accounted, since they do not influence the interaction mechanism between the PMs and armature excitation. The air-gap permeance waveform shown in Fig. 3.5 can be expressed as Fourier series,

$$\begin{cases} P(\theta, t) = P_0 + S_2 \sum_{k=1}^{\infty} \{M_{2k} \cos[kN_r(\theta - \Omega_r t - \theta_0)]\} \\ S_2 = \frac{4P_2}{\pi} \\ M_{2k} = \frac{\sin(kN_r\theta_2)}{k} \end{cases} \quad (3.3)$$

where P_0 is the DC component of air-gap permeance. P_2 is the peak-to-peak component of air-gap permeance. S_2 is the constant in air-gap permeance. M_{2k} is the Fourier coefficient of air-gap permeance determined by k . θ_2 is half of the rotor pole arc.

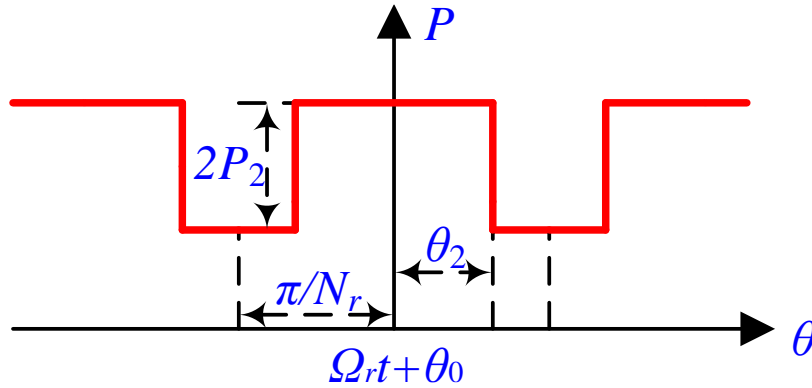


Fig. 3.5. Air-gap permeance waveform with consideration of slots between rotor iron pieces.

Due to the modulation of the rotor iron pieces to the inner air-gap open-circuit PM MMF, complex field harmonics will be produced in the outer air-gap. By multiplying the inner air-gap open-circuit PM MMF Fourier series $F(\theta)$ from (3.2) and the air-gap permeance Fourier series $P(\theta, t)$ from (3.3), the outer air-gap open-circuit PM flux density distribution $B_{PMout}(\theta, t)$ can be deduced as,

$$\left\{ \begin{aligned}
B_{PMout}(\theta, t) &= P_0 S_{PM} \sum_{i=1}^{\infty} \{M_{PMi} \sin[(2i-1)p_{PM}\theta]\} \\
&+ \frac{S_{PM} S_2}{2} \sum_{i=1}^{\infty} \sum_{k=1}^{\infty} [M_{PMi} M_{2k} (\cos \alpha_1 + \cos \alpha_2)] \\
\alpha_1 &= [kN_r + (2i-1)p_{PM}] \left[\theta - \frac{kN_r(\Omega_r t + \theta_0) + \frac{\pi}{2}}{kN_r + (2i-1)p_{PM}} \right] \\
\alpha_2 &= [kN_r - (2i-1)p_{PM}] \left[\theta - \frac{kN_r(\Omega_r t + \theta_0) - \frac{\pi}{2}}{kN_r - (2i-1)p_{PM}} \right]
\end{aligned} \right. \quad (3.4)$$

Similarly, due to the modulation of the rotor iron pieces to the outer air-gap armature excitation MMF, the inner air-gap armature excitation flux density distribution $B_{ABCin}(\theta, t)$ can be calculated from (3.2) and (3.4), as shown in (3.5) and (3.6) when $q=3r-2$. When $q=3r-1$, B_{ABCin} can also be expressed by them with the coefficient of q multiplied by '-1'. It should be noted that $j=1$ in (3.5) and (3.6) as well as (3.2) for 12/10-pole PS-SFPM machine, as previously mentioned.

$$\begin{aligned}
B_{ABCin}(\theta, t) &= \frac{3P_0 S_{ABC}}{2} \sum_{q=1}^{\infty} \left\{ M_{ABCq} \cos \left[4jq\theta - N_r \Omega_r t + \frac{\pi}{2} \right] \right\} \\
&+ \frac{3S_{ABC} S_2}{4} \sum_{q=1}^{\infty} \sum_{k=1}^{\infty} [M_{ABCq} M_{2k} (\cos \beta_1 + \cos \beta_2)]
\end{aligned} \quad (3.5)$$

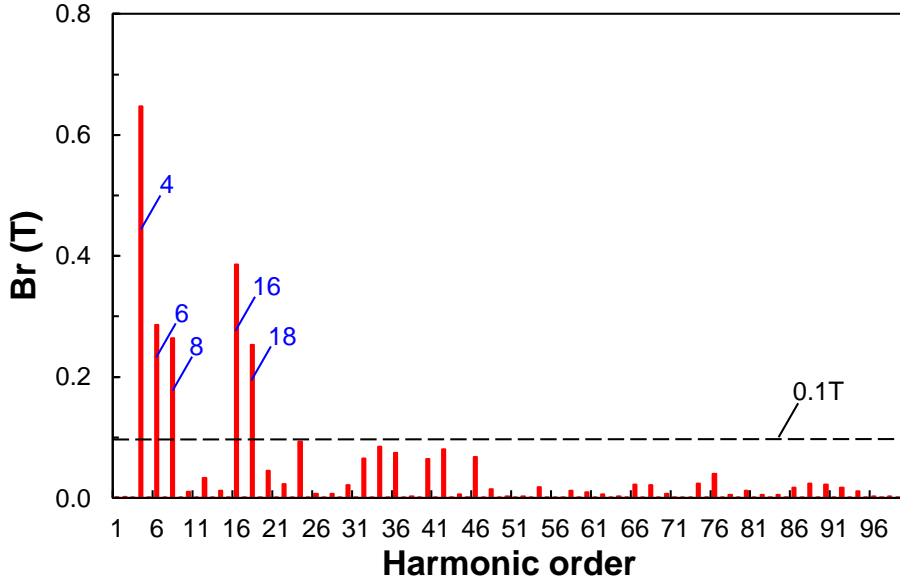
$$\left\{ \begin{aligned}
\beta_1 &= (kN_r - 4jq) \left[\theta - \frac{(k-1)N_r \Omega_r t + kN_r \theta_0 + \frac{\pi}{2}}{kN_r - 4jq} \right] \\
\beta_2 &= (kN_r + 4jq) \left[\theta - \frac{(k+1)N_r \Omega_r t + kN_r \theta_0 - \frac{\pi}{2}}{kN_r + 4jq} \right]
\end{aligned} \right. \quad (3.6)$$

The outer air-gap open-circuit PM radial field components, (3.4), predicted by the MMF-permeance model can be synthesized in Table 3.2. There are both static and rotating field harmonics in the outer air-gap. The static field harmonics are generated since those of the inner stator PMs are static, whilst the rotating ones are caused by the modulation of the rotor iron pieces to the open-circuit PM MMF. The pole-pairs and rotating speeds listed in Table 3.2 can be verified by FE analysis without and with consideration of saturation in steel, as shown in

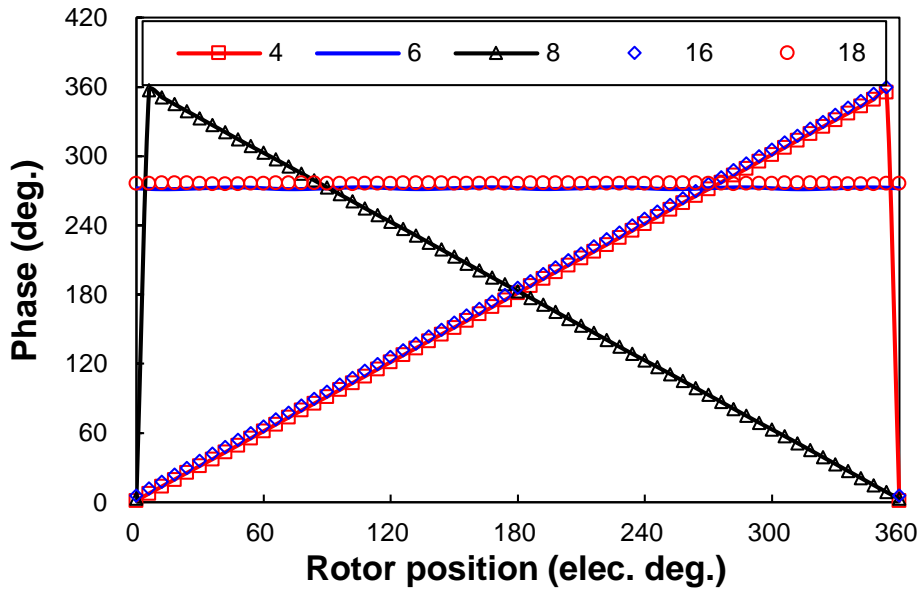
Fig. 3.6 and Fig. 3.7. In Fig. 3.6 and Fig. 3.7, the PS-SFPM machine operates under brushless AC (BLAC) mode with zero d -axis current control, i.e. phase current and phase back-EMF have the same phase angle. The orders of these FE predicted field harmonics with magnitude $>0.1T$ are in good agreement with those predicted by the MMF-permeance model, *i.e.* with pole pair numbers $(2i-1)p_{PM}$ ($i=1, 2$) for 6 and 18, $kN_r+(2i-1)p_{PM}$ ($k=1, i=1$) for 16, and $|kN_r-(2i-1)p_{PM}|$ ($k=1, i=1, 2$) for 4 and 8. The rotating speeds of these harmonics in Table 3.2 can also be verified by FE from the phases shown in Fig. 3.6(b) and Fig. 3.7(b). For example, the 6th and 18th field harmonics are stationary, whilst the rotating speed of the 8th field harmonic is negative and backward rotating, opposite to that of the 4th and 16th field harmonics. It is worth noting that the saturation in the steel only has impact on the outer air-gap harmonic amplitudes. Generally, as expected, the outer air-gap harmonics without consideration of saturation in steel have higher amplitudes than their counterparts with consideration saturation, as shown in Fig. 3.6 and Fig. 3.7. However, there is no influence of saturation in steel on the outer air-gap harmonic phases and hence the rotating speeds. This indicates that although the saturation in steel is neglected, the adopted simple MMF-permeance model can predict both the open-circuit outer air-gap harmonic orders and rotating speeds in the saturated PS-SFPM machine, for investigating the magnetic gearing effect. It should also be noted that the same order field harmonics will also be produced in the inner air-gap due to the modulation of the rotor iron pieces to the inner air-gap PM MMF, albeit with different amplitudes from the outer air-gap ones.

Table 3.2 Characteristics of outer air-gap open-circuit pm field harmonics in PS-SFPM machines ($i=1,2,3,\dots$)

Pole-Pairs	Rotating Speed, $N_r\Omega_r$
$(2i - 1)p_{PM}$	0 (stationary)
$kN_r + (2i - 1)p_{PM}$	$\frac{k}{kN_r + (2i - 1)p_{PM}}$
$ kN_r - (2i - 1)p_{PM} $	$\frac{k}{kN_r - (2i - 1)p_{PM}}$

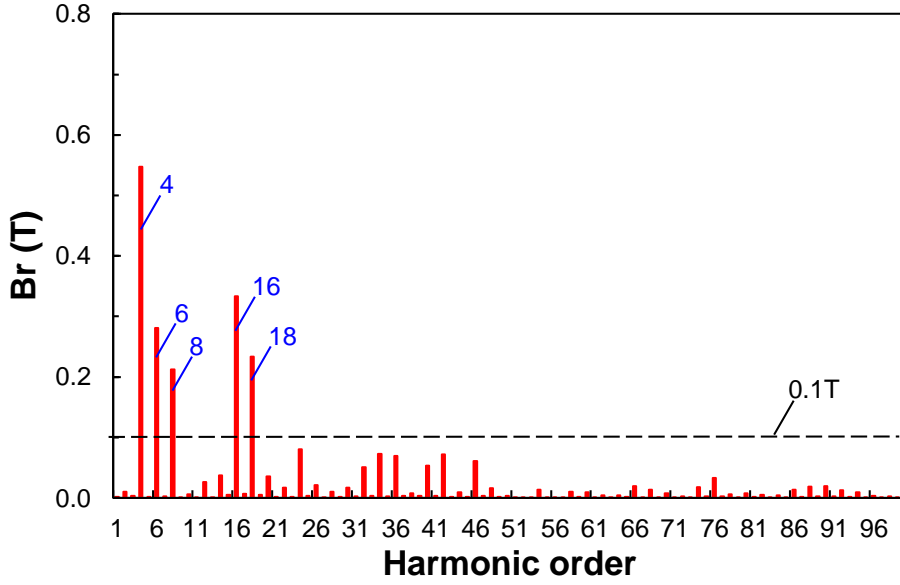


(a) Amplitude (rotor position $\delta=0$)

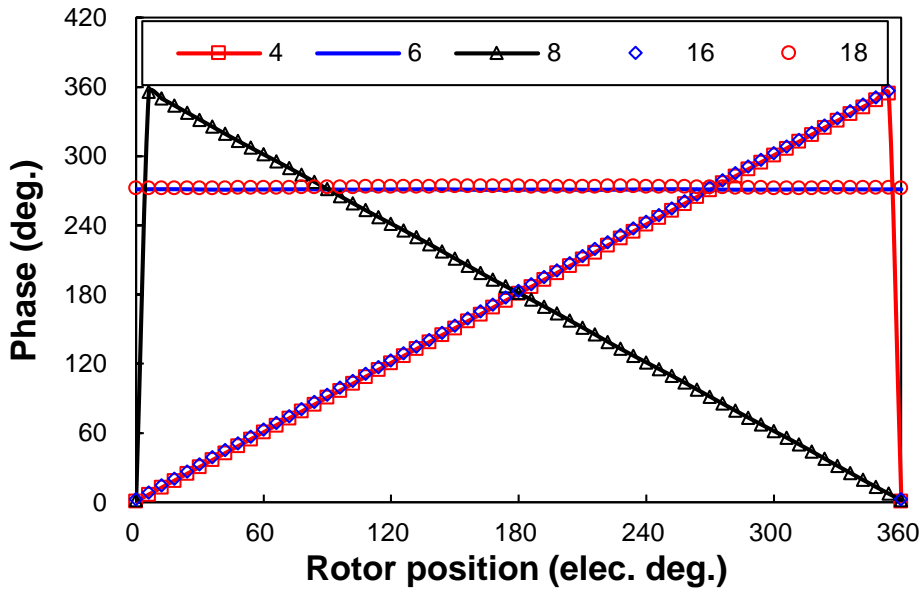


(b) Phases of harmonics with amplitudes $> 0.1T$

Fig. 3.6. FE predicted outer air-gap open-circuit PM radial field in 12/10-pole PS-SFPM machine without consideration of saturation in steel.



(a) Amplitude (rotor position $\delta=0$)



(b) Phases of harmonics with amplitudes $> 0.1T$

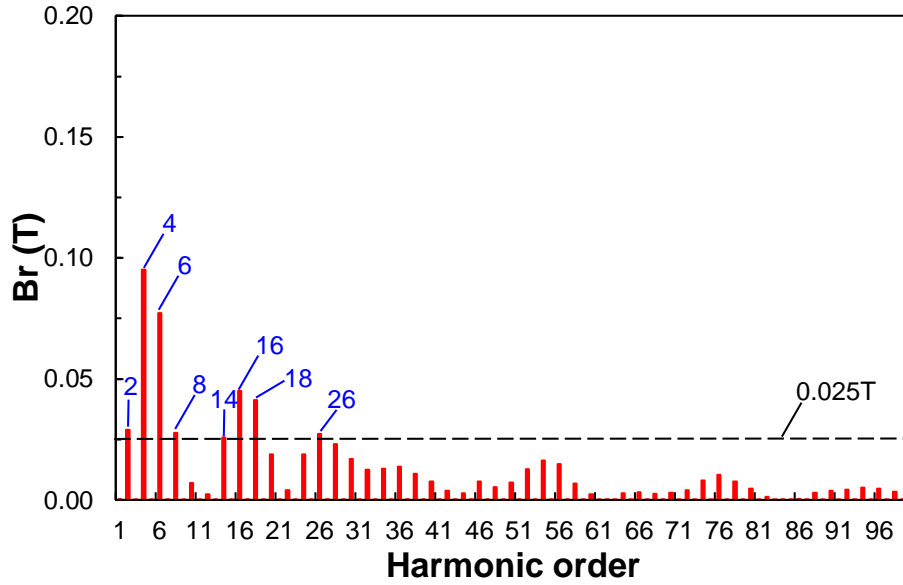
Fig. 3.7. FE predicted outer air-gap open-circuit PM radial field in 12/10-pole PS-SFPM machine with consideration of saturation in steel.

As for the inner air-gap armature excitation radial field components, (3.5) and (3.6), predicted by the MMF-permeance model, they can also be synthesized in Table 3.3. Although the outer air-gap armature excitation MMF is rotating, static field harmonics will be produced in the inner air-gap after being modulated by the rotor iron piece's fundamental permeance with $k=1$, as shown in Table 3.3, together with rotating harmonics. The FE predicted field

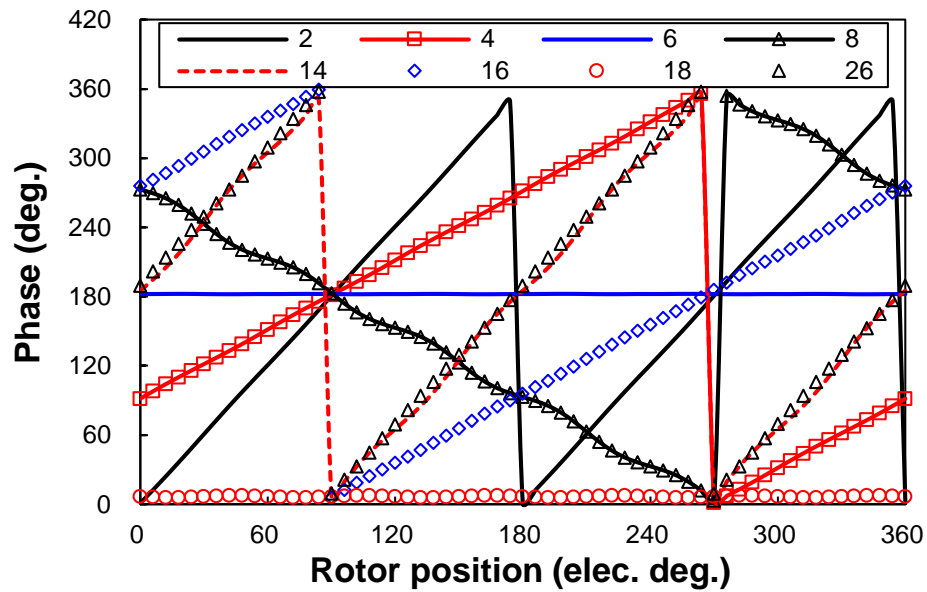
harmonics with magnitude $>0.025T$ are in good agreement with those predicted by the MMF-permeance model, having pole pair numbers $4q$ ($q=1, 4$) for 4 and 16, $|kN_r-4q|$ ($k=1, 2, q=1, 4$) for 6, 16 and 4, and kN_r+4q ($k=1, q=1, 4$) for 14 and 26. And also $4q$ ($q=2$) for 8, kN_r+4q ($k=1, q=2$) for 18 and $|kN_r-4q|$ ($k=1, q=2$) for 2. As shown in Fig. 3.8(a) and Fig. 3.9(a), the inner air-gap harmonic amplitudes without and with consideration of saturation in steel are similar, as the saturation level in steel is low. The rotating speeds of these harmonics can also be verified by FE from the phases shown in Fig. 3.8(b) and Fig. 3.9(b). Again, the adopted simple MMF-permeance model can predict both the inner air-gap harmonic orders and rotating speeds with and without consideration of saturation in steel, for investigating the magnetic gearing effect. Similar to the modulation of the rotor iron pieces to the inner air-gap PM MMF, the modulation to the outer air-gap armature excitation MMF not only generates field harmonics in the inner air-gap but also produces field harmonics in the outer air-gap with the same harmonics orders but different amplitudes.

Table 3.3 Characteristics of inner air-gap armature excitation field harmonics in 12/10-pole PS-SFPM machines ($r=1,2,3,\dots$)

q	Pole-Pairs	Rotating Speed, $N_r\Omega_r$
$3r-2$	$4q$	$\frac{1}{4q}$
	$ kN_r - 4q $	$\frac{k-1}{kN_r - 4q}$
	$kN_r + 4q$	$\frac{k+1}{kN_r + 4q}$
$3r-1$	$4q$	$-\frac{1}{4q}$
	$kN_r + 4q$	$\frac{k-1}{kN_r + 4q}$
	$ kN_r - 4q $	$\frac{k+1}{kN_r - 4q}$

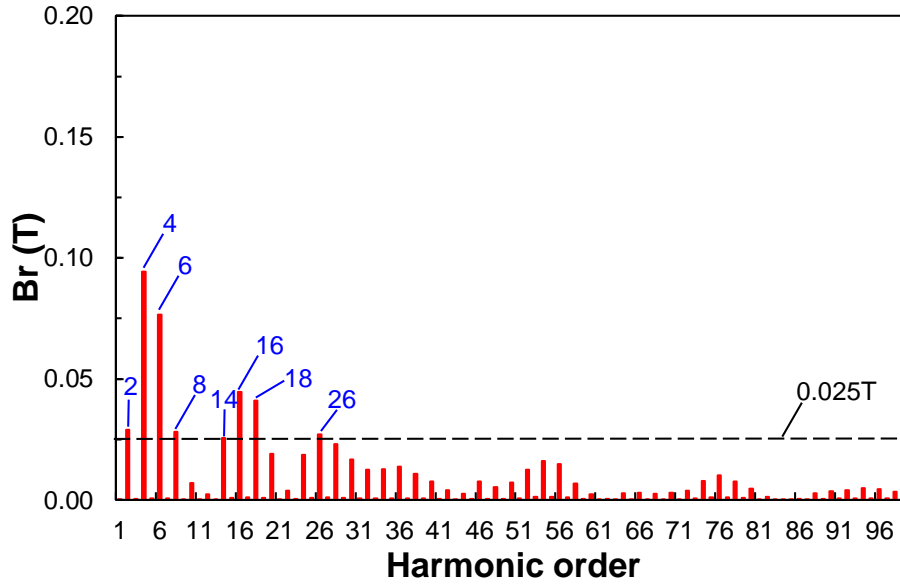


(a) Amplitude (rotor position $\delta=0$)

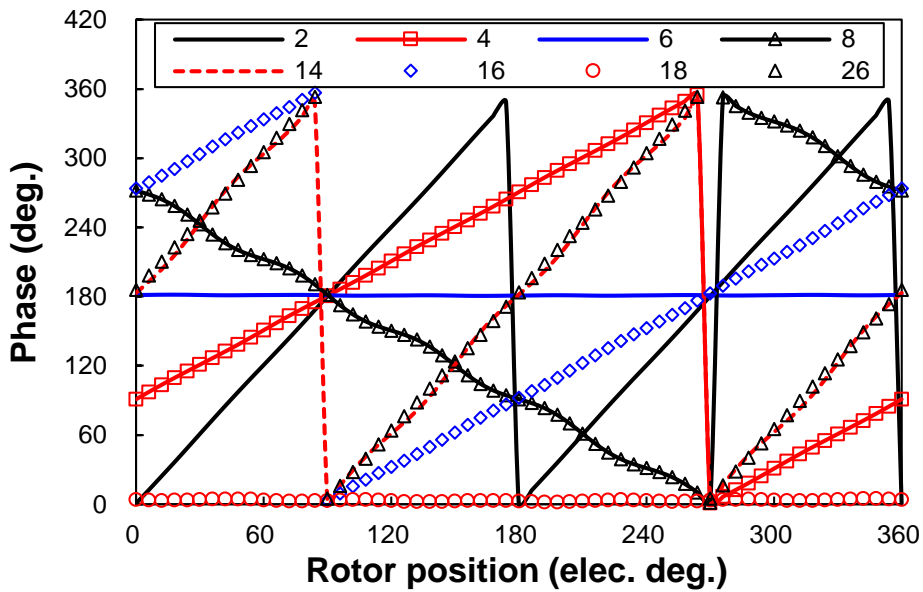


(b) Phases of low order harmonics with amplitudes $> 0.025T$

Fig. 3.8. FE predicted inner air-gap armature excitation radial field in 12/10-pole PS-SFPM machine without consideration of saturation in steel ($p_{cu}=20W$, phase current and phase back-EMF have the same phase angle).



(a) Amplitude (rotor position $\delta=0$)



(b) Phases of low order harmonics with amplitudes $> 0.025T$

Fig. 3.9. FE predicted inner air-gap armature excitation radial field in 12/10-pole PS-SFPM machine with consideration of saturation in steel ($p_{cu}=20W$, phase current and phase back-EMF have the same phase angle).

As the foregoing analysed, after being modulated by the sandwiched rotor iron pieces, abundant field harmonics can be produced in the outer air-gap and the inner air-gap. This is similar to the modulation of iron pieces in the magnetic gear [ATA01] [ATA04] [RAS05a] [JIA10a] and the MG machine [WAN08a] [WAN09a].

In the analysed 12/10-pole PS-SFPM machine, the PM pole-pair number in the inner stator is $p_{PM}=6$. The winding layout in the 12/10-pole PS-SFPM machine is exactly the same as that in the conventional 12-slot/4-pole-pair fractional-slot surface-mounted PM (SPM) machine [ZHU13a]. Consequently, the equivalent pole-pair number of armature windings in the outer stator is $p_{ea}=4$. p_{ea} is defined as the one with highest amplitude among those forward rotating field harmonics having the same electrical angular speed as the rotor, *i.e.* ω_e . With consideration of the rotor pole (iron piece) number $N_r=10$, p_{PM} , p_{ea} and N_r also match the equation,

$$p_{PM} + p_{ea} = N_r \quad (3.7)$$

It can be concluded from (2.19), (2.20), and (3.7) that the 12/10-pole PS-SFPM machine can be regarded as the equivalent MG machine of an inserted-PM magnetic gear having rotating iron pieces and outer PMs with $p_o=4$, $p_i=6$ and $N_{ip}=10$, according to [ATA04a]. By substituting the rotating outer PMs using the 12-stator-slot non-overlapping concentrated three-phase armature windings with sinusoidal symmetric currents, a 12/10-pole PS-SFPM machine can be obtained as shown in Fig. 3.1(a). The magnetic gearing ratio G_r in the 12/10-pole PS-SFPM machine can be expressed according to the magnetic gear with rotating outer PMs and iron pieces [ATA04a],

$$G_r = \frac{N_r}{p_{ea}} = \frac{10}{4} = 2.5 \quad (3.8)$$

3.3 Further Analysis of Developed PS-SFPM Machines

3.3.1 All poles wound PS-SFPM machines having different rotor pole numbers

In the previous section, it was revealed that the operation of the 12/10-pole PS-SFPM machine is based on the magnetic gearing principle. The sum of $p_{PM}=6$ and $p_{ea}=4$ is equal to $N_r=10$ in the 12/10-pole PS-SFPM machine, as illustrated in (3.7). In [EVA15a], the 12/11-, 12/13- and 12/14-pole PS-SFPM machines are also presented and compared with the 12/10-pole one. Their cross-sections are similar to that in Fig. 3.1, and the dimensional parameters are given in Table 3.1. The magnetic gearing effect in these machines can be similarly analysed as follows.

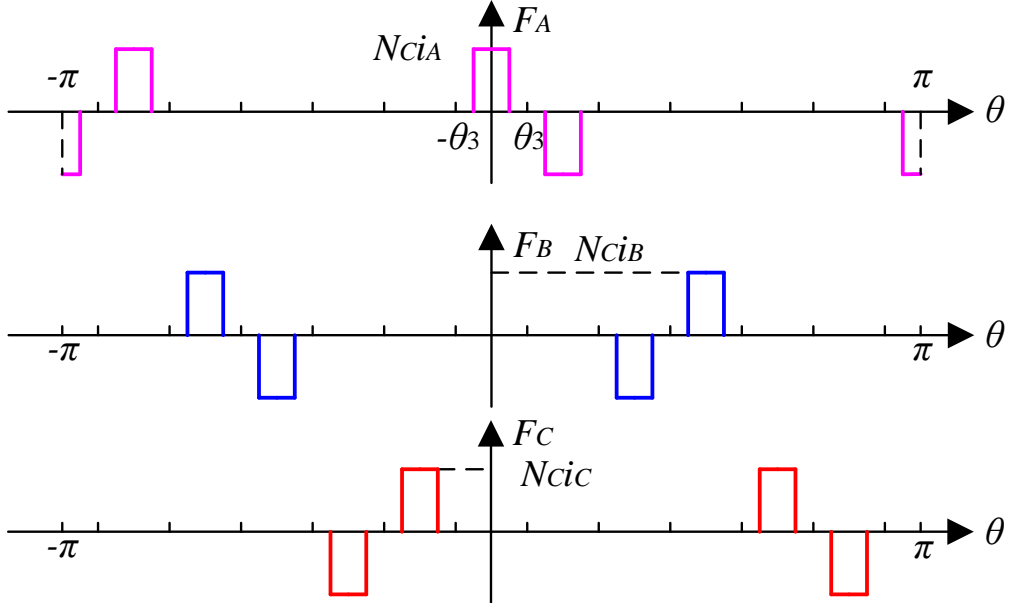


Fig. 3.10. Outer air-gap armature excitation MMF in 12/11-pole PS-SFPM machine.

For a 12/11-pole PS-SFPM machine, Fig. 3.1(b), the outer air-gap armature excitation MMF waveform can be plotted in Fig. 3.10. That of the 12/13-pole PS-SFPM machine is similar to the 12/11-pole one, except the exchange of *B*- and *C*-phases. This can be seen from the winding layouts given in Fig. 3.1(b) and 1(c). The Fourier series expansion of 12/11- and 12/13-pole PS-SFPM machines is given by,

$$\left\{ \begin{array}{l} F_{ABC}(\theta, t) = \sum_{q=1}^{\infty} \left[\frac{3S_{ABC}}{2} M_{ABCq} \sin(\xi) \right] \\ S_{ABC} = \frac{8\sqrt{2}N_c I_{rms}}{\pi} \\ M_{ABCq} = \frac{1}{q} \sin\left(\frac{q\pi}{2}\right) \sin\left(\frac{q\pi}{12}\right) \sin(q\theta_3) \\ \xi = \begin{cases} jq\left(\theta + \frac{5\pi}{12}\right) + N_r \Omega_r t, q = 6r - 5 \\ -jq\left(\theta + \frac{5\pi}{12}\right) + N_r \Omega_r t, q = 6r - 1 \\ 0, q = \textit{else} \end{cases} \end{array} \right. \quad (3.9)$$

where $j=1$ and -1 for 12/11- and 12/13-pole PS-SFPM machines, respectively.

Similar to (3.5) and (3.6) for 12/10-pole PS-SFPM machine, B_{ABCin} in the 12/11- and 12/13-pole PS-SFPM machine can be given in (3.10) and (3.11) for $q=6r-5$. When $q=6r-1$, B_{ABCin} can also be expressed by them with the coefficient of q multiplied by '-1'.

$$\begin{aligned}
B_{ABCin}(\theta, t) = & \frac{3P_0 S_{ABC}}{2} \sum_{q=1}^{\infty} \left\{ M_{ABCq} \cos \left[jq\theta + N_r \Omega_r t + \frac{(5jq - 6)\pi}{12} \right] \right\} \\
& + \frac{3V_{ABC} S_2}{4} \sum_{q=1}^{\infty} \sum_{k=1}^{\infty} [M_{ABCq} M_{2k} (\cos \gamma_1 + \cos \gamma_2)]
\end{aligned} \tag{3.10}$$

where $j=1$ and -1 for 12/11- and 12/13-pole PS-SFPM machines, respectively.

$$\begin{cases} \gamma_1 = (kN_r + jq) \left[\theta - \frac{(k-1)N_r \Omega_r t + kN_r \theta_0 - \frac{(5jq-6)\pi}{12}}{kN_r + jq} \right] \\ \gamma_2 = (kN_r - jq) \left[\theta - \frac{(k+1)N_r \Omega_r t + kN_r \theta_0 + \frac{(5jq-6)\pi}{12}}{kN_r - jq} \right] \end{cases} \tag{3.11}$$

where $j=1$ and -1 for 12/11- and 12/13-pole PS-SFPM machines, respectively.

As for the 12/14-pole PS-SFPM machine illustrated in Fig. 3.1(d), it has a similar winding layout as the 12/10-pole one, Fig. 3.1(a), except the exchange of B - and C -phases. The Fourier series expansion of the outer air-gap armature excitation MMF waveform 12/14-pole PS-SFPM machine can be given by (3.3) with $j=-1$. Also, B_{ABCin} in the 12/14-pole PS-SFPM machine can be given in (3.5) and (3.6) with $j=-1$ for $q=3r-2$. When $q=3r-1$, B_{ABCin} can also be expressed by them with the coefficient of q multiplied by ‘-1’.

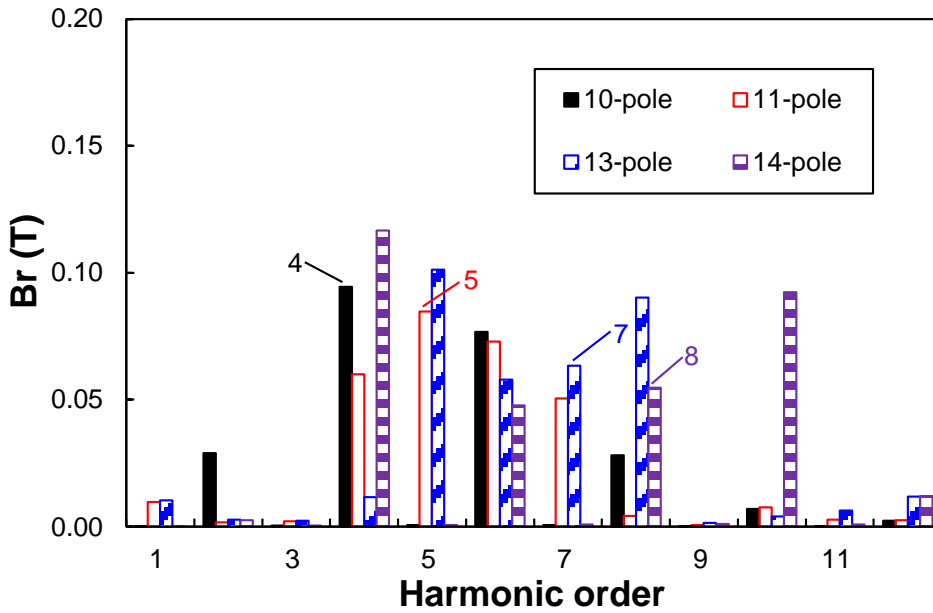


Fig. 3.11. FE predicted inner air-gap armature excitation radial field spectra in 12-stator-pole PS-SFPM machines having different rotor pole numbers.

As shown in (3.10) (3.11) with $j=1$ and -1 , and (3.5) (3.6) with $j=-1$ for the 12/11-, 12/13- and 12/14-pole PS-SFPM machines respectively, many field harmonics will be generated in the air-gap due to the modulation of the rotor iron pieces to the open-circuit PM and armature excitation fields. The FE predicted inner air-gap armature excitation radial field spectra in 12/10-, 12/11-, 12/13- and 12/14-pole PS-SFPM machines are shown in Fig. 3.11. As aforementioned, p_{ea} is defined as the one with the highest amplitude among those forward rotating field harmonics having the same electrical angular speed as the rotor. As shown in Fig. 3.11, p_{ea} are 4, 5, 7 and 8 for 12/10-, 12/11-, 12/13- and 12/14-pole PS-SFPM machines respectively. Consequently, (3.8) can also be matched in the 12/11-, 12/13- and 12/14-pole PS-SFPM machines. The magnetic gearing characteristics are listed in Table 3.4. The gear ratio in the 12-stator-pole PS-SFPM machines decreases with the rotor pole number.

Table 3.4 Magnetic gearing effect in 12/10-, 12/11, 12/12-, 12/13- and 12/14-pole PS-SFPM machines

N_r	p_{PM}	p_{ea}	G_r
...	6
10		4	2.5
11		5	2.2
12		6	2
13		7	1.86
14		8	1.75
...	

3.3.2 Alternate poles wound PS-SFPM machines

In the previous analysis, PS-SFPM machines with all poles wound winding were analysed and it was found that they operate based on the magnetic gearing effect. Here, the magnetic gearing effect in the 12/10-pole alternate poles wound is analysed. Its dimensional parameters are the same as those in the 12/10-pole all poles wound PS-SFPM machine as given in Table 3.1.

The winding type in the 12/10-pole alternate poles wound PS-SFPM machine is A1- C1- B1- A2- C2- B2 anti-clockwise, as shown in Fig. 3.12. This is doubled in the previously analysed 12/14-pole all poles wound PS-SFPM machine, Fig. 3.1(d), *i.e.* A1- C1- B1- A2- C2- B2- A3- C3- B3- A4- C4- B4 anti-clockwise. Consequently, p_{ea} in the 12/10-pole alternate poles wound PS-SFPM machine is half of that in the 12/14-pole SFPM machine with all poles wound, *i.e.* 4 and 8 respectively. With consideration of $p_{PM}=6$ and $N_r=10$, it is found that (3.8) can also be matched in the 12/10-pole PS-SFPM machine with alternate poles wound.

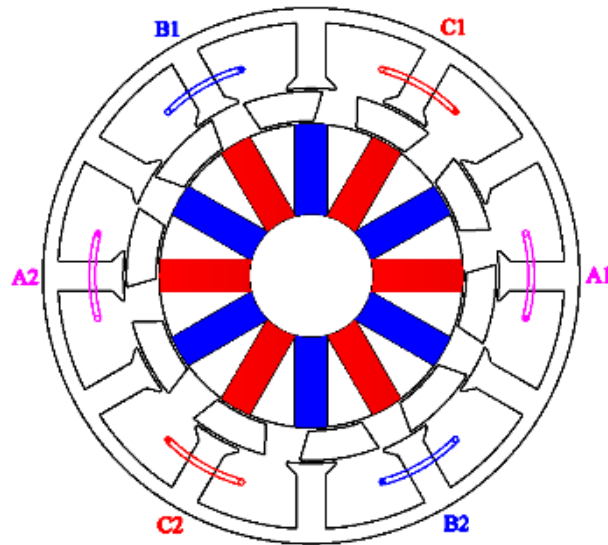


Fig. 3.12. 12/10-pole PS-SFPM machine having alternate poles wound armature windings.

3.3.3 E-core and C-core PS-SFPM machines

Here, the magnetic gearing effects in the 6/10-pole E-core and C-core PS-SFPM machines are analysed. Their dimensional parameters are also the same as those in the 12/10-pole all poles wound PS-SFPM machine as given in Table 3.1.

Fig. 3.13(a) and Fig. 3.13(b) illustrate the cross-sections of 6/10-pole E-core and C-core PS-SFPM machines, respectively. The 6/10-pole E-core PS-SFPM machine, Fig. 3.13(a), also has 6 alternate pole wound coils in the outer stator, similar to 12/10-pole alternate pole wound PS-SFPM machine Fig. 3.12, albeit with different winding layouts. However, the PM number in the E-core machine is half, *i.e.* 6. In 6/10-pole E-core and C-core PS-SFPM machines, the outer air-gap armature excitation MMF is given in Fig. 3.14, which can be expanded to Fourier series as,

$$\begin{cases} F_{ABC}(\theta, t) = \sum_{q=1}^{\infty} \left[\frac{3S_{ABC}}{2} M_{ABCq} \sin(\xi) \right] \\ S_{ABC} = \frac{4\sqrt{2}N_c I_{rms}}{\pi} \\ \xi = \begin{cases} -q\theta + n_r \Omega_r t, q = 6r - 5 \\ q\theta + n_r \Omega_r t, q = 6r - 1 \\ 0, q = \text{else} \end{cases} \end{cases} \quad (3.12)$$

where M_{ABCq} for the E-core PS-SFPM machine is

$$M_{ABCq} = \frac{1}{q} \left[1 + 2 \cos\left(\frac{q\pi}{6}\right) \right] \sin(q\theta_3) \quad (3.13)$$

and M_{ABCq} for the C-core PS-SFPM machine is

$$M_{ABCq} = \frac{1}{q} \sin(q\theta_3) \quad (3.14)$$

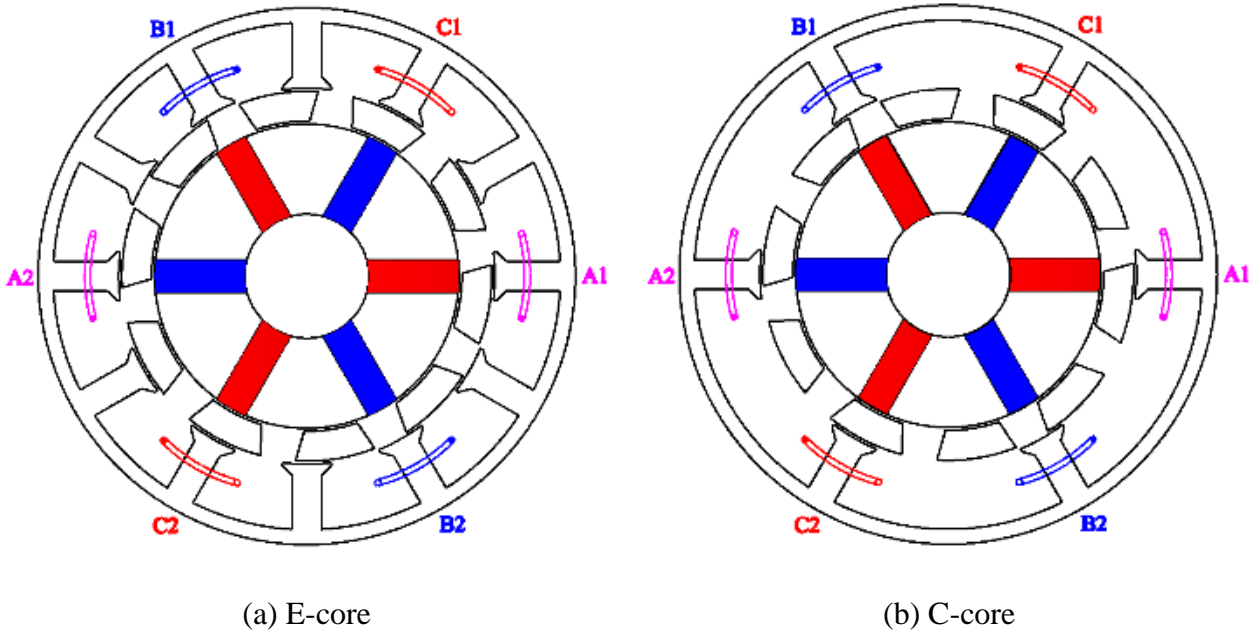


Fig. 3.13. Cross-sections of 6/10-pole E- and C-core PS-SFPM machines.

It can be concluded from (3.9) with $j=-1$ and (3.12)-(3.14) that the 6/10-pole E- and C-core PS-SFPM machines shown in Fig. 3.13 have the same armature excitation MMF harmonic orders as the 12/13-pole PS-SFPM machine, Fig. 3.1(c), albeit with different magnitudes. Therefore, p_{ea} is the same in these three machines, *i.e.* 7. Again, (3.8) can be matched in the

6/10-pole E- and C-core PS-SFPM machines.

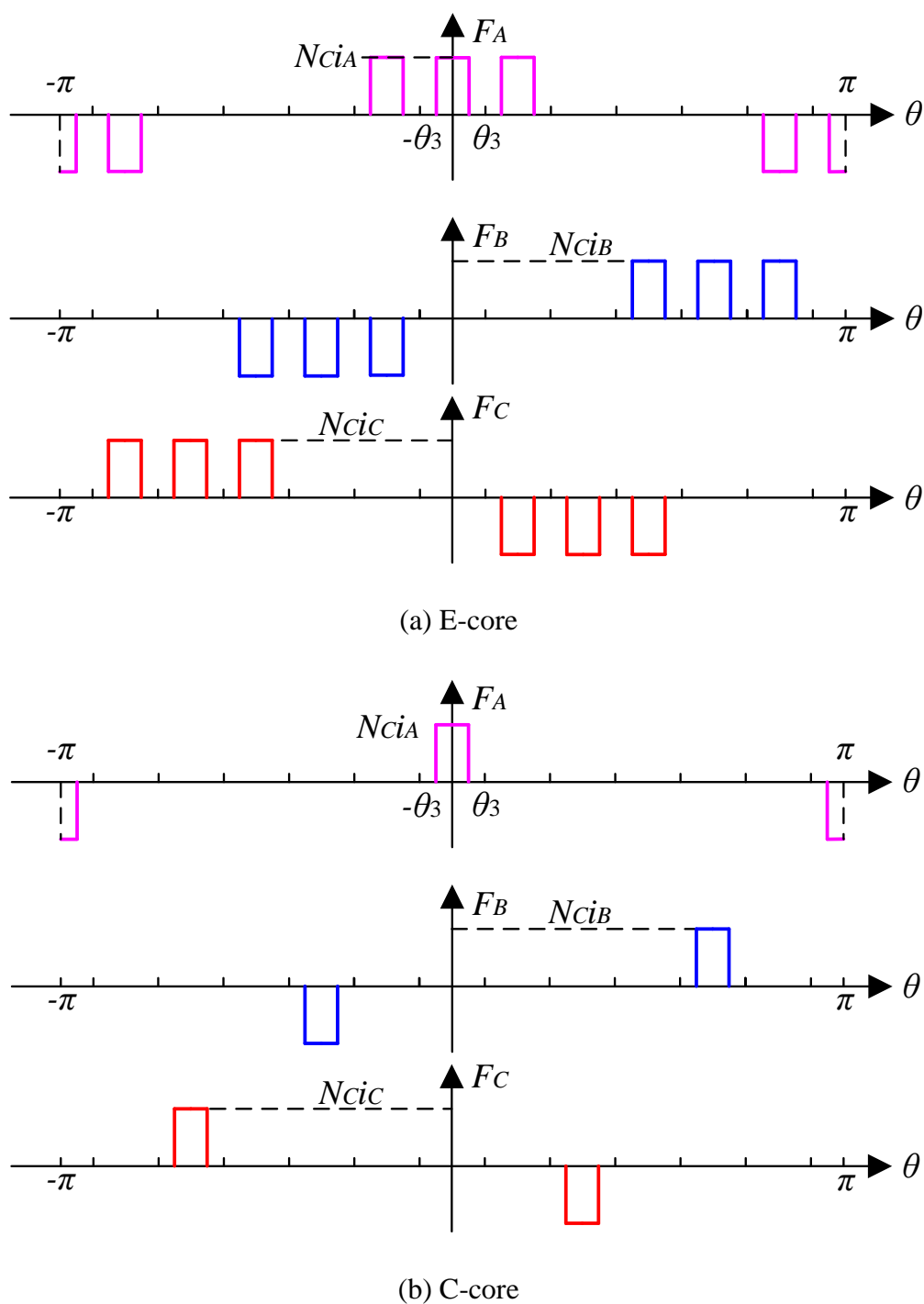


Fig. 3.14. Outer air-gap armature excitation MMF generated in 6/10-pole E- and C-core PS-SFPM machines.

The magnetic gearing characteristics of the 12/10-pole alternate poles wound, 6/10-pole E- and C-core PS-SFPM machines are synthesised in Table 3.5, compared with the 12/10-pole all poles wound one. Due to the same $N_r=10$ and $p_{ea}=4$ between 12/10-pole all and alternate poles

wound PS-SFPM machines, magnetic gearing ratio G_r are the same as 2.5. However, in the 6/10-pole E- and C-core PS-SFPM machines, it is 1.43 due to a higher $p_{ea}=7$.

Table 3.5 Magnetic gearing effect in 12/10-pole all and alternate poles wound, 6/10-pole E- and C-core PS-SFPM machines

Machine	N_r	p_{PM}	p_{ea}	G_r
12/10-pole all poles wound	10	6	4	2.5
12/10-pole alternate poles wound		6	4	2.5
6/10-pole E-core		3	7	1.43
6/10-pole C-core		3	7	1.43

3.4 Torque Contributions of Dominant Field Harmonics

In the previous analysis, it was shown that the PS-SFPM machines operate based on the magnetic gearing principle, by the MMF-permeance model. Due to the modulation of the rotor iron pieces to the open-circuit PM and armature excitation MMFs, abundant field harmonics will be generated in both air-gaps. Their orders and rotating speeds predicted by the MMF-permeance model can be validated by the FE results, *e.g.* some dominant harmonics as illustrated in Fig. 3.7 and Fig. 3.9. In this section, the average torque contributions by these field harmonics are investigated.

According to the Maxwell stress tensor, the instantaneous electromagnetic torque in the outer air-gap $T_{emout}(t)$ can be expressed as,

$$T_{emout}(t) = \frac{R_{go}^2 L_s}{\mu_0} \int_0^{2\pi} B_{rout}(t, \theta) B_{tout}(t, \theta) d\theta = \sum_n T_{emoutn}(t) \quad (3.15)$$

where R_{go} and μ_0 are the outer air-gap radius and the vacuum permeability, respectively. $B_{rout}(t, \theta)$ and $B_{tout}(t, \theta)$ are the instantaneous outer air-gap radial and tangential flux density components, respectively. $T_{emoutn}(t)$ is the instantaneous electromagnetic torque generated by the n^{th} radial and tangential field harmonics in the outer air-gap.

$B_{rout}(t, \theta)$ and $B_{tout}(t, \theta)$ in (3.15) can be expanded by Fourier series,

$$\begin{cases} B_{rout}(t, \theta) = \sum_n B_{routn}(t) \cos[n\theta - \theta_{routn}(t)] \\ B_{tout}(t, \theta) = \sum_n B_{toutn}(t) \cos[n\theta - \theta_{toutn}(t)] \end{cases} \quad (3.16)$$

where $B_{routn}(t)$ and $B_{toutn}(t)$ are the n^{th} Fourier coefficients of B_{rout} and B_{tout} , respectively. $\theta_{routn}(t)$ and $\theta_{toutn}(t)$ are their phases, respectively.

Based on (3.16), $T_{emoutn}(t)$ in (3.15) can be rewritten as,

$$T_{emoutn}(t) = \frac{\pi R_{go}^2 L_s}{\mu_0} B_{routn}(t) B_{toutn}(t) \cos[\theta_{routn}(t) - \theta_{toutn}(t)] \quad (3.17)$$

The electromagnetic torque waveforms generated in the outer and inner air-gaps predicted by FE are shown in Fig. 3.15(a) and Fig. 3.15(b), respectively. The contributions of field harmonics to these two average electromagnetic torques are given in Fig. 3.16(a) and Fig. 3.16(b), respectively. By ways of example, the spectra in Fig. 3.16(a) are obtained as follows,

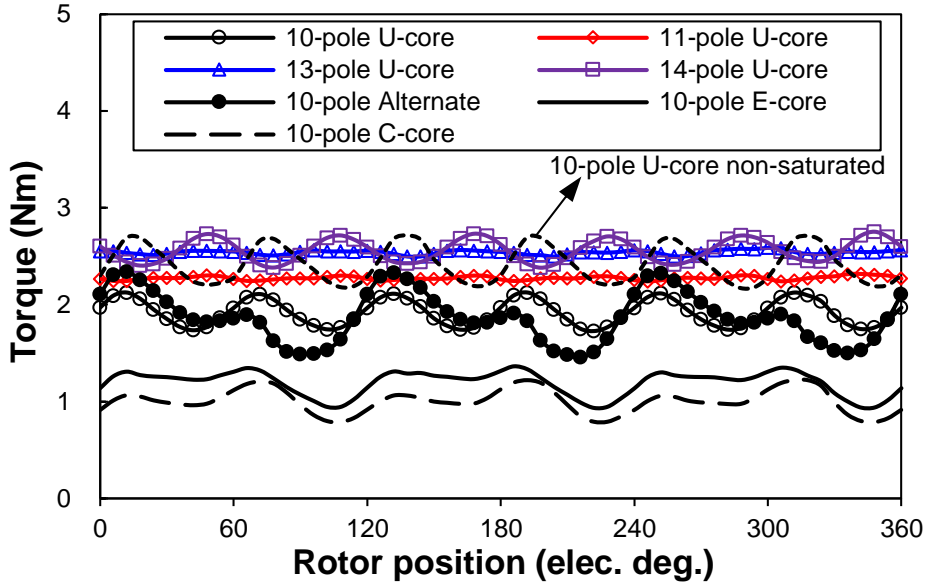
(1) Firstly, $B_{rout}(t, \theta)$ and $B_{tout}(t, \theta)$ at different times t can be expanded to Fourier series based on (3.16), and hence $B_{routn}(t)$, $B_{toutn}(t)$, $\theta_{routn}(t)$ and $\theta_{toutn}(t)$ can be obtained.

(2) Secondly, according to (3.17), $T_{emoutn}(t)$ can be calculated from $B_{routn}(t)$, $B_{toutn}(t)$, $\theta_{routn}(t)$ and $\theta_{toutn}(t)$.

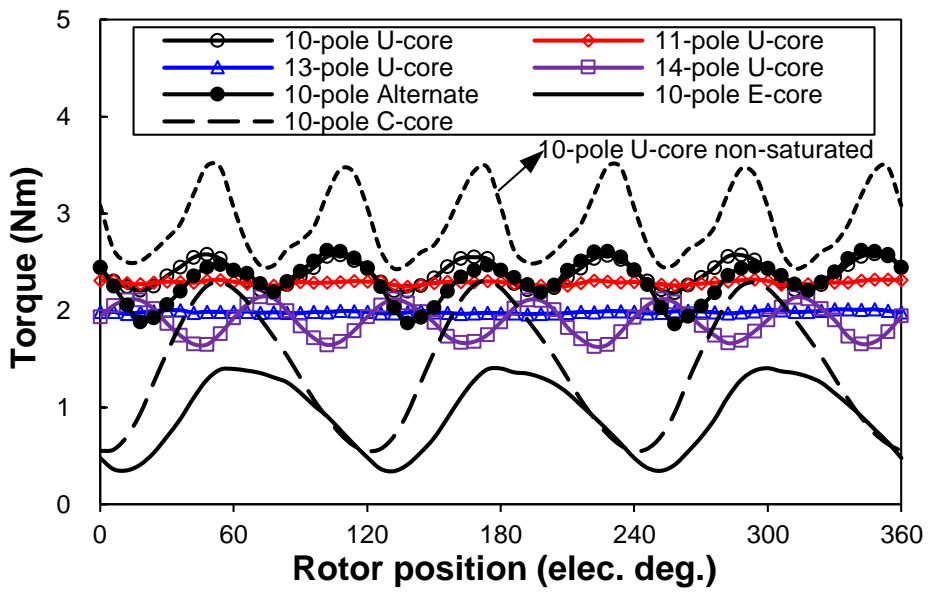
(3) Finally, the average torque generated by the n^{th} radial and tangential field harmonics $T_{emoutnavg}$ and hence the torque contribution shown in Fig. 3.16(a) can be obtained.

The contribution of the main air-gap field harmonics having pole-pairs of $(2i-1)p_{PM}$ and $|N_r \pm (2i-1)p_{PM}|$ ($i=1,2,3$) is given in Table 3.6 and Table 3.7 for the outer and inner air-gaps respectively, as well as the electromagnetic torque of rotor iron pieces as Table 3.8. As shown in Table 3.6-Table 3.8, more than 93% average electromagnetic torques are generated by these main field harmonics for both the outer and inner air-gaps, and also the electromagnetic torque of the rotor iron piece. This is different from the magnetic gear analysed in [ATA01a] and [ATA04a] in which the main electromagnetic torque is transmitted via two dominant air-gap harmonics having pole-pair number with p_o and p_i . This is caused by the smaller gear ratios in PS-SFPM machines, and the slotted topology with non-overlapping concentrated armature windings which exhibit abundant MMF harmonics. It should be noted that the electromagnetic torque waveforms shown in Figs. 15 and 16, and the torque contribution of the main field

harmonics listed in Table 3.6-Table 3.8 are obtained by FE, for depicting that the average electromagnetic torques are generated by the main field harmonics in the PS-SFPM machines. It is worth noting that when the saturation in steel is neglected, both the outer and inner air-gap electromagnetic torques will be higher than their saturated components, as shown in Fig. 3.15 for the 12/10-pole U-core PS-SFPM machine with and without consideration of saturation in steel. However, more than 95.40% of the outer and inner air-gap average electromagnetic torques are still generated by the main field harmonics, as well as the electromagnetic torque of the rotor iron piece, as shown in Table 3.6-Table 3.8 for the 12/10-pole U-core PS-SFPM machine without consideration of saturation in steel, *i.e.* the steel is non-saturated. This again indicates that whether the saturation in steel is taken into consideration or not, the electromagnetic torques in the PS-SFPM machines are mainly contributed by the main field harmonics, due to the magnetic gearing effect. It is worth noting that the number of elements in air-gap for finite element analysis is 1200 in this chapter.

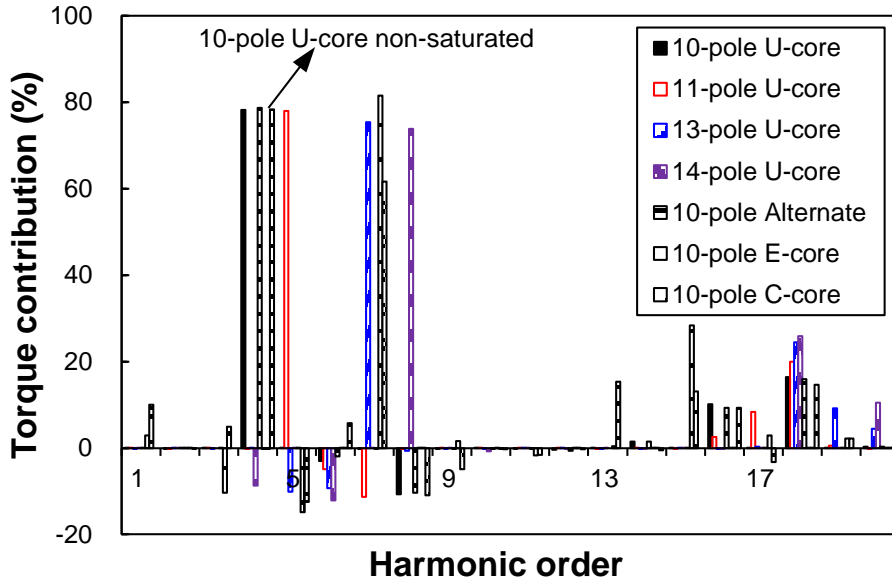


(a) Outer air-gap

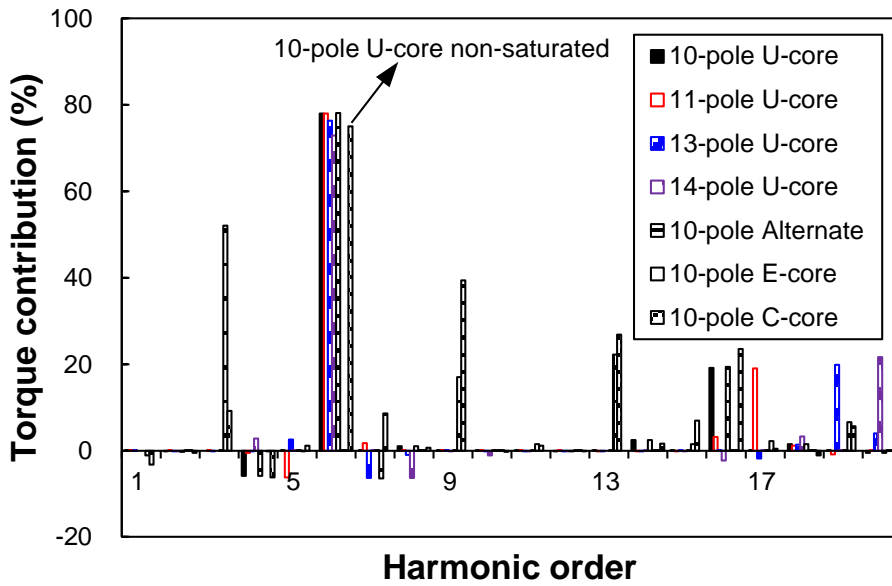


(b) Inner air-gap

Fig. 3.15. Electromagnetic torque waveforms generated in the air-gaps in PS-SFPM machines with consideration of saturation in steel.



(a) Outer air-gap



(b) Inner air-gap

Fig. 3.16. Contribution of field harmonics to average electromagnetic torque in outer and inner air-gaps in PS-SFPM machines with consideration of saturation in steel.

Table 3.6 Outer air-gap torque contribution of main field harmonics in 12-stator-pole PS-SFPM machines (%)

Harmonic order	U-core					Alternate	E-core	C-core
	10 non-saturated	10	11	13	14			
N_r	10 non-saturated	10	11	13	14	10	10	10
p_{PM}	5.73	-3.03	-4.86	-9.25	-12.15	-1.93	-10.32	4.88
$ N_r - p_{PM} $	78.36	78.22	78.01	75.35	73.84	78.73	81.53	61.67
$N_r + p_{PM}$	9.33	10.16	8.34	9.18	10.47	9.28	0.41	15.29
$3p_{PM}$	14.60	16.47	19.99	24.48	25.94	15.91	1.57	-4.96
$ N_r - 3p_{PM} $	-10.90	-10.69	-11.36	-10.07	-8.71	-10.35	2.85	9.97
$N_r + 3p_{PM}$	1.48	2.15	2.38	3.39	4.39	2.45	2.18	2.23
$5p_{PM}$	0.40	-0.02	-0.04	-0.52	-0.56	0.07	28.32	13.11
$ N_r - 5p_{PM} $	0.12	0.35	0.57	0.32	-0.21	0.26	-14.84	-12.53
$N_r + 5p_{PM}$	0.03	0.43	0.62	0.94	1.08	0.34	4.06	5.69
SUM	99.14	94.03	93.67	93.82	94.09	94.76	95.75	95.36

Table 3.7 Inner air-gap torque contribution of main field harmonics in 12-stator-pole PS-SFPM machines (%)

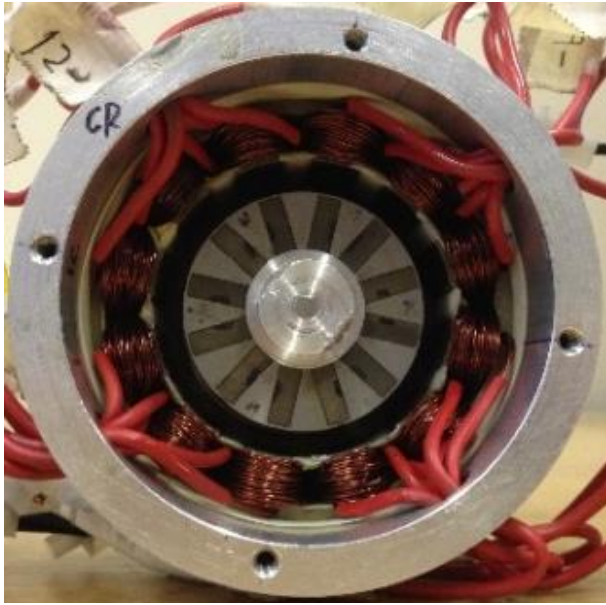
Harmonic order	U-core					Alternate	E-core	C-core
	10 non-saturated	10	11	13	14			
N_r	10 non-saturated	10	11	13	14	10	10	10
p_{PM}	75.09	78.06	77.98	76.37	72.95	78.12	52.11	9.24
$ N_r - p_{PM} $	-6.24	-5.85	-6.27	-6.34	-6.38	-5.85	-6.44	8.53
$N_r + p_{PM}$	23.57	19.19	19.06	19.88	21.67	19.33	22.25	26.80
$3p_{PM}$	-1.12	1.53	1.19	1.39	3.28	1.46	17.01	39.42
$ N_r - 3p_{PM} $	0.62	1.04	1.67	2.59	2.74	1.00	-1.15	-3.22
$N_r + 3p_{PM}$	2.49	0.40	0.55	1.13	1.50	0.44	6.54	5.58
$5p_{PM}$	0.93	0.17	0.57	1.02	1.20	0.18	1.50	6.89
$ N_r - 5p_{PM} $	-0.66	-0.53	-0.83	-1.78	-2.29	-0.54	-0.03	1.14
$N_r + 5p_{PM}$	0.71	0.50	0.50	0.52	0.51	0.50	3.46	1.70
SUM	95.40	94.51	94.41	94.77	95.18	94.64	95.24	96.08

Table 3.8 Electromagnetic torque contribution of main field harmonics in 12-stator-pole PS-SFPM machines (%)

Harmonic order	U-core					Alternate	E-core	C-core
	10 non-saturated	10	11	13	14			
N_r	10 non-saturated	10	11	13	14	10	10	10
p_{PM}	43.53	41.87	36.67	28.29	23.96	42.31	16.93	7.41
$ N_r - p_{PM} $	32.26	31.66	35.76	39.53	39.80	31.99	43.13	30.78
$N_r + p_{PM}$	17.09	15.16	13.72	13.87	15.22	14.83	9.94	21.98
$3p_{PM}$	6.03	8.20	10.57	14.36	16.33	7.92	8.31	20.84
$ N_r - 3p_{PM} $	-4.62	-4.20	-4.83	-4.52	-3.85	-4.07	1.10	2.30
$N_r + 3p_{PM}$	2.03	1.18	1.46	2.40	3.16	1.34	4.08	4.18
$5p_{PM}$	0.69	0.08	0.26	0.15	0.19	0.13	16.61	9.49
$ N_r - 5p_{PM} $	-0.31	-0.14	-0.13	-0.60	-1.09	-0.18	-8.37	-4.58
$N_r + 5p_{PM}$	0.40	0.47	0.56	0.75	0.83	0.43	3.80	3.37
SUM	97.10	94.30	94.04	94.24	94.55	94.69	95.53	95.78

3.5 Experimental Validation

In this section, a prototype machine of 12/10-pole PS-SFPM machine is fabricated, Fig. 3.17, for verifying the FE analysis. The dimensions of the prototype machine are given in Table 3.9. The 2D FE predicted and measured static torque waveforms under different currents are given in Fig. 3.18. Good agreements have been achieved between the measured and 2D FE predicted ones, although the measured values are slightly smaller due to end effect, similarly for the average static torques listed in Table 3.10.



(a) Partitioned stators



(b) Rotor

Fig. 3.17. Photos of 12/10-Pole PS-SFPM prototype machine.

Table 3.9 Dimensions of the 12/10-pole PS-SFPM prototype machine

Parameters	Prototype	Parameters	Prototype	Parameters	Prototype
L_s (mm)	25	R_{isy} (mm)	21.75	θ_{osy} ($^\circ$)	6.14
R_{oso} (mm)	45	R_{isi} (mm)	10.4	θ_{ot} ($^\circ$)	4.94
R_{osy} (mm)	42	T_{PM} (mm)	4	l_{ott} (mm)	1
R_{osi} (mm)	31.75	T_{bri} (mm)	0.5	l_{otb} (mm)	3
R_{ro} (mm)	31.25	g_o (mm)	0.5	θ_{ro} ($^\circ$)	18
R_{ri} (mm)	26.25	g_i (mm)	0.5	θ_{ri} ($^\circ$)	24
R_{iso} (mm)	25.75	θ_{ost} ($^\circ$)	8.12	θ_{PM} ($^\circ$)	30

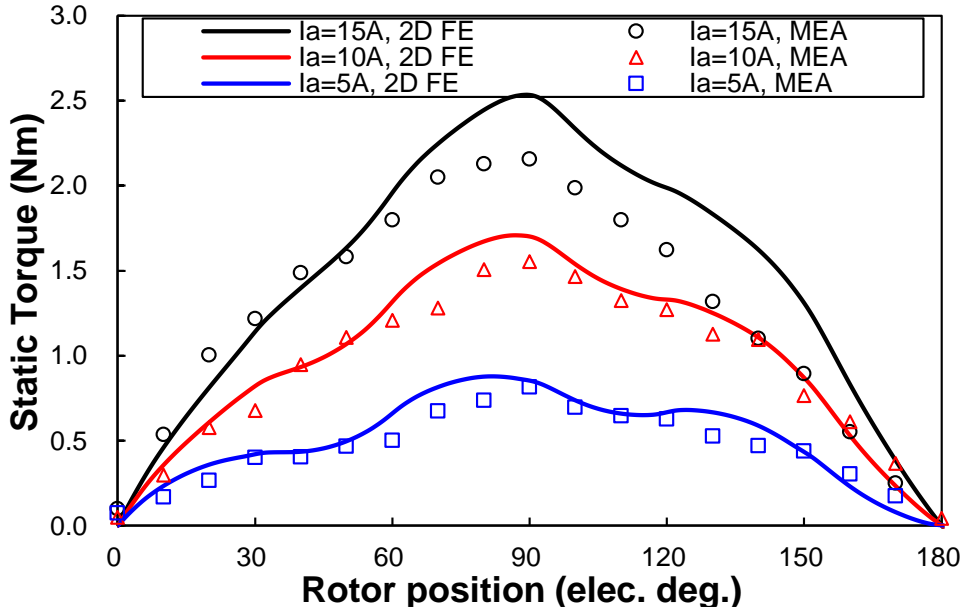


Fig. 3.18. 2D FE predicted and measured static torques under different currents in the 12/10-pole PS-SFPM prototype machine ($I_A=-2I_B=-2I_C$).

Table 3.10 Comparison of 2D FE predicted average static torques and measured ones under different currents ($I_a=-2I_b=-2I_c$)

I_a (A)	2D FE Predicted (Nm)	Measured (Nm)
0	0	0
5	0.51	0.44
10	1.01	0.91
15	1.50	1.23

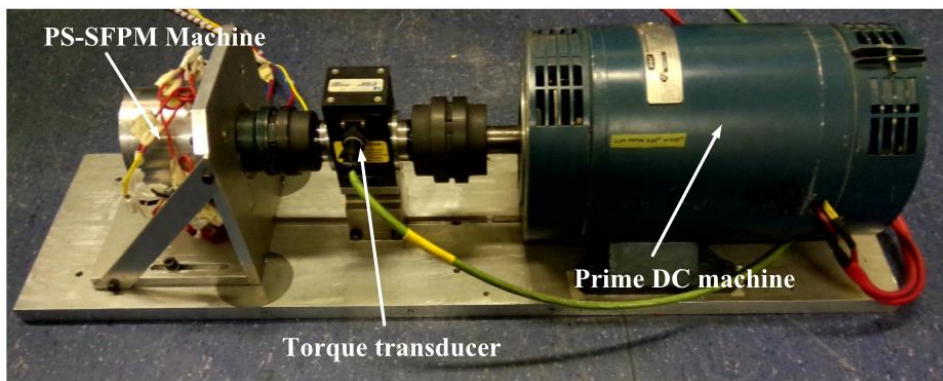


Fig. 3.19. Test rig for the PS-SFPM machine ($U_{dc}=18V$, $I_{dc}=7.5A$).

Based on the test rig shown in Fig. 3.19, the measured and 3D FE predicted torque-speed curves of the 12/10-stator/rotor-pole PS-SFPM machine are comparatively shown in Fig. 3.20, whilst the corresponding power-speed curves are illustrated in Fig. 3.21. As shown in Fig. 3.20

and Fig. 3.21, the measured values are slightly smaller than the 3D FE predicted values due to the short-circuit current and hence loss in the nonmagnetic but current conducting sticks and Allium holder, which is larger at higher speed. This can be observed in Fig. 3.22.

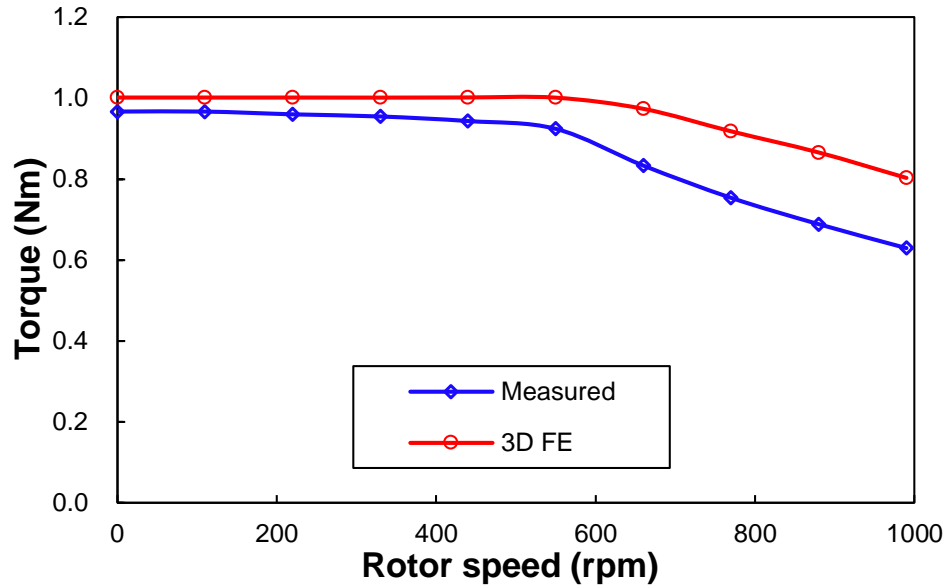


Fig. 3.20. 3D FE predicted and measured torque-speed curves of the 12/10-stator/rotor-pole PS-SFPM machine.

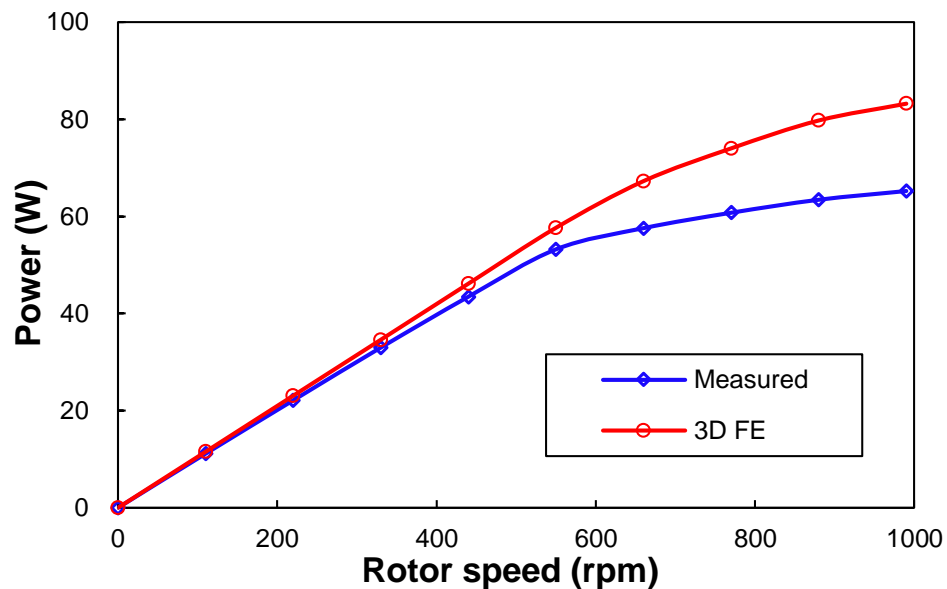


Fig. 3.21. 3D FE predicted and measured power-speed curves of the 12/10-stator/rotor-pole PS-SFPM machine.

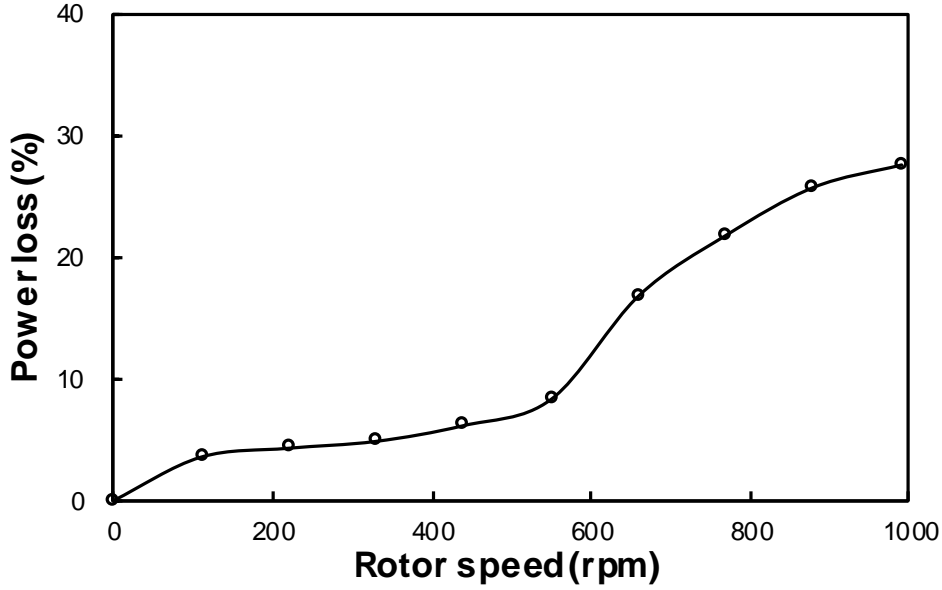


Fig. 3.22. Power loss between 3D FE predicted and measured power-speed curves of the 12/10-stator/rotor-pole PS-SFPM machine.

3.6 Conclusions

In this chapter, the magnetic gearing effect in the PS-SFPM machines is analysed in terms of the air-gap field harmonics based on a simple MMF-permeance model, and verified by FE analysis. It is found that the PS-SFPM machines operate based on the magnetic gearing principle. The modulation of the rotor iron pieces to the open-circuit PM and armature excitation MMFs is similar to that in the magnetic gear and MG machines. More than 93% of the electromagnetic torques generated in both the outer and inner air-gaps is contributed by the dominant rotating field harmonics in open-circuit and armature excitation fields with the same pole-pair number of $|kN_{r\pm}(2i-1)p_{PM}|$ ($k=1, i=1, 2, 3$) and static field harmonics with the same pole-pair number of $(2i-1)p_{PM}$ ($i=1, 2, 3$).

4 Partitioned Stator Flux Reversal Permanent Magnet Machine with Consequent Pole Permanent Magnets

In the previous Chapter 3, it is found that the partitioned stator permanent magnet (PM) machines operate based on the magnetic gearing effect, similar to magnetic gears and magnetically geared (MG) machines, as well as the conventional single-stator-PM machines as presented in Chapter 2. In this chapter, based on the magnetic gearing effect in the partitioned-stator-PM machines, a consequent-pole PM (CPM) inner stator is applied to the partitioned stator flux reversal PM (FRPM) (PS-FRPM) machines referred in Appendix B to reduce the PM volume and hence cost. It is found that the 12-stator-pole PS-FRPM machine having 10-, 11-, 13- and 14-rotor-pole rotors with a CPM inner stator can generate 98.59%, 96.69%, 95.50% and 97.15% torque density of their corresponding surface-mounted PM (SPM) inner stator counterparts, respectively, whilst the PM volume can be saved by 28.33%, 30%, 30% and 33.33%. The PS-FRPM machines with a CPM inner stator exhibit less than 1% lower efficiency than their corresponding SPM inner stator counterpart.

This part has been published in IEEE Transactions on Energy Conversion.

4.1 Introduction

Compared with doubly salient PM (DSPM) machines with yoke-inserted PMs and switched flux PM (SFPM) machines with tooth-inserted PMs, FRPM machines with surface-mounted PMs have the benefit of robust integral stator lamination which makes them easier to make and assemble [ZHU09a]. However, similar to DSPM and SFPM machines, FRPM machines also suffer from an obvious demerit which is the geometric conflict of PMs and armature windings, resulting in that the total area of PMs and armature windings and hence the torque density are restricted. In [ZHU15a], a new FRPM machine with partitioned stator in which the PMs and armature windings are separately placed in inner and outer stators is described and analysed, which can be referred to Appendix B. By utilizing the inner space, the electromagnetic load can be enlarged resulting in higher torque density in PS-FRPM machines. In PS-FRPM machines, the outer and inner stators perform different field functions, *i.e.* armature excitation and PM fields, respectively. This is different from the conventional double stator machines [ZON14a] [TOB99a] [ABB00a], in which the two stators are identical.

However, the PM material especially the high energy-product PM, such as NdFeB, is expensive. To reduce the cost, the research on the less-PM and non-PM machines has drawn much attention over last few years [BOL14a]. An effective way is to introduce wound field winding. With the hybrid excitation by both PMs and field winding the PMs are exempted cost effectively due to less or zero PM volume [LUO00a] [GAP14a] [SRI11a] [BAS11a] [HUA09a] [WAN12a] [GAO14a] [ZUL10a] [SUL11a] [FUK12a]. For stator-excitation machines, less-PM hybrid excitation and non-PM wound field ones are analysed in [HUA09a] [WAN12a] [GAO14a] and [ZUL10a] [SUL11a], respectively. However, the introduction of field winding will cause higher copper loss and therefore lower efficiency. Another effective way to reduce the PM volume is to adopt consequent-pole PMs (CPM) in machines, including stator-PM machine [CHU08a] and rotor-PM machine [CHU11a] [CHU12a] [CHU15a], as well as magnetic gear [LIU09a]. As pointed out in [CHU15a], fractional-slot machine with CPM rotor can achieve similar electromagnetic performance with 33% PM volume reduction. In this chapter, the CPM is employed in the PS-FRPM machines to reduce the PM volume while remain the torque density and efficiency.

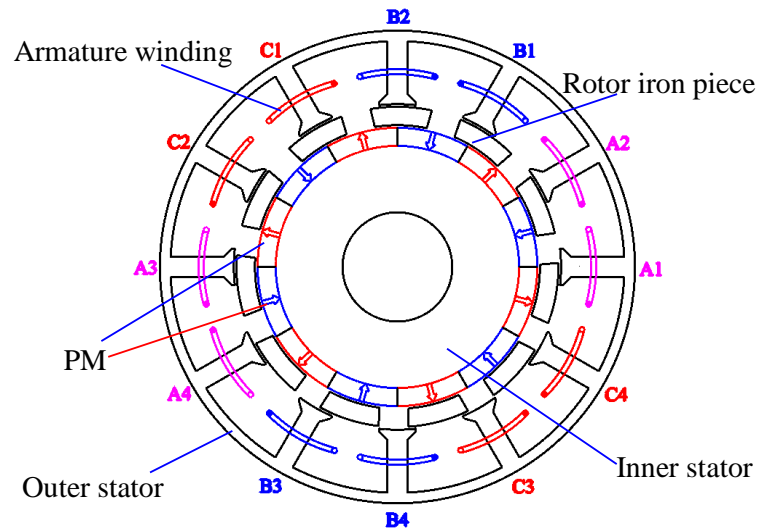
This chapter is organized as follows. In section 4.2, the 12/11-pole PS-FRPM machine with CPM inner stator is proposed and analysed. In section 4.3, different stator/rotor pole combinations are employed and designed, of which the electromagnetic performance is given in section 4.4. In section 4.5, the prototype machine with CPM inner stator is built and tested to verify the finite element (FE) analysis.

4.2 12/11-Pole PS-FRPM Machine with CPM Inner Stator

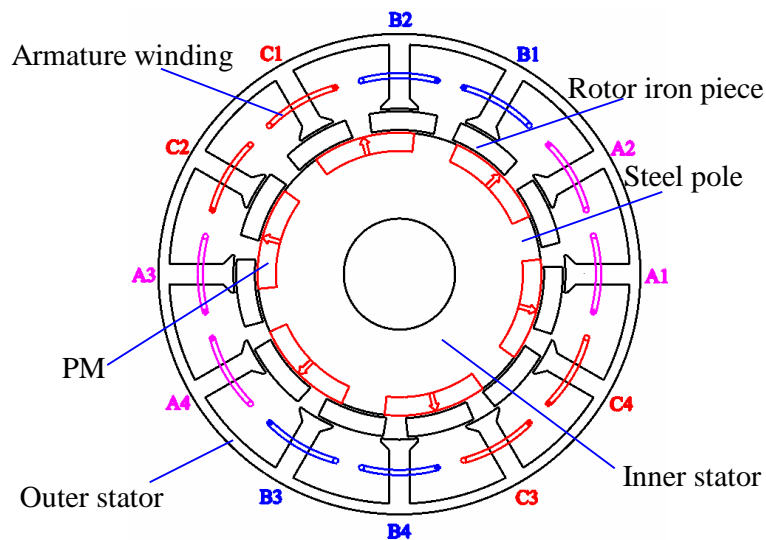
In [ZHU15a], three-phase 12-stator-pole PS-FRPM machines with surface-mounted PM (SPM) inner stator having different rotor pole numbers, *i.e.* 10, 11, 13 and 14, are comparatively analysed. Their main design parameters are given in Table B.1. It shows that the 12/11-pole PS-FRPM machine with SPM inner stator shown in Fig. 4.1(a) can produce the largest torque density among these four machines.

As shown in Fig. 4.1(a), there are two stators and one sandwiched rotor made up of iron pieces in PS-FRPM machine with SPM inner stator. The PMs and armature windings are separately placed in the inner and outer stators respectively. Two adjacent PMs in the SPM inner stator have opposite polarities consisting of one PM pair, consistent with those in SPM machine [ELR06a]. However, this is different in the CPM inner stator. As shown in Fig. 4.1(b),

all the PMs have the same polarity, between which iron consequent poles are sandwiched. The PM numbers in CPM inner stator, Fig. 4.1(b), is only half of that in SPM one, Fig. 4.1(a). However, the equivalent pole pair number of the CPM inner stator is the same as that in the SPM one, *i.e.* 6, due to the alternate PMs and iron poles, Fig. 4.1(b), as pointed out in [DOR10a]. It is worth noting that the coil connection of the PS-FRPM machines having both SPM and CPM inner stators can be referred to Fig. 1.2.



(a) Existing PS-FRPM machine with SPM inner stator



(b) Proposed PS-FRPM machine with CPM inner stator

Fig. 4.1. Cross-section of 12/11-pole PS-FRPM machines with existing SPM and proposed CPM inner stators.

Fig. 4.2 shows the variation of 2D FE predicted average electromagnetic torque with PM arc

θ_{PM} in the 12/11-pole PS-FRPM machine with CPM inner stator when the copper loss is set as the rated value $p_{cu}=20W$, under brushless AC (BLAC) and zero d -axis current control, *i.e.* phase current and phase back-EMF have the same phase angle. The largest torque can be achieved with 2.84Nm when the PM arc $\theta_{PM}=42^\circ$, whilst that of 12/11-pole PS-FRPM machine with SPM inner stator is 2.94Nm. Therefore, the 12/11-pole PS-FRPM machine with CPM inner stator can maintain 97.1% torque density whilst the PM volume can be saved by 30%.

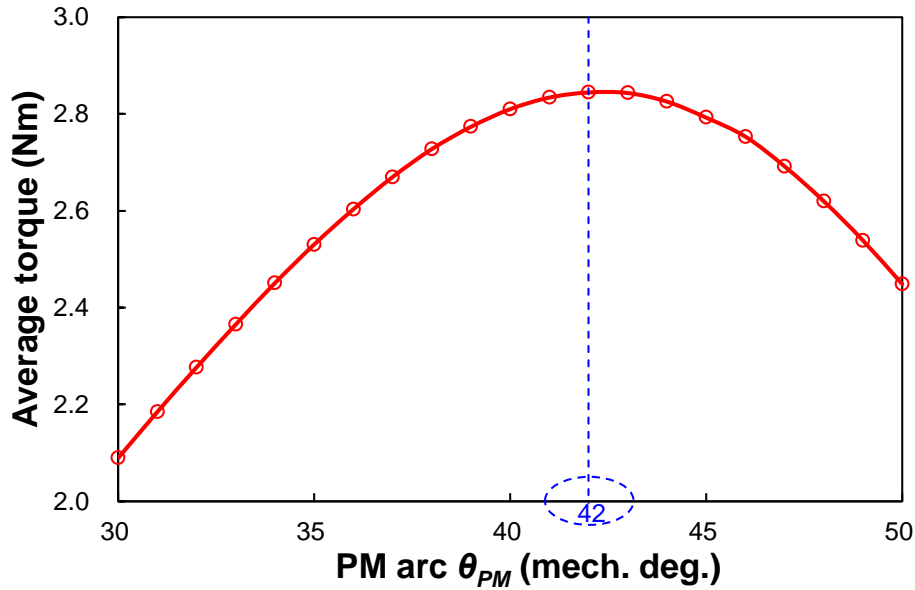


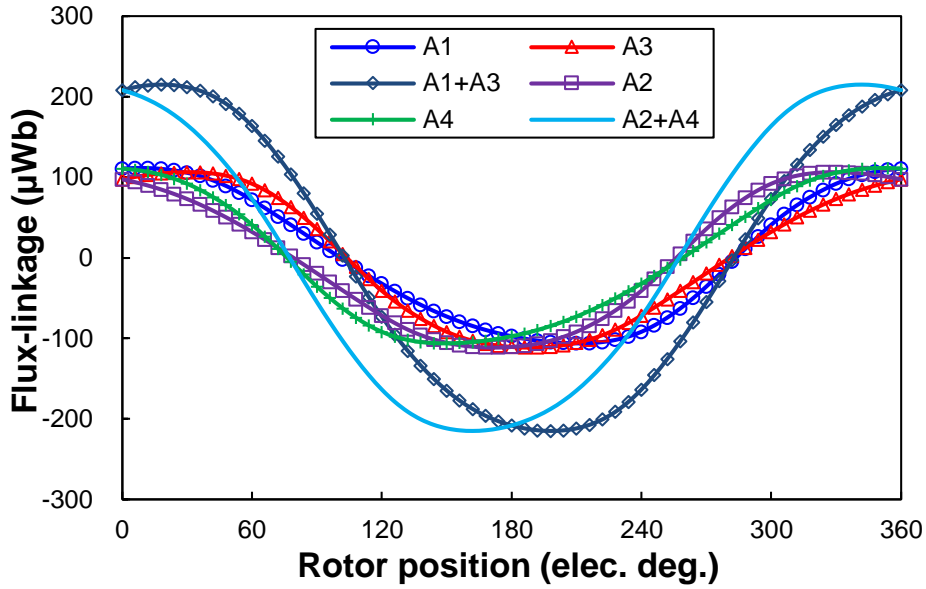
Fig. 4.2. 2D FE predicted average torque against PM arc of 12/11-pole PS-FRPM machine with CPM inner stator ($p_{cu}=20W$, BLAC, phase current and phase back-EMF have the same phase angle).

Fig. 4.3 shows the coil flux-linkage waveforms of the 12/11-pole PS-FRPM machine with CPM inner stator. In Fig. 4.3, N_c is the number of coil turns. Although the coil flux-linkages suffer from even harmonics similar to the SPM counterpart [ZHU15a], there is no even harmonic in the phase flux-linkage due to cancellation. This is similar to that in the 12/11-pole PS-FRPM machine with SPM inner stator. The flux-linkage even harmonics in coils A1 and A3 can cancel each other due to 180 electric degrees phase difference, whilst those of the odd harmonics including the fundamental component are the same, resulting in doubled value, as evidenced by Fig. 4.3(b). This can be explained as follows.

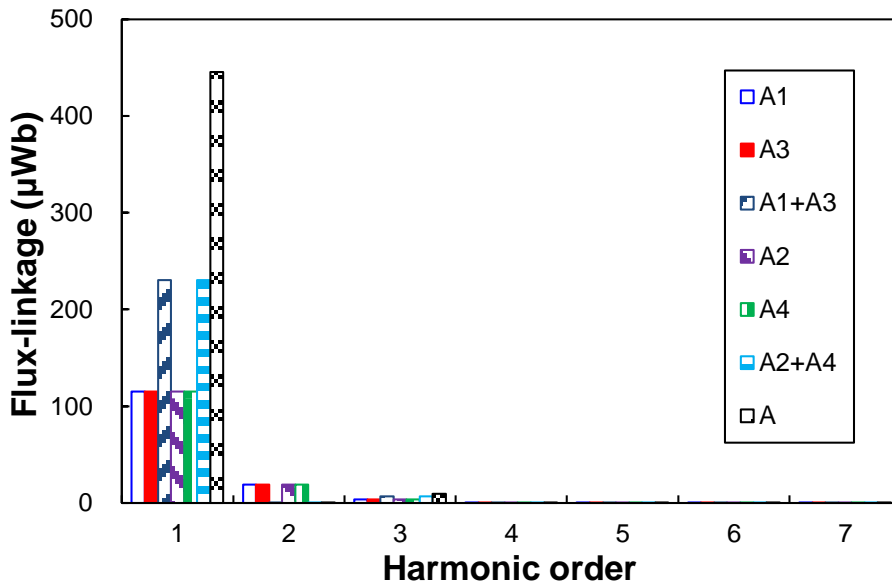
The instantaneous open-circuit coil A1 flux-linkage, $\Phi_{A1}(t)$, in Fourier series can be given by,

$$\Phi_{A1}(t) = \sum_{v=1}^{\infty} \Phi_{A1v}(t) = \sum_{v=1}^{\infty} \Phi_v \sin(vN_r \Omega_r t + \theta_v) \quad (4.1)$$

where t is time. Φ_v is the v^{th} harmonic amplitude. θ_v is the v^{th} harmonic phase. N_r is the rotor pole number. Ω_r is the rotor mechanical angular speed.



(a) Waveforms



(b) Spectra

Fig. 4.3. Coil flux-linkage waveforms of 12/11-pole PS-FRPM machines with CPM inner stator ($N_c=1$).

Similarly, the open-circuit coil A3 flux-linkage, $\Phi_{A3}(t)$ can be given by,

$$\Phi_{A3}(t) = \sum_{v=1}^{\infty} \Phi_{A3v}(t) = \sum_{v=1}^{\infty} \Phi_v \sin(vN_r \Omega_r t + \theta_v - \beta_{31v}) \quad (4.2)$$

where β_{31v} is the lag angle between Φ_{A3v} and Φ_{A1v} . It is given by,

$$\beta_{31v} = -\frac{2N_r C_{t31} v \pi}{N_s} + \theta_{ad31} \quad (4.3)$$

where C_{t31} is the distance between coils A1 and A3 in stator slot number. θ_{ad31} is the additional phase angle resulted from the polarity of the coil A3 and its corresponding PM. N_s is the stator pole number.

As shown in Fig. 4.1(b), all the 6 PMs are magnetized outwards whilst the coils A1 and A3 have inverse polarities. Consequently, θ_{ad31} in the 12/11-pole PS-FRPM machine having CPM inner stator is π , the same as that having SPM inner stator in which the relative polarities of the coil and its corresponding PMs are also inverse for coils A1 and A3, as shown in Fig. 4.1(a). Consequently, β_{31v} can be calculated by,

$$\beta_{31v} = (-11v + 1)\pi \quad (4.4)$$

Based on (4.4), it can be observed that β_{31v}/π for even harmonics ($v=2n, n=1, 2, 3, \dots$) are odd, resulting in 180 electric degrees phase difference between Φ_{A3v} and Φ_{A1v} . Consequently, the even harmonics will cancel each other when coil A1 and coil A3 are connected in series. As for odd harmonics as well as fundamental component ($v=2n-1, n=1, 2, 3, \dots$), β_{31v}/π are even numbers according to (4.4). Therefore, Φ_{A3v} and Φ_{A1v} are exactly the same. The analysis is also applicable to the flux-linkages of coils A2 and A4. Consequently, there is no even harmonic in the phase flux-linkage when the coils constitute one phase are connected in series, as shown in Fig. 4.3(b).

The fundamental coil flux-linkages shown in Fig. 4.3(a) are listed in Table 4.1, for the 12/11-pole PS-FRPM machine with SPM and CPM inner stators, respectively. The fundamental coil flux-linkage of the machine with CPM inner stator is 97.01% of that with SPM inner stator. The fundamental distribution factor in the 12/11-pole PS-FRPM machine with SPM inner stator is 0.966, i.e. the angle between the fundamental back-EMF phasors of coil A₁(A₃) and A₂(A₄) is 30 electric degrees. However, it is not 30 electric degrees whilst the fundamental distribution factor is 0.972 in the CPM inner stator machine according to the 2D FE predicted

results listed in Table 4.1. This is caused by the asymmetric magnetic path in the CPM inner stator machine. Therefore, the fundamental phase flux-linkage and hence the fundamental phase back-EMF of the machine with CPM inner stator can maintain 97.65% of that with SPM inner stator, whilst the PM volume is only 70%. This is due to that the PM arc $\theta_{PM}=42^\circ$ in the machine with CPM inner stator, Fig. 4.2, which is 0.7 times of the PM arc of a pair of north and south poles of SPM machine having same other dimensions.

Table 4.1 Comparison of Fundamental Coil and Phase Flux-linkages in 12/11-Pole PS-FRPM Machines with CPM and SPM Inner Stators predicted by 2D FE (μWb)

Items	CPM	SPM
ψ_{A1}, ψ_{A3}	111.8	115.3
$\psi_{A1}+\psi_{A3}$	223.6	230.6
ψ_{A2}, ψ_{A4}	111.8	115.3
$\psi_{A2}+\psi_{A4}$	223.6	230.6
$\psi_{A1}+\psi_{A2}+\psi_{A3}+\psi_{A4}$	434.9	445.43

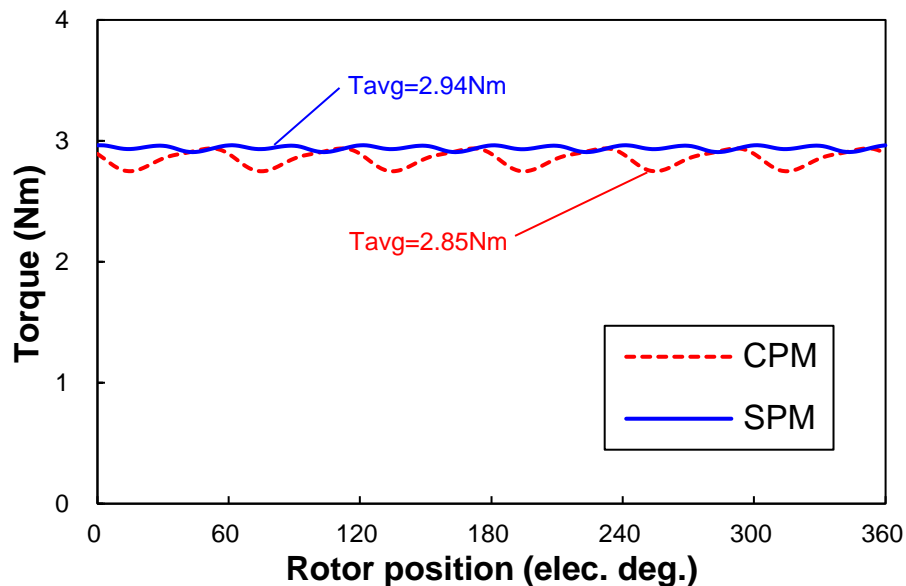


Fig. 4.4. Comparison of the on-load electromagnetic torque waveforms of 12/11-pole PS-FRPM machines with CPM and SPM inner stators predicted by 2D FE ($p_{cu}=20\text{W}$, BLAC, phase current and phase back-EMF have the same phase angle).

The rated on-load electromagnetic torque waveforms of the 12/11-pole PS-FRPM machine with CPM and SPM inner stators are shown in Fig. 4.4. The average torque T_{avg} of the machine with CPM inner stator is 97.1% of that with SPM machine, *i.e.* 2.85Nm and 2.94Nm, respectively. However, the torque ripple is slightly higher in the machine with CPM inner stator, 6.64% and 1.87%, respectively. This is caused by the higher cogging torque which will be given later. The torque ripple T_r is defined as,

$$T_r = \frac{T_{max} - T_{min}}{T_{avg}} \times 100\% \quad (4.5)$$

where T_{max} , T_{min} and T_{avg} are the maximum, minimum, and average electromagnetic torque, respectively.

4.3 Stator and Rotor Pole Combinations

Fig. 4.5 shows the average torque and torque ripple versus PM arc θ_{PM} in 12-stator-pole PS-FRPM machines with CPM inner stator having different rotor pole numbers. The dimensional parameters of these 12-stator-pole PS-FRPM machines with CPM inner stator are the same as those 12-stator-pole PS-FRPM machines with SPM inner stator shown in Table 4.2, except the PM arc θ_{PM} . As shown in Fig. 4.5, the optimal PM arc θ_{PM} for the largest average electromagnetic torque are 43° , 42° , 42° and 40° for 10-, 11-, 13- and 14-rotor-pole machines, respectively. Similar to that in PS-FRPM machines with SPM inner stator [ZHU11a], 12/11- and 12/13-pole PS-FRPM machines with CPM inner stator can produce higher torque than 12/10- and 12/14-pole ones. Moreover, the torque ripple in 12/10- and 12/14-pole machines are higher, which is caused by the larger cogging torque as shown in Fig. 4.6.

Table 4.2 Design Parameters of 12-Stator-Pole PS-FRPM Machines with SPM Inner Stator

Parameters	Unit	Value			
		10	11	13	14
Rotor pole number, N_r	-	10	11	13	14
Stack length, L_s	mm	25			
Outer stator outer radius, R_{oso}	mm	45			
Inner stator inner radius, R_{isi}	mm	10.4			
Outer air-gap length, g_o	mm	0.5			
Inner air-gap length, g_i	mm	0.5			
Outer stator tip top length, l_{ott}	mm	0.5			
Outer stator tip bottom length, l_{otb}	mm	2			
PM arc, θ_{PM}	°	30			
Outer stator yoke radius, R_{osy}	mm	43	43	43	43.5
Outer stator inner radius, R_{osi}	mm	31	31	32	32.5
Rotor inner edge radius, R_{ri}	mm	26.5	27	28.5	29
Outer stator tooth arc, θ_{ost}	°	7	7	6	5
Outer stator tip arc, θ_{ot}	°	3	3	3	3
Rotor pole outer arc, θ_{ro}	°	23	22	20	20
Rotor pole inner arc, θ_{ri}	°	24	21	16	13

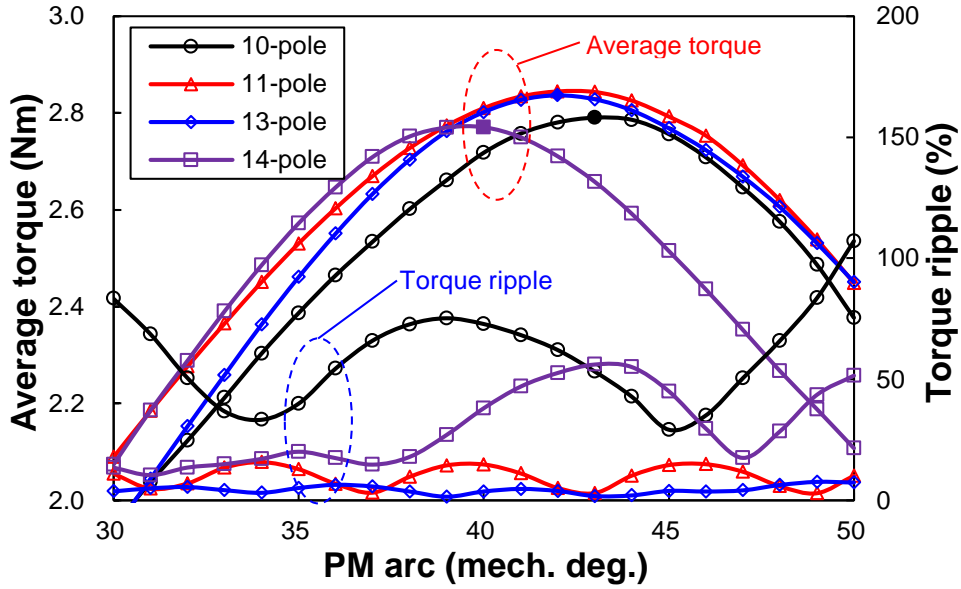


Fig. 4.5. Average torque and torque ripple against PM arc of 12-stator-pole PS-FRPM machines with CPM inner stator ($p_{cu}=20W$, BLAC, phase current and phase back-EMF have the same phase angle).

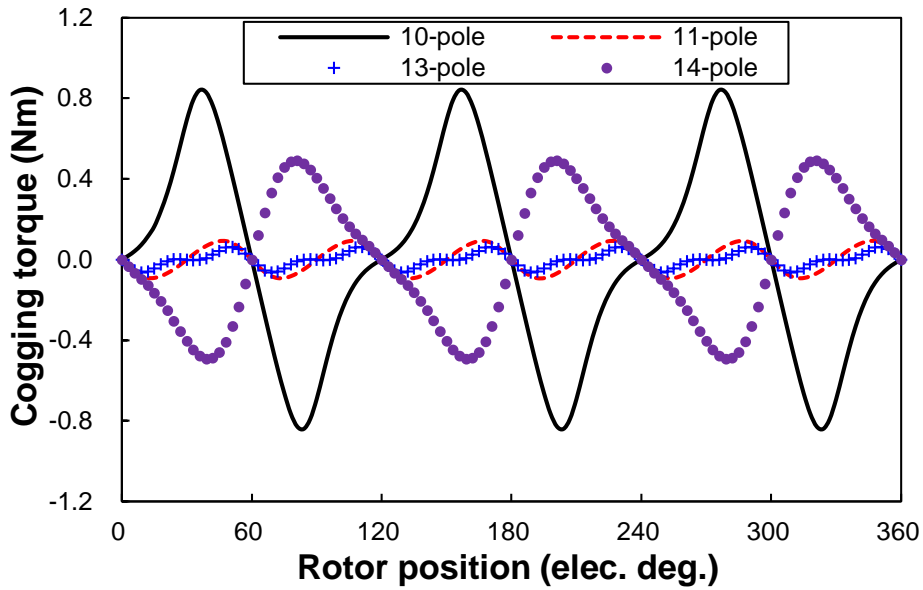


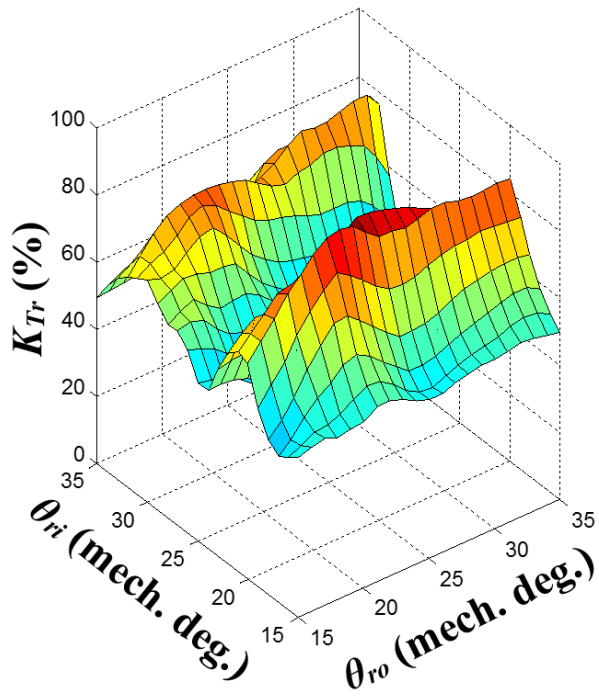
Fig. 4.6. Cogging torque waveforms of 12-stator-pole PS-FRPM machines with CPM inner stator.

The larger cogging torque and hence torque ripple may cause higher vibration and acoustic noise. It is usually useful to suppress the cogging torque, which is caused by the variable air-gap permeance. An effective way to suppress the cogging torque in PM machines is to modify the slot openings [ZHU09a]. To conduct a fair comparison between the PS-FRPM machines

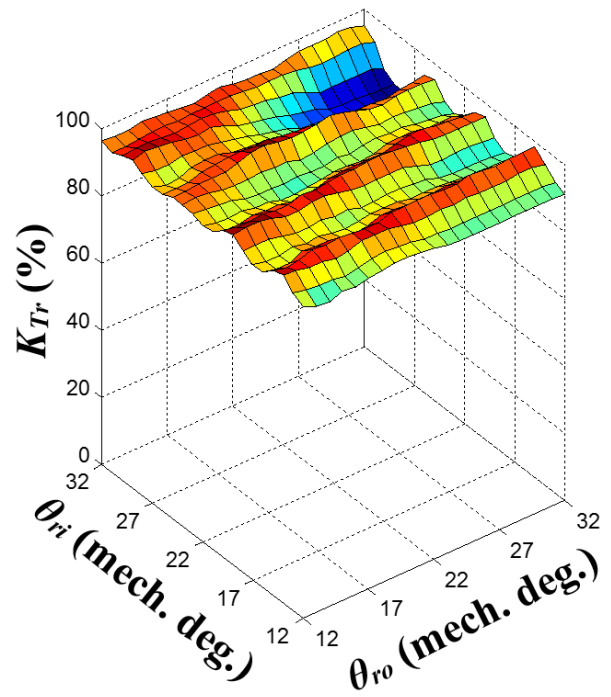
with CPM and SPM inner stators, the outer stators of the former ones are kept the same with the later ones respectively. Consequently, the armature winding slot and hence the ampere turns are the same between each pairs of machines with CPM and SPM inner stators respectively. The inner stators are also set the same, except the arcs of PM θ_{PM} are 43° , 42° , 42° and 40° for 10-, 11-, 13- and 14-rotor-pole machines with CPM inner stator, respectively, whilst that in all the machines with SPM inner stator is the same, *i.e.* 30° . The feasible design parameters are the rotor outer pole arc θ_{ro} and the rotor inner pole arc θ_{ri} , which can be referred to Fig. B.6. Fig. 4.7 and Fig. 4.8 show the torque ripple coefficient K_{Tr} and average torque T_{avg} with θ_{ro} and θ_{ri} in the four analysed CPM inner stator machines, respectively. The torque ripple coefficient K_{Tr} is defined as,

$$K_{Tr} = 100\% - T_r \quad (4.6)$$

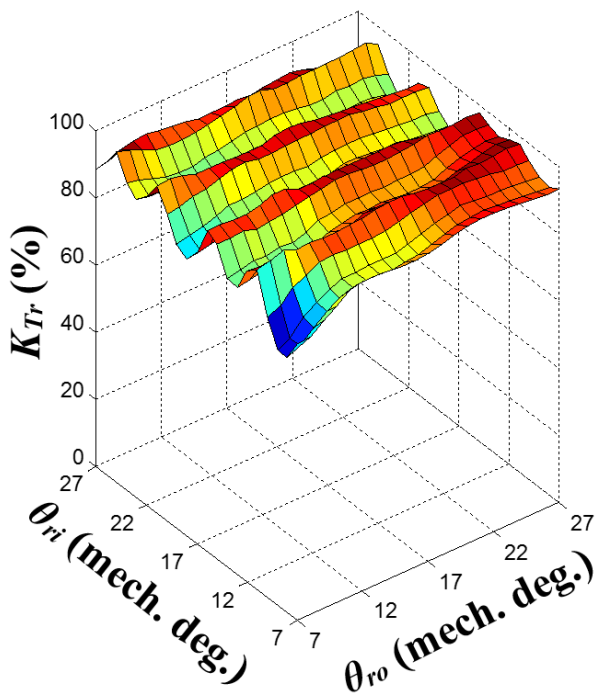
There is no apparent trend but variation of K_{Tr} with θ_{ro} and θ_{ri} , as shown in Fig. 4.7. Generally, 12/11- and 12/13-pole PS-FRPM machines with CPM inner stator have lower torque ripple than other two. However, for 12/10- and 12/14-pole machines, modifying the rotor slot opening is an effective way to suppress the torque ripple by changing θ_{ro} and θ_{ri} , as shown in Fig. 4.7(a) and Fig. 4.7(d), respectively. As for T_{avg} , there is a peak point for the largest average torque for all the four machines, as shown in Fig. 4.8.



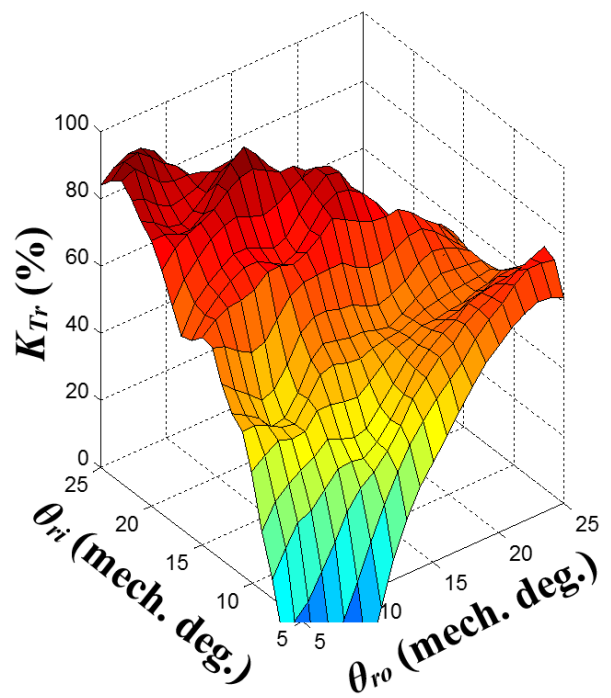
(a) 10-rotor-pole rotor



(b) 11-rotor-pole rotor

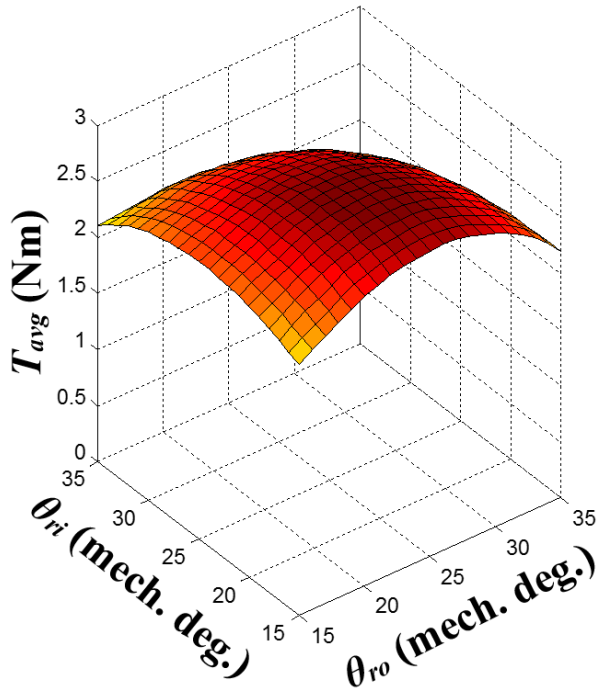


(c) 13-rotor-pole rotor

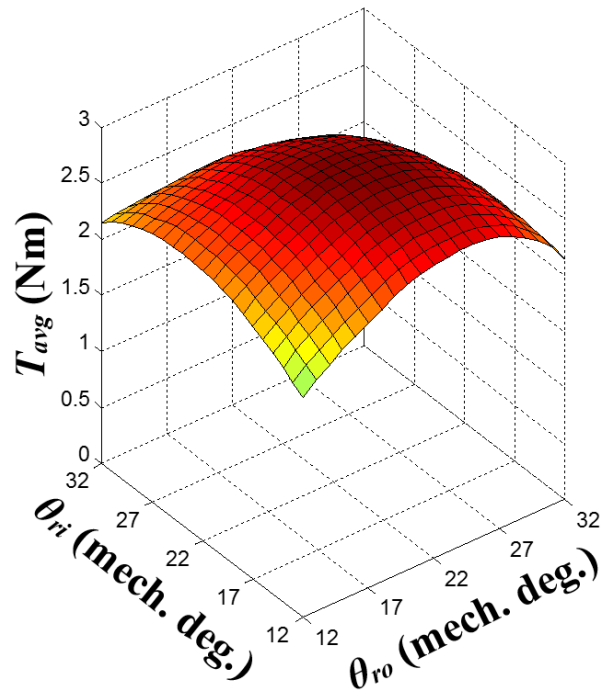


(d) 14-rotor-pole rotor

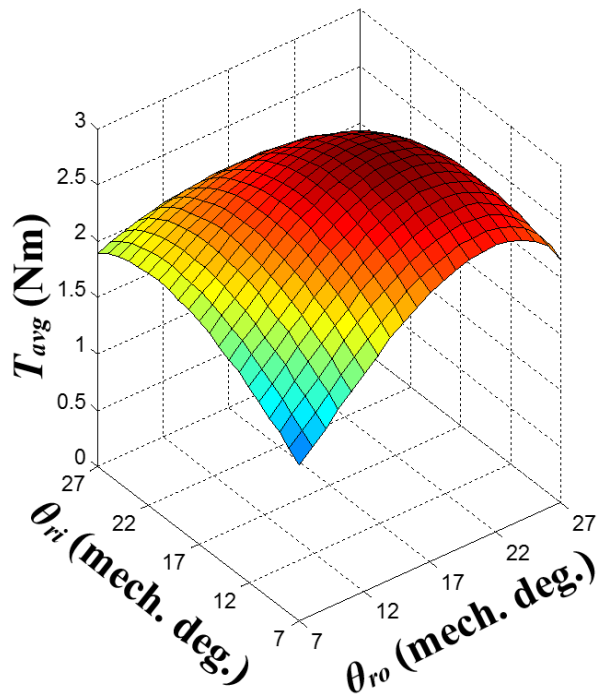
Fig. 4.7. Torque ripple coefficient against rotor pole arcs of 12-stator-pole PS-FRPM machines with CPM inner stator.



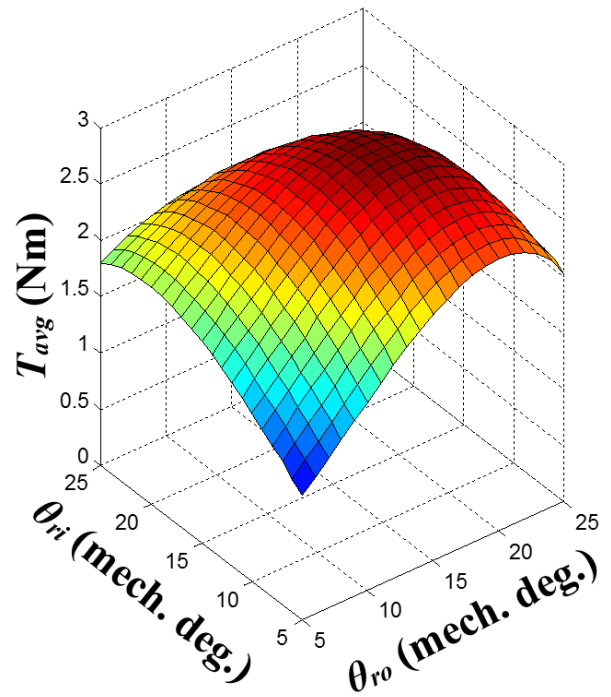
(a) 10-rotor-pole rotor



(b) 11-rotor-pole rotor



(c) 13-rotor-pole rotor



(d) 14-rotor-pole rotor

Fig. 4.8. Average torque against rotor pole arcs of 12-stator-pole PS-FRPM machines with CPM inner stator.

For reducing T_r and also maintain T_{avg} , the modified θ_{ro} and θ_{ri} are obtained by two steps:

(1) The combinations of $(\theta_{ro}, \theta_{ri})$ are discarded if the corresponding T_{avg} is lower than 95% of that of the SPM counterpart.

(2) Among the remaining combinations of $(\theta_{ro}, \theta_{ri})$, the one with the smallest torque ripple is selected as the modified values for θ_{ro} and θ_{ri} .

The modified combinations of $(\theta_{ro}, \theta_{ri})$ are $(22^\circ, 20^\circ)$, $(24^\circ, 20^\circ)$, $(23^\circ, 15^\circ)$ and $(16^\circ, 17^\circ)$ for 12/10-, 12/11-, 12/13- and 12/14-pole PS-FRPM machines with CPM inner stator, respectively. The electromagnetic torque characteristics are synthesized in Table 4.3, in which CPM1 and CPM2 mean before and after modification, respectively. After modifying θ_{ro} and θ_{ri} for smaller torque ripple, the CPM machines having 10-, 11-, 13-, and 14-rotor-pole can generate 98.59%, 96.69%, 95.50% and 97.15% torque density of their corresponding SPM counterparts, respectively. More importantly, as shown in Fig. 4.9, the PM volume can be saved by 28.33%, 30%, 30% and 33.33% in the PS-FRPM machines with CPM inner stator having 10-, 11-, 13-, and 14-rotor-pole, respectively. In Fig. 4.9, the PM volume in 12-stator-pole PS-FRPM machines with CPM inner stator having 10-, 11-, 13- and 14-rotor-pole are 9613.8mm^3 , 9390.2mm^3 , 9390.2mm^3 , 8943.1mm^3 , respectively, whilst that in all the four SPM inner stator machines is 13414.6mm^3 [ZHU15a]. It should be noted that each PS-FRPM machine with CPM inner stator has the same PM outer and inner radii as its counterpart with SPM inner stators, respectively, except the PM arc θ_{PM} as illustrated in Fig. 4.5.

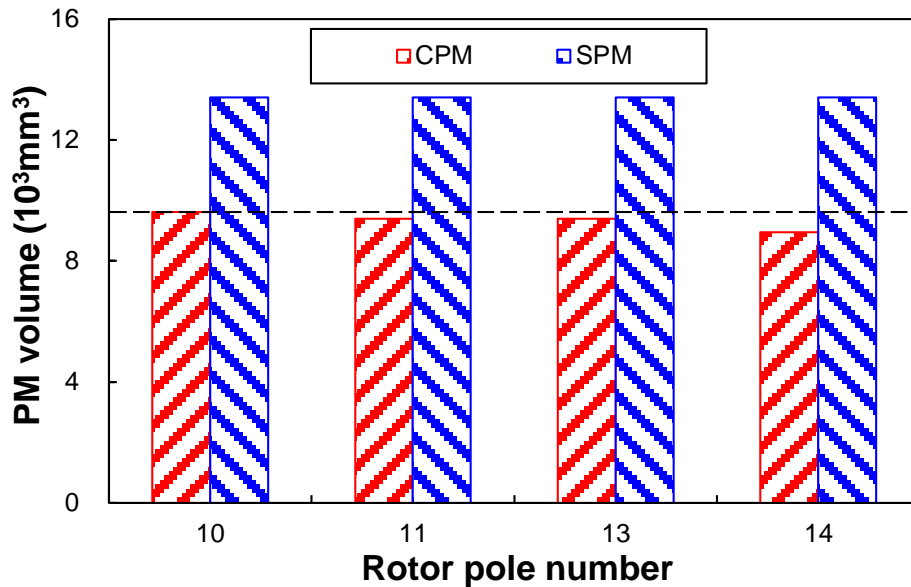


Fig. 4.9. Comparison of PM volumes of 12-stator-pole PS-FRPM machines with CPM and SPM inner stators.

Table 4.3 Electromagnetic Torque Characteristics of PS-FRPM Machines with CPM and SPM Inner Stators

Items		12-stator-pole PS-FRPM			
N_r		10	11	13	14
SPM	T_{avg} (Nm)	2.83	2.94	2.89	2.81
	T_r (%)	18.95	1.87	0.62	6.96
CPM1	T_{avg} (Nm)	2.78	2.85	2.83	2.76
	T_r (%)	59.24	6.64	5.46	37.22
CPM2	T_{avg} (Nm)	2.79	2.84	2.76	2.72
	T_r (%)	6.62	1.76	3.99	14.80

4.4 Electromagnetic Performance

In the previous section, 12-stator-pole PS-FRPM machines with CPM inner stator having 10-, 11-, 13- and 14-rotor-pole are presented and the rotor pole arcs are modified to achieve smaller torque ripples. In this section, the electromagnetic performance of these machines with CPM inner stator are evaluated and compared to their counterparts with SPM inner stator to evaluate the proposed machine with CPM inner stator comprehensively.

4.4.1 Open-circuit flux-linkage and back-EMF

Fig. 4.10 shows the open-circuit phase flux-linkage of 12-stator-pole PS-FRPM machine with CPM and SPM inner stators having different rotor pole numbers. Although the PMs have the same polarity in the machines with CPM inner stator, the phase flux-linkages are bipolar.

Fig. 4.11 illustrates the phase back-EMFs of these machines with CPM and SPM inner stators. As shown in Fig. 4.11, there is no phase back-EMF even harmonic in the PS-FRPM machine with SPM inner stator due to the cancellation of the coils' ones, as pointed out in [ZHU15a] [ZHU15b]. This is also applicable to the 12-stator-pole PS-FRPM machines with CPM inner stator having 11- and 13-rotor-pole, as evidenced for the 12/11-pole one in Fig. 4.3(b). However, as shown in Fig. 4.11 (b), the even harmonics cannot be cancelled in the 12/10- and 12/14-pole PS-FRPM machines with CPM inner stator due to the unbalanced

magnetic circuit.

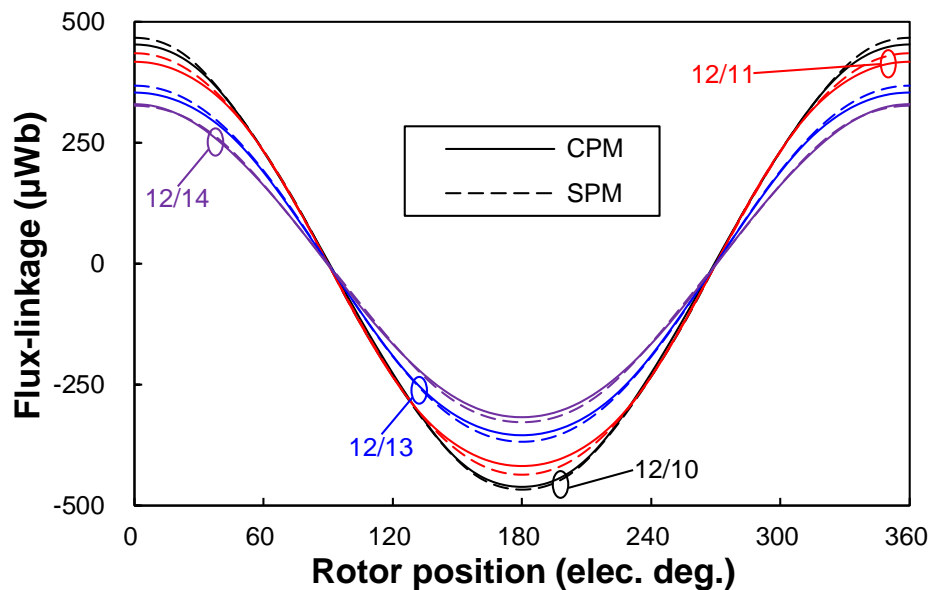
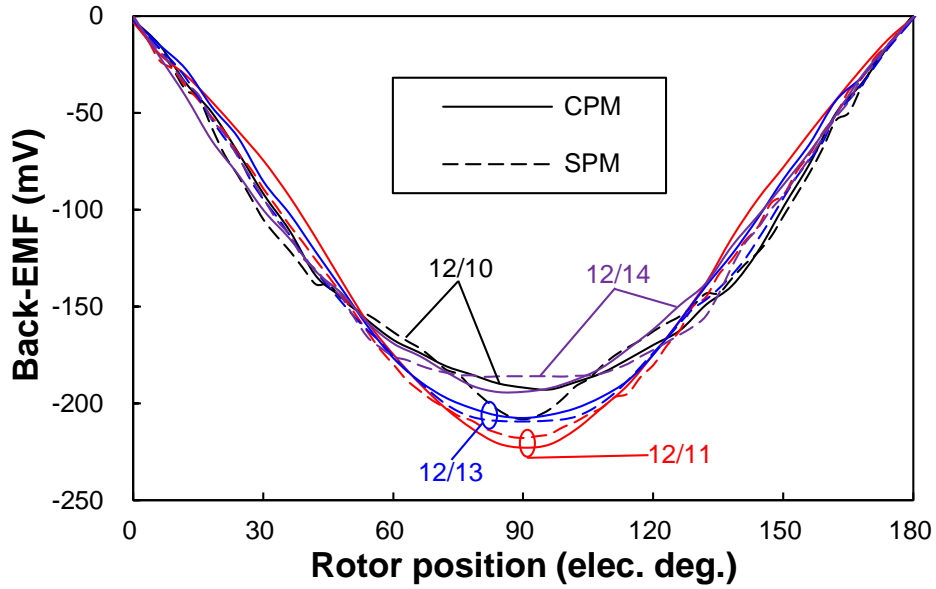


Fig. 4.10. Open-circuit phase flux-linkage waveforms of 12-stator-pole PS-FRPM machines with CPM and SPM inner stators.

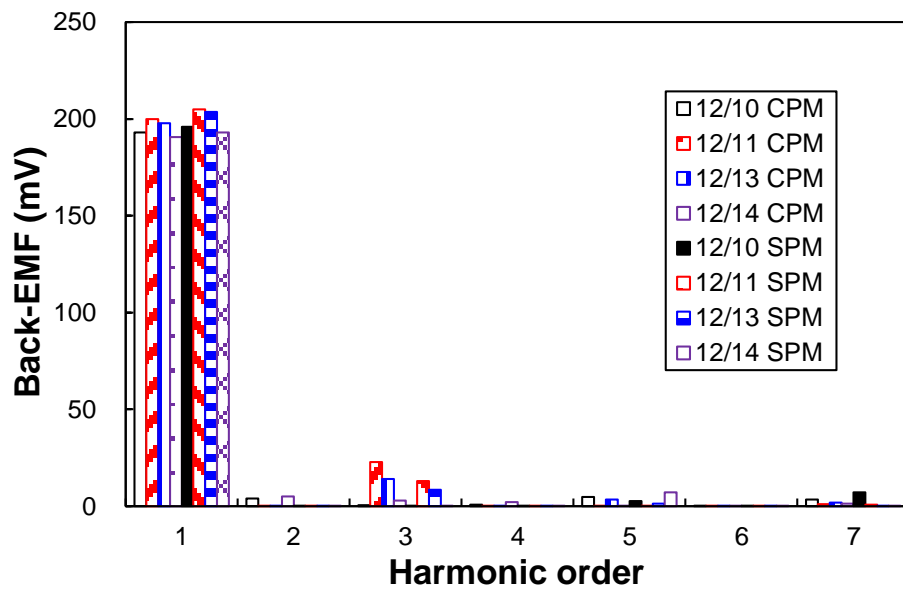
The fundamental phase back-EMF characteristics are listed in Table 4.4, in which the ratio is defined as that of the fundamental back-EMF value of the machine with CPM inner stator to the SPM one. As listed in Table 4.4, the PS-FRPM machines with CPM inner stator can exhibit similar fundamental phase back-EMFs, *i.e.* more than 97%, compared to their corresponding SPM inner stator one.

Table 4.4 Fundamental Phase Back-EMF Characteristics of PS-FRPM Machines with CPM and SPM Inner Stators, $N_c=1$ @400rpm

Item	Unit	12-stator-pole PS-FRPM			
		10	11	13	14
N_r	-	10	11	13	14
CPM	mV	193.08	199.99	197.87	190.78
SPM	mV	196.09	205.07	203.56	193.08
Ratio	%	98.46	97.52	97.21	98.81



(a) Waveforms



(b) Spectra

Fig. 4.11. Phase back-EMFs of 12-stator-pole PS-FRPM machines with CPM and SPM inner stators, $N_c=1$ @400rpm.

4.4.2 Torque characteristics

The interaction of slots and PMs in PM machines will cause cogging torque, which leads to torque ripple, noise and vibration. In the foregoing analysis, it is found that the cogging torques in 12/10- and 12/14-pole PS-FRPM machines are generally higher than the other two. This is

due to the larger greatest common divisor between the stator and rotor pole numbers. The cogging torque of the 12-stator-pole PS-FRPM machines with CPM and SPM inner stators is shown in Fig. 4.12 and listed in Table 4.5. The cogging torque cycles per electric period n_{ce} in CPM machines is half of their corresponding SPM counterpart, respectively. n_{ce} is given by,

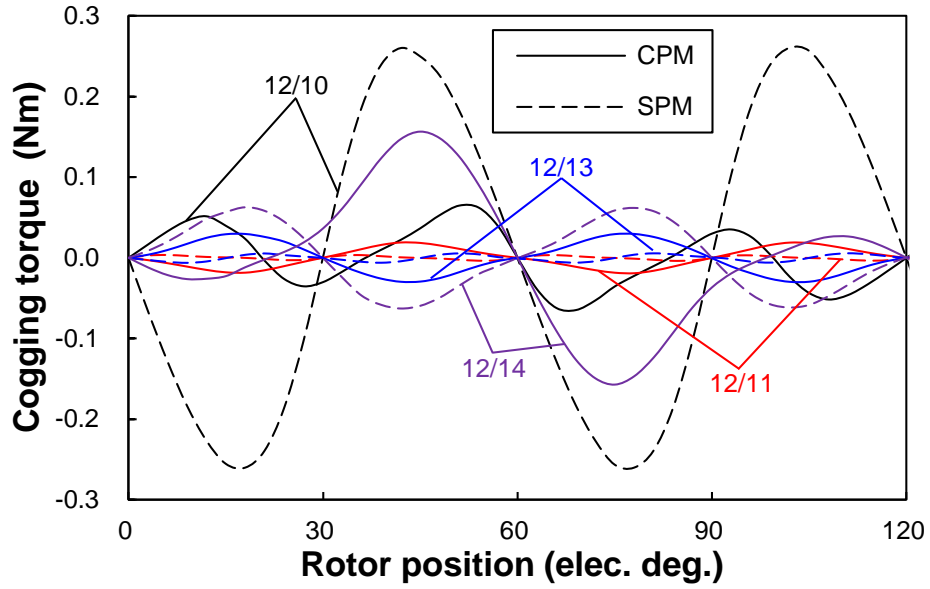
$$n_{ce} = \frac{LCM(N_s, N_r)}{kN_r} \quad (4.7)$$

where LCM is the least common multiple. $k=1$ for SPM inner stator machines and $k=2$ for CPM ones.

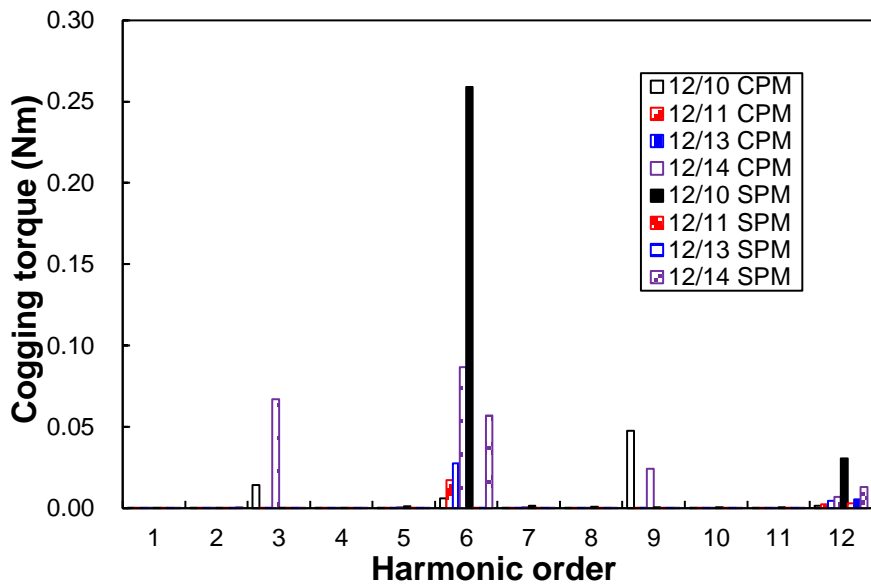
As shown in Table 4.5, 12/10-pole PS-FRPM machine with CPM inner stator has smaller cogging torque than its SPM counterpart, whilst 12/11- and 12/13- and 12/14-pole ones are higher.

Table 4.5 Cogging Torque of PS-FRPM Machines with CPM and SPM Inner Stators (Nm)

Item	12-stator-pole PS-FRPM				
	N_r	10	11	13	14
CPM		0.13	0.04	0.06	0.31
SPM		0.53	0.01	0.02	0.13



(a) Waveforms



(b) Spectra

Fig. 4.12. 2D FE predicted cogging torques of 12-stator-pole PS-FRPM machines with CPM and SPM inner stators.

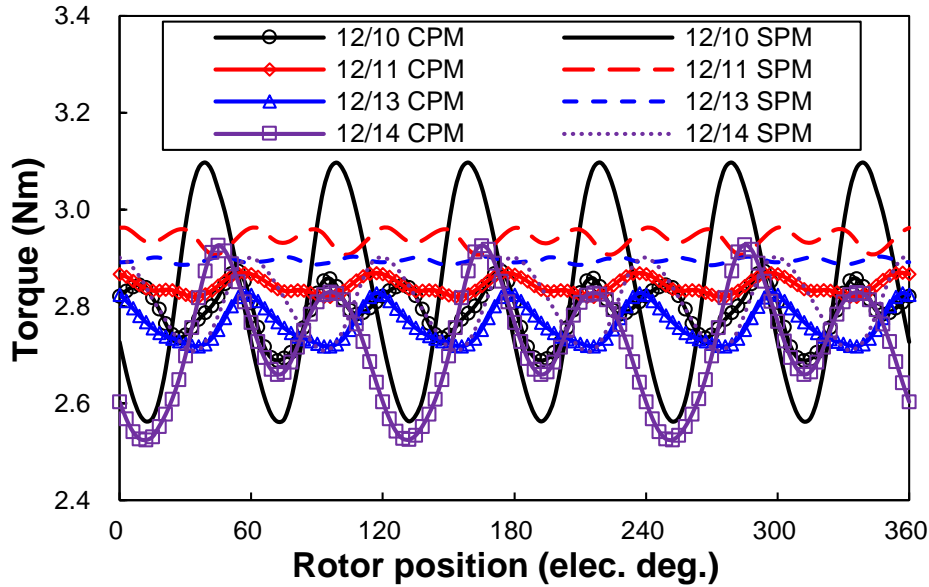


Fig. 4.13. Electromagnetic torque waveforms of 12-stator-pole PS-FRPM machines with CPM and SPM inner stators (BLAC, $p_{cu}=20W$, phase current and phase back-EMF have the same phase angle).

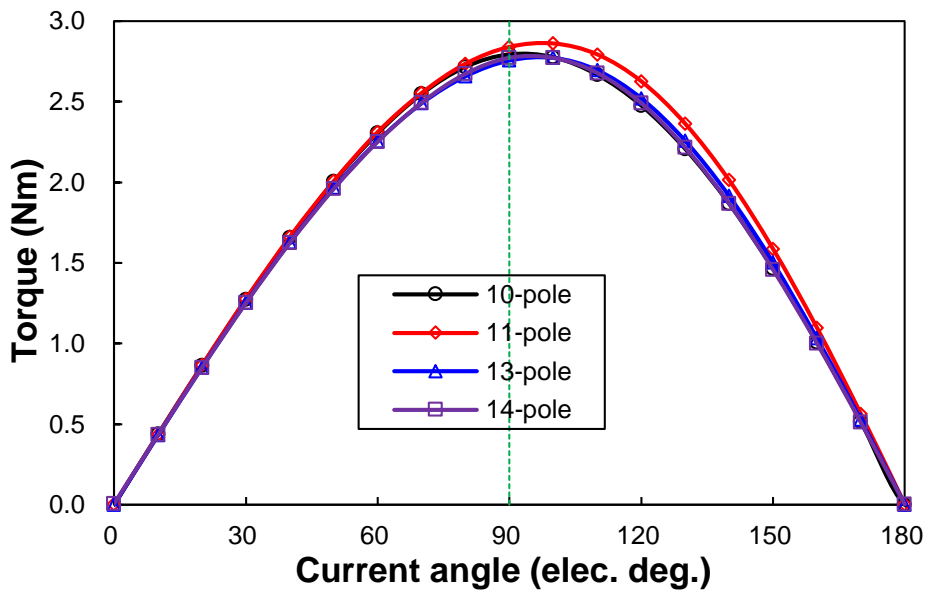


Fig. 4.14. Average torque with current angle of 12-stator-pole PS-FRPM machines with CPM inner stator (BLAC, $p_{cu}=20W$).

Fig. 4.13 illustrates the on-load electromagnetic torque waveforms of the 12-stator-pole PS-FRPM machines with CPM inner stator. The torque characteristics are listed in Table 4.3 as CPM2. The average torque with current angle in the 12-stator-pole PS-FRPM machines with CPM inner stator is given in Fig. 4.14. Similar to those with SPM inner stator [ZHU15a], the

reluctance torque in the PS-FRPM machines with CPM inner stator is also negligible. Therefore, phase current and phase back-EMF have the same phase angle in PS-FRPM machines with both SPM and CPM inner stators in this chapter.

4.4.3 Loss and efficiency

Table 4.6 gives the iron loss, PM eddy current loss and efficiency of PS-FRPM machines with CPM and SPM inner stators calculated by FE [WAN14a]. In Table 4.6, p_{feos} , p_{fer} , p_{feis} and p_{fe} are the outer stator, rotor iron pieces, inner stator and total iron loss, respectively. p_{PMe} is the PM eddy current loss. η is the efficiency. The iron loss p_{fe} is calculated by the FE software Ansys/Maxwell based on (4.8). Here, it is worth noting that the variation of the direction of flux density B should be accounted in the iron loss calculation, as studied in [ATA93a]. In Ansys/Maxwell, to take consideration of the variation of the direction of flux density B , B is broken into B_r and B_t firstly. Then, the corresponding iron losses of B_r and B_t are calculated based on (4.8) and then the total iron loss accounting for the variation of the direction of flux density B can be obtained as a sum [LIN04a]. In (4.8), the iron loss p_{fe} is calculated by three parts including hysteresis loss p_{hfe} , eddy current loss p_{cfe} , and excess loss p_{efe} ,

$$p_{fe} = p_{hfe} + p_{cfe} + p_{efe} = k_{hfe} f B_{max}^2 + k_{cfe} f^2 B_{max}^2 + k_{efe} f^{1.5} B_{max}^{1.5} \quad (4.8)$$

where $k_{hfe}=251.69\text{W/m}^3$, $k_{cfe}=0.34899\text{W/m}^3$ and $k_{efe}=0$ are the hysteresis, eddy current and excess loss coefficients, respectively. B_{max} is the maximum flux density.

The efficiency η can be expressed as the ratio of output power P_{out} and the input power P_{in} ,

$$\eta = \frac{P_{out}}{P_{in}} * 100\% = \frac{P_{EM} - p_{fe} - p_{PMe}}{P_{EM} + p_{cu}} * 100\% \quad (4.9)$$

where P_{EM} is the average electromagnetic power.

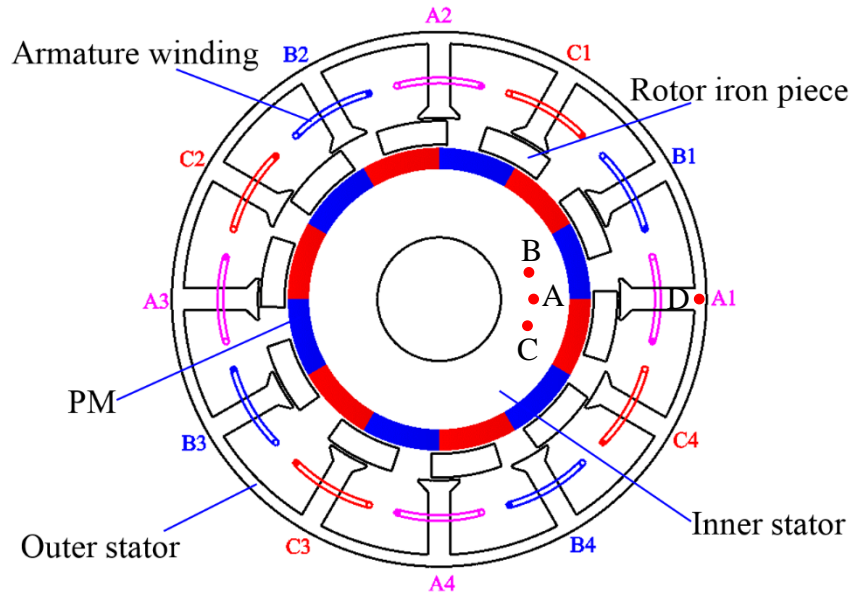
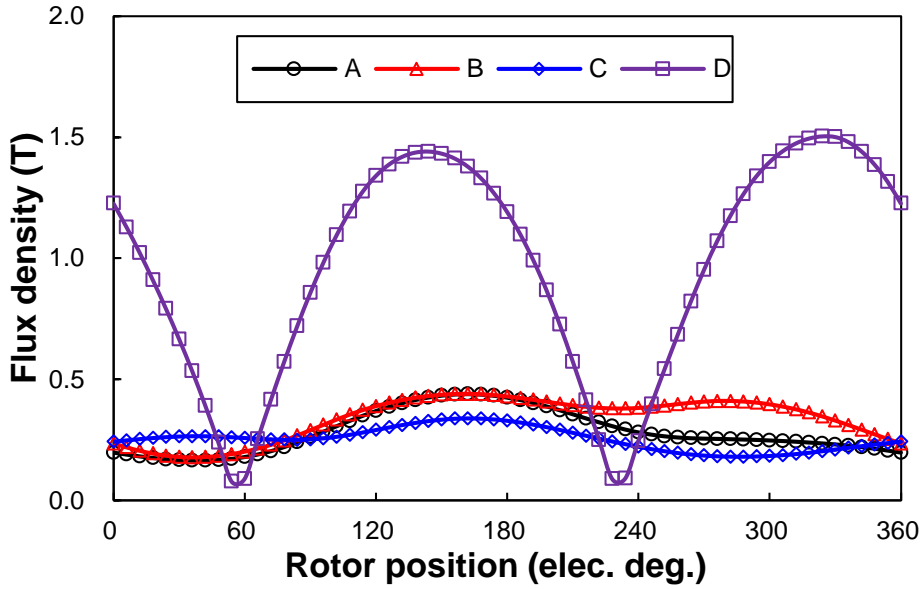
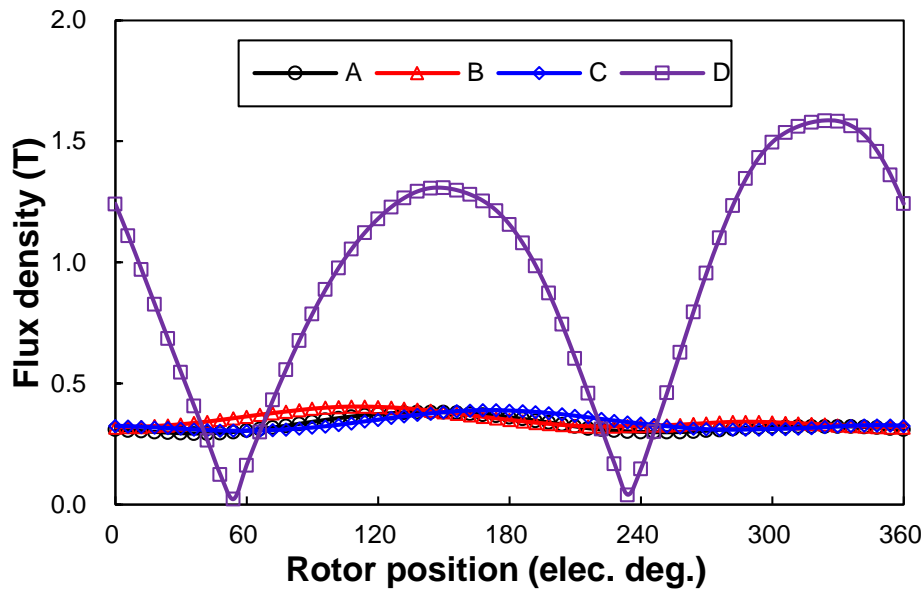


Fig. 4.15. Illustration of points A, B, C and D in the 12/10-pole PS-FRPM machines with CPM inner stator.

As given in Table 4.6, in PS-FRPM machines with both CPM and SPM inner stators, the outer stator iron loss is more than twice the rotor iron pieces one, both of which are much higher than that of the inner stator. This can be explained as follows. The outer stator iron loss is more than twice the rotor iron pieces mainly due to the high volume of outer stator, whilst the influence of the difference of the flux density and its variation is smaller. The inner stator iron loss is much smaller than those of the outer stator and the iron pieces, as the stable flux density in the inner stator beneficial from the surface-mounted PMs, as shown in Fig. 4.16 for 12/10-pole PS-FRPM machines. This is similar to the rotor of the conventional rotor-PM machine with surface-mounted PMs. The points A, B, and C are in the inner stator with the same radius, *i.e.* half value of PM inner radius and inner stator inner radius, whilst different angles with 0, 15 mechanical degrees, -15 mechanical degrees, as shown in Fig. 4.15. The point D is in the outer stator tooth, of which the radius is half of the outer stator yoke radius and the outer stator inner radius, and the arc is 0.



(a) CPM



(b) SPM

Fig. 4.16. Variation of flux density at points A, B, C, D versus rotor position in 12/10-pole PS-FRPM machines with CPM and SPM inner stators (BLAC, $p_{cu}=20W$, phase current and phase back-EMF have the same phase angle).

More importantly, 12/11-, 12/13- and 12/14-pole PS-FRPM machines with CPM inner stator have higher iron loss than their corresponding SPM inner stator counterpart, respectively. However, the iron loss in 12/10-pole PS-FRPM machine is lower than its corresponding SPM inner stator counterpart. The PM eddy current loss is much smaller than the iron loss in all the

analysed machines. However, both of them are smaller than the copper loss due to low rotor speed, *i.e.* 400rpm. All the PS-FRPM machines with CPM inner stator can exhibit less than 1% lower efficiency than their corresponding SPM inner stator counterpart, as given in Table 4.6.

Table 4.6 Iron Losses, PM Eddy Current Loss and Efficiency of PS-FRPM Machines with CPM and SPM Inner Stators

Items		12-stator-pole PS-FRPM			
N_r		10	11	13	14
CPM	p_{feos} (W)	1.08	1.24	1.16	1.29
	p_{fer} (W)	0.42	0.47	0.47	0.41
	p_{feis} (W)	0.055	0.046	0.044	0.066
	p_{fe} (W)	1.55	1.75	1.68	1.76
	p_{PMe} (W)	0.09	0.11	0.11	0.13
	P_{EM} (W)	116.94	119.06	115.79	114.08
	η (%)	84.19	84.28	83.95	83.67
SPM	p_{feos} (W)	1.17	1.18	1.12	1.18
	p_{fer} (W)	0.46	0.44	0.43	0.42
	p_{feis} (W)	0.003	0.004	0.006	0.007
	p_{fe} (W)	1.63	1.62	1.56	1.62
	p_{PMe} (W)	0.10	0.10	0.14	0.17
	P_{EM} (W)	118.36	123.14	121.24	117.52
	η (%)	84.30	84.82	84.64	84.16

4.4.4 Winding inductance

The average self-inductance of phase A L_{AA} and average mutual inductance of phase A and B M_{BA} and that of M_{CA} when only phase A is excited are listed in Table 4.7. Both the self and mutual inductances in 12/11-, 12/13- and 12/14-pole PS-FRPM machines with CPM inner stator are smaller than their corresponding SPM inner stator counterpart, respectively. However, 12/10-pole PS-FRPM machines with CPM and SPM inner stators exhibit similar self and mutual inductances. In machines with both the different inner stator types, 12/11- and 12/13-pole ones have higher self-inductance and lower mutual inductance in absolute values than 12/10- and 12/14-pole ones. Therefore, the former two machines have higher fault-tolerance capability to restrict the short-circuit current [BIA06a].

Table 4.7 Winding Inductances of PS-FRPM Machines with CPM and SPM Inner Stators, $N_c=18$ (mH)

Item	12-stator-pole PS-FRPM				
N_r	10	11	13	14	10
CPM	L_{AA}	0.17	0.26	0.24	0.17
	M_{BA}	-0.08	-0.02	-0.02	-0.07
	M_{CA}	-0.08	-0.02	-0.02	-0.07
SPM	L_{AA}	0.17	0.23	0.21	0.14
	M_{BA}	-0.08	-0.02	-0.01	-0.06
	M_{CA}	-0.08	-0.02	-0.01	-0.06

4.4.5 Unbalanced magnetic force

The unbalanced magnetic force (UMF), which is also known as unbalanced magnetic pull, may cause noise and vibration as well as reduction of bearing life in electrical machines. Although the 12/11- and 12/13-pole PS-FRPM machines have higher fault-tolerance capability as aforementioned, they suffer from UMF due to the odd rotor pole number. This can be evidenced by Fig. 4.17 and Fig. 4.18 for open-circuit and rated on-load operations, respectively. There is no significant change in UMF due to load. There is no UMF in the 10- and 14-pole

machines. More importantly, the UMFs in the 12/11- and 12/13-pole PS-FRPM machines with CPM inner stator are lower than their corresponding SPM inner stator counterparts, respectively. It should be noted that the UMFs in 12/11- and 12/13-pole PS-FRPM machines can be relieved by multiplying both the stator and rotor pole numbers to achieve an even rotor pole number.

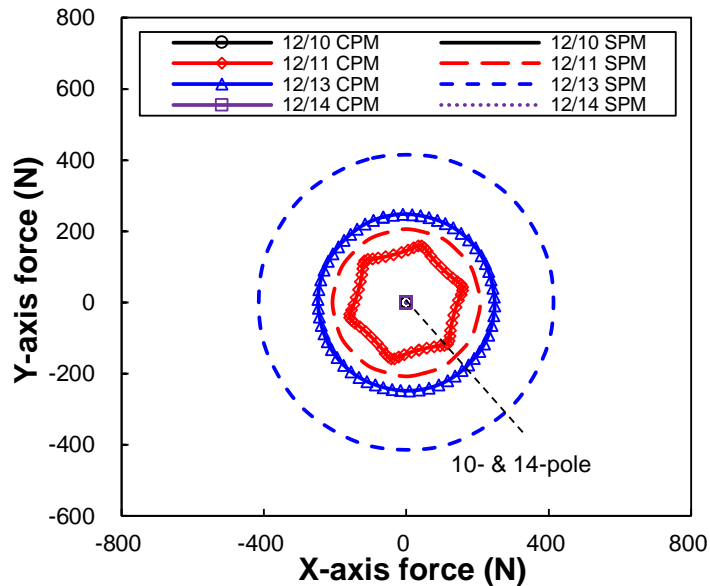


Fig. 4.17. Open-circuit UMF of 12-stator-pole PS-FRPM machines with CPM and SPM inner stators.

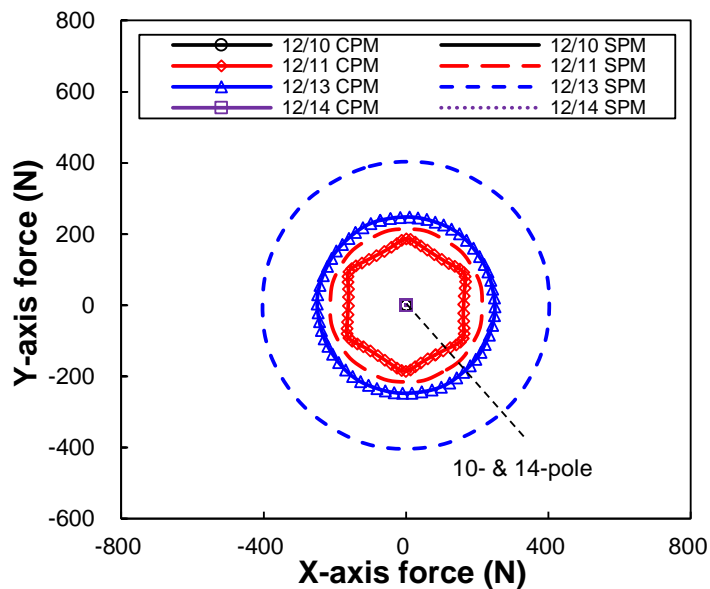


Fig. 4.18. Rated on-load UMF of 12-stator-pole PS-FRPM machines with CPM and SPM inner stators (BLAC, $p_{cu}=20W$, phase current and phase back-EMF have the same phase angle).

4.5 Experimental Validation

The PS-FRPM machines with the proposed CPM and existing SPM inner stators are compared in the foregoing analysis. In the proposed PS-FRPM machines with CPM inner stator, 12/11- and 12/10-pole ones can generate larger torque. Also, the 12/10-pole one can get rid of the UMF. In this section, the 12/10-pole PS-FRPM machine with CPM inner stator is built and tested.



(a) Outer stator



(b) Cup rotor



(c) Inner stator



(d) Rotor lamination

Fig. 4.19. Photos of 12/10-pole prototype PS-FRPM machine with CPM inner stator.

The prototype machine consists of three parts, *i.e.* outer stator with 12-stator-pole wound by 12 non-overlapping concentrated armature coils as shown in Fig. 4.19(a), 10-pole cup rotor, Fig. 4.19(b), and the CPM inner stator, Fig. 4.19(c). The dimensional parameters of the prototype machine are given in Table 4.8. The symbols in Table 4.8 are the same with those in Table 2.2. The rotor iron pieces are connected by $T_{bri}=0.5\text{mm}$ thick iron rib between the two adjacent pieces to ease the manufacturing. The iron rib is placed close to the inner air-gap, which can be observed from the rotor lamination shown in Fig. 4.19(d). The back-EMF and static torque are tested on the prototype machine to verify the FE analysis.

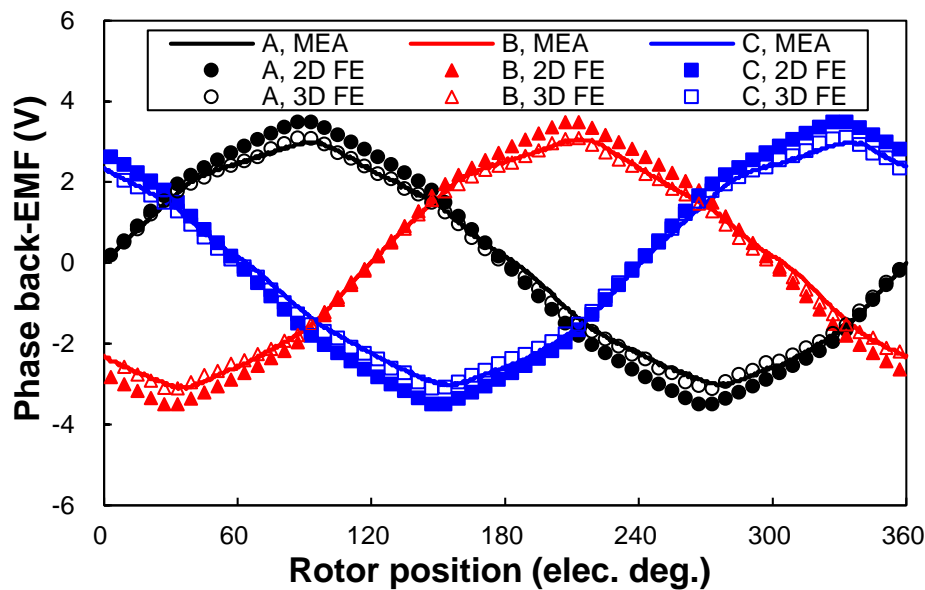
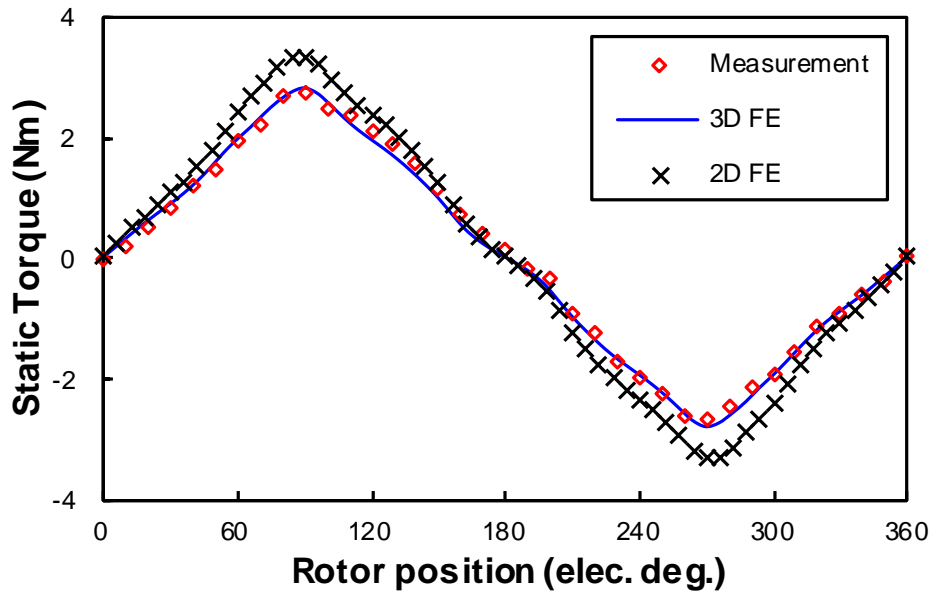


Fig. 4.20. Variation of FE predicted and measured phase back-EMF waveforms with rotor position of the prototype machines @400rpm.

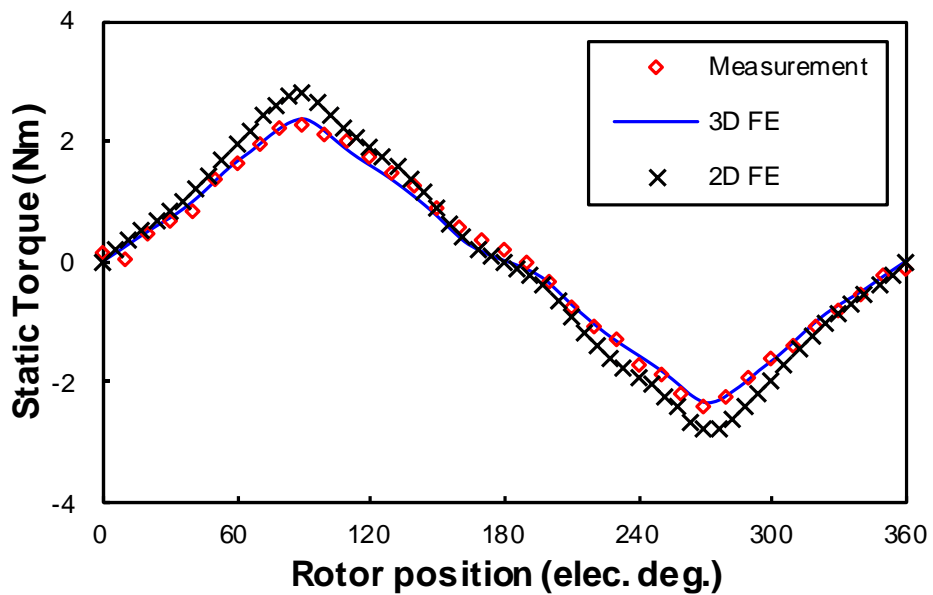
The measured and FE predicted phase back-EMF and static torque waveforms, as well as peak static torque, are compared in Fig. 4.20, Fig. 4.21, and Fig. 4.22. Both the measured and FE predicted phase back-EMF and static torque waveforms are slightly asymmetric due to even harmonics, as foregoing analysed. Good agreement can be achieved between the measured and 3D FE predicted values. However, they are more than 10% smaller than the 2D FE predicted ones due to end effect. As shown in Fig. 4.20, the 3D FE predicted peak phase back-EMF is only 88.59% of that of the 2D FE, *i.e.* 3.09V and 3.49V, respectively. As for the peak static torques under different q -axis currents, the 3D FE predicted values are also more than 10% lower than those predicted by 2D FE, as shown in Figs. 20 and 21, and listed in Table 4.9. The detailed comparative analysis of the end effect in PS-FRPM machines having both SPM and

CPM inner stators are analysed and shown in Appendix C. In the measurement of static torque, the phase A current I_A , phase B current I_B and phase C current I_C are set as,

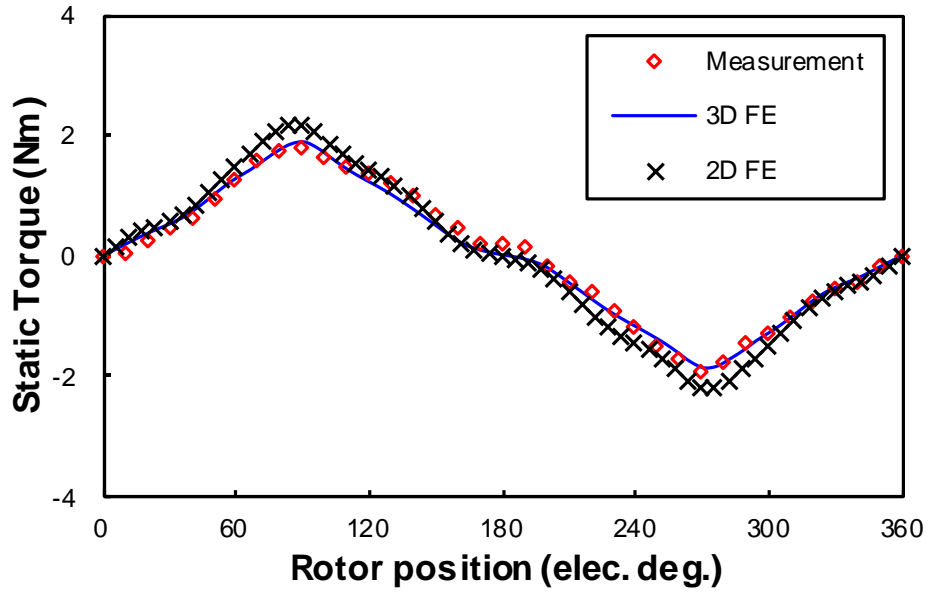
$$I_A = -2I_B = -2I_C \quad (4.10)$$



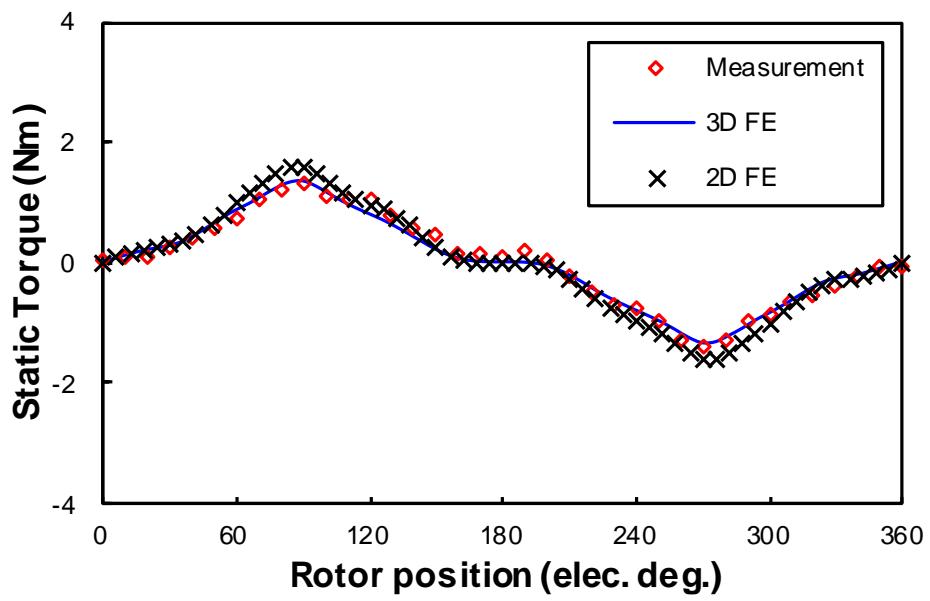
(a) $I_a=25A$



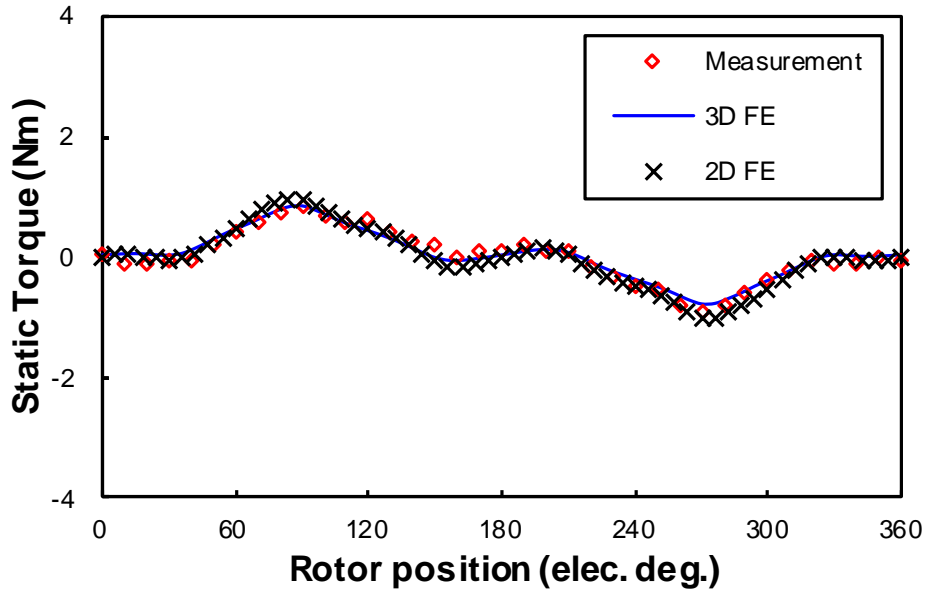
(b) $I_a=20A$



(c) $I_a=15A$



(d) $I_a=10A$



(e) $I_a=5A$

Fig. 4.21. Variation of FE predicted and measured static torques with rotor position of the prototype machines ($I_A=-2I_B=-2I_C$).

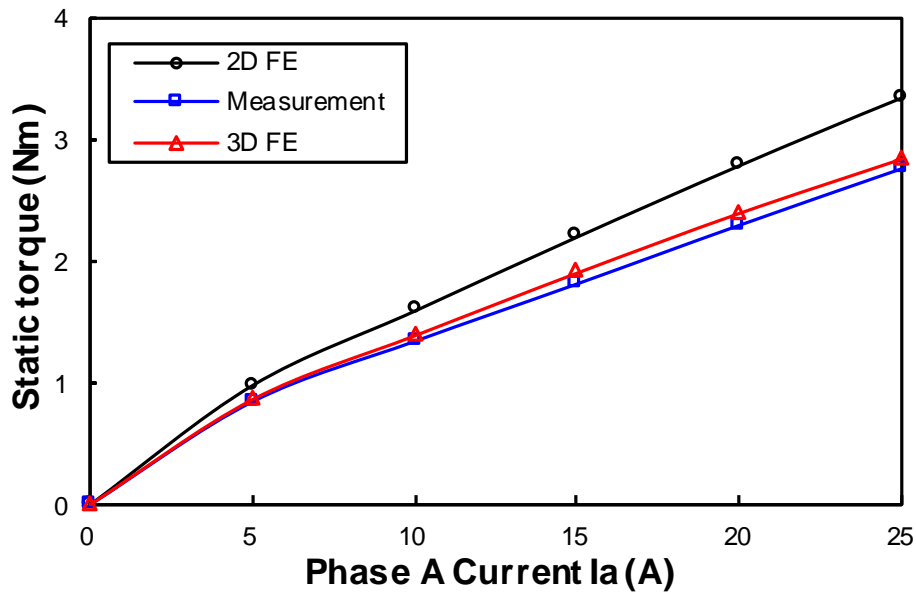


Fig. 4.22. Measured and FE analysed peak static torques of prototype machine with CPM inner stator ($I_A=-2I_B=-2I_C$).

Table 4.8 Design Parameters of 12-Stator-Pole PS-SFPM Machine with CPM Inner Stator

Items	Prototype	Items	Prototype
L_s (mm)	25	g_o (mm)	0.5
R_{oso} (mm)	45	g_i (mm)	0.5
R_{osy} (mm)	42	θ_{ost} (°)	8.12
R_{osi} (mm)	31.75	θ_{osy} (°)	6.14
R_{ro} (mm)	31.25	θ_{ot} (°)	4.94
R_{ri} (mm)	26.25	l_{ott} (mm)	1
R_{iso} (mm)	25.75	l_{otb} (mm)	3
R_{isy} (mm)	21.75	θ_{ro} (°)	18
R_{isi} (mm)	10.4	θ_{ri} (°)	24
T_{PM} (mm)	4	θ_{PM} (°)	42
T_{bri} (mm)	0.5	N_{ac}	18

Table 4.9 Comparison of Measured Static Torques Under Different Q-Axis Currents
(MEA=Measured)

Q-axis current (A)	MEA (Nm)	3D FE (Nm)	2D FE (Nm)	3D FE / 2D FE (%)
5	0.85	0.87	0.98	88.43
10	1.34	1.40	1.60	87.51
15	1.82	1.91	2.21	86.79
20	2.30	2.41	2.79	86.18
25	2.77	2.86	3.35	85.21

4.6 Conclusions

In this chapter, a novel PS-FRPM machine with CPM inner stator having less PM volume but similar torque density and efficiency to that with SPM inner stator is proposed and its static performance is validated experimentally. Different stator/rotor pole combinations are employed in the proposed PS-FRPM machines with CPM inner stator. The FE results show that the 12-stator-pole PS-FRPM machine having 10-, 11-, 13- and 14-rotor-pole with CPM inner stator can generate 98.59%, 96.69%, 95.50% and 97.15% torque density of their corresponding SPM inner stator counterparts, respectively, whilst the PM volume can be saved by 28.33%, 30%, 30% and 33.33%. The PS-FRPM machines with CPM inner stator can exhibit similar efficiency with their corresponding SPM inner stator counterpart, i.e. only <1 smaller.

5 Partitioned Stator Flux Reversal Permanent Magnet Machine Having Overlapping Windings

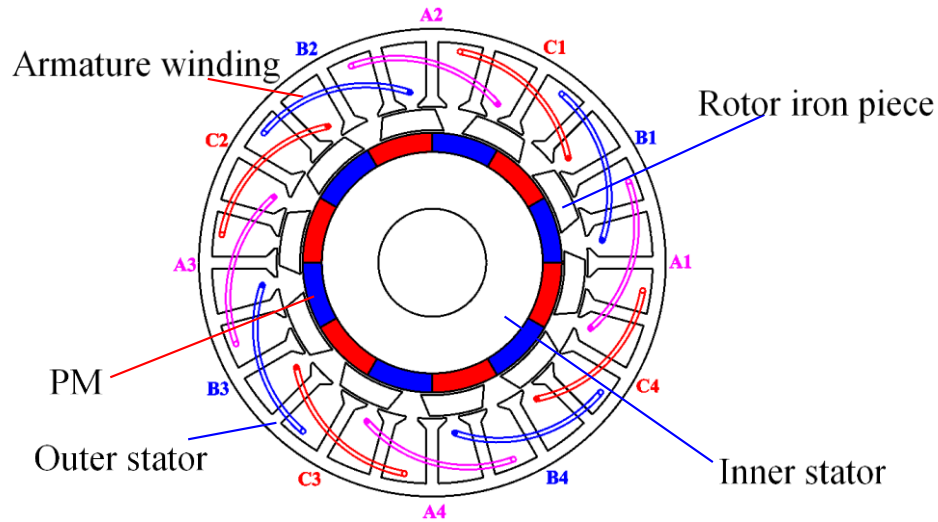
In all existing papers and also the previous chapters, the partitioned stator permanent magnet (PM) machines are based on the concentrated non-overlapping stator windings. In this chapter, based on the magnetic gearing effect in the partitioned-stator-PM machines, overlapping armature winding topology is applied to the partitioned stator flux reversal PM (FRPM) (PS-FRPM) machines and the electromagnetic performance is comparatively analysed with the counterpart having the concentrated winding referred to Appendix B. It is found that compared with the existing 12/10/12-outer stator pole/rotor pole/inner stator pole PS-FRPM machine having non-overlapping armature windings, the proposed 24/10/12-pole PS-FRPM machine having overlapping armature windings exhibits smaller iron loss and PM eddy current loss, larger open-circuit fundamental phase flux-linkage and back-EMF and hence higher torque density but smaller torque ripple, higher efficiency, higher self-inductance and lower mutual inductance, and hence a higher self/mutual-inductance ratio and better capability to restrict the short-circuit current, much higher flux-weakening capability. However, the proposed 24/10/12-pole PS-FRPM machine having overlapping armature winding suffers from longer end winding and hence larger total copper loss when the machine stack length is short.

This part has been published in IEEE Transactions on Energy Conversion.

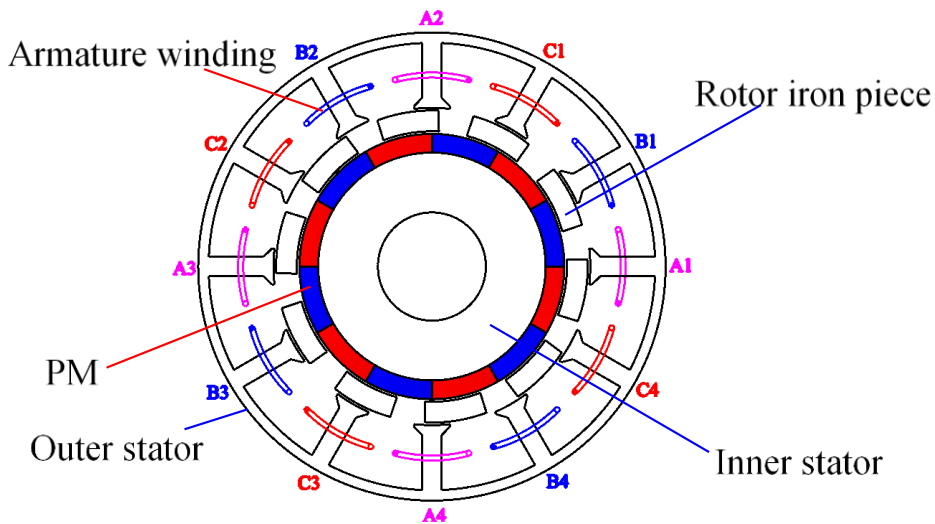
5.1 Introduction

Fractional-slot non-overlapping windings are commonly used in the stator-PM machines, including both single-stator-PM and partitioned-stator-PM machines, since machines with fractional-slot non-overlapping windings have shorter end-winding length than those with integer-slot overlapping windings [MOR10a] [TAN13a] [LI15a]. However, machines with fractional-slot non-overlapping windings have less sinusoidal armature excitation magnetomotive force (MMF) distribution, resulting in higher loss and other parasitic effects such as torque ripple, noise and vibration due to the additional spatial harmonics [ELR10a]. In this chapter, the PS-FRPM machine equipped with fractional-slot non-overlapping windings [Fig. 5.1(b)] in [ZHU15a], which can be referred to Appendix B, is extended to integer-slot overlapping armature winding having slot number per pole per phase $q=1$ [Fig. 5.1(a)], based on the magnetic gearing principle [ZHU14a] [MCF14a] [WU15a] [LI15a] [MCF15a] [SHI16a]

[DU16a]. The electromagnetic performance of the proposed PS-FRPM machine having $q=1$ integer-slot overlapping windings will be investigated and compared with the existing PS-FRPM machine with $q=0.5$ fractional-slot non-overlapping windings. It is worth noting that the coil connection of the PS-FRPM machines having both overlapping and non-overlapping windings can be referred to Fig. 1.2.



(a) Proposed overlapping winding with $q=1$



(b) Existing non-overlapping winding with $q=0.5$

Fig. 5.1. Cross-sections of proposed 24/10/12-pole overlapping windings and existing 12/10/12-pole non-overlapping windings PS-FRPM machines.

This chapter is organized as follows. In 5.2, the operation principle of PS-FRPM machine is analysed based on magnetic gearing principle and the overlapping winding layout is proposed

and employed. In section 5.3, electromagnetic performance of the 24/10/12-pole PS-FRPM machine with $q=1$ overlapping windings and the 12/10/12-pole PS-FRPM machine with $q=0.5$ non-overlapping windings are comparatively analysed by finite element (FE) analysis. In section 5.4, both prototype machines with $q=1$ overlapping windings and $q=0.5$ non-overlapping windings are built and tested to validate the FE predicted electromagnetic performance, followed by conclusions in section 5.5.

5.2 PS-FRPM Machine with Non-Overlapping and Overlapping Windings

5.2.1 Fractional-slot non-overlapping winding with $q=0.5$

In a magnetic gear, the two rotating parts transmitting torque can be any two of inner PMs, middle iron pieces and outer PMs, exhibiting variable gearing ratios as analysed in [ATA04a]. If the two rotating parts are iron pieces and outer PMs, the gearing ratio G_r can be expressed as,

$$G_r = \frac{N_p}{p_o} \quad (5.1)$$

where N_{ip} and p_o are the iron piece number and outer PM pole-pair number, respectively. The relationship between N_{ip} , p_o and inner PM pole-pair number p_i can be governed by,

$$N_{ip} = p_o + p_i \quad (5.2)$$

For a magnetic gear with $p_o=4$, $N_{ip}=10$ and $p_i=6$, if the outer rotating PMs are substituted by 3-phase armature windings made of twelve non-overlapping coils injected by symmetric sinusoidal currents, the magnetic gear can be extended to a PS-FRPM machine. The cross-section of 12/10/12-pole PS-FRPM machine having non-overlapping windings is shown in Fig. 5.1(b). The equivalent pole-pair number of armature excitation of 12/10/12-pole PS-FRPM machine is 4 which is defined as the highest forward rotating MMF harmonic order. This can be derived as follows.

The 3-phase symmetric sinusoidal currents i_A , i_B , and i_C can be expressed as (2.4). In 12/10/12-pole non-overlapping winding PS-FRPM machine, the armature excitation MMF can be illustrated in Fig. 5.2, in which N_c is the number of coil turns and θ_1 is half of the coil pitch θ_{coil} . With non-overlapping winding, θ_{coil} is equal to outer stator slot pitch θ_{osp} ,

$$\theta_1 = \frac{\theta_{coil}}{2} = \frac{\theta_{osp}}{2} = \frac{\pi}{N_{os}} \quad (5.3)$$

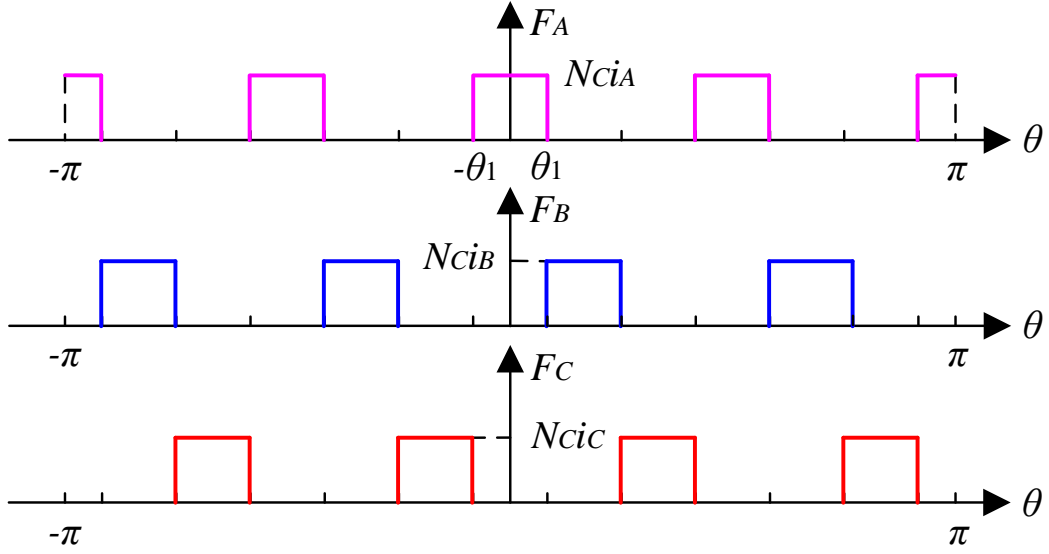


Fig. 5.2. Armature excitation MMF in 12/10/12-pole PS-FRPM machine with non-overlapping windings.

The Fourier series expansion of armature excitation MMF in Fig. 5.2 can be expressed as,

$$\left\{ \begin{array}{l} F_{ABC}(\theta, t) = \frac{3S_{ABC}}{2} \sum_{q=1}^{\infty} [M_{ABCq} \sin(\xi)] \\ S_{ABC} = \frac{2\sqrt{2}N_c I_{rms}}{\pi} \\ M_{ABCq} = \frac{1}{q} \sin(4q\theta_1) \\ \xi = \begin{cases} -4q\theta + N_r \Omega_r t, & q = 3r - 2 \\ 4q\theta + N_r \Omega_r t, & q = 3r - 1 \\ 0, & q = 3r \end{cases} \end{array} \right. \quad (5.4)$$

where S_{ABC} and M_{ABCq} are the Fourier series coefficients, and r is a positive integer.

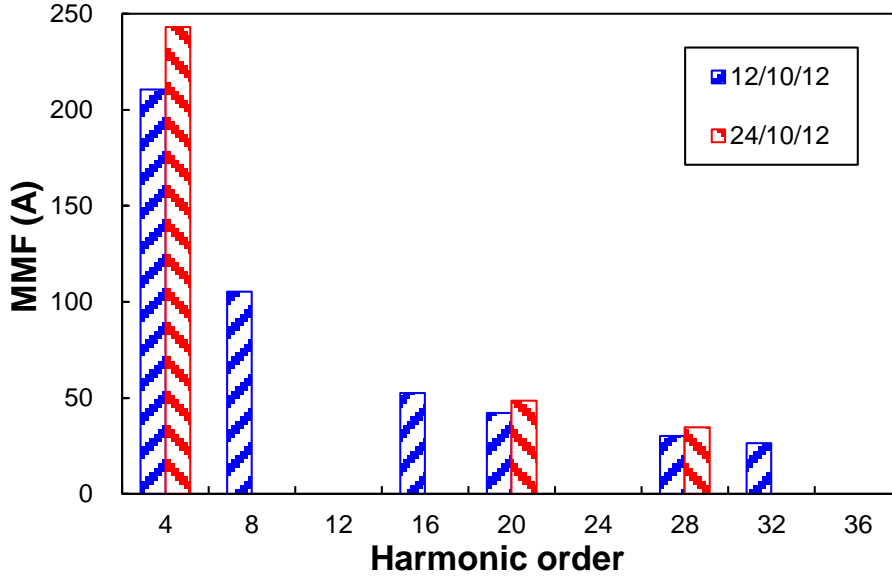


Fig. 5.3. Armature excitation MMF spectrum in the existing 12/10/12-pole non-overlapping windings and the proposed 24/10/12-pole overlapping windings PS-FRPM machines ($N_c=18$, $I_{rms}=10A$).

According to (5.4), the armature excitation MMF spectrum can be shown in Fig. 5.3. In Fig. 5.3, the largest forward rotating harmonic is the 4th MMF harmonic. Actually, the winding layout of the 12/10/12-pole PS-FRPM machine is exactly the same as that in the 12-slot/4-pole-pair fractional-slot surface-mounted PM (SPM) machine [ZHU09a]. Consequently, the equivalent pole-pair numbers in these two machines are the same, *i.e.* 4. Therefore, the equivalent pole-pair number of armature excitation p_{ea} can be defined as 4 in the 12/10/12-pole PS-FRPM machine. The PM pole-pair number and rotor iron piece number are 6 and 10, respectively. Due to the modulation of the 10-pole rotor iron pieces to the 6th static PM field, the 4th rotating field will be generated in the outer air-gap, synchronizing with armature excitation MMF and the interaction of them will produce average electromagnetic torque. Similarly, due to the modulation of the 10-pole rotor iron pieces to the 4th rotating armature excitation field with the same electric rotating speed, the 6th static field will be generated in the inner air-gap, synchronizing with PM MMF and the interaction of them will also produce average electromagnetic torque. Therefore, the relationship between p_{ea} , N_r and the PM pole-pair number p_{PM} is given by [WU15a],

$$N_r = p_{PM} + p_{ea} \quad (5.5)$$

Therefore, the slot number per pole per phase q in fractional-slot SPM machine can also be

employed in the PS-FRPM machine. In 12/10/12-pole PS-FRPM machine, it can be calculated as,

$$q = \frac{N_{os}}{2p_{ea}m} = \frac{12}{2 * 4 * 3} = 0.5 \quad (5.6)$$

where N_{os} is the outer stator pole number, m is the phase number.

5.2.2 Integer-slot overlapping winding with $q=1$

As shown in (5.6), due to $q=0.5$, the 12/10/12-pole non-overlapping winding PS-FRPM machine is a fractional-slot machine. In this section, its integer-slot counterpart with overlapping windings having the same p_{ea} , N_r and p_{PM} is introduced.

In integer-slot machines, the slot number per pole per phase q is an integer. With the same $p_{ea}=4$, $N_r=10$ and $p_{PM}=6$, in the integer-slot PS-FRPM machine with overlapping windings having $q=k$ ($k=1, 2, 3, \dots$), N_{os} is $24k$ based on (5.6). In 24/10/12-pole PS-FRPM machine, q can be calculated by,

$$q = \frac{N_{os}}{2p_{ea}m} = \frac{24}{2 * 4 * 3} = 1 \quad (5.7)$$

The cross-section of the 24/10/12-pole overlapping winding PS-FRPM machine with $q=1$ is given in Fig. 5.1(a). The winding layout in the proposed 24/10/12-pole overlapping winding PS-FRPM machine is the same as that of the conventional 24-slot/4-pole-pair integer-slot SPM machine with $q=1$ overlapping winding [CRO02a]. It can be observed from Fig. 5.1(a) and Fig. 5.1(b) that both the machines have the same rotor pole number $N_r=10$ and the same PM pole-pair number $p_{PM}=6$. The proposed overlapping winding machine has 24-pole outer stator, which is twice of the non-overlapping winding one. However, due to different winding layouts with overlapping and non-overlapping windings respectively, the same p_{ea} can be obtained, *i.e.* 4. The non-overlapping winding machine with $p_{ea}=4$ is analysed as aforementioned. Here, the overlapping winding one is analysed as follows.

Fig. 5.4 shows the armature excitation MMF in the 24/10/12-pole PS-FRPM machine with $q=1$. Compared with that of the 12/10/12-pole PS-FRPM machine with $q=0.5$ non-overlapping windings, three-phase MMFs are overlapped in the 24/10/12-pole PS-FRPM machine with $q=1$ overlapping windings. In Fig. 5.4, θ_1 is also the half of the coil pitch θ_{coil} , which is three times of outer stator slot pitch θ_{osp} in the 24/10/12-pole PS-FRPM machine with $q=1$ overlapping

windings,

$$\theta_1 = \frac{\theta_{coil}}{2} = \frac{3\theta_{osp}}{2} = \frac{3\pi}{N_{os}} \quad (5.8)$$

The Fourier series expansion of the armature excitation MMF in the 24/10/12-pole PS-FRPM machine can be expressed as,

$$\begin{cases} F_{ABC}(\theta, t) = \frac{3S_{ABC}}{2} \sum_{q=1}^{\infty} [M_{ABCq} \sin(\xi)] \\ S_{ABC} = \frac{2\sqrt{2}N_c I_{rms}}{\pi} \\ M_{ABCq} = \frac{1}{q} \sin(4q\theta_1) \\ \xi = \begin{cases} -4q\theta + N_r\Omega_r t, q = 3r - 2 \\ 4q\theta + N_r\Omega_r t, q = 3r - 1 \\ 0, q = 3r \end{cases} \end{cases} \quad (5.9)$$

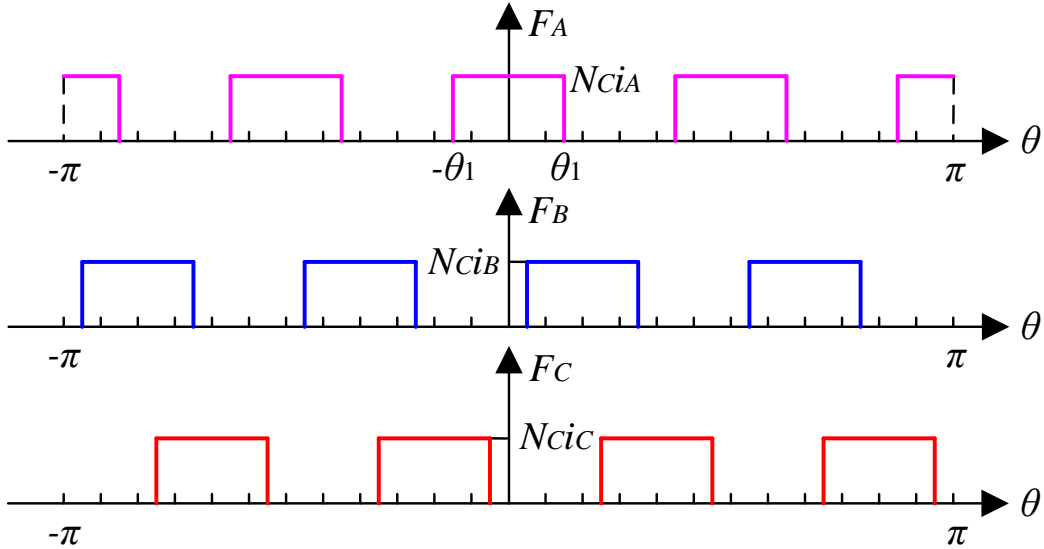


Fig. 5.4. Armature excitation MMF in 24/10/12-pole PS-FRPM machine with overlapping windings.

The armature excitation MMF spectrum of 24/10/12-pole PS-FRPM machine is illustrated in Fig. 5.3 based on (5.9). The largest forward rotating harmonic is still the 4th MMF harmonic and hence $p_{ea}=4$ in the 24/10/12-pole PS-FRPM machine. Similar to the 12/10/12-pole PS-FRPM machine having non-overlapping winding with $q=0.5$, the 24/10/12-pole overlapping winding PS-FRPM machine with $q=1$ also operates based on the magnetic gearing principle. The modulation of rotor iron pieces to the PM static and armature excitation rotating MMFs

make them synchronise with each other in both outer and inner air-gaps, resulting in average electromagnetic torque production [WU15a].

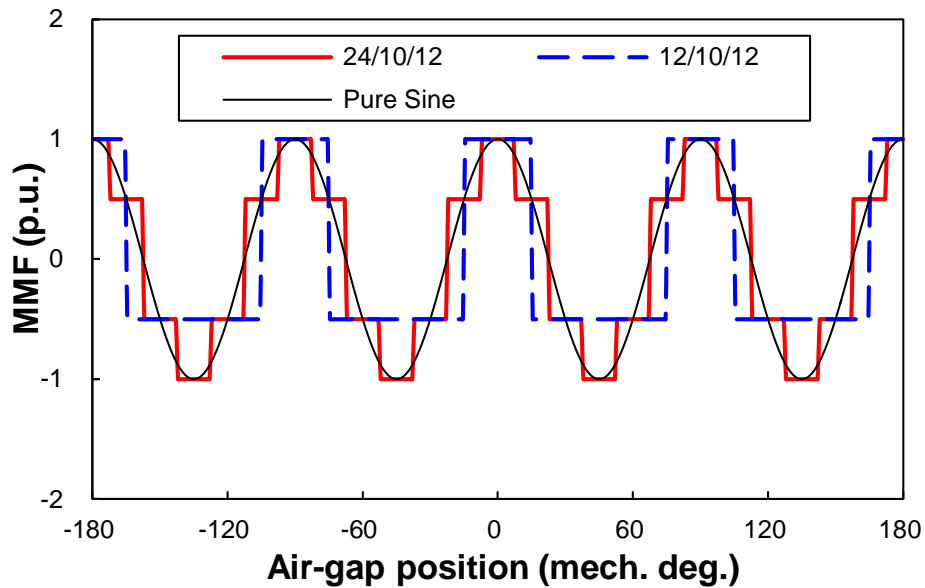
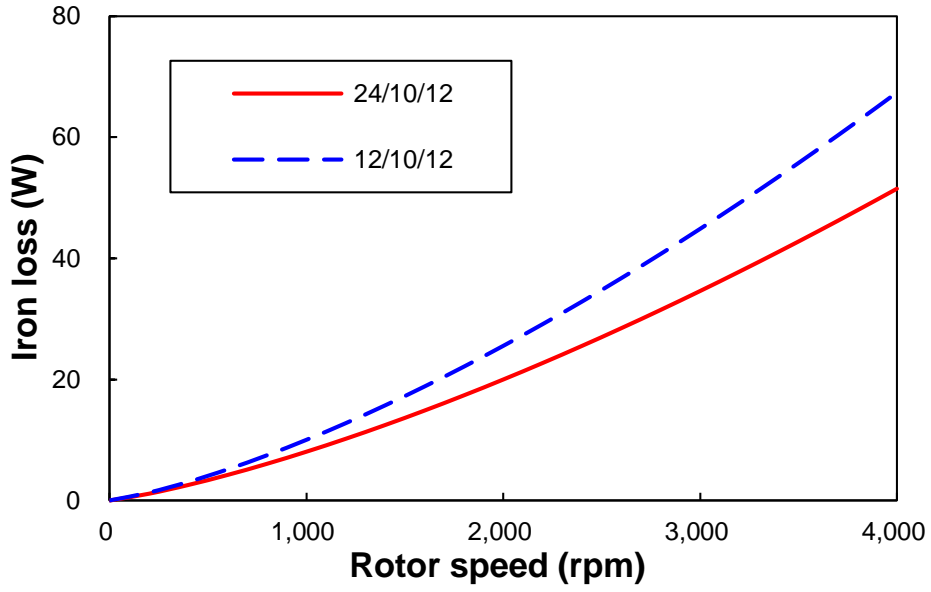
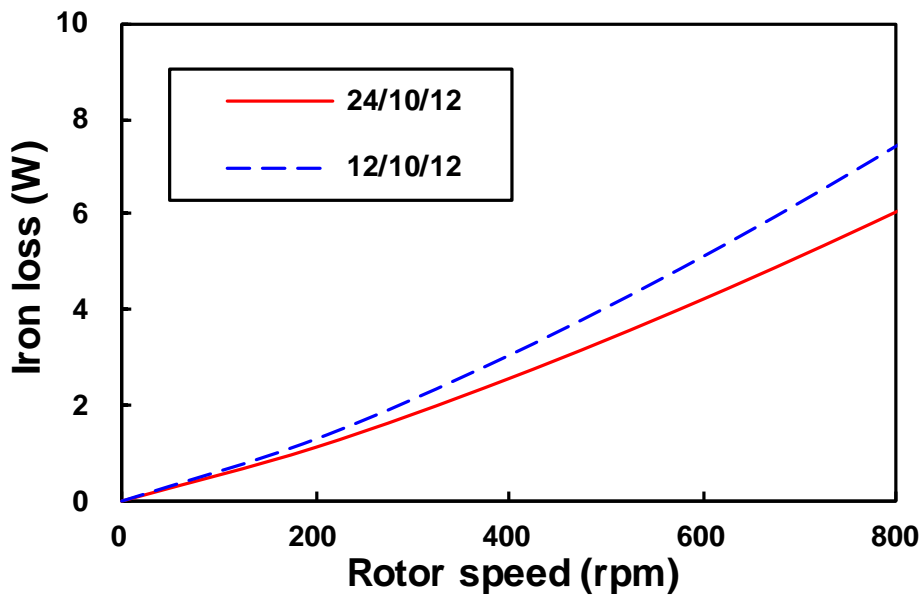


Fig. 5.5. Normalized MMF distributions in 24/10/12-pole PS-FRPM machine with overlapping windings.

More importantly, compared with that of the 12/10/12-pole PS-FRPM machine with non-overlapping windings, a more sinusoidal armature excitation MMF can be achieved in the 24/10/12-pole PS-FRPM machine with overlapping windings, Fig. 5.5. The total harmonic distortions of the normalized MMFs of the 12/10/12- and 24/10/12-pole PS-FRPM machines are 43.85% and 8.60%, respectively. As shown in Fig. 5.3, the magnitude of the 4th MMF harmonic can be enhanced, whilst other harmonics can be significantly reduced to 0 despite 20th and 28th harmonic will be slightly increased. This indicates that the proposed 24/10/12-pole PS-FRPM machine with integer-slot overlapping armature winding has lower loss than the existing 12/10/12-pole PS-FRPM machine with fractional-slot non-overlapping armature winding, as evidenced by Fig. 5.6 and Fig. 5.7 for FE predicted iron loss and PM eddy current loss, respectively. The iron loss p_{fe} is calculated based on equation (4.8).

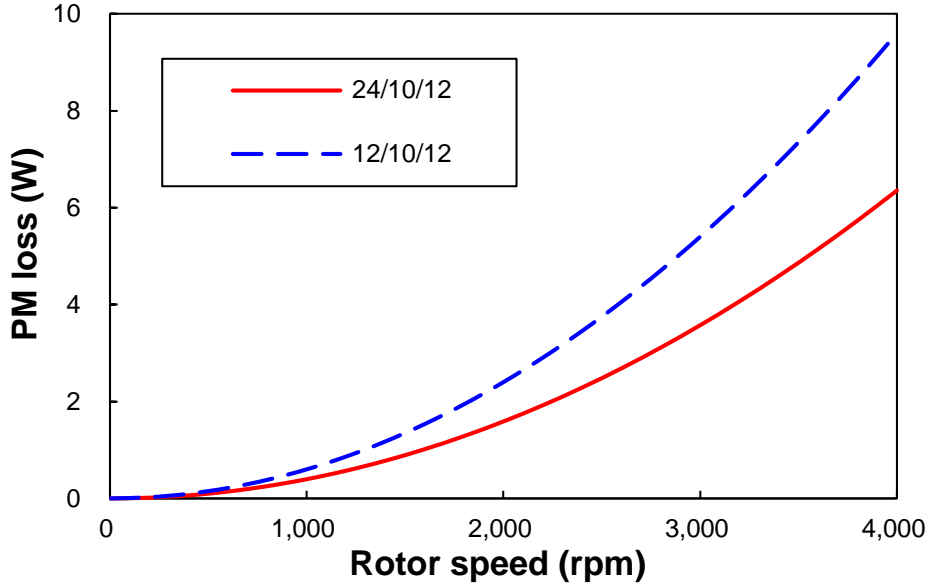


(a) 0-4000rpm

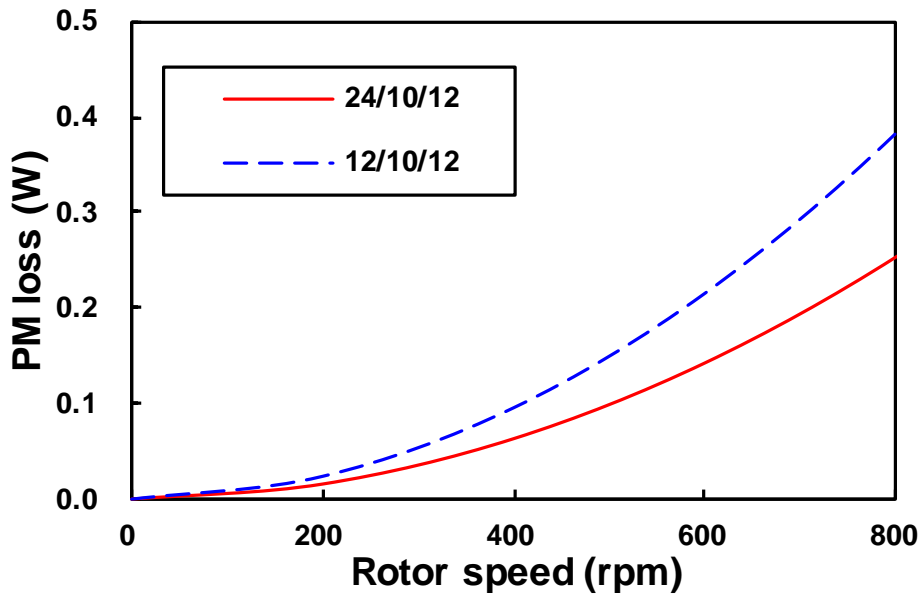


(b) 0-800rpm

Fig. 5.6. FE predicted rated on-load iron loss versus rotor speed for 24/10/12-pole and 12/10/12-pole PS-FRPM machines ($p_{cu}=20W$, phase current and phase back-EMF have the same phase angle).



(a) 0-4000rpm



(b) 0-800rpm

Fig. 5.7. FE predicted rated on-load PM eddy current loss versus rotor speed for 24/10/12-pole and 12/10/12-pole PS-FRPM machines ($p_{cu}=20W$, phase current and phase back-EMF have the same phase angle).

5.3 Electromagnetic Performance

In the previous section, based on the magnetic gearing analysis of the existing PS-FRPM machine with non-overlapping windings, the PS-FRPM machine with overlapping windings

having more sinusoidal armature excitation MMF and lower losses is introduced. In this section, the electromagnetic performance of these two types of PS-FRPM machines, *i.e.* 24/10/12-pole one with $q=1$ one and 12/10/12-pole one with $q=0.5$, are comparatively analysed as follows.

The design parameters of the proposed 24/10/12-pole PS-FRPM machine are listed in Table 5.1, together with those of the existing 12/10/12-pole one [ZHU15a]. The design parameters R_{osy} to θ_{ri} shown in Table 5.1 are optimized with other parameters fixed, under brushless AC (BLAC) operation, copper loss $p_{cu}=20\text{W}$, and zero d -axis current control, *i.e.* phase current and phase back-EMF have the same phase angle, for the largest average electromagnetic torque. For a fair comparison, the PM volume in the proposed 24/10/12-pole PS-FRPM machine is fixed to be the same as that in the existing 12/10/12-pole one, *i.e.* 13414.6mm^3 , during the optimization [ZHU15a].

Table 5.1 Design Parameters of Proposed 24/10/12-Pole and Existing 12/10/12-Pole PS-FRPM Machines

Parameters	Unit	Optimized		Prototypes	
		24/10/12	12/10/12	24/10/12	12/10/12
Stack length, L_s	mm	25			
Outer stator outer radius, R_{oso}	mm	45			
Inner stator inner radius, R_{isi}	mm	10.4			
Outer (inner) air-gap width, g_o (g_i)	mm	0.5			
Outer stator tip top length, l_{ott}	mm	0.5		1	1
Outer stator tip bottom length, l_{otb}	mm	2		2	3
PM volume, V_{PM}	mm ³	13414.6		14922.6	
PM arc, θ_{PM}	°	30			
PM remanence, B_{rPM}	T	1.2			
PM relative permeability, μ_{rPM}	-	1.05			
PM bulk conductivity	S/m	625000			
Number of turns per coil, N_c	-	18			
Outer stator yoke radius, R_{osy}	mm	42.5	43	42	42
Outer stator inner radius, R_{osi}	mm	30	31	31.75	
Rotor inner edge radius, R_{ri}	mm	25.5	26.5	26.25	
Outer stator tooth arc, θ_{ost}	°	4.5	7	5	8.12
Outer stator tooth tip arc, θ_{ot}	°	3	3	2	4.94
Rotor pole outer arc, θ_{ro}	°	20	23	18	
Rotor pole inner arc, θ_{ri}	°	28	24	24	
Inner stator yoke radius, R_{isy}	mm	21.31	22.48	21.75	

5.3.1 Open-circuit flux-Linkage and back-EMF

The open-circuit flux distributions of the two optimized machines at d -axis position are given in Fig. 5.8. As shown in Fig. 5.8, some flux paths in the rotor iron piece ‘R1’ are shorter in the 24/10/12-pole PS-FRPM machine due to the doubled outer stator teeth, resulting in smaller magnetic reluctance and hence higher phase peak flux-linkage and fundamental phase back-EMF as shown in Fig. 5.9 and Fig. 5.10(b), respectively. The 24/10/12-pole PS-FRPM machine has 5.56% higher fundamental phase back-EMF than the 12/10/12-pole one, *i.e.* 3.72V and 3.52V, respectively. It is worth noting that the 3rd phase back-EMF harmonic in the 24/10/12-pole PS-FRPM machine is caused by the non-zero corresponding pitch factor, *i.e.* 0.62 calculated by FE. However, the 3rd pitch factor k_{p3} is zero in the 12/10/12-pole PS-FRPM machine as,

$$k_{p3} = \cos \left[3\pi \left(\frac{N_r}{N_{os}} - 1 \right) \right] = 0 \quad (5.10)$$

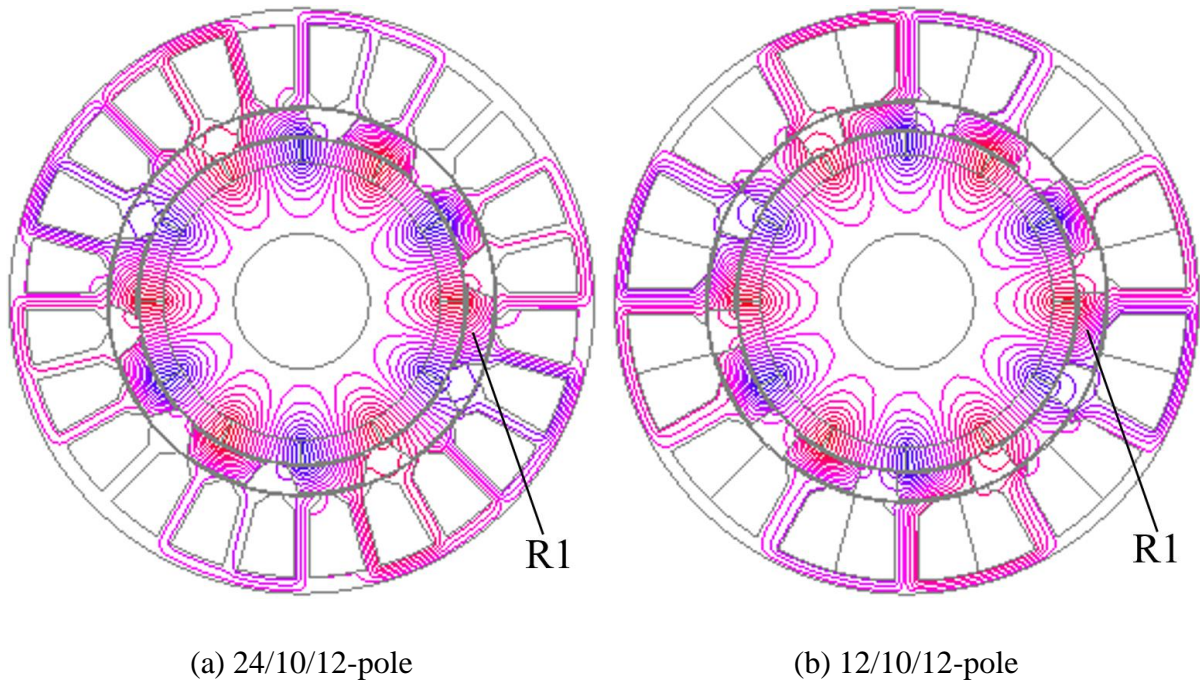


Fig. 5.8. Open-circuit field distributions of 24/10/12-pole and 12/10/12-pole PS-FRPM machines at d -axis position.

It should be noted that the 3rd phase back-EMF harmonic makes no contribution to the line one in machines with Y-connection windings.

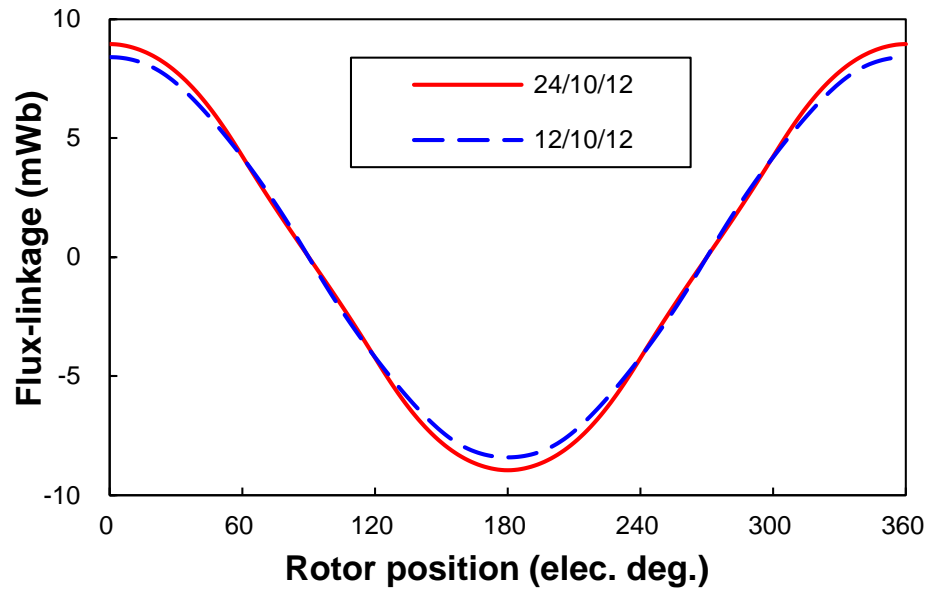
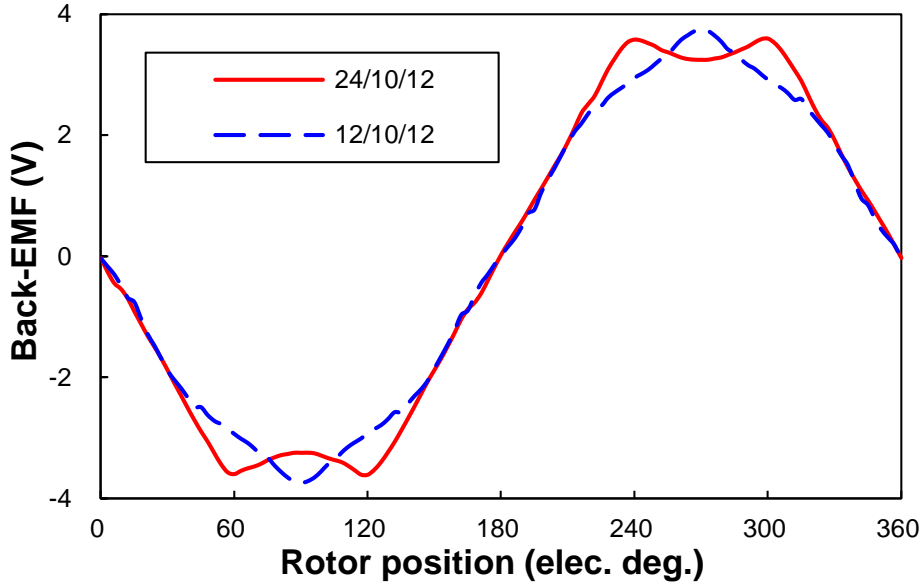
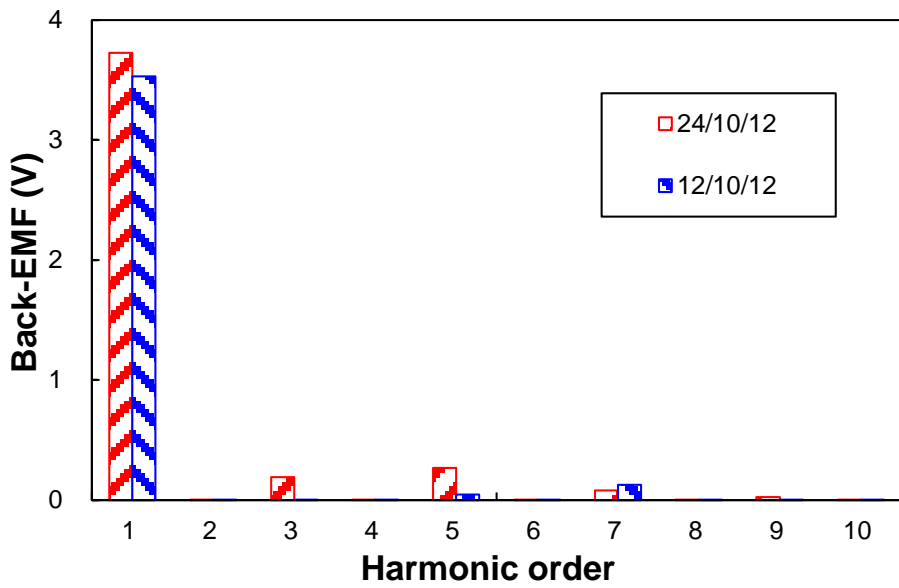


Fig. 5.9. Phase flux-linkage waveforms of 24/10/12-pole and 12/10/12-pole PS-FRPM machines, $N_c=18$.



(a) Waveforms



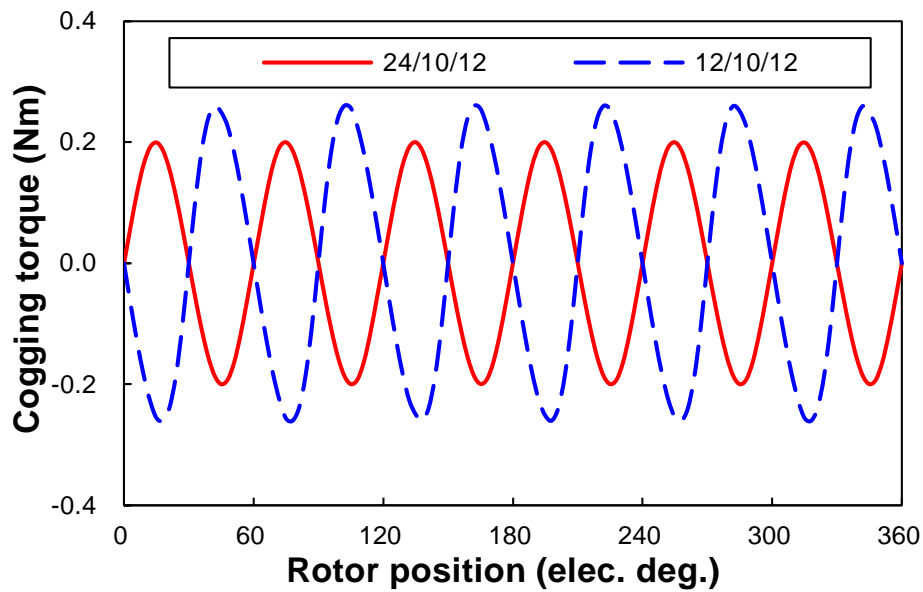
(b) Spectra

Fig. 5.10. Phase back-EMFs of 24/10/12-pole and 12/10/12-pole PS-FRPM machines, $N_c=18$ @400rpm.

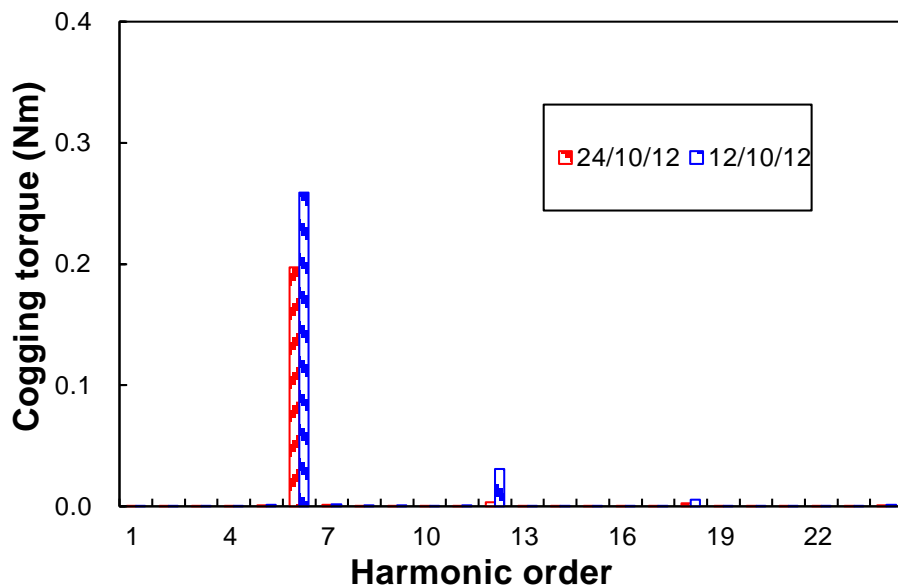
5.3.2 Torque characteristics

Cogging torque in PM machines is resulted from the interaction of PMs and slots. As shown in Fig. 5.11(a), the cogging torque of the proposed 24/10/12-pole PS-FRPM machine is 23.6% lower than that of the existing 12/10/12-pole one, *i.e.* 0.20Nm and 0.26Nm respectively.

However, the harmonic orders in these two machines are the same as shown in Fig. 5.11(b), *i.e.* 6th, 12th, 18th, *etc.*



(a) Waveforms



(b) Spectra

Fig. 5.11. Cogging torque of 24/10/12-pole and 12/10/12-pole PS-FRPM machines.

As pointed out in [ZHU15a], the reluctance torque in the 12/10/12-pole PS-FRPM machine is negligible. For the proposed 24/10/12-pole PS-FRPM machine, it is also approximately zero and hence the maximum torque occurs at current angle of ~ 90 elec. deg., as shown in Fig. 5.12.

Therefore, in this chapter, phase current and phase back-EMF have the same phase angle in PS-FRPM machines with both non-overlapping and overlapping windings.

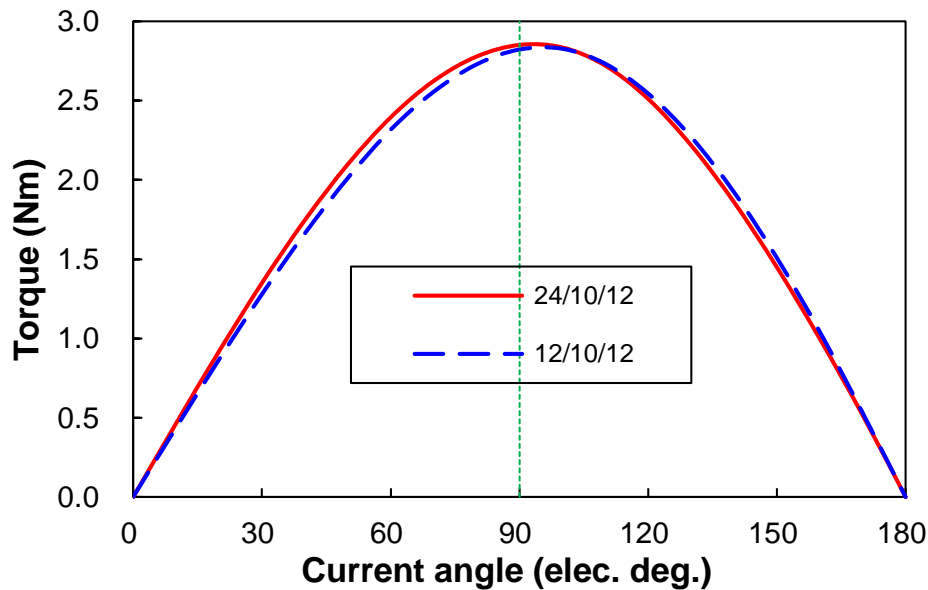


Fig. 5.12. Torque with current angle for 24/10/12-pole and 12/10/12-pole PS-FRPM machines (BLAC, $P_{cu}=20W$).

The electromagnetic torque waveforms of the two machines with $p_{cu}=20W$ are given in Fig. 5.13. In Fig. 5.13, when the copper loss is 20W, the rated q -axis currents i_q are 22.39A and 23.19A for the proposed 24/10/12-pole and the existing 12/10/12-pole PS-FRPM machines, respectively. The slight difference of i_q is caused by the smaller winding area of the optimized designs of the proposed 24/10/12-pole machine than that of the existing 12/10/12-pole machine. The RMS current densities in slot are 3.34A/mm² and 3.23A/mm², respectively, as the cross-section slot area for each coil one side are 85.28mm² and 91.51mm², respectively. The current densities in the winding are twice of that in the slot in both machines, due to the slot packing factor is designed as $k_{pf}=0.5$. As shown in Fig. 5.13, the average electromagnetic torques are 2.87Nm and 2.83Nm for the proposed 24/10/12-pole and the existing 12/10/12-pole PS-FRPM machines, respectively, and the corresponding torque ripples are 13.71% and 18.95%, respectively. The proposed overlapping winding PS-FRPM machine exhibits 1.53% higher torque density and 2.77% lower torque ripple than the existing non-overlapping winding one. Although the fundamental back-EMF of the 24/10/12-pole PS-FRPM machine is 5.56% higher, the average electromagnetic torque is only 1.53% larger than the 12/10/12-pole PS-FRPM machine. This is caused by the smaller slot area and hence the lower ampere turns with same copper loss $p_{cu}=20W$ in the 24/10/12-pole PS-FRPM machine. Due to the overlapping winding

layout, the back iron is thicker and hence the slot area is reduced in the 24/10/12-pole PS-FRPM machine. The torque ripple T_r is defined as,

$$T_r = \frac{T_{max} - T_{min}}{T_{avg}} \quad (5.11)$$

where T_{max} , T_{min} and T_{avg} are the maximum, minimum and average electromagnetic torques.

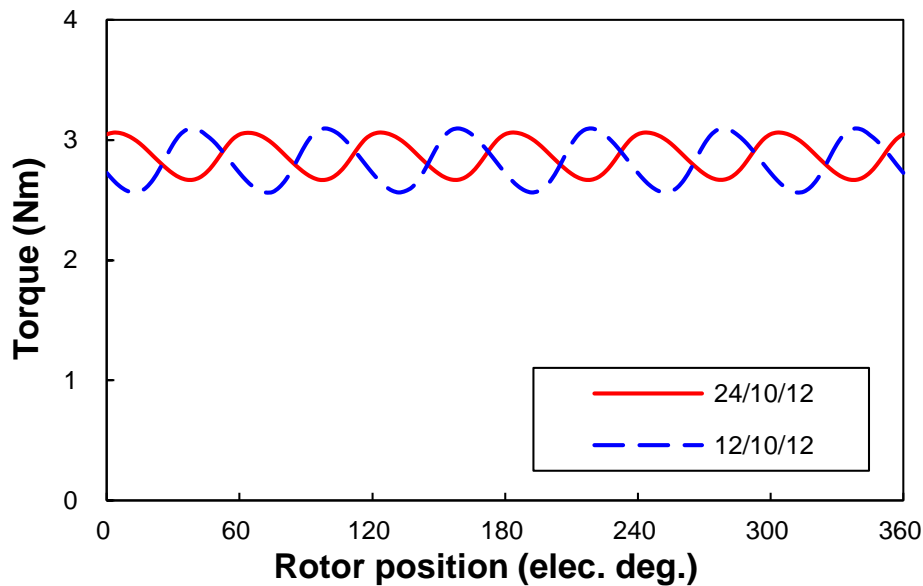


Fig. 5.13. 2D FE predicted on-load torque for 24/10/12-pole and 12/10/12-pole PS-FRPM machines (BLAC, phase current and phase back-EMF have the same phase angle, $p_{cu}=20W$).

To comparatively evaluate the overload capabilities of the proposed 24/10/12-pole PS-FRPM machine and its existing 12/10-/12-pole counterpart, the variation of average electromagnetic torques against the q -axis current for the two machines is illustrated in Fig. 5.14. As aforementioned, the rated q -axis currents i_q are 22.39A and 23.19A for the proposed 24/10/12-pole and the existing 12/10/12-pole PS-FRPM machines, respectively. The proposed 24/10/12-pole PS-FRPM machine can produce higher average electromagnetic torque in the whole q -axis current range due to larger fundamental phase back-EMF shown in Fig. 5.10. It is worth noting that when the q -axis current i_q is overloaded by more than twice to 50A when phase current and phase back-EMF have the same phase angle. The slot RMS current density will be 7.46A/mm² and 6.95A/mm² for the proposed 24/10/12-pole and the existing 12/10/12-pole PS-FRPM machines, respectively, resulting in 13.91A/mm² and 14.92A/mm² winding RMS current densities, respectively, as $k_{pf}=0.5$. The overloaded higher winding RMS current density will increase the copper loss and the heat. Although the overload operation is short time,

this will make challenge to the cooling system, which may need to be taken into consideration.

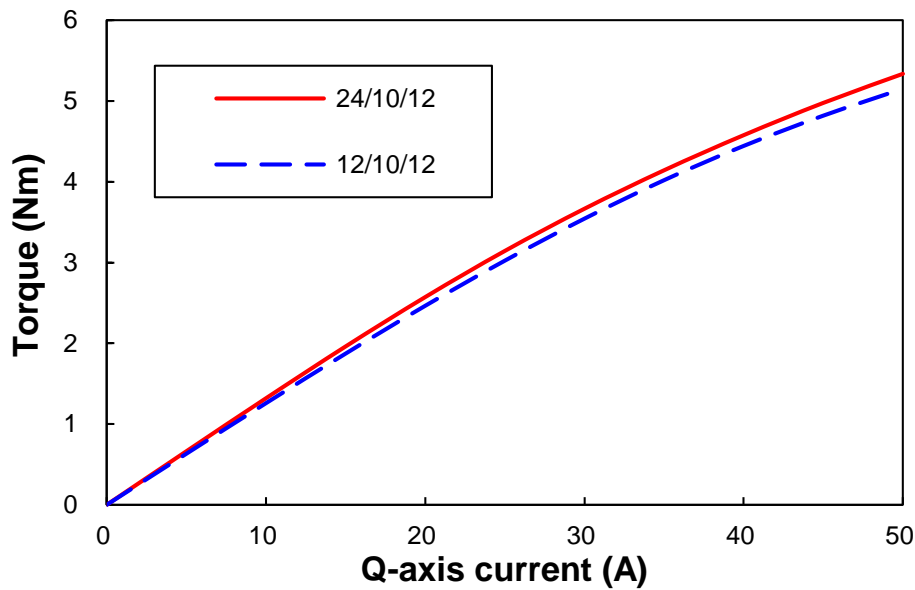


Fig. 5.14. Torque against q -axis current for 24/10/12-pole and 12/10/12-pole PS-FRPM machines (BLAC, phase current and phase back-EMF have the same phase angle).

5.3.3 Loss and efficiency

As shown in Fig. 5.6 and Fig. 5.7, due to the more sinusoidal armature excitation MMF, the proposed 24/10/12-pole PS-FRPM machine with integer-slot overlapping armature winding has lower iron loss and PM eddy current loss than the existing 12/10/12-pole PS-FRPM machine with fractional-slot non-overlapping armature winding. Due to the higher torque density benefitted from shorter magnetic circuit and lower loss, the proposed 24/10/12-pole PS-FRPM machine with integer-slot overlapping armature winding can exhibit higher efficiency than the existing 12/10/12-pole PS-FRPM machine with fractional-slot non-overlapping armature winding, as evidenced by Fig. 5.15. In Fig. 5.15, efficiency η is calculated based on (4.9).

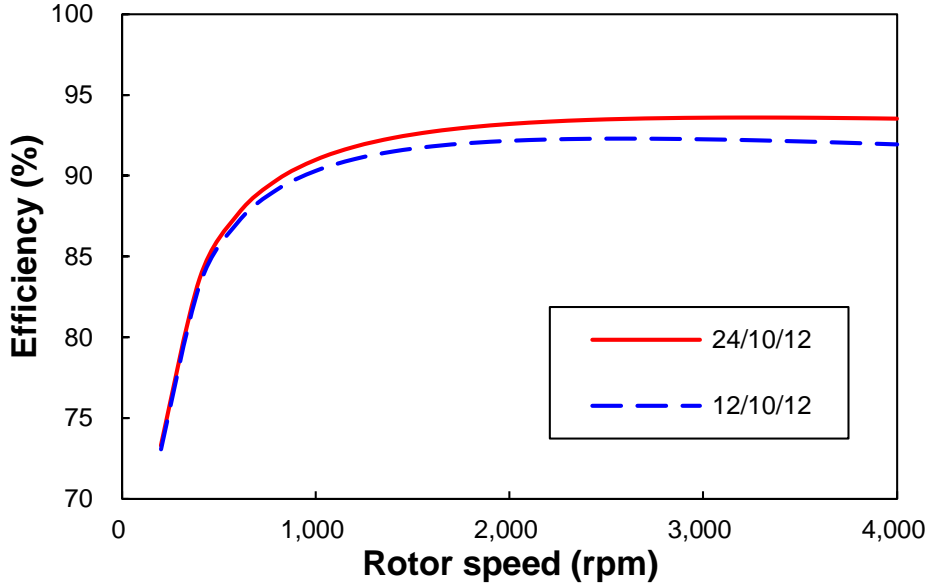


Fig. 5.15. Efficiency versus rotor speed for 24/10/12-pole and 12/10/12-pole PS-FRPM machines ($p_{cu}=20W$, phase current and phase back-EMF have the same phase angle).

5.3.4 Winding inductances

In both analysed PS-FRPM machines, winding inductances are calculated by,

$$L_{XA} = \frac{\psi_{XA} - \psi_{XPM}}{I_A} \quad (5.12)$$

where X is A, B or C, ψ_{XA} and ψ_{XPM} are the average flux-linkages under constant phase A current I_A and open-circuit of phase X respectively.

Self and mutual inductances of both machines are listed in Table 5.2. As shown in Table 5.2, the proposed 24/10/12-pole machine has 74.47% higher self-inductance and 28.46% lower mutual inductance. The increase of self-inductance can be explained by the field distribution of these two machines with only phase A excited, Fig. 5.16. As shown in Fig. 5.16, due to doubled outer stator poles and $q=1$ overlapping windings, the 24/10/12-pole PS-FRPM machine has higher phase A flux-linkage. Consequently, with both higher self-inductance and lower mutual inductance, the 24/10/12-pole PS-FRPM machine has higher self/mutual inductance ratio which is beneficial to restrict the short-circuit current [BIA06a] [CHE14a].

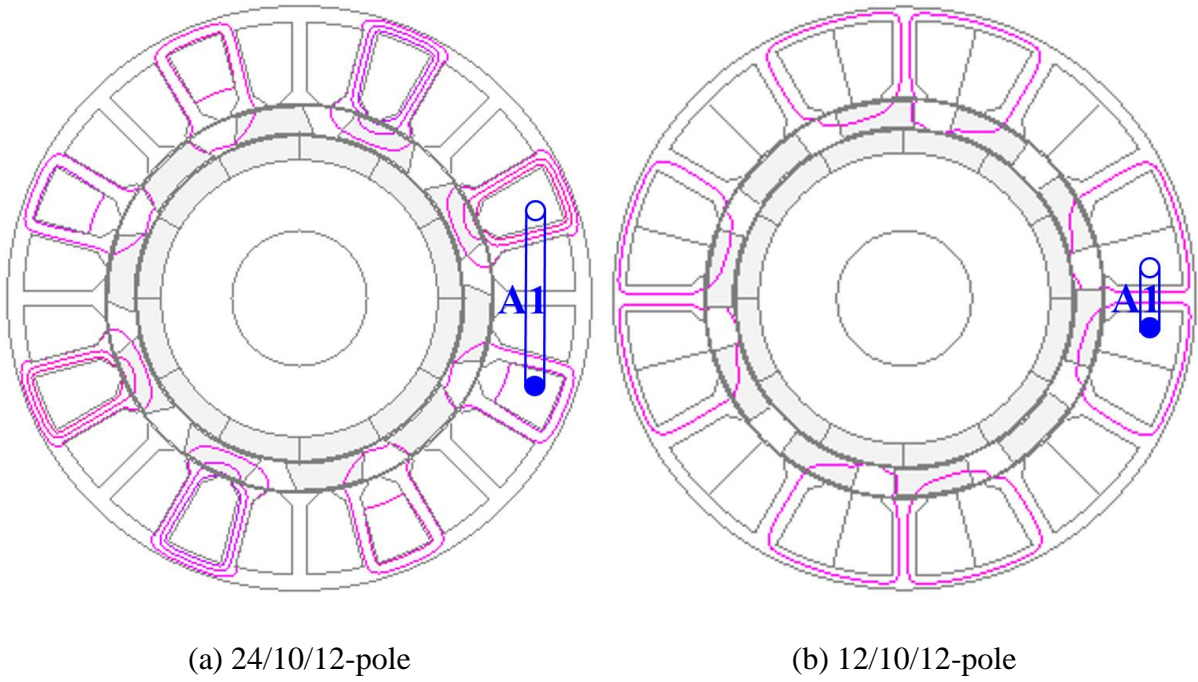


Fig. 5.16. Flux distributions in 24/10/12-pole and 12/10/12-pole PS-FRPM machines at d -axis position with only phase A excited ($p_{cu}=20W$, phase current and phase back-EMF have the same phase angle).

Table 5.2 Self and Mutual Inductances in 24/10/12-Pole and 12/10/12-Pole PS-FRPM Machines

Parameter	Unit	24/10/12	12/10/12
Self-inductance, L_{AA}	mH	0.29	0.17
Mutual inductance, L_{BA}	mH	0.05	0.08
Mutual inductance, L_{CA}	mH	0.05	0.08

In PM machines, flux-weakening capability which is related to winding inductances plays an important role on the power-constant operation region [JAH87a] [JAH04a]. The flux-weakening capability is evaluated by the flux-weakening coefficient k_{fw} ,

$$k_{fw} = \frac{L_d(i_d = -I_{max}, i_q = 0)I_{max}}{\psi_{PM}(i_q = 0)} \quad (5.13)$$

where L_d and ψ_{PM} are the d -axis inductance and the PM flux-linkage with consideration of cross-coupling [QI09a]. I_{max} is the maximum current of the controller. k_{fw} in 24/10/12-pole and

12/10/12-pole PS-FRPM machines are 1.10 and 0.77, respectively, with a controller has maximum current $I_{max}=25A$. The maximum rotor speed in the 24/10/12-pole PS-FRPM machine is infinite whilst that in the 12/10/12-pole PS-FRPM machine is 2801rpm as listed in Table 5.3.

Table 5.3 Some Control Characteristics in 24/10/12-Pole and 12/10/12-Pole PS-FRPM Machines

Parameters	Unit	24/10/12	12/10/12
D-axis inductance, L_d	mH	0.39	0.26
Maximum phase current, I_{max}	A	25	
PM flux-linkage, ψ_{PM}	mWb	8.84	8.40
Flux-weakening coefficient, k_{fw}	-	1.10	0.77
Rated rotor speed, Ω_r	rpm	400	
Maximum rotor speed, Ω_{rmax}	rpm	Infinite	2801

5.3.5 Influence of end winding

In the previous analysis, the end-windings of both machines are neglected, and the copper loss is the stack active winding copper loss only. However, as shown in Table 5.4, the proposed 24/10/12-pole integral-slot overlapping winding machine suffers from 34.20% larger end winding length than its fractional-slot non-overlapping 12/10-12-pole counterpart, due to the larger coil pitch. In Table 5.4, half turn coil total length L_{half} is,

$$L_{half} = L_s + L_e \quad (5.14)$$

where L_e is the half turn coil end length,

$$L_e = K_s \tau_y \quad (5.15)$$

where K_s is the end winding empirical coefficient, which is related to the pole number. For the 24/10/12-pole and 12/10/12-pole PS-FRPM machines, it is selected as 1.25 and 1.35, respectively [CHE90a]. τ_y is the coil pitch in terms of circumferential length,

$$\tau_y = \frac{(R_{osy} + R_{osi} + l_{otb})}{2} \theta_{coil} \quad (5.16)$$

where θ_{coil} is the coil pitch in unit of rad, which is $\pi/4$ and $\pi/6$ for the 24/10/12-pole and 12/10/12-pole PS-FRPM machines, respectively.

As shown in Table 5.4, due to larger L_e , the total length of half turn coil L_{half} in the proposed 24/10/12-pole machine, and hence the total copper loss, is 11.86% higher than the existing 12/10/12-pole design, when the copper loss per active stack length is set as 20W/25mm. The machine volume $V_{machine}$ in the proposed 24/10/12-pole machine is 17.62% larger than the existing 12/10/12-pole design. Consequently, the average torque per total copper loss T_{avg}/p_{cu} and the average torque per machine volume $T_{avg}/V_{machine}$ of the proposed 24/10/12-pole machine are 9.24% and 13.68% lower than the existing 12/10/12-pole machine, although the average electromagnetic torque is 1.53% higher, as foregoing analysed.

Table 5.4 Evaluation of End Windings in 24/10/12-Pole and 12/10/12-Pole PS-FRPM Machines (BLAC, $p_{cus}=20W$)

Parameters	Unit	24/10/12	12/10/12
Stack length, l_s	mm	25	
Stack copper loss, p_{cus}	W	20	
Half turn coil end length, L_e	mm	17.82	13.28
End winding copper loss, p_{cue}	W	14.25	10.62
Half turn coil total length, L_{half}	mm	42.82	38.28
Total copper loss, p_{cu}	W	34.25	30.62
Average torque, T_{avg}	Nm	2.87	2.83
Torque/copper loss, T_{avg}/p_{cu}	Nm/W	0.08	0.09
Machine volume, $V_{machine}$	dm ³	0.39	0.33
Torque/machine volumn, $T_{avg}/V_{machine}$	Nm/dm ³	7.44	8.62

However, as well known, the influence of end-winding will be smaller if the stack length is longer, as the end winding axial thickness is constant when the machine cross-section is fixed [WAN14a] [WAN14b]. This is evidenced in Fig. 5.17 and Fig. 5.18 for both the proposed 24/12/10-pole and the existing 12/10/12-pole PS-FRP machines. In both machines, $T_{average}/p_{cu}$ and $T_{avg}/V_{machine}$ can be effectively enhanced with longer stack length L_s , although the increment becomes smaller with L_s . More importantly, T_{avg}/p_{cu} and $T_{avg}/V_{machine}$ in the proposed 24/10/12-pole machine increase faster than the existing 12/10/12-pole machine, due to the higher average electromagnetic torque. When the stack length $L_s=287.5\text{mm}$ and $L_s=587.5\text{mm}$, the proposed 24/10/12-pole machine even has similar T_{avg}/p_{cu} and $T_{avg}/V_{machine}$ as the existing 12/10/12-pole machine, respectively. It is worth noting that the longer end winding in the proposed 24/10/12-pole PS-FRPM machine with overlapping winding also brings higher inductance, and hence further enhancing the fault-tolerant capability. This will be verified by experiments.

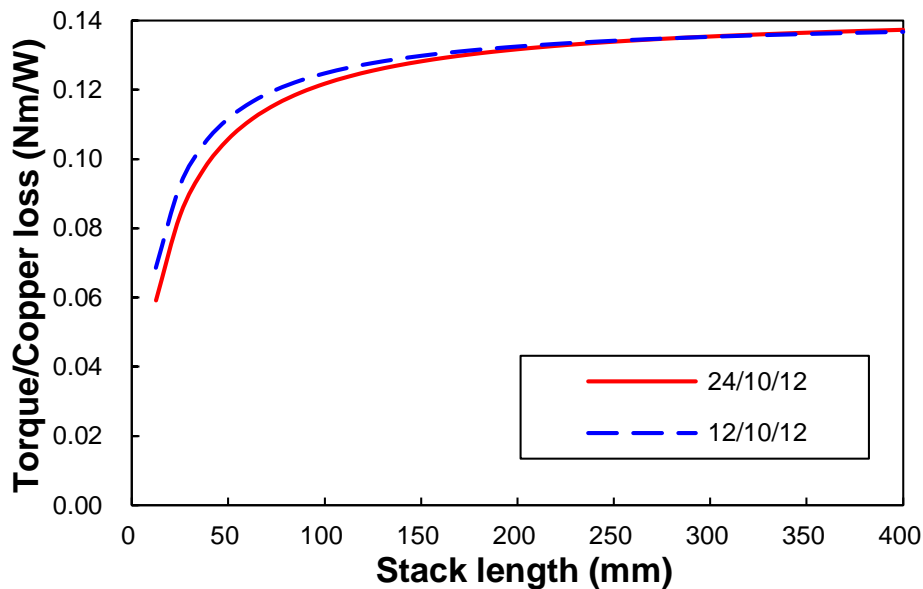


Fig. 5.17. Torque/copper loss versus stack length for 24/10/12-pole and 12/10/12-pole PS-FRPM machines.

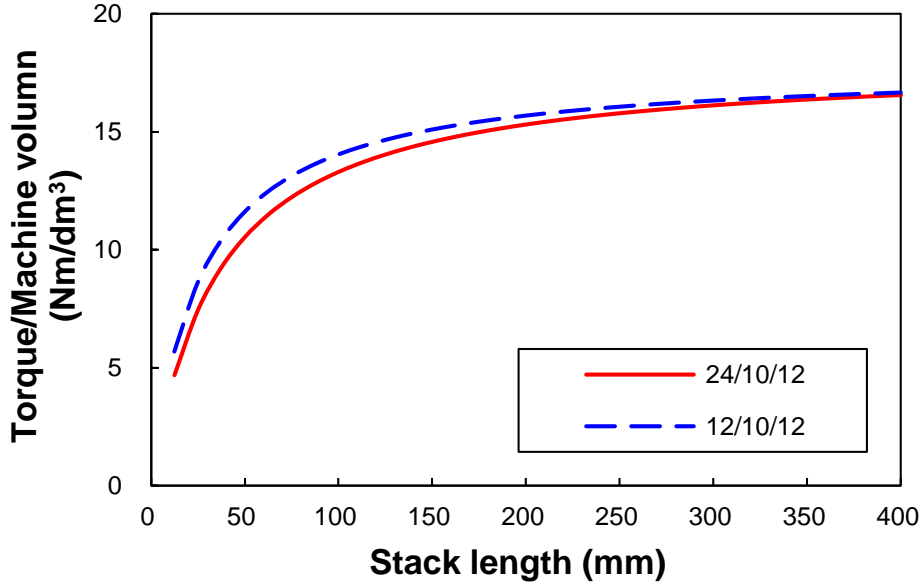


Fig. 5.18. Torque/machine volume versus stack length for 24/10/12-pole and 12/10/12-pole PS-FRPM machines.

5.4 Experimental Validation

In the previous analysis, the electromagnetic performance of the 24/10/12-pole PS-FRPM machine with $q=1$ overlapping windings is analysed and compared to the 12/10/12-pole PS-FRPM machine with $q=0.5$ non-overlapping windings, which is built and measured in [ZHU15a] in terms of phase back-EMF and static torque. In this section, the 24/10/12-pole PS-FRPM prototype machine with $q=1$ overlapping windings is manufactured and measured to validate both the phase back-EMF and static torque, which will be compared with the 12/10/12-pole PS-FRPM prototype. Moreover, the dynamic performances of the both prototype machines are tested and given in this section to validate the FE analysis.

The pictures of the 24/10/12-pole and 12/10/12-pole PS-FRPM prototype machines are shown in Fig. 5.19. The dimensions of the 24/10/12-pole prototype machine are listed in Table 5.1, whilst those of the 12/10/12-pole prototype machine are given in [ZHU15a]. For simplifying manufacturing, only the outer stator of the proposed 24/10/12-pole PS-FRPM machine is built, Fig. 5.19(a), and the two prototypes share the same rotor, Fig. 5.19(c), and the inner stator, Fig. 5.19(e). Consequently, it should be noted that the dimensional parameters of the 24/10/12-pole prototype machine listed in Table 5.1 are slightly different from those by optimization. To ease the manufacture of the cup rotor, $T_{bri}=0.5\text{mm}$ thick iron bridge close to the inner air-gap are introduced to link the adjacent rotor iron pieces, as can be seen from Fig.

5.19(d). Due to the different dimensional parameters from the optimized designs as aforementioned, the electromagnetic performance of the 24/10/12-pole PS-FRPM prototype machine with $q=1$ integer-slot overlapping winding will be compromised. However, the tested electromagnetic performance of both prototypes agree well with the FE predicted results, as given as follows.

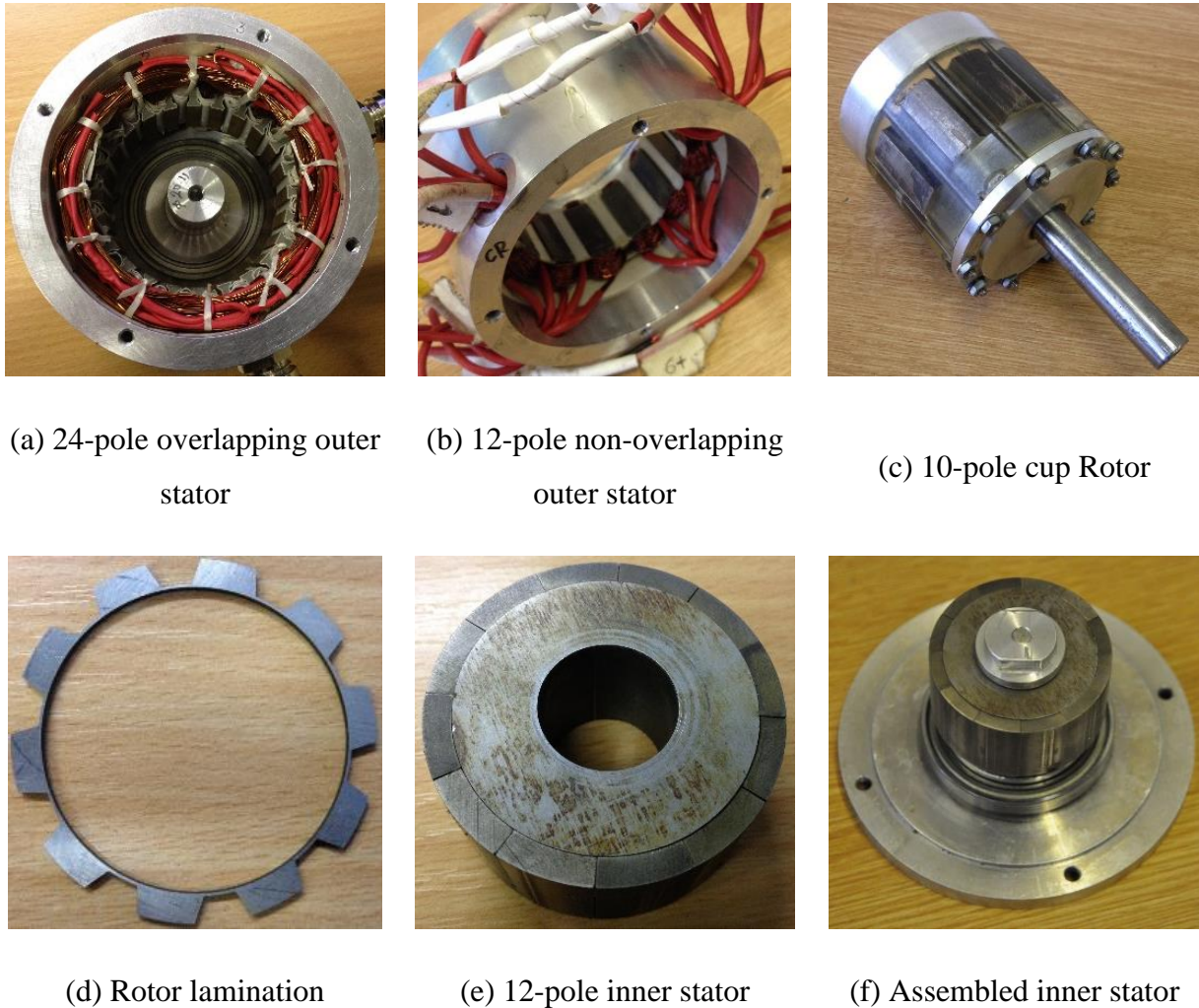
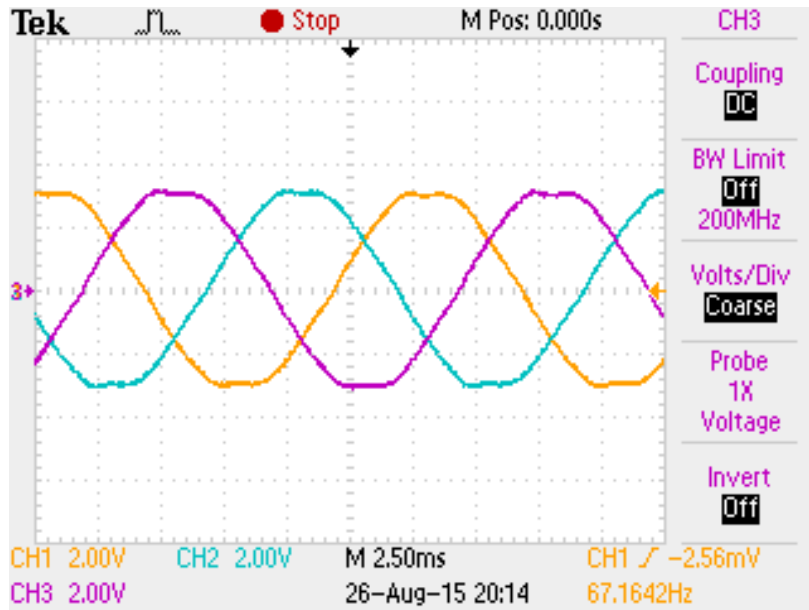


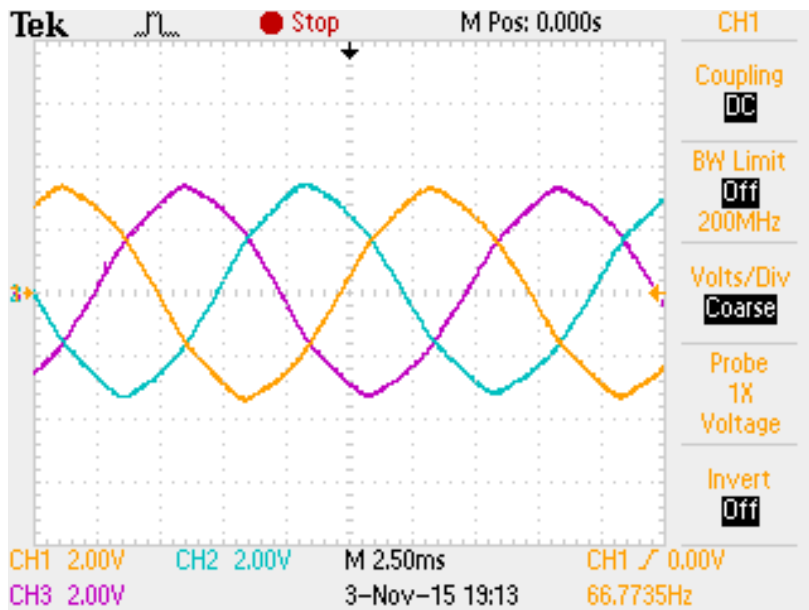
Fig. 5.19. Photos of 24/10/12-pole and 12/10/12-pole PS-FRPM prototype machines.

The 2D FE predicted phase back-EMFs at 400rpm of the 24/10/12-pole and 12/10/12-pole PS-FRPM machines are shown in Fig. 5.20(a) and Fig. 5.20(b), respectively. Due to manufacturing tolerance, the back-EMF waveforms are slightly asymmetric. The comparison of 2D FE predicted and measured phase back-EMFs is given in Fig. 5.21 and Fig. 5.22. In both machines, the 2D FE predicted values agree well with the measured ones, although the measured back-EMFs are slightly lower due to end effect. As shown in Fig. 5.21 and Fig. 5.22, the phase fundamental back-EMF of the proposed machine is even slightly smaller than that of

the existing machine, since the dimensional parameters of the former one are compromised, as aforementioned.

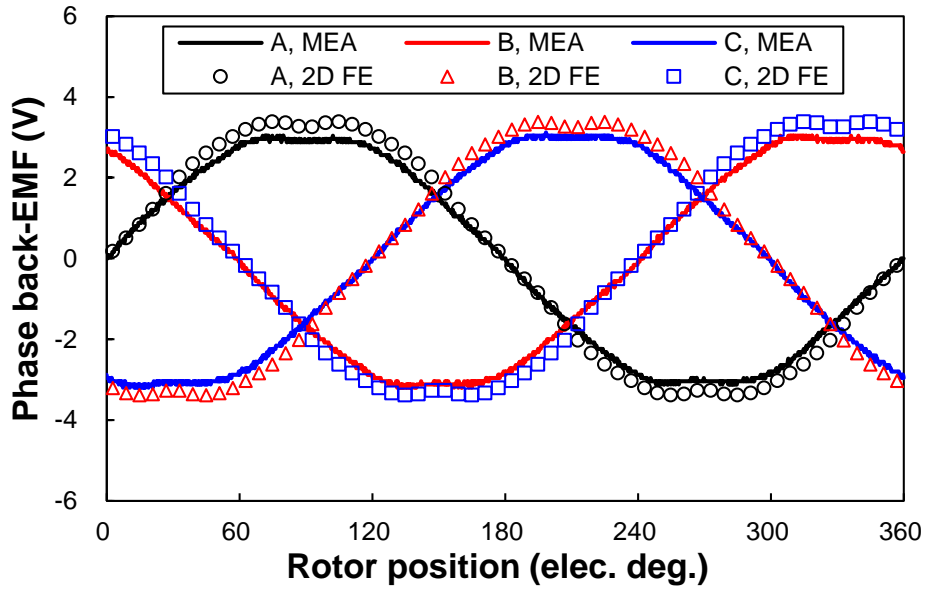


(a) 24/10/12-pole

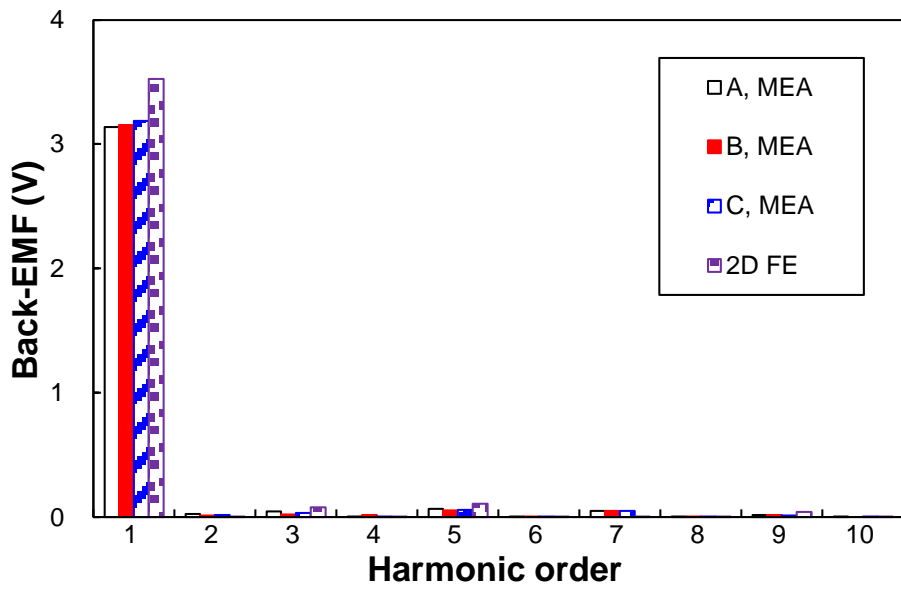


(b) 12/10/12-pole

Fig. 5.20. Measured three-phase back-EMF waveforms @400rpm.

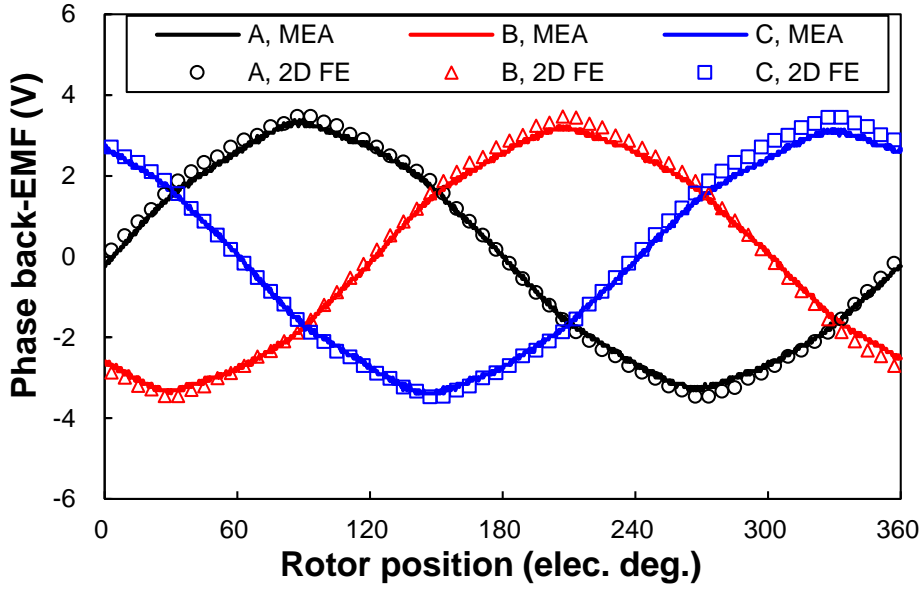


(a) Waveform

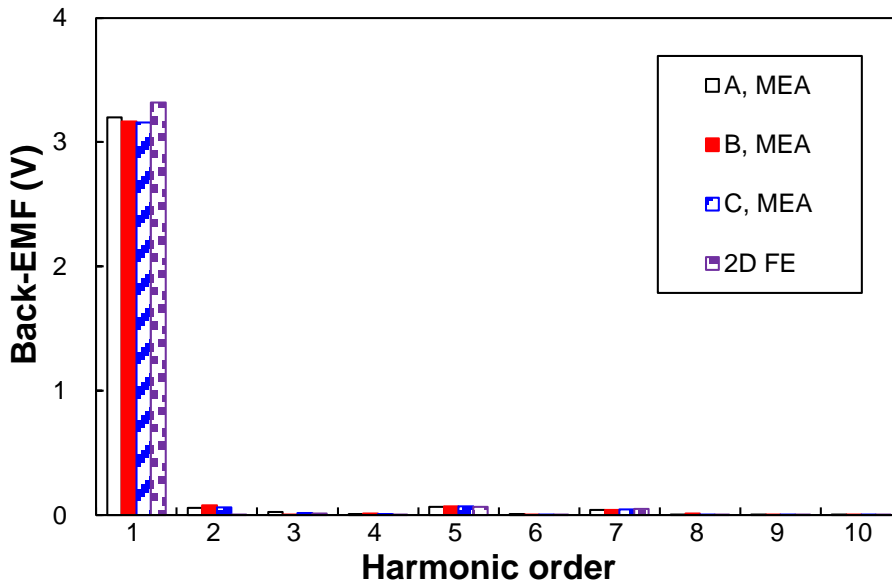


(b) Spectra

Fig. 5.21. Comparison of 2D FE predicted and measured phase back-EMFs in the 24/10/12-pole PS-FRPM prototype machine.



(a) Waveform

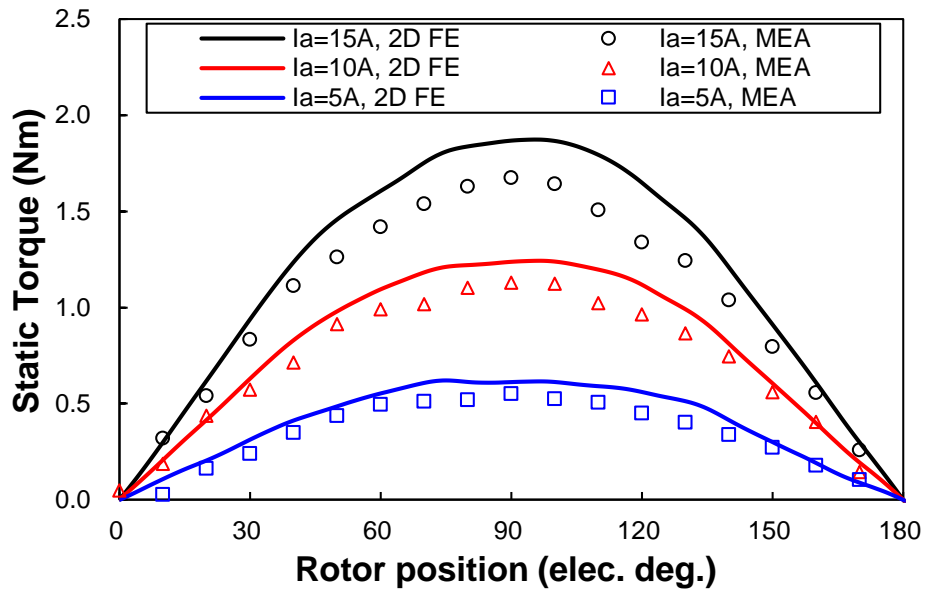


(b) Spectra

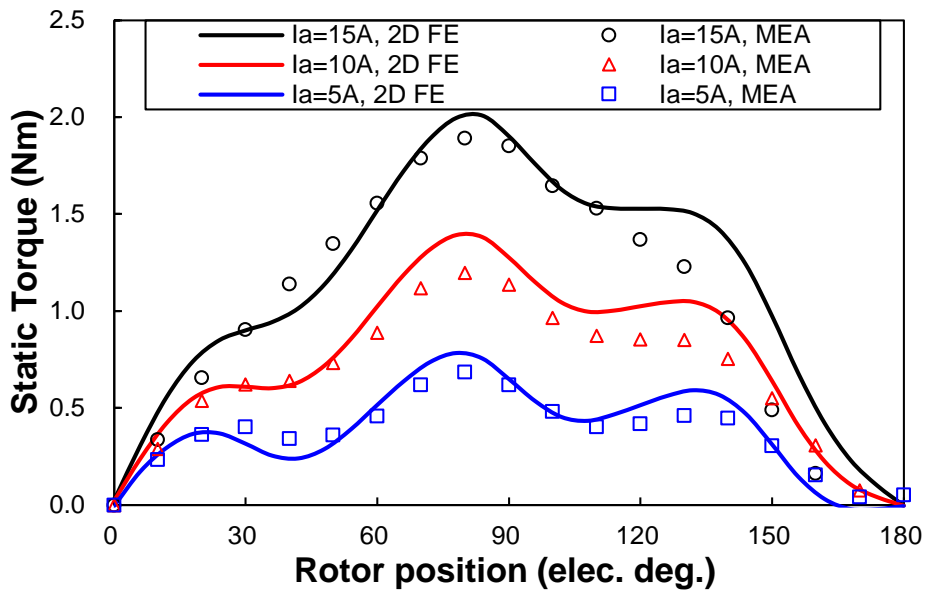
Fig. 5.22. Comparison of 2D FE predicted and measured phase back-EMFs in the 12/10/12-pole PS-FRPM prototype machine.

The 2D FE predicted static torque waveforms of the 24/10/12-pole and 12/10/12-pole PS-FRPM machines are shown in Fig. 5.23(a) and Fig. 5.23(b), respectively. The static torque is defined as the electromagnetic torque with constant phase A current I_A , phase B current I_B and phase C current I_C when the relationship between them are set as $I_A = -2I_B = -2I_C$. Although the peak static torque in the 24/10/12-pole PS-FRPM machine is slightly smaller than its 12/10/12-

pole counterpart due to manufacturing compromise, there is a good agreement between the 2D FE predicted static torques and the measured values, as shown in Fig. 5.23 and Fig. 5.24. Again, the measured ones are slightly smaller due to end effect.



(a) 24/10/12-pole



(b) 12/10/12-pole

Fig. 5.23. Comparison of 2D FE predicted and measured static torque waveforms ($I_A = -2I_B = -2I_C$).

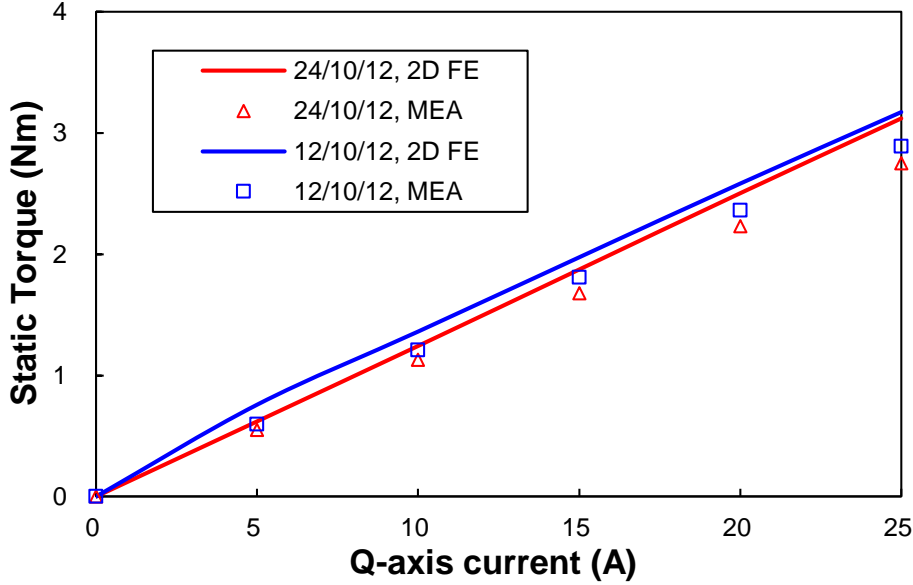


Fig. 5.24. Comparison of 2D FE predicted and measured peak static torques waveforms ($I_A = -2I_B = -2I_C$).

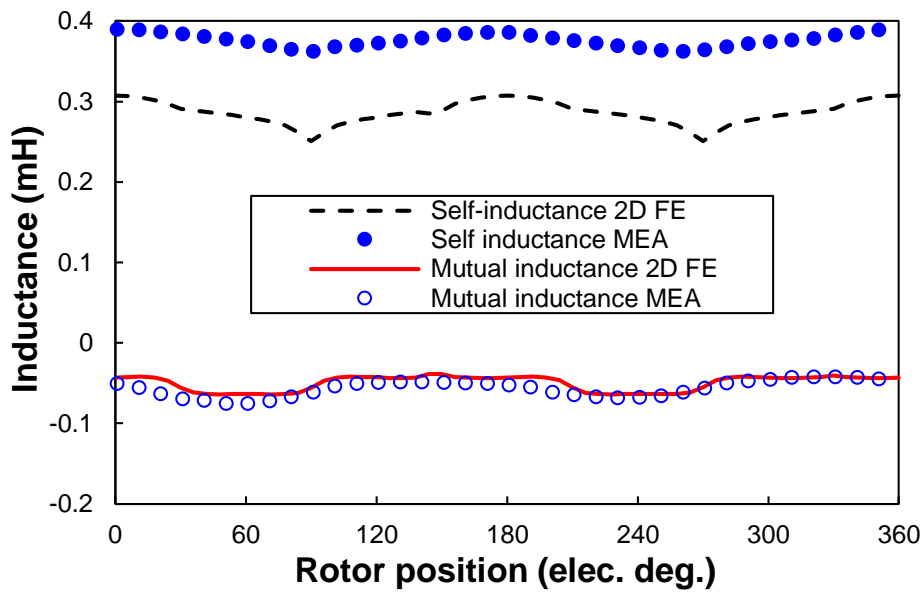
Fig. 5.25(a) and Fig. 5.25(b) compare the measured and 2D FE predicted self- and mutual inductances of the 24/10/12-pole and 12/10/12-pole PS-FRPM prototypes. The self-inductance is measured directly by LCR meter, whilst the mutual inductance is calculated by,

$$M_{BA} = \frac{L_{A+B} - L_{AA} - L_{BB}}{2} \quad (5.17)$$

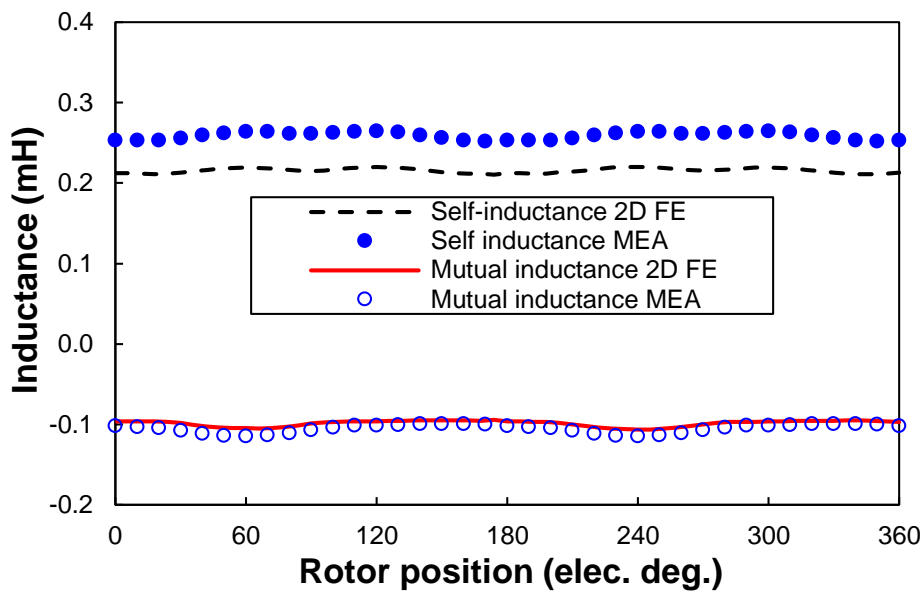
where M_{BA} is the calculated mutual inductance between phase A and phase B. L_{A+B} is the measured self-inductance of the serially connected windings of phase A and phase B. L_{AA} and L_{BB} are the measured self-inductance of phase A and phase B, respectively.

As shown in Fig. 5.25, since the 2D FE analysis cannot accounting for the end winding inductance, the measured self-inductances are slightly higher than the 2D FE predicted ones in both machines. It should be noted that, as the 24/10/12-pole machine with overlapping winding has longer end winding than the 12/10/12-pole machine with non-overlapping winding, the gap between the measured and 2D FE predicted self-inductance in the 24/10/12-pole machine is larger than that in the 12/10/12-pole machine. However, this influence can be eliminated in the calculated mutual inductance based on (5.17), resulting in good agreement between the measured and 2D FE predicted mutual inductances in both machines, as shown in Fig. 5.25. More importantly, it can be observed from Fig. 5.25 that the 24/10/12-pole machine has higher self-inductance but lower mutual inductance than the 12/10/12-pole machine with or without

consideration of end winding, which is beneficial to restrict the short-circuit current, as analysed in sub-section 5.3.4.



(a) 24/10/12-pole



(b) 12/10/12-pole

Fig. 5.25. Comparison of 2D FE predicted and measured self- and mutual inductances.

Based on the test rig shown in Fig. 5.26, the dynamic performance of the two prototypes are tested. The DC bus voltage and current are $U_{dc}=18V$ and $I_{dc}=7.5A$, respectively. Fig. 5.27 shows the transient response with speed reference stepping 0-400rpm-0 with load torque

$T_L=0.28\text{Nm}$. The 24/10/12-pole machine has slightly higher q -axis current i_q than the 12/10/12-pole machine, *i.e.* 2.91A and 2.64A, respectively, as shown in Fig. 5.27(c). The 2D FE predicted corresponding average electromagnetic torques are 0.36Nm and 0.33Nm, respectively. The difference between 2D FE predicted corresponding average electromagnetic torques and measured 0.28Nm is caused by end effect and friction. In both machines, phase current and phase back-EMF have the same phase angle, which means there is no flux-weakening due to the lower load torque due to $i_d=0$.

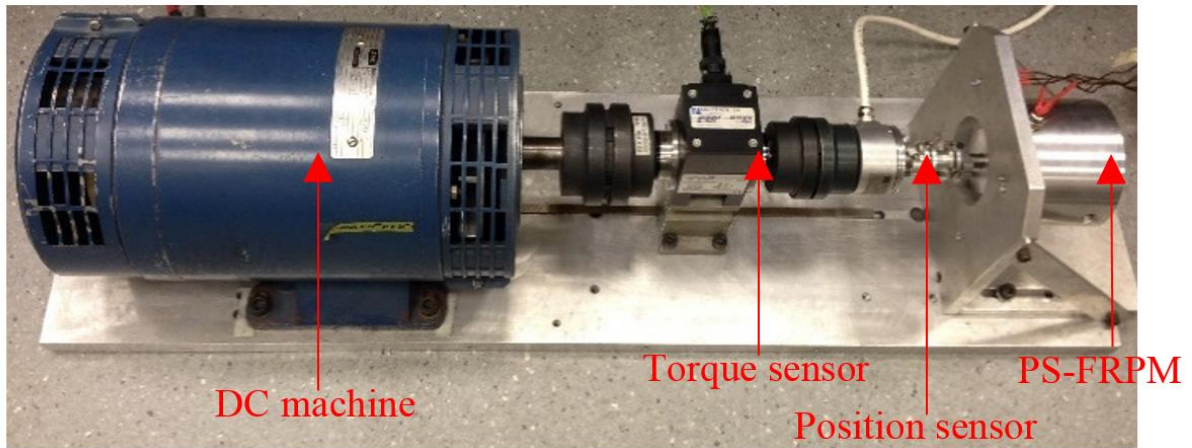
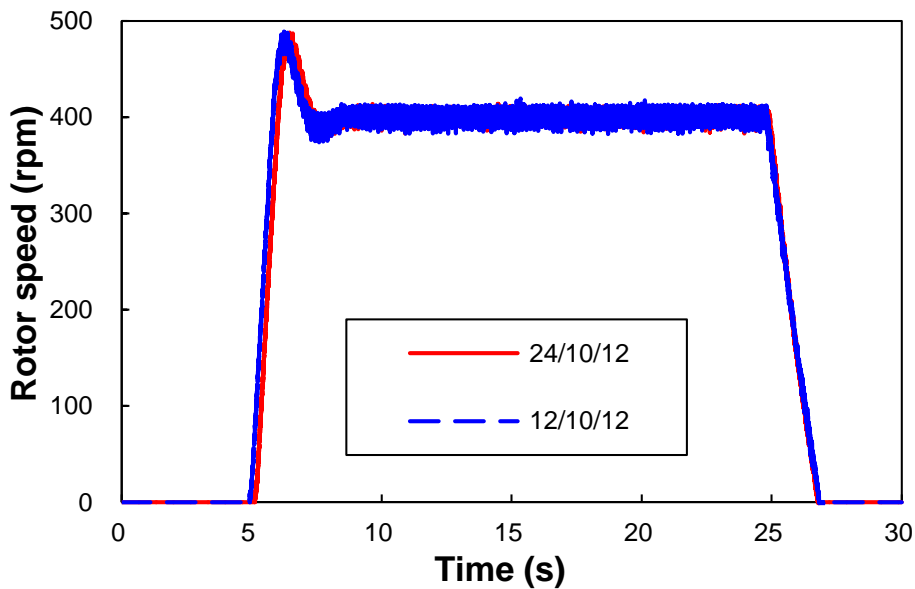
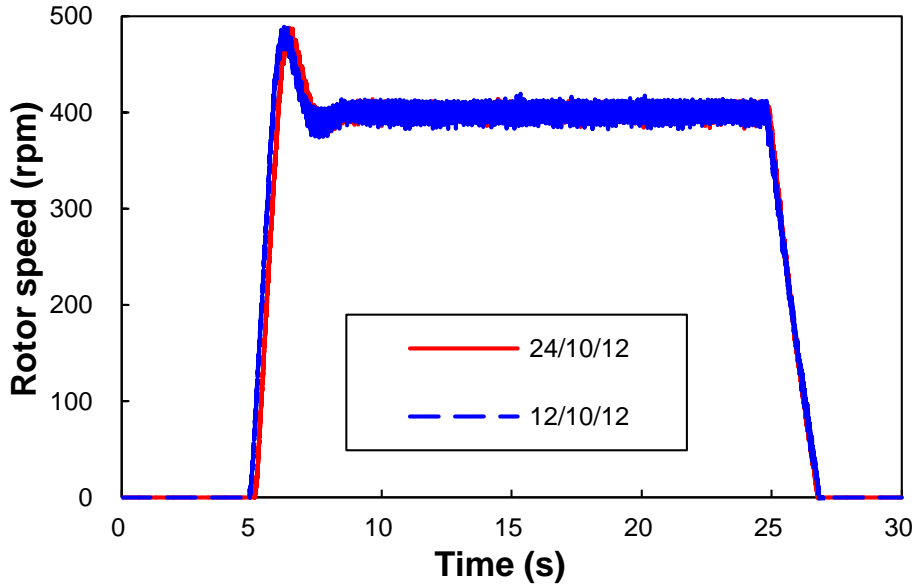


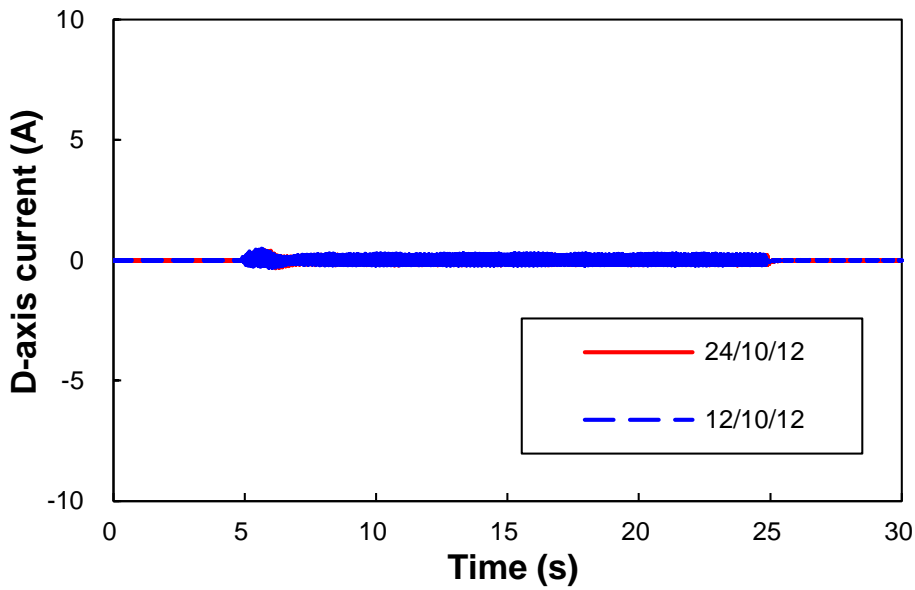
Fig. 5.26. Test rig configuration ($U_{dc}=18\text{V}$, $I_{dc}=7.5\text{A}$).



(a) Rotor speed



(b) *D*-axis current



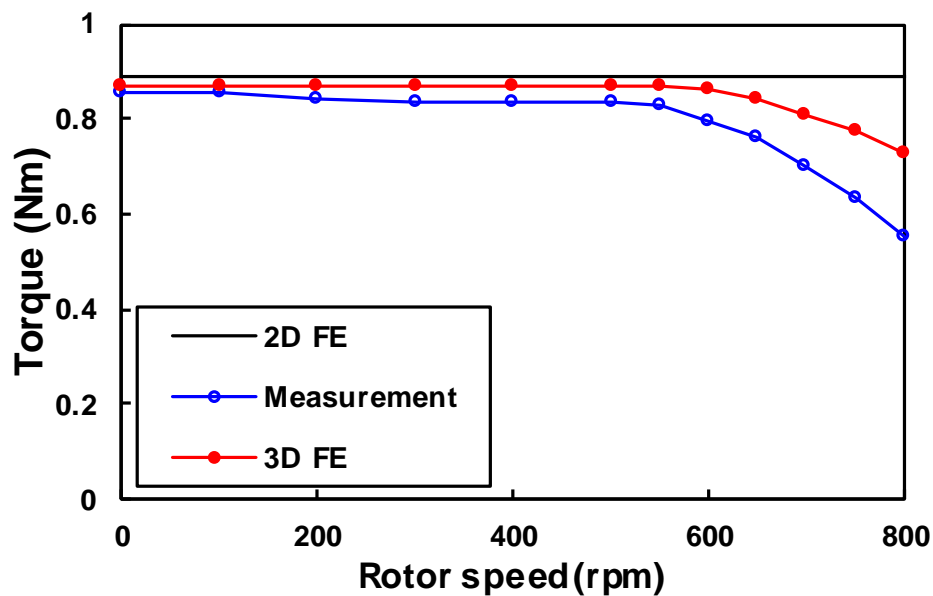
(c) *Q*-axis current

Fig. 5.27. Transient response with speed reference stepping 0-400rpm-0 with load torque $T_L=0.28\text{Nm}$ (phase current and phase back-EMF have the same phase angle).

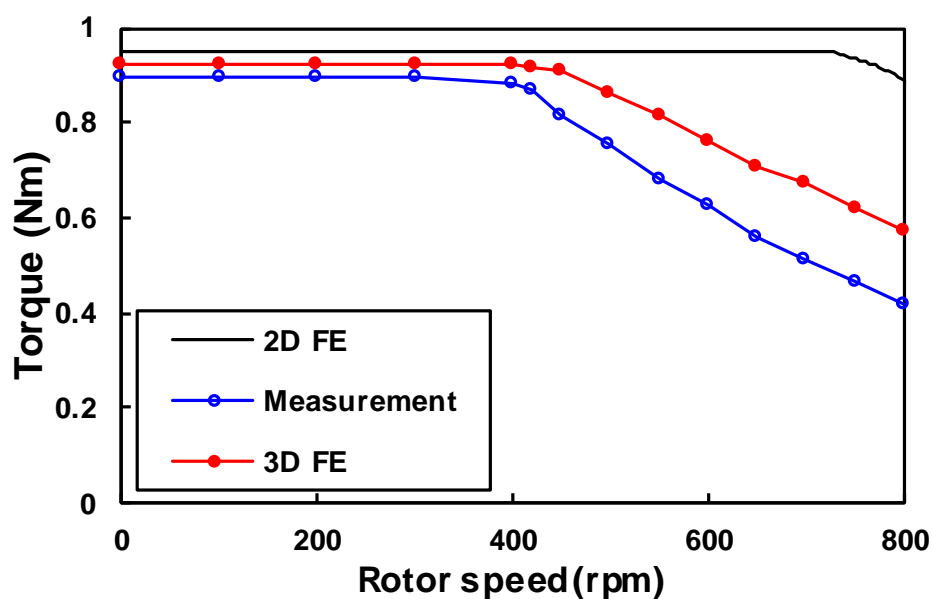
As for the flux-weakening performance, torque-speed curves of the two prototypes are measured and compared with those predicted by FE, as shown in Fig. 5.28. In the constant-torque region, 2D FE predicted torque-speed lines have slightly higher torque in both machines, due to end effect. Also, 2D FE predicted characteristic speed is higher than that measured in both machines, since that the end winding inductance cannot be accounted for in the 2D FE

analysis, as aforementioned.

Good agreement can be achieved between the 3D FE predicted and measured torque-speed curves in Fig. 5.28. The gap between the between the 3D FE predicted and measured torques becomes larger with the rotor speed, as the friction goes higher. More importantly, the 24/10/12-pole machine has smaller characteristic rotor speed than the 12/10/12-pole machine, as the former one has a higher winding inductance, Fig. 5.25, but a similar phase back-EMF, Fig. 5.20, Fig. 5.21, and Fig. 5.22.



(a) 12/10/12-pole



(b) 24/10/12-pole

Fig. 5.28. Torque-speed curves ($U_{dc}=18V$, $I_{dc}=7.5A$).

The measured efficiencies versus various speed of two prototypes are shown in Fig. 5.29, which are calculated as the percentage of the output mechanical power to the input electric power.

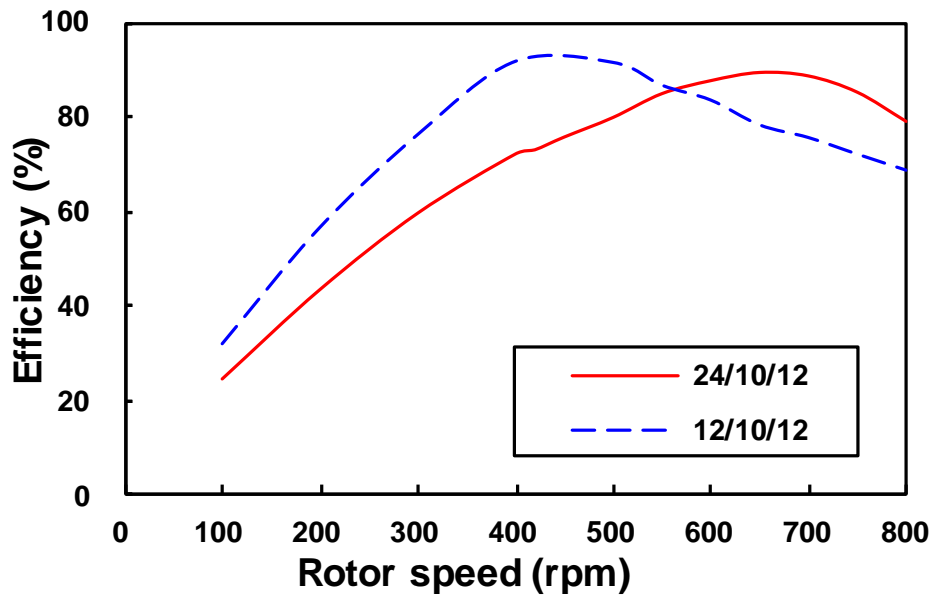


Fig. 5.29. Measured efficiencies versus various rotor speed ($U_{dc}=18V$, $I_{dc}=7.5A$).

5.5 Conclusions

In this chapter, based on the analysis of PS-FRPM machine from the perspective of the magnetic gearing principle, a PS-FRPM machine with overlapping winding having more sinusoidal armature excitation MMF is proposed. Based on the optimized designs for the highest average electromagnetic torque, compared with the existing 12/10/12-pole PS-FRPM machine,

- 1) The proposed 24/10/12-pole PS-FRPM machine has smaller iron loss and PM eddy current loss, due to more sinusoidal armature excitation MMF.
- 2) The proposed 24/10/12-pole PS-FRPM machine has 5.56% larger open-circuit fundamental phase flux-linkage and back-EMF, since some flux paths in the rotor iron piece are shorter in the proposed 24/10/12-pole PS-FRPM machine as the outer stator pole number is doubled, resulting in smaller magnetic reluctance.
- 3) The proposed 24/10/12-pole PS-FRPM machine has 1.53% higher torque density, due to

the higher phase fundamental back-EMF, but 2.77% smaller torque ripple due to 23.6% lower cogging torque, despite of higher 5th and 7th phase back-EMF harmonics. Due to higher torque density and lower loss, the proposed 24/10/12-pole PS-FRPM machine with integer-slot overlapping armature winding can exhibit higher efficiency than the existing 12/10/12-pole PS-FRPM machine with fractional-slot non-overlapping armature winding.

4) The proposed 24/10/12-pole PS-FRPM machine has 74.47% higher self-inductance and 28.46% lower mutual inductance, and hence a higher self/mutual-inductance ratio and better capability to restrict the short-circuit current.

5) The proposed 24/10/12-pole PS-FRPM machine has 50.97% larger d -axis inductance but only 5.17% higher PM flux-linkage, resulting in much higher flux-weakening capability.

6) The proposed 24/10/12-pole PS-FRPM machine suffers from 34.20% larger end winding thickness, hence 11.86% larger total copper loss and 17.62% larger machine volume, 9.24% lower torque/copper loss and 13.68% lower torque/machine volume, although the average electromagnetic torque is 1.53% higher in the designed machine with 25mm stack length. However, when the stack length is longer, the influence of the end-winding will be smaller. The proposed 24/10/12-pole machine will have similar torque/copper loss and torque/machine volume when the stack length is 287.5mm and 587.5mm, respectively.

6 Comparison of Partitioned Stator Flux Reversal PM Machine and Magnetically Geared Machine Operating in Static-PM and Rotating-PM Modes

As found in Chapter 3, the partitioned stator permanent magnet (PM) machines operate based on the magnetic gearing effect, similar to magnetic gears and magnetically geared (MG) machines. In this chapter, the partitioned stator flux reversal PM (FRPM) (PS-FRPM) machines and the conventional MG machines both of which have surface-mounted PMs operating in both static-PM (STPM) type and rotating-PM (RTPM) type are comparatively analysed in terms of electromagnetic performance. It is found that in both the PS-FRPM and MG machines, the STPM machine has higher phase back-EMF and hence higher torque density than its RTPM counterpart, due to higher electric frequency. However, higher iron piece number and PM pole-pair number cause higher synchronous reactance and lower power factor in the MG-STPM and MG-RTPM machines, as well as larger iron loss and hence lower efficiency. Overall, the PS-FRPM machine operates in STPM mode has the highest torque density within the whole copper loss range, the highest efficiency and also the largest power factor. It is also found that to reduce the flux-leakage in a MG machine for obtaining a larger electromagnetic torque and a higher power factor, smaller iron piece number and PM number are preferred. Also, a STPM type machine is recommended to enhance the electric frequency, and hence phase back-EMF and electromagnetic torque.

This part has been submitted to IEEE Transactions on Energy Conversion, which is under revision.

6.1 Introduction

Based on the operation principle of conventional stator-PM machines having single stator, as presented in Chapter 2, PMs and armature windings in the conventional FRPM machine are separately placed in two stators to form the PS-FRPM machine with enlarged total stator areas and hence torque density, *e.g.* 12/10-stator/rotor-pole PS-FRPM machine shown in Fig. 6.1. The coil connection of the PS-FRPM machines can be referred to Fig. 1.2. As shown in Fig. 6.1, the topology of the PS-FRPM machine is similar to the MG machine illustrated in Fig. 6.2. The coil connection of the MG machines can also be referred to Fig. 1.2. The PS-FRPM machines can be referred to Appendix B. Indeed, the PS-FRPM machines also operate based

on the modulation effect of iron pieces to open-circuit PM and armature excitation MMFs, similar to the partitioned stator switched flux PM (PS-SFPM) machine presented in Chapter 3. The modulation of the iron pieces to the open-circuit PM and armature excitation fields makes them synchronous in the air-gaps, generating average electromagnetic torque, similar to the MG machine shown in Fig. 6.2. Similar to a magnetic gear, the armature excitation equivalent pole-pair p_{ea} , the iron piece number N_{ip} and PM pole-pair number p_{PM} in both machines satisfy,

$$N_{ip} = p_{ea} + p_{PM} \quad (6.1)$$

However, two major differences between the PS-FRPM machine shown in Fig. 6.1 and the conventional MG machine shown in Fig. 6.2 are,

1) In the PS-FRPM machine shown in Fig. 6.1, the PMs are static whilst the iron pieces are rotating. However, the PMs are rotating in the MG machine as illustrated in Fig. 6.2, whilst the iron pieces are static.

2) Although both the PS-FRPM machine shown in Fig. 6.1 and the MG machine shown in Fig. 6.2 have the same outer stator pole number $N_{os}=12$, the same winding topology and hence the armature excitation equivalent pole-pair $p_{ea}=4$, [WU15a], the iron piece number N_{ip} and the PM pole-pair number p_{PM} are quite different. Similar to the conventional FRPM machines, $N_{os}=2p_{PM}$ in the PS-FRPM machine, and $N_{ip}=N_{os} \pm 2$ or $N_{ip}=N_{os} \pm 1$. However, in the conventional MG machines, N_{ip} is several times of p_{ea} .

Based on the aforementioned two differences, electromagnetic performance of the conventional MG machine shown in Fig. 6.2, and the PS-FRPM machine shown in Fig. 6.1 operating in both static-PM (STPM) and rotating-PM (RTPM) modes will be comprehensively compared in this paper. This chapter is organized as follows. In section II, the magnetic gearing effect of a conventional MG machine or a PS-FRPM machine operating in either STPM or RTPM mode will be introduced from the perspective of modulation effect of iron pieces to open-circuit PM and armature excitation MMFs by a simple MMF-permeance model. The contribution of the main air-gaps harmonics to the average electromagnetic torque is also comparatively investigated for both the conventional MG machine and the PS-FRPM machine in section II. In section III, electromagnetic performance of the conventional MG machine shown in Fig. 6.2 and the PS-FRPM machine shown in Fig. 6.1 operating in STPM and RTPM modes will be compared by finite element (FE) analyses. In section IV, prototypes of both MG machine operating in RTPM mode and PS-FRPM machine operating in STPM mode will be

built and tested to verify the FE predicted results.

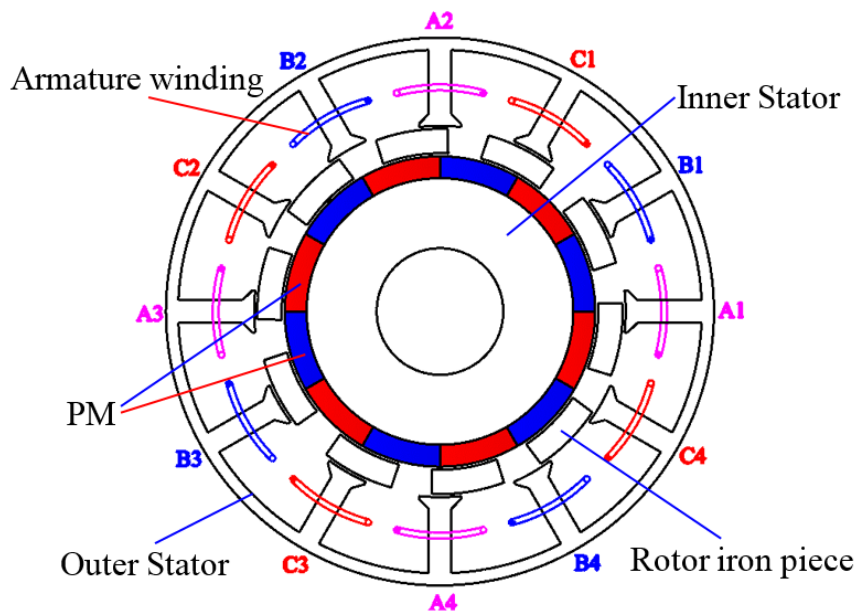


Fig. 6.1. Cross-section of PS-FRPM machine having 12/10/6 outer stator pole / iron piece / inner PM pole-pair.

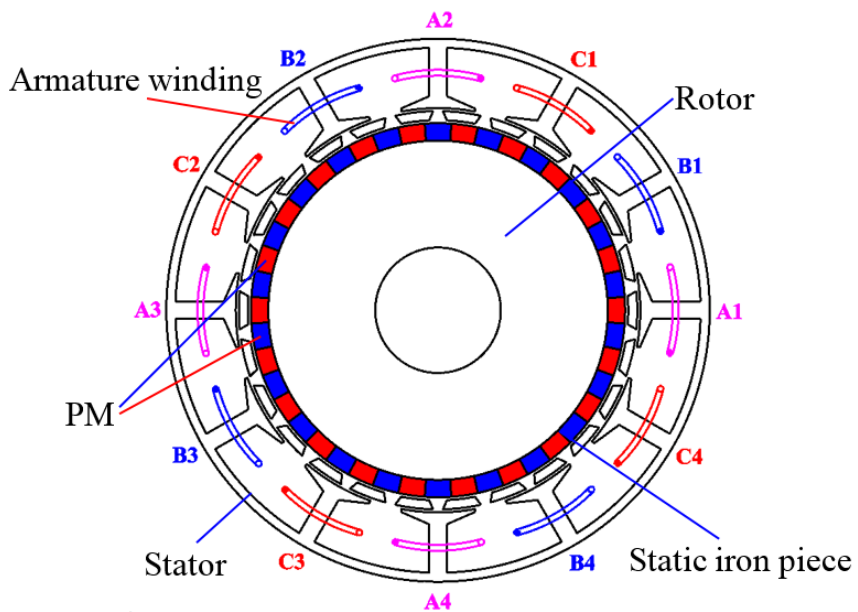


Fig. 6.2. Cross-section of MG machine having 12/26/22 outer stator pole / iron piece / inner PM pole-pair.

6.2 Operation Principle

In this section, firstly the magnetic gearing effect in the conventional MG machine and PS-

FRPM machine operating in both STPM and RTPM modes is introduced based on a simple MMF-permeance model. Then, the contribution of main air-gap field harmonics to the average electromagnetic torque in both PS-FRPM and MG machines is analysed, as given as follows.

The air-gap permeance waveform accounting for slots between iron pieces is shown in Fig. 6.3, which can be expressed in Fourier series by,

$$\begin{cases} P(\theta, t) = P_0 + S_{ip} \sum_{i=1}^{\infty} \{M_{ipk} \cos[kN_{ip}(\theta - \Omega_{ip}t - \alpha_{ip0})]\} \\ S_{ip} = \frac{4P_{ip}}{\pi} \\ M_{ipk} = \frac{\sin(kN_{ip}\theta_2)}{k} \end{cases} \quad (6.2)$$

where P_0 is the DC component of air-gap permeance. P_{ip} is the peak-to-peak component of air-gap permeance. Ω_{ip} is the mechanical angular speed of iron pieces in unit of rad/s, of which the positive direction is anticlockwise. In RTPM machines, $\Omega_{ip}=0$. S_{ip} is the constant in air-gap permeance. M_{ipk} is the Fourier coefficient of air-gap permeance determined by k . θ_2 is half of the rotor iron piece arc.

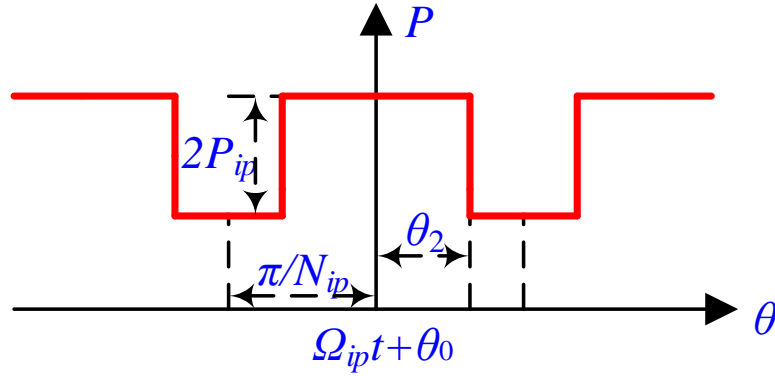


Fig. 6.3. Air-gap permeance waveform accounting for slots between iron pieces.

For the open-circuit PM MMF shown in Fig. 6.4, it can be expressed in Fourier series by,

$$\begin{cases} F_{PM}(\theta, t) = S_{PM} \sum_{i=1}^{\infty} \{M_{PMi} \sin[(2i - 1)p_{PM}(\theta - \Omega_{PM}t - \alpha_{PM0})]\} \\ V_{PM} = \frac{4F_{PMs}}{\pi} \\ M_{PMi} = \frac{\cos[(2i - 1)p_{PM}\theta_1]}{2i - 1} \end{cases} \quad (6.3)$$

where S_{PM} is the constant in PM MMF. M_{PMi} is the Fourier coefficient of PM MMF waveform determined by i . p_{PM} is the PM pole-pair number. F_{PMs} is the PM MMF square waveform peak value. θ_1 is the half of arc between PMs. Ω_{PM} is the mechanical angular speed of PMs in unit of rad/s, of which the positive direction is clockwise. In STPM machines, $\Omega_{PM}=0$.

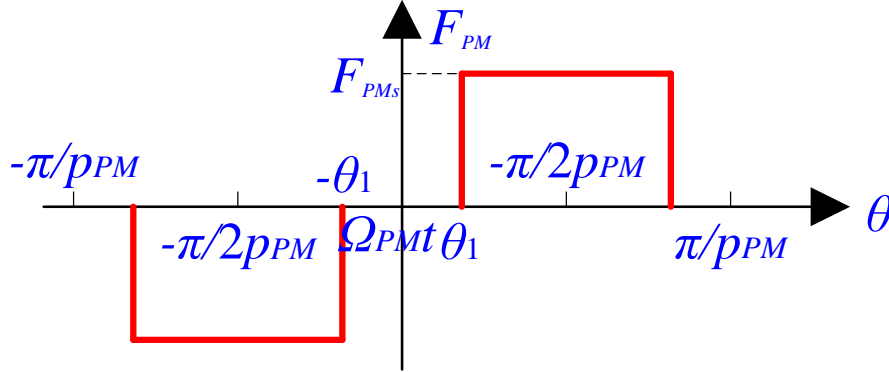


Fig. 6.4. PM MMF.

Similarly, the armature excitation MMF waveform illustrated in Fig. 6.5 can be expressed in Fourier series by,

$$\begin{cases} F_{ABC}(\theta, t) = \frac{3S_{ABC}}{2} \sum_{q=1}^{\infty} [M_{ABCq} \sin(\xi)] \\ S_{ABC} = \frac{2\sqrt{2}N_c I_{rms}}{\pi} \\ M_{ABCq} = \frac{1}{q} \sin(4q\theta_3) \\ \xi = \begin{cases} -4q\theta + \omega_e t, q = 3r - 2 \\ 4q\theta + \omega_e t, q = 3r - 1 \\ 0, q = 3r \end{cases} \end{cases} \quad (6.4)$$

where F_{ABC} is the three-phase armature excitation MMF. F_A , F_B , and F_C are the A-, B-, and C-phase armature excitation MMFs, respectively. S_{ABC} is a constant in armature excitation MMF. M_{ABCq} is the Fourier coefficient of armature excitation MMF waveform determined by q . N_c is the number of coil turns. θ_3 is half of outer stator tooth arc θ_{ost} plus outer stator tooth tip arc θ_{ot} . r is a positive integer mathematically. ω_e is the rotor electrical angular speed in rad/s. The 3-phase sinusoidal currents are calculated by (2.4).

Based on (6.2) and (6.3), the air-gap open-circuit PM fields can be calculated by,

$$\begin{aligned}
B_{PM}(\theta, t) &= F_{PM}(\theta, t)P(\theta, t) \\
&= P_0 S_{PM} \sum_{i=1}^{\infty} [M_{PMi} \cos \alpha_1] \\
&\quad + \frac{S_{PM} S_{ip}}{2} \sum_{i=1}^{\infty} \sum_{k=1}^{\infty} [M_{PMi} M_{ipk} (\cos \alpha_2 + \cos \alpha_3)]
\end{aligned} \tag{6.5}$$

where α_j ($j=1,2,3$) is given by,

$$\alpha_j = H_j \left(\theta - \frac{\omega_j t + \beta_j}{H_j} \right) \tag{6.6}$$

where H_j , ω_j and β_j/H_j are harmonics order, electric rotating speed and initial phases of air-gap field harmonics. They are given by,

$$\begin{cases} H_1 = (2i - 1)p_{PM} \\ H_2 = kN_{ip} + (2i - 1)p_{PM} \\ H_3 = kN_{ip} - (2i - 1)p_{PM} \end{cases} \tag{6.7}$$

and,

$$\begin{cases} \omega_1 = (2i - 1)p_{PM}\Omega_{PM} \\ \omega_2 = kN_{ip}\Omega_{ip} + (2i - 1)p_{PM}\Omega_{PM} \\ \omega_3 = kN_{ip}\Omega_{ip} - (2i - 1)p_{PM}\Omega_{PM} \end{cases} \tag{6.8}$$

and,

$$\begin{cases} \beta_1 = (2i - 1)p_{PM} \left(\alpha_{PM0} + \frac{\pi}{2} \right) \\ \beta_2 = kN_{ip}\alpha_{ip0} + (2i - 1)p_{PM}\alpha_{PM0} + \frac{\pi}{2} \\ \beta_3 = kN_{ip}\alpha_{ip0} - (2i - 1)p_{PM}\alpha_{PM0} - \frac{\pi}{2} \end{cases} \tag{6.9}$$

respectively.

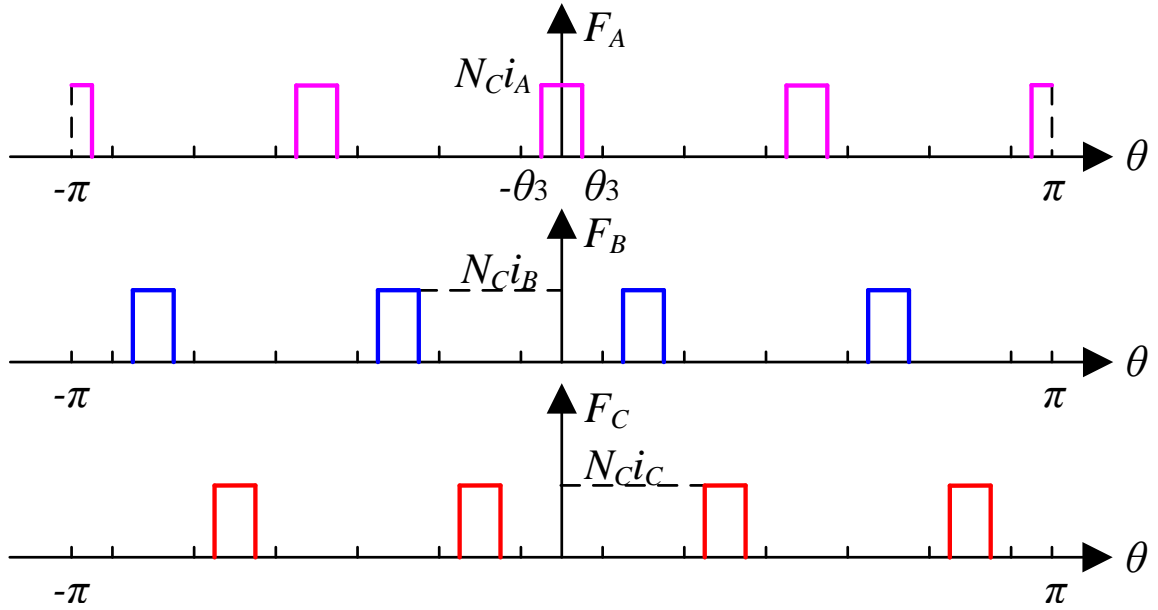


Fig. 6.5. Armature excitation MMF.

Similarly, the air-gap armature excitation fields $B_{ABC}(\theta, t)$ can be calculated from (6.2) and (6.4), as shown in (6.10) and (6.11) when $q=3r-2$. When $q=3r-1$, B_{ABCin} can also be expressed by them with the coefficient of q multiplied by '-1'.

$$\begin{aligned}
 B_{ABC}(\theta, t) &= F_{ABC}(\theta, t)P(\theta, t) \\
 &= \frac{3P_0V_{ABC}}{2} \sum_{q=1}^{\infty} \left\{ M_{ABCq} \cos \left[4q\theta - \omega_e t + \frac{\pi}{2} \right] \right\} \\
 &\quad + \frac{3V_{ABC}V_2}{4} \sum_{q=1}^{\infty} \sum_{k=1}^{\infty} [M_{ABCq} M_{ipk} (\cos \sigma_1 + \cos \sigma_2)]
 \end{aligned} \tag{6.10}$$

where σ_1 and σ_2 are given as,

$$\left\{ \begin{array}{l} \sigma_1 = (kN_{ip} - 4q) \left[\theta - \frac{(k-1)\omega_e t + kN_{ip}\theta_0 + \frac{\pi}{2}}{kN_{ip} - 4q} \right] \\ \sigma_2 = (kN_{ip} + 4q) \left[\theta - \frac{(k+1)\omega_e t + kN_{ip}\theta_0 - \frac{\pi}{2}}{kN_{ip} + 4q} \right] \end{array} \right. \tag{6.11}$$

Table 6.1 Characteristics of Air-Gap Open-Circuit PM Flux-Density Harmonics ($i=1,2,3,\dots$)

Pole-Pairs	Electric Rotating Speed
$(2i - 1)p_{PM}$	$(2i - 1)p_{PM}\Omega_{PM}$
$kN_{ip} + (2i - 1)p_{PM}$	$kN_{ip}\Omega_{ip} + (2i - 1)p_{PM}\Omega_{PM}$
$ kN_{ip} - (2i - 1)p_{PM} $	$kN_{ip}\Omega_{ip} - (2i - 1)p_{PM}\Omega_{PM}$

Table 6.2 Characteristics of Air-Gap Armature-Reaction PM Flux-Density Harmonics
($i=1,2,3,\dots$)

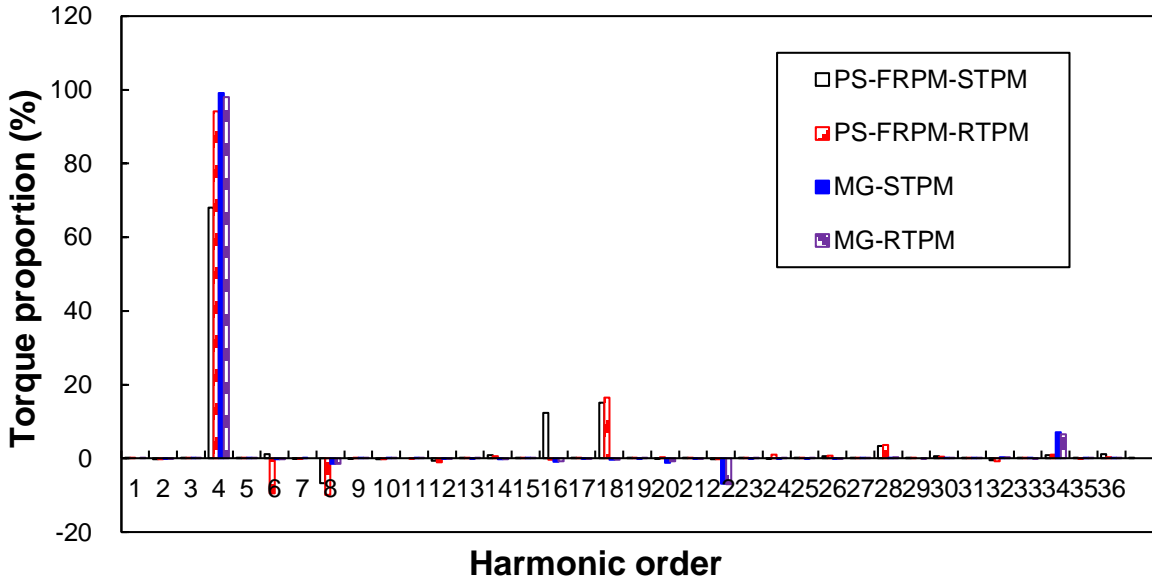
q	Pole-Pairs	Electric Rotating Speed
$3r-2$	$4q$	$\frac{\omega_e}{4q}$
	$ kN_r - 4q $	$\frac{k-1}{kN_r - 4q}\omega_e$
	$kN_r + 4q$	$\frac{k+1}{kN_r + 4q}\omega_e$
$3r-1$	$4q$	$-\frac{\omega_e}{4q}$
	$kN_r + 4q$	$\frac{k-1}{kN_r + 4q}\omega_e$
	$ kN_r - 4q $	$\frac{k+1}{kN_r - 4q}\omega_e$

Based on the foregoing analytically deduced open-circuit and armature excitation air-gap fields shown in (6.5) and (6.10), pole-pairs and electric rotating speed of the open-circuit and armature excitation air-gap fields harmonics can be listed as Table 6.1 and Table 6.2, respectively. Since the open-circuit air-gap fields harmonics listed in Table 6.1 synchronous with those of armature excitation listed in Table 6.2 due to the modulation of iron pieces, electromagnetic torque can be generated in both outer and inner air-gaps in both PS-FRPM and MG machines, based on magnetic gearing principle [WU15a]. This can be evidenced by FE predicted air-gap average electromagnetic torque proportion of main harmonics, as shown in Fig. 6.6, Table 6.3 and Table 6.4. As listed in Table 6.3 and Table 6.4, in all the 4 analysed PS-FRPM and MG machines operating in both STPM and RTPM modes, more than 93% of the average electromagnetic torque is contributed by several dominant air-gap filed harmonics, *i.e.*

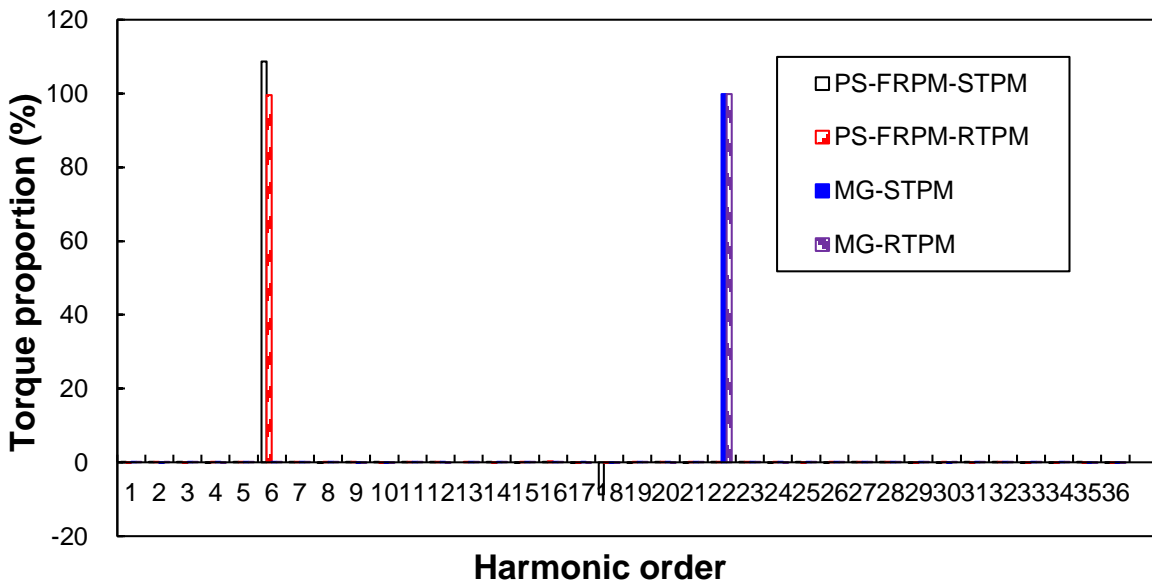
those having pole-pairs of $(2i-1)p_{PM}$ ($i=1, 2$), $|kN_{ip}\pm(2i-1)p_{PM}|$ ($k=1, i=1$), and $|N_{os}\pm(2i-1)p_{PM}|$. This is different from the conventional magnetic gear [ATA04a], in which the average electromagnetic torque is generated by 2 dominant air-gap filed harmonics having pole-pairs of outer and inner PM pole-pairs. It is worth noting that the air-gap filed harmonics having pole-pairs of $|N_{os}\pm(2i-1)p_{PM}|$ are due to the modulation of the outer stator slots to the open-circuit PM and armature excitation MMFs, similar to vernier machines [QU11a].

Table 6.3 Contribution of Main Air-Gap Field Harmonics to Average Electromagnetic Torque in PS-FRPM Machines (%)

Harmonic Order		STPM		RTPM	
		Outer	Inner	Outer	Inner
p_{PM}	6	1.17	108.71	-9.44	99.60
$N_{ip}-p_{PM}$	4	68.03	-0.03	94.13	0.01
$N_{ip}+p_{PM}$	16	12.36	0.03	-0.29	0.31
$3p_{PM}$	18	15.15	-8.71	16.55	-0.17
$ N_{ip}-3p_{PM} $	8	-6.73	-0.01	-9.89	0.00
$N_{ip}+3p_{PM}$	28	3.44	0.01	3.63	0.07
$N_{os}+p_{PM}$	18	-	-	-	-
$ N_{os}-p_{PM} $	6	-	-	-	-
SUM	-	93.42	~100	94.69	99.82



(a) Outer air-gap (Base torque is the outer air-gap average torque of each machine, respectively.)



(b) Inner air-gap (Base torque is the inner air-gap average torque of each machine, respectively.)

Fig. 6.6. Air-gap average electromagnetic torque proportion of main harmonics.

Table 6.4 Contribution of Main Air-Gap Field Harmonics to Average Electromagnetic Torque in MG Machines (%)

Harmonic Order		STPM		RTPM	
		Outer	Inner	Outer	Inner
p_{PM}	22	-6.87	99.85	-6.98	99.83
$N_{ip-p_{PM}}$	4	99.17	0.01	98.04	-0.04
$N_{ip+p_{PM}}$	48	-1.53	0.00	-1.92	0.04
$3p_{PM}$	66	0.03	-0.01	0.01	0.02
$ N_{ip-3p_{PM}} $	40	0.47	0.00	0.59	-0.00
$N_{ip+3p_{PM}}$	92	-0.03	-0.00	-0.06	-0.00
$N_{os+p_{PM}}$	34	7.06	0.07	6.59	0.08
$ N_{os-p_{PM}} $	10	0.20	-0.05	0.12	-0.05
SUM	-	98.51	99.87	96.39	99.88

6.3 Electromagnetic Performance

In the foregoing analysis, it is found that the PS-FRPM machine and the MG machine have the same operation principle, operating based on the modulation effect of iron pieces to open-circuit PM and armature excitation MMFs. In this section, the electromagnetic performance of PS-FRPM and MG machines operating in both STPM and RTPM modes will be comparatively analysed. Their design parameters are shown in Table 6.5, of which the parameters can be referred in the linear illustration shown in Fig. 6.7. Parameters from N_{os} to l_{otbs} in Table 6.5 are fixed for each machine, whilst those from R_{oy} to θ_{ipo} are optimized for the highest average electromagnetic torque with a fixed copper loss $p_{cu}=20W$, under zero d -axis current control, *i.e.* phase current and phase back-EMF have the same phase angle. It should be noted that in the optimization the PM volume is fixed as 13414.6mm^3 , similar to the PS-FRPM-STPM machine in [ZHU15a].

Table 6.5 Design Parameters of PS-FRPM and MG Machines

Parameters	Unit	PS-FRPM		MG	
		STPM	RTPM	STPM	RTPM
Operation modes	-	STPM	RTPM	STPM	RTPM
Stack length, L_s	mm	25			
Winding body outer radius, R_{oo}	mm	45			
PM body inner radius, R_{ii}	mm	10.4			
Outer air-gap width, g_o	mm	0.5			
Inner air-gap width, g_i	mm	0.5			
Winding body tooth tip top length, l_{ott}	mm	0.5			
Winding body tip bottom length, l_{otb}	mm	2			
Winding body yoke radius, R_{oy}	mm	43	42.5	43.5	43.5
Winding body inner radius, R_{oi}	mm	31	32	34	33.5
Iron piece inner edge radius, R_{ipi}	mm	26.5	27	32	31.5
Winding body tooth arc, θ_{ot}	°	7	9	5	5
Winding body tooth tip arc, θ_{otip}	°	3	4	8	8
Iron piece outer edge arc, θ_{ipo}	°	23	23	11	11
Iron piece inner edge arc, θ_{ipi}	°	24	26.5	8.5	8.5
PM remanence, B_{rPM}	T	1.2			
PM relative permeability, μ_{rPM}	-	1.05			
PM bulk conductivity, κ_{PM}	s/m	625000			

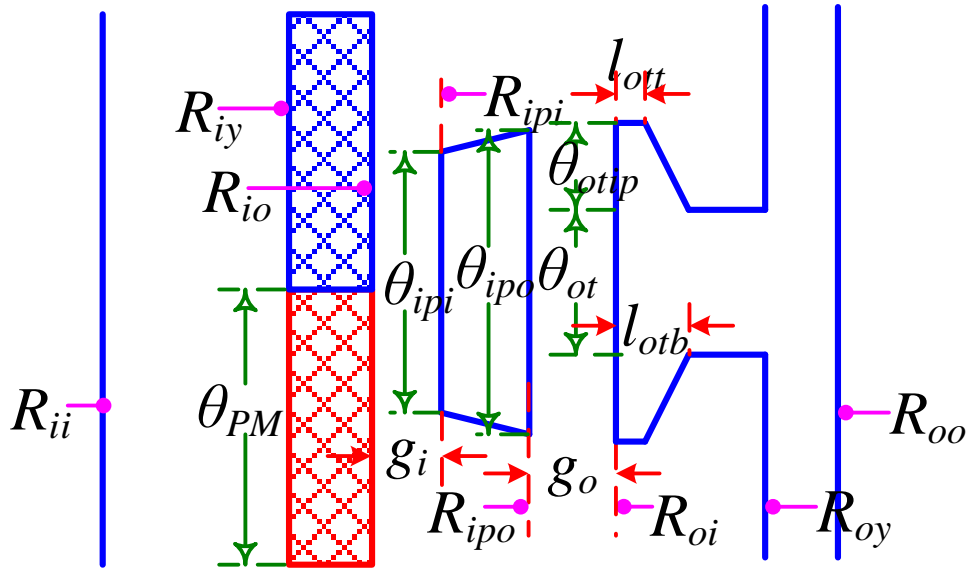
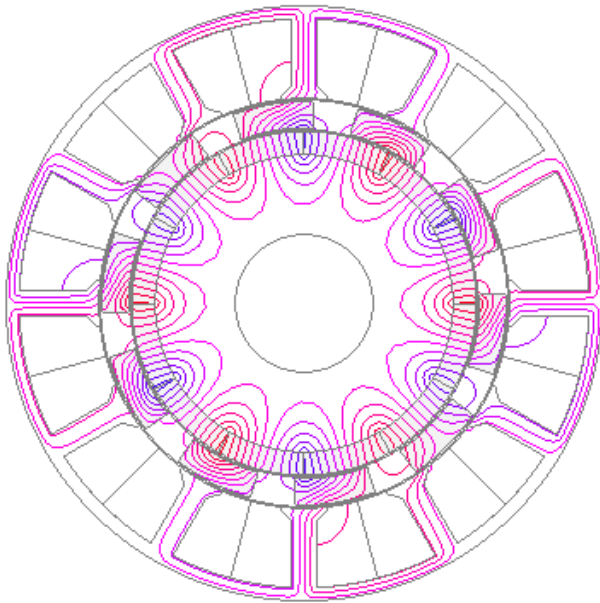


Fig. 6.7. Illustration of design parameters in PS-FRPM and MG machines.

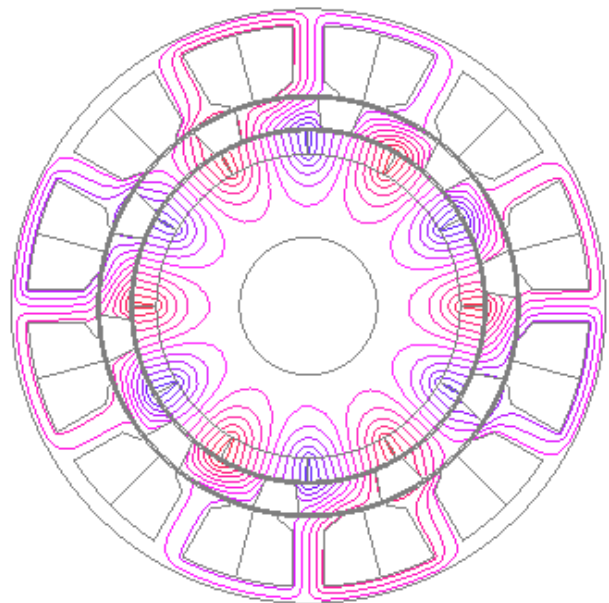
6.3.1 Open-circuit flux-linkage and back-EMF

Fig. 6.8 illustrates the open-circuit flux distribution at d -axis rotor position. Compared with the PS-FRPM machines, the MG machines suffer from more severe flux-leakage between iron pieces and PMs, of which the corresponding flux line does not cross armature teeth. This is due to higher iron piece number and also PM pole-pair number. As a consequence, the MG-STPM and MG-RTPM machines have lower phase flux-linkages, as shown in Fig. 6.9.

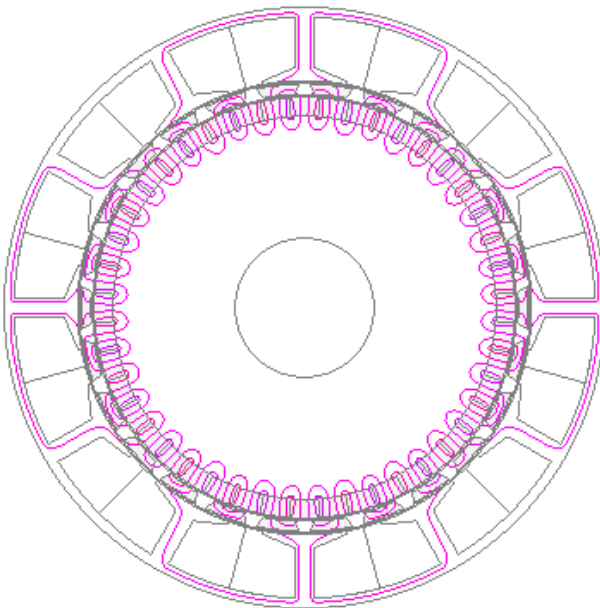
However, due to higher iron piece number and also PM pole-pair number, the MG-STPM and MG-RTPM machines exhibit larger fundamental phase back-EMFs than the PS-FRPM-STPM and PS-FRPM-RTPM machines, respectively, as shown in Fig. 6.10, even the fundamental phase back-EMFs in the MG-STPM machine is higher than the PS-FRPM-STPM machine. More importantly, it can be observed that the PS-FRPM-STPM machine has larger fundamental phase back-EMF than the PS-FRPM-RTPM machine, although the flux-linkage of the PS-FRPM-STPM machine is even lower. This is due to that the 66.67% higher electric frequency in the PS-FRPM-STPM machine than the PS-FRPM-RTPM machine, as $N_{ip} > p_{PM}$. Similar trend can be observed between the MG-STPM and MG-RTPM machines. However, the electric frequency in the MG-STPM machine is only 18.2% higher than the MG-RTPM machine.



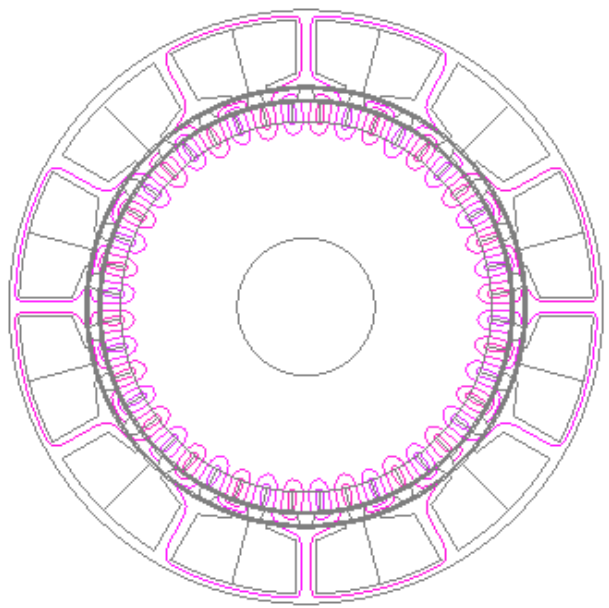
(a) PS-FRPM-STPM



(b) PS-FRPM-RTPM



(c) MG-STPM



(d) MG-RTPM

Fig. 6.8. Open-circuit flux distributions at d -axis rotor position ($-7\text{mWb/m} \sim 7\text{mWb/m}$).

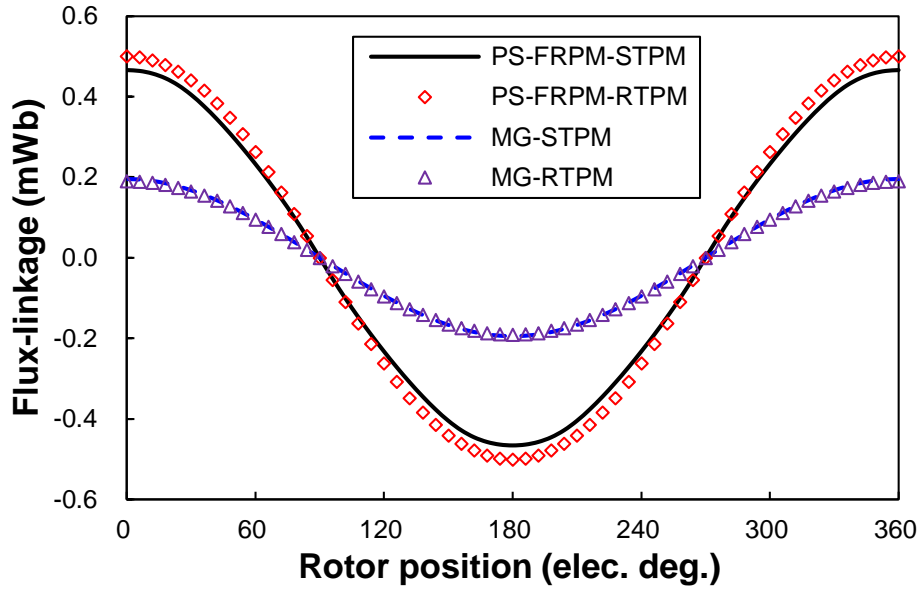
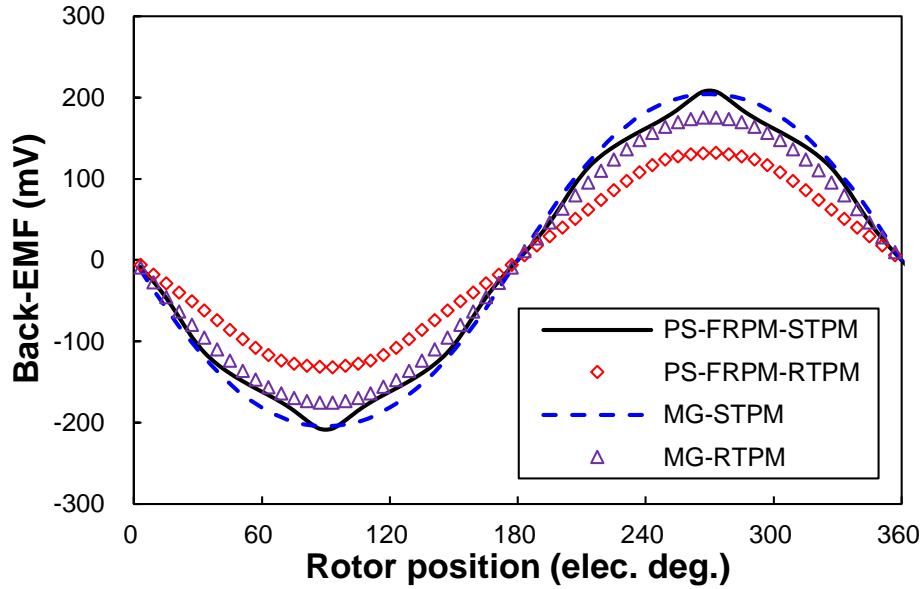
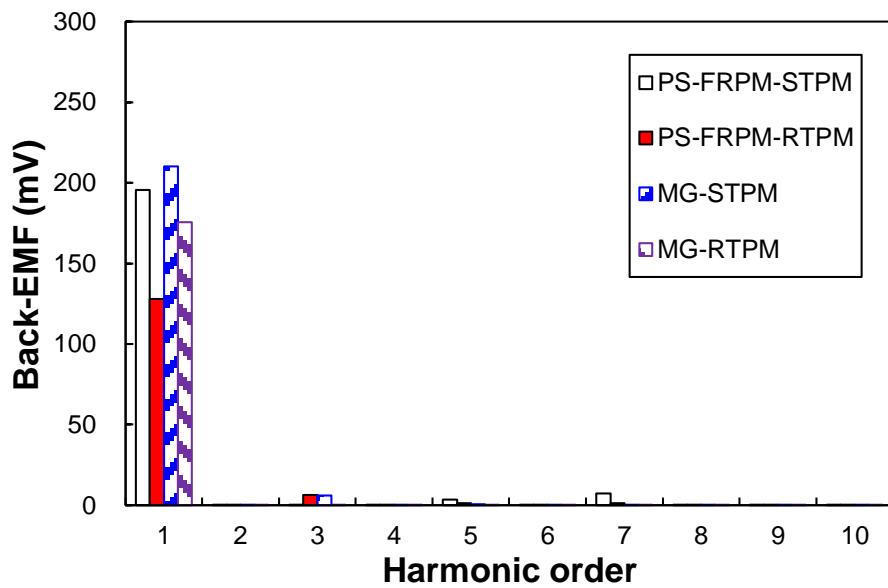


Fig. 6.9. Open-circuit phase A flux-linkage waveforms ($N_c=1$).

As shown in (6.1), N_{ip} is typically larger than p_{PM} . Therefore, for obtaining a higher phase back-EMF and hence electromagnetic torque, not only smaller iron piece number and PM number are needed to reduce the flux-leakage, but also a STPM type machine is recommended to enhance the electric frequency.



(a) Waveforms



(b) Spectra

Fig. 6.10. Open-circuit phase A back-EMFs ($N_c=1$, 400rpm).

6.3.2 Torque characteristics

On-load average electromagnetic torque versus current angle for the four analysed machines are illustrated in Fig. 6.11. It can be observed that the reluctance torque of all these machines are negligible due to similar d - and q -axis inductances L_d and L_q , which will be shown later. Therefore, zero d -axis current control, *i.e.* phase current and phase back-EMF have the same

phase angle, is applied to all of them, in brushless AC mode. The rated on-load electromagnetic torque waveforms with same copper loss $p_{cu}=20\text{W}$ are comparatively shown in Fig. 6.12, of which the characteristics are listed in Table 6.6. Generally, the STPM machines have higher torque density than their RTPM counterparts for both the PS-FRPM and MG machines, due to the higher fundamental phase back-EMF caused by $N_{ip}>p_{PM}$. However, the MG-RTPM machine has the smallest torque ripple. The PS-FRPM-RTPM machine exhibits the worst torque characteristics, *i.e.* the lowest average torque and the largest torque ripple due to unbalanced magnetic circuit. In Table 6.6, the torque ripple T_r is defined as,

$$T_r = \frac{T_{max} - T_{min}}{T_{avg}} \times 100\% \quad (6.12)$$

where T_{max} , T_{min} and T_{avg} are the maximum, minimum, and average electromagnetic torque, respectively.

Fig. 6.13 shows the average electromagnetic torque versus copper loss. It can be observed that within the whole copper loss range, the PS-FRPM-STPM machine exhibits the highest torque density, whilst the PS-FRPM-RTPM machine suffers from the smallest values. Although the PS-FRPM-STPM machine suffers from 6.98% lower fundamental phase back-EMF than the MG-STPM machine, as shown in Fig. 6.10, the torque density is slightly higher by 1.81%. This is due to the 19.39% larger half slot area in PS-FRPM-STPM machine than the MG-STPM machine, *i.e.* 76.65mm^2 and 91.51mm^2 . More importantly, the average torque difference between the PS-FRPM-STPM and MG-STPM machines becomes higher with copper loss, since the MG-STPM having thinner iron piece is easier to be saturated.

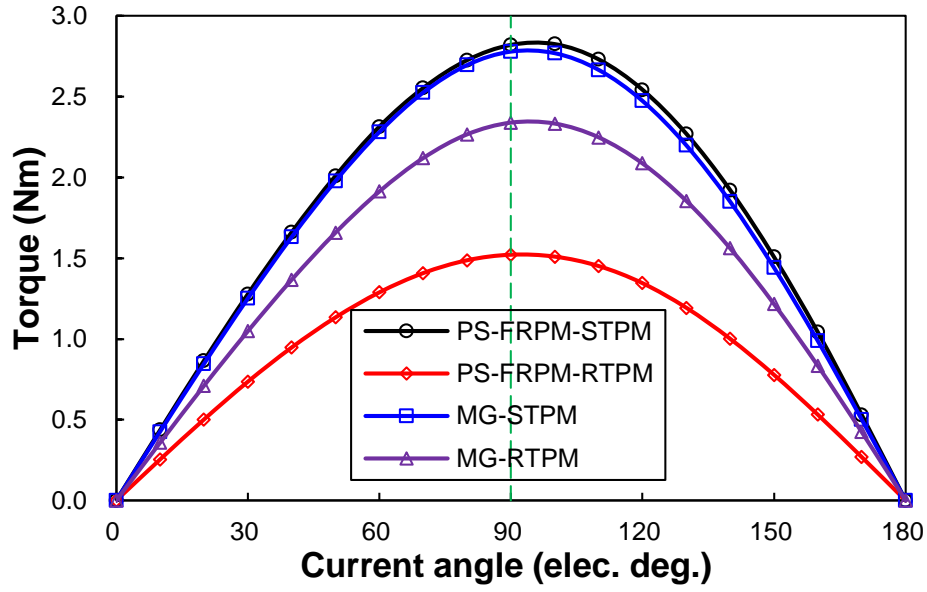


Fig. 6.11. Average torque versus current angle (BLAC, $p_{cu}=20W$).

Table 6.6 On-Load Torque Characteristics of MG Machines

Item	Unit	PS-FRPM		MG	
		STPM	RTPM	STPM	RTPM
T_{avg}	Nm	2.82	1.52	2.77	2.34
T_{max}	Nm	3.09	1.80	2.91	2.37
T_{min}	Nm	2.56	1.25	2.62	2.30
T_r	%	18.56	35.92	10.43	3.01

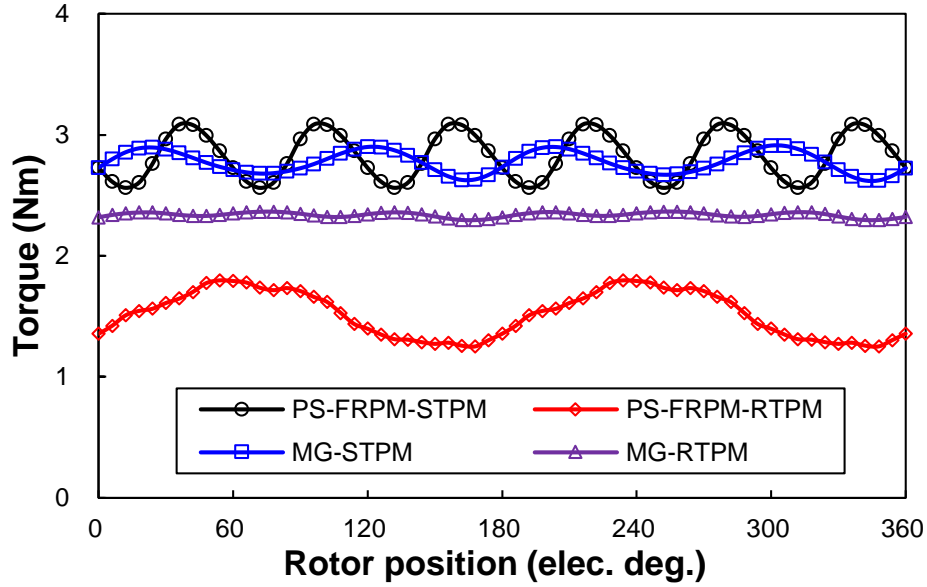


Fig. 6.12. On-load electromagnetic torque waveforms (BLAC, phase current and phase back-EMF have the same phase angle, $p_{cu}=20W$).

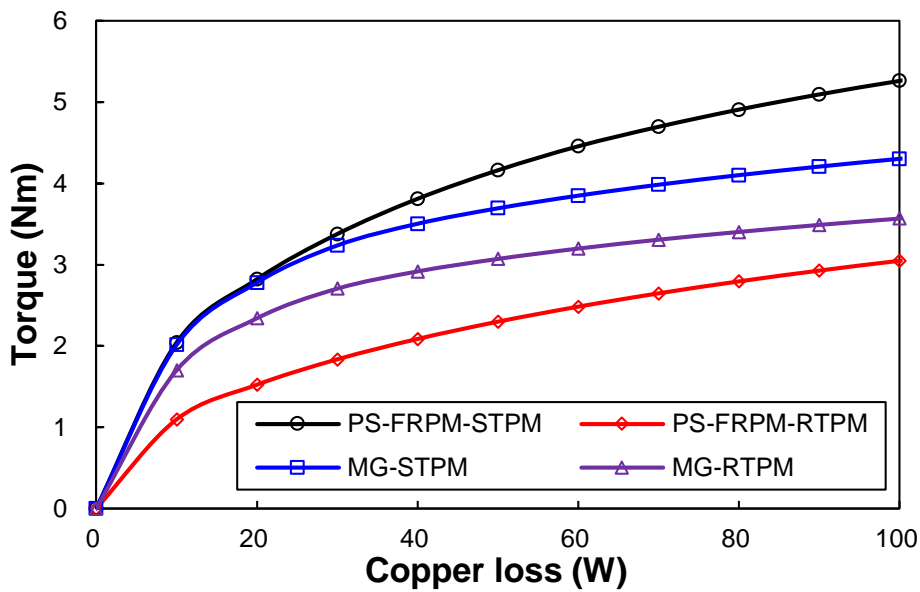


Fig. 6.13. Average electromagnetic torque versus copper loss (BLAC, phase current and phase back-EMF have the same phase angle).

6.3.3 Loss and efficiency

Fig. 6.14 and Fig. 6.15 show the iron loss and PM eddy current loss versus rotor speed, respectively. Due to higher electric frequency, the MG-STPM and MG-RTPM machines suffer from higher iron loss p_{ir} than the PS-FRPM-STPM and PS-FRPM-RTPM machines. However, the PM eddy current loss p_{PMe} of the MG-STPM and MG-RTPM machines are smaller than the

PS-FRPM-STPM and PS-FRPM-RTPM machines. This is due to the smaller PM bulk volume in the MG-STPM and MG-RTPM machines having higher PM pole-pair number. It is worth noting that, when the rotor speed is 400rpm, both the iron loss p_{ir} and the PM eddy current loss p_{PM} are much smaller than the copper loss $p_{cu}=20W$. This is why in the optimization, the iron loss and PM eddy current loss is not accounted. In Fig. 6.14, the iron loss is calculated by FE software Ansys/Maxwell based on equation (4.8).

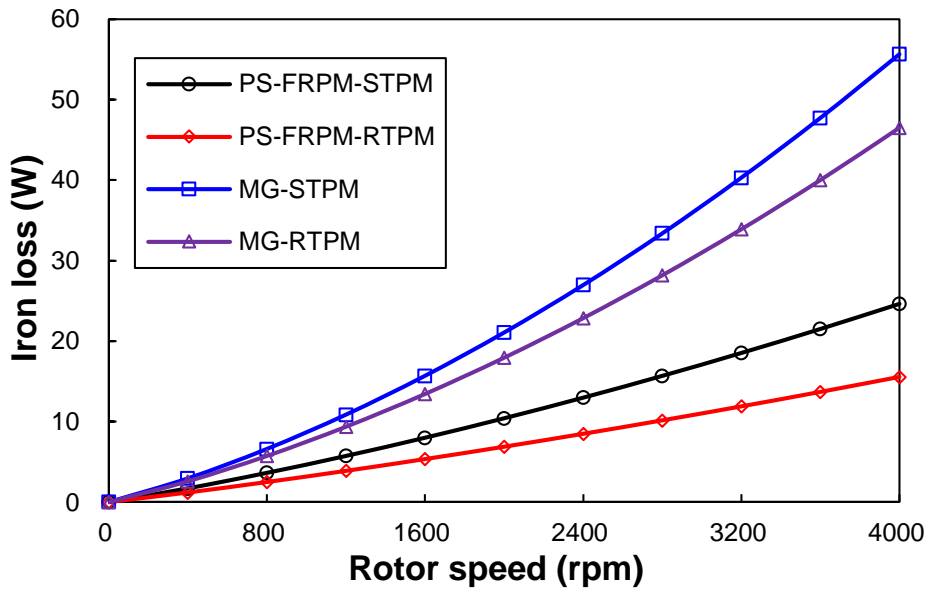


Fig. 6.14. Iron loss versus rotor speed.

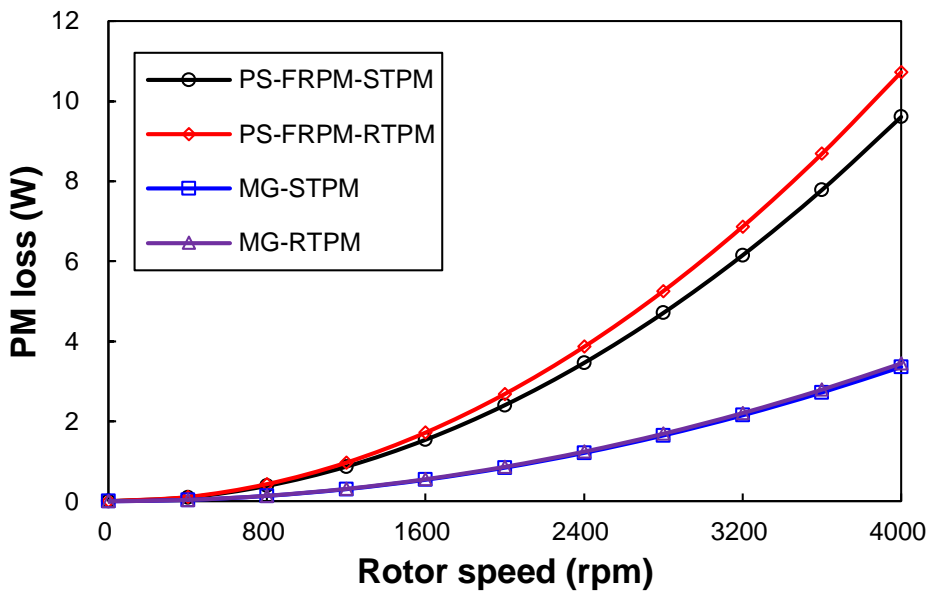


Fig. 6.15. PM eddy current loss versus rotor speed.

Table 6.7 Torque, Loss, Efficiency Characteristics of PS-FRPM and MG Machines at 400rpm

Item	Unit	PS-FRPM		MG	
		STPM	RTPM	STPM	RTPM
Operation mode	-	STPM	RTPM	STPM	RTPM
T_{avg}	Nm	2.82	1.52	2.77	2.34
P_{EM}	W	118.3	63.6	116.2	98.0
p_{ir}	W	1.7	1.2	2.9	2.6
p_{PMe}	W	0.096	0.107	0.034	0.034
P_{out}	W	116.5	62.3	113.2	95.4
T_{out}	Nm	2.78	1.49	2.70	2.28
V	mm ³	159043			
P_{out}/V	W/m ³	732665	391960	712025	599587
T_{out}/V	Nm/m ³	17491	9357	16998	14314
p_{cu}	W	20			
P_{in}	W	138.3	83.6	136.2	118.0
η	%	84.24	74.53	83.13	80.83

Table 6.7 lists torque, loss, efficiency characteristics of the analysed four machines at 400rpm. Generally, the STPM machines can exhibit higher torque density and efficiency than the RTPM machines, in spite of larger iron loss due to higher electric frequency. The power density of the PS-FRPM-STPM and MG-STPM machines can reach 732665 and 712025 W/m³, respectively. In Table 6.7, T_{avg} is the average electromagnetic torque. P_{EM} is the average electromagnetic power. P_{out} and T_{out} are the average output torque and power, respectively. V is the machine volume. It is worth noting that the efficiency η in Table 6.7 is calculated based on (4.9).

6.3.4 Winding inductances

Table 6.8 lists self-inductance and mutual-inductance of the four MG machines. They have similar mutual-inductance, whilst the PS-FRPM-STPM machine has smaller self-inductance than the others three machines, as well as d - and q -axis inductances. As shown in Table 6.8, in all the four analysed machines, d - and q -axis inductances are similar and hence the reluctance torques are negligible, as shown in Fig. 6.11. This is due to the d - and q -axis similar magnetic paths via iron pieces and inner PM body.

Table 6.8 Inductances PS-FRPM and MG Machines

Item	Unit	PS-FRPM		MG	
		STPM	RTPM	STPM	RTPM
Operation mode	-	STPM	RTPM	STPM	RTPM
Self-inductance, L_{AA}	mH	0.17	0.21	0.22	0.23
Mutual-inductance, M_{BA}	mH	-0.08	-0.09	-0.10	-0.10
Mutual-inductance, M_{CA}	mH	-0.08	-0.09	-0.10	-0.10
d -axis inductance, L_d	mH	0.23	0.30	0.33	0.33
q -axis inductance, L_q	mH	0.26	0.30	0.32	0.33

Based on the phasor diagram shown in Fig. 6.16 in which phase resistance voltage drop is neglected, the power factors of the four analysed machines can be calculated as the cosine value of the angle between U_{ph} and I , as listed in Table 6.9. In Fig. 6.16, E_{ph} is the open-circuit phase back-EMF. U_{ph} is the on-load phase terminal voltage. X_q is the q -axis reactance. I_q is the q -axis current. All of these parameters are in per unit (p.u.) value. As listed in Table 6.9, the PS-FRPM-STPM machine has similar power factor as its RTPM counterpart, and the MG-STPM and MG-RTPM machines have similar power factor as well. However, due to higher electric frequencies, the MG-STPM and MG-RTPM machines suffer from lower power factor. This makes challenges to the inverter power rating.

Table 6.9 Synchronous Reactance and Power Factor of PS-FRPM and MG Machines at 400rpm

Item	PS-FRPM		MG	
	STPM	RTPM	STPM	RTPM
Synchronous reactance	0.58	0.62	0.90	0.90
Power factor	0.81	0.78	0.45	0.43

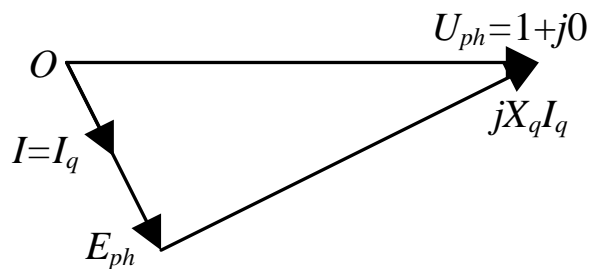
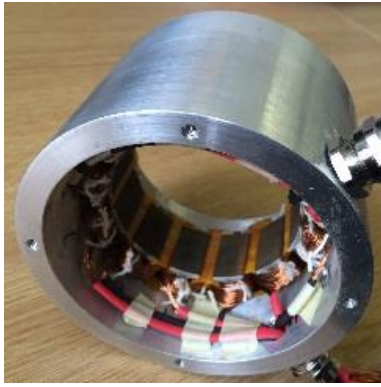


Fig. 6.16. Phasor diagram when phase current and phase back-EMF have the same phase angle.

6.4 Experimental Validation

In the foregoing analysis, electromagnetic performance of the PS-FRPM machine and the conventional MG machine operating in both STPM and RTPM modes are comprehensively compared by FE analyses. FE results show that the PS-FRPM machine operating in STPM mode exhibits the highest torque density, efficiency, and power factor. The experiment results of the PS-FRPM-STPM prototype machine have been reported in [ZHU15a]. Here, the MG-RTPM machine is built and the phase back-EMF, static torque, and winding inductances including both self- and mutual-inductances are tested. These measured results will be presented together with comparison to those of the PS-FRPM-STPM prototype to verify the FE predicted results.

Fig. 6.17 and Fig. 6.18 show the pictures of the two prototypes, respectively. Both prototypes are wound with number of turns per phase $N_{ac}=72$. It is worth noting that to ease manufacturing, the PM thickness is modified to 4mm in both machines. Also, for easier assembling the rotor iron pieces, an iron bridge of thickness $T_{bri}=0.5\text{mm}$ is introduced adjacent to the inner air-gap to connected iron pieces in both prototypes.



(a) Stator



(b) Static iron pieces



(c) Rotor

Fig. 6.17. Photos of MG-RTPM prototype machine.



(a) Outer stator



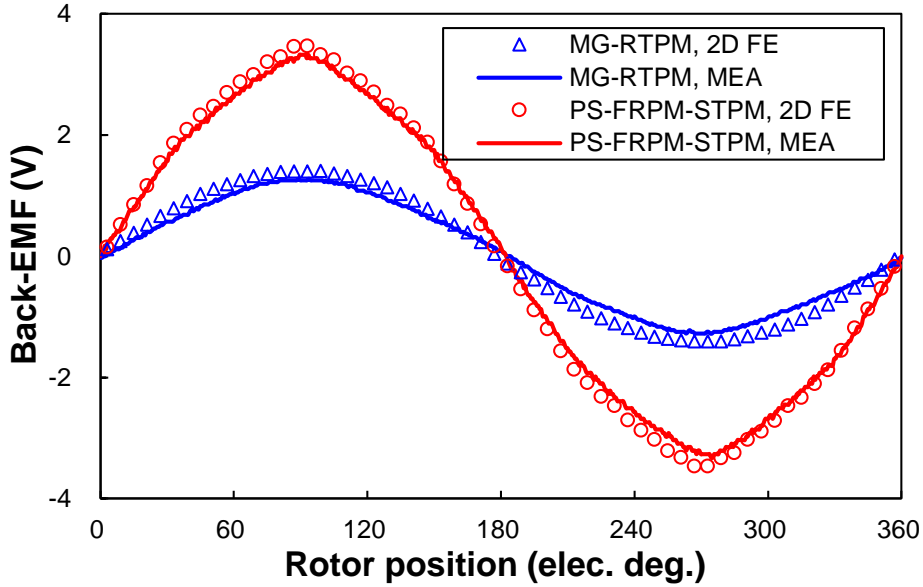
(b) Cup-rotor



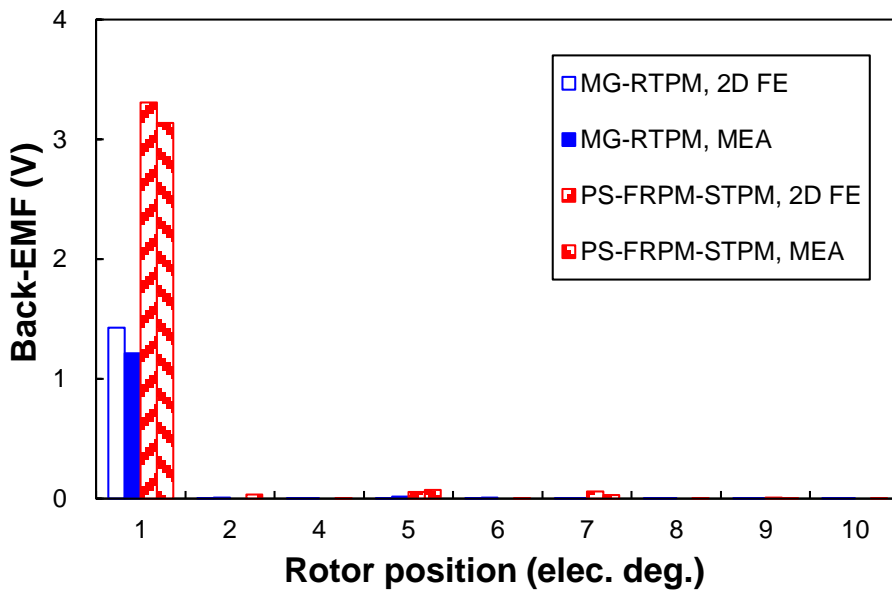
(c) Inner stator

Fig. 6.18. Photos of PS-FRPM-STPM prototype machine.

Fig. 6.19 show the comparison of the measured and 2D FE predicted phase back-EMFs, from which it can be observed that 2D FE predicted values are slightly lower than the measured ones due to end effect in both machines. As shown in Fig. 6.19, the measured phase back-EMF of the PS-FRPM-STPM prototype is more than twice of that of the MG-RTPM prototype. It is worth noting that the phase fundamental back-EMF dropped 53.83% in the MG-RTPM machine, due to the introduction of the 0.5mm iron bridge for the static iron pieces which is one third of the total thickness of iron pieces, *i.e.* 1.5mm.



(a) Waveform

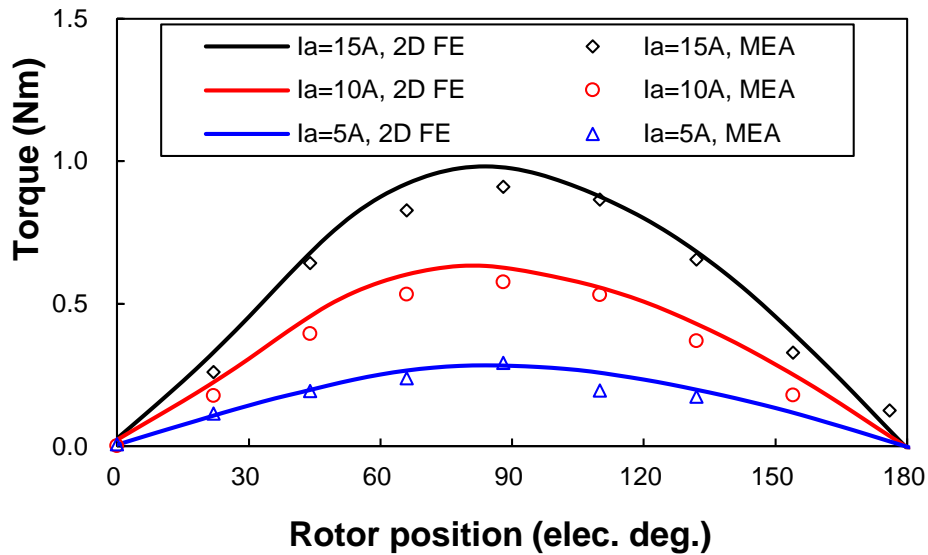


(b) Spectra

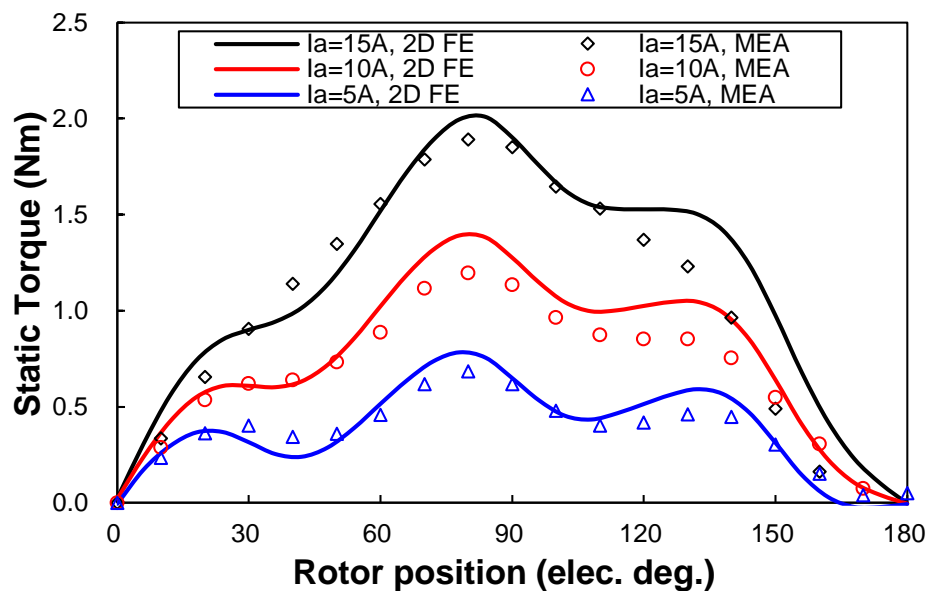
Fig. 6.19. Comparison of measured and FE predicted phase back-EMFs in MG-RTPM and PS-FRPM-STPM machines at 400rpm.

Fig. 6.20 shows the comparison of the measured and 2D FE predicted static torque waveforms. As for the peak static torque, the comparison between the measured and 2D FE predicted results under different phase A current I_A is shown in Fig. 6.21. Again, the 2D FE predicted and measured static torques agree well with each other, although the 2D FE predicted results are slightly smaller in both prototypes due to end effect. As shown in Fig. 6.20 and Fig.

6.21, the measured static torque of the PS-FRPM-STPM prototype is higher than that of the MG-RTPM prototype. Nevertheless, the MG-RTPM prototype is easier to be saturated than the PS-FRPM-STPM prototype, as predicted by FE in Fig. 6.13. It is worth noting that in the measurement of static torque, three-phase currents I_A , I_B , and I_C are set as $I_A = -2I_B = -2I_C$.



(a) MG-RTPM



(b) PS-FRPM-STPM

Fig. 6.20. Comparison of measured and FE predicted static torques ($I_A = -2I_B = -2I_C$).

The end-effect coefficient of two prototypes versus various phase A current I_A is shown in

Fig. 6.22, which is defined as the ratio of the measured peak static torque to the 2D FE predicted values. It is worth noting that, the end effect coefficient higher than 100% for the MG-RTPM machine at 5A is due to the eccentricity of the prototype which cause higher measured torque than the 2D predicted values, as shown in Fig. 6.20(a).

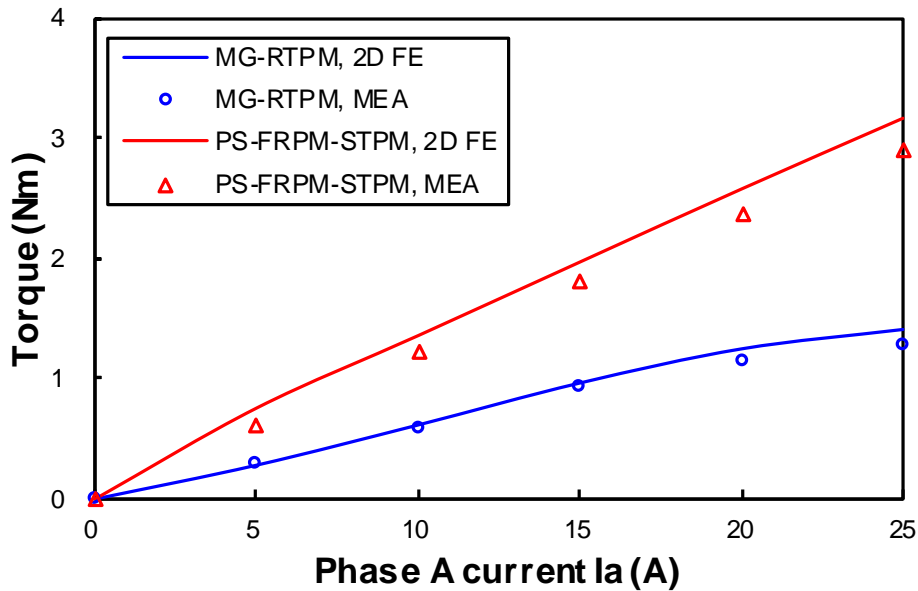


Fig. 6.21. Comparison of measured and FE predicted peak static torques versus various phase A current I_A ($I_A = -2I_B = -2I_C$).

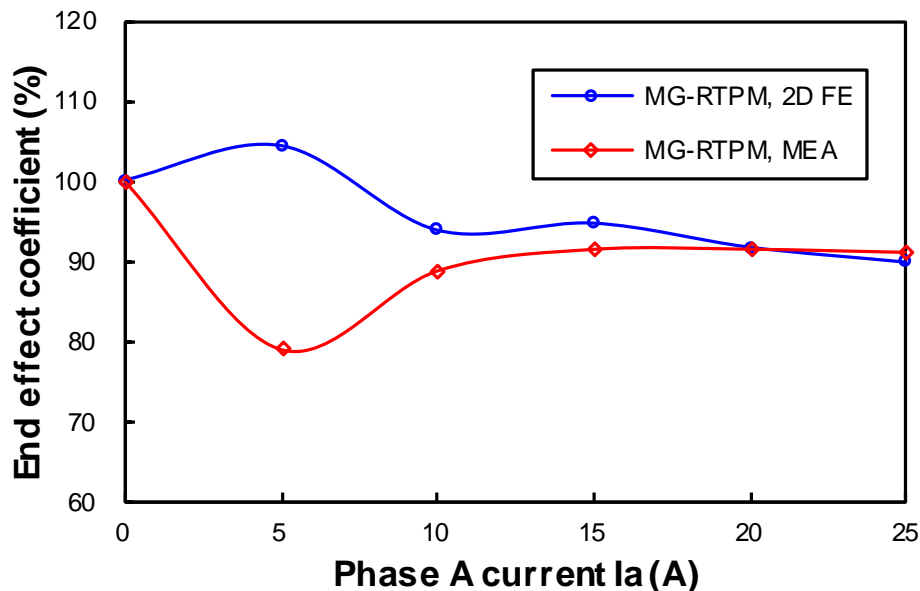


Fig. 6.22. Influence of phase A current I_A on end effect coefficient in two prototypes ($I_A = -2I_B = -2I_C$).

For the winding inductances including both self- and mutual-inductance, the comparison

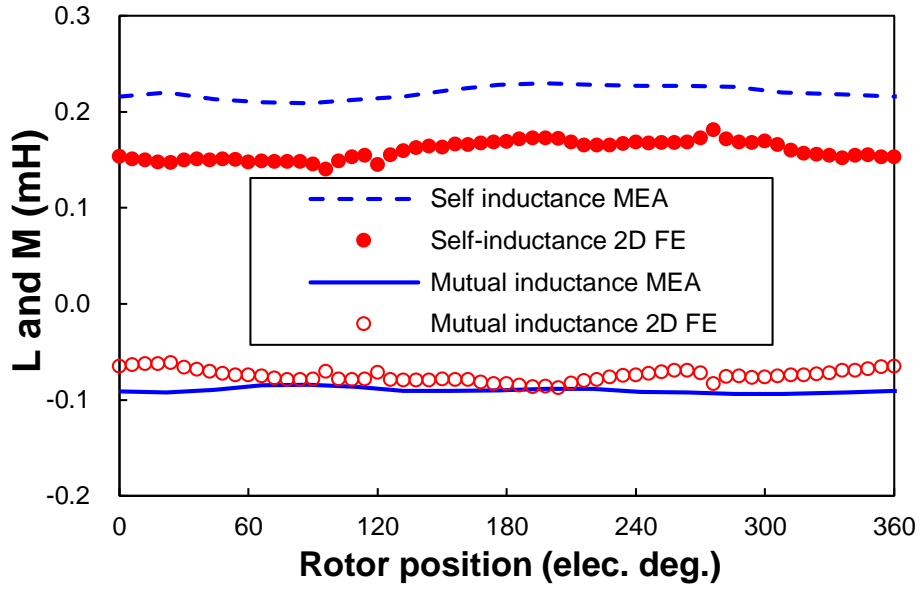
between the 2D FE predicted values and those measured by LCR meter are shown in Fig. 6.23. It is worth noting that the self-inductance shown in Fig. 6.23 is directly measured by the LCR meter, whilst the mutual-inductance between phase A and B, M_{BA} is calculated by,

$$M_{BA} = \frac{L_{A+B} - L_{AA} - L_{BB}}{2} \quad (6.13)$$

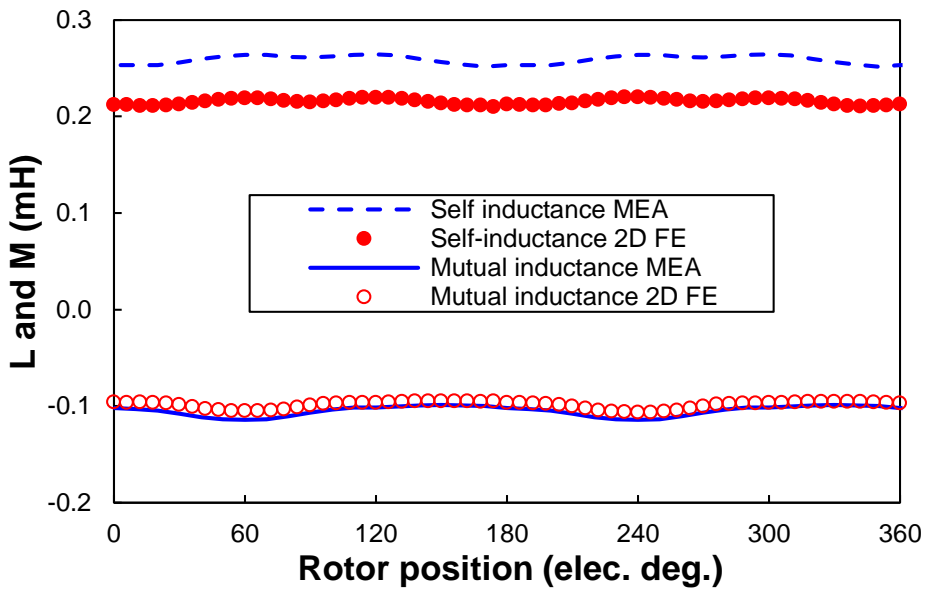
where L_{AB} is the measured self-inductance when the windings of phase A and phase B are serially connected. L_{AA} is the measured self-inductance of phase A winding. L_{BB} is the measured self-inductance of phase B winding.

As can be observed from Fig. 6.23, the mutual-inductance predicted by 2D FE and those calculated based on (6.13) agree well with each other in both prototypes. However, the 2D FE predicted self-inductance is slightly smaller than the measured one. This can be explained as follows. Since the 2D FE predicted self-inductance cannot account for the end winding inductance, it is slightly smaller than that measured by LCR meter. However, this influence can be eliminated based on (6.13) for the calculation of the mutual-inductance between phase A and B, M_{BA} . Therefore, the 2D FE predicted mutual-inductance and that calculated based on (6.13) agree well with each other in both prototypes.

It is worth noting that the FE predicted and measured inductances shown in Fig. 6.23 are obtained at a low phase current, i.e. 0.1A. The d - and q -axis inductances of both prototypes at rated condition are also tested based on the standstill frequency response method [WIE97a]. The d - and q -axis inductances L_d and L_q can be obtained as the values of the inductance L_{A-B} , i.e. the self-inductance when the windings of phase A and phase B are oppositely connected, at d - and q -axis positions, respectively [WIE97a]. As shown in Fig. 6.24, the measured inductance L_{A-B} is slightly higher than the 2D FE predicted values again in both prototypes due to the end winding inductance, and hence L_d and L_q .



(a) MG-RTPM



(b) PS-FRPM-STPM

Fig. 6.23. Comparison of 2D FE predicted and measured inductances.

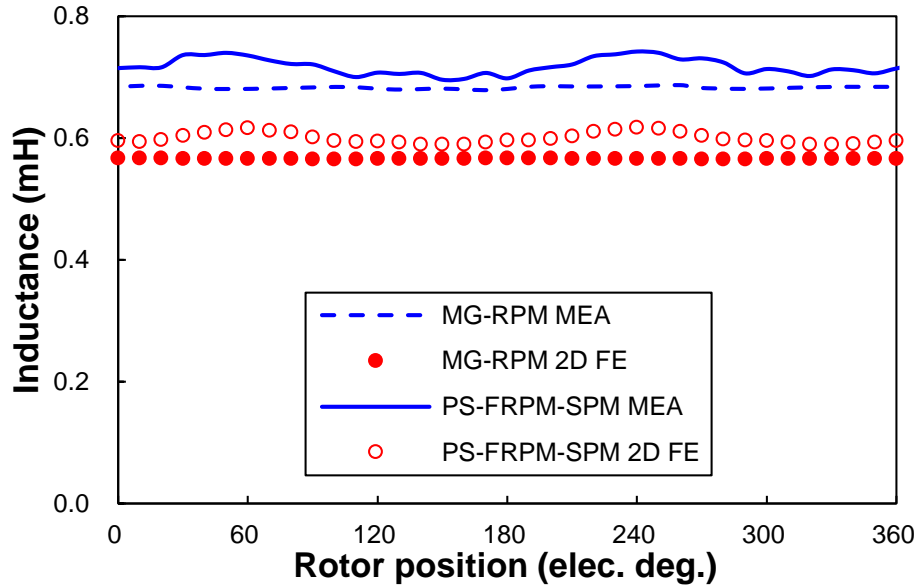


Fig. 6.24. Comparison of 2D FE predicted and measured inductances L_{A-B} .

6.5 Conclusions

The PS-FRPM and MG machines operating in STPM and RTPM modes are comparatively analysed in this paper. It is found that in both the PS-FRPM and MG machines, the STPM machine has higher phase back-EMF and hence torque density than its RTPM counterpart, due to higher electric frequency. However, higher iron piece number and PM pole-pair number cause higher synchronous reactance and lower power factor in the MG-STPM and MG-RTPM machines, as well as larger iron loss and hence lower efficiency. Overall, the PS-FRPM machine operating in STPM mode has the highest torque density within the whole copper loss range, the highest efficiency and also the largest power factor. It is also found that to reduce the flux-leakage in a MG machine for obtaining a larger electromagnetic torque and a higher power factor, smaller iron piece number and PM number are preferred. Also, a STPM type machine is recommended to enhance the electric frequency, and hence phase back-EMF and electromagnetic torque.

7 General Conclusions and Future Work

7.1 Summary

In this thesis, the operation and interaction mechanisms between the open-circuit and armature excitation magnetomotive forces (MMFs) in the conventional single-stator-PM machines are firstly explained as the magnetic gearing effect. It is found that the conventional single-stator-PM machines operate based on the magnetic gearing effect, similar to magnetic gears and magnetically geared (MG) machines. It is also found that similar to the magnetic gears and MG machines, as well as the conventional single-stator-PM machines, the partitioned-stator-PM machines also operate based on the magnetic gearing effect.

Based on the magnetic gearing effect in the partitioned-stator-PM machines, consequent-pole PM topology and overlapping armature winding topology are applied to reduce the PM volume and obtain more sinusoidal armature excitation MMF, respectively. Compared with the surface-mounted PM topology, the partitioned stator flux reversal PM (FRPM) (PS-FRPM) machines having consequent-pole PMs can save $\sim 1/3$ PM volume, whilst the torque density and efficiency are similar. As for the PS-FRPM machine with overlapping armature windings, it exhibits smaller iron loss and PM eddy current loss due to more sinusoidal armature excitation MMF, larger open-circuit fundamental phase flux-linkage and back-EMF and hence higher torque density, higher efficiency, etc.

Comparative analysis between the PS-FRPM machine and the conventional MG machine both of which have surface-mounted PMs show that the PS-FRPM machine operating at static PM (STPM) mode has higher torque density within the whole copper loss range, higher efficiency and also larger power factor than the MG machine operating in rotating PM (RTPM) mode. It is also found that to reduce the flux-leakage in a MG machine for obtaining a larger electromagnetic torque and a higher power factor, smaller iron piece number and PM number are preferred. Also, a STPM type machine is recommended to enhance the electric frequency, and hence phase back-EMF and electromagnetic torque.

7.2 Magnetic Gearing Effect in Single- and Partitioned-Stator-PM Machines

Based on a simple MMF-permeance model, the pole-pair numbers and rotating speeds of the open-circuit and armature excitation air-gap fields in switched flux PM (SFPM) machines are

analytically obtained and verified by finite element analysis. Based on the analysis of open-circuit and armature excitation air-gap fields, it is found that similar to magnetic gears and MG machines, SFPM machines operate based on the modulation effect of the rotor to the open-circuit and armature excitation MMFs. After modulation, the open-circuit and armature excitation air-gap field harmonics are multi-synchronised, generating average electromagnetic torque in the air-gap. It is also found that more than 95% of the average electromagnetic torque in SFPM machines having N_r -pole rotor and p_{PM} -pole-pair PMs are contributed by the dominant rotating air-gap field harmonics with the same pole-pair number of $|kN_r \pm (2i-1)p_{PM}|$ ($k=1, i=1, 2, 3$) and static air-gap field harmonics with the same pole-pair number of $(2i-1)p_{PM}$ ($i=1, 2, 3$). The analysis is also applicable for other types of stator-excitation machines.

Similarly, based on the analysis of the open-circuit and armature excitation air-gaps field harmonics, it is found that the partitioned stator PM machines also operate based on the magnetic gearing effect. The modulation of the rotor iron pieces to the open-circuit and armature excitation MMFs is similar to magnetic gears and MG machines, as well as the single-stator-PM machines. It is also found that more than 93% of the electromagnetic torques in the PS-SFPM machines having N_r -pole rotor and p_{PM} -pole-pair PMs generated in both the outer and inner air-gaps is contributed by the dominant rotating field harmonics in open-circuit and armature excitation fields with the same pole-pair number of $|kN_r \pm (2i-1)p_{PM}|$ ($k=1, i=1, 2, 3$) and static field harmonics with the same pole-pair number of $(2i-1)p_{PM}$ ($i=1, 2, 3$).

7.3 Partitioned Stator Flux Reversal PM Machines

Based on the magnetic gearing effect in the conventional single-stator-PM machines, PMs and armature windings in FRPM machines are separately placed in the inner and outer stators, respectively, forming PS-FRPM machines having higher torque density than the conventional single stator FRPM machines. As the partition-stator-PM machines also operate based on the magnetic gearing effect, consequent-pole pole PM topology and overlapping armature winding topology are applied in partitioned-stator-PM machines to reduce the PM volume and obtain more sinusoidal armature excitation MMF, respectively. They are summarized and compared as follows.

7.3.1 Basic topology having surface-mounted PMs and non-overlapping armature windings

As for the basic topology of PS-FRPM machines having surface-mounted PM and non-overlapping armature windings, they can exhibit higher torque density than the conventional single stator FRPM machines having surface-mounted PMs and non-overlapping armature windings, which can be referred to the Appendix B. The investigation of the influence of rotor pole numbers in a 12-stator-pole PS-FRPM machine shows that amongst the 12/10-, 12/11-, 12/13- and 12/14-stator/rotor-pole PS-FRPM machines, the 11-rotor-pole and 13-rotor-pole machines exhibit larger back-EMF and hence electromagnetic torque as well as lower cogging torque and torque ripple, albeit with potentially higher unbalanced magnetic force due to odd rotor pole numbers. In addition, the investigation of the influence of leading design parameters shows that in PS-FRPM machines electromagnetic torque increases and saturates with the PM thickness, whilst for the conventional FRPM machines, there will be an optimal PM thickness for the maximum torque.

7.3.2 Developed topology having consequent-pole PMs and non-overlapping armature windings

As for the developed PS-FRPM machine having consequent-pole PMs and non-overlapping armature windings, they have $\sim 1/3$ less PM volume but similar torque density and efficiency, compared to those with basic topologies having surface-mounted PMs. The investigation of the influence of different stator/rotor pole combinations on electromagnetic performance shows that the 12-stator-pole PS-FRPM machine having 10-, 11-, 13- and 14-rotor-pole with consequent-pole PMs can generate 98.59%, 96.69%, 95.50% and 97.15% torque density of their corresponding surface-mounted PMs counterparts, respectively, whilst the PM volume can be saved by 28.33%, 30%, 30% and 33.33%, respectively. The PS-FRPM machines with consequent-pole PMs can exhibit less than 1% lower efficiency than their corresponding surface-mounted PM counterpart.

7.3.3 Developed topology having surface-mounted PMs and overlapping armature windings

Compared with the basic topology having surface-mounted PMs and non-overlapping armature windings, the developed PS-FRPM machine having surface-mounted PMs and overlapping armature windings has smaller iron loss and PM eddy current loss, due to the more

sinusoidal armature excitation MMF. The overlapping PS-FRPM machine also has larger open-circuit fundamental phase flux-linkage and back-EMF and hence torque density, higher self-inductance and lower mutual inductance, and hence a higher self/mutual-inductance ratio and better capability to restrict the short-circuit current, larger d -axis inductance but similar higher PM flux-linkage, and hence higher flux-weakening capability. However, the overlapping PS-FRPM machine suffers from larger end winding thickness and hence larger total copper loss when the machine stack length is short. However, when the stack length is longer, the influence of the end-winding will be smaller.

7.3.4 Comparison of conventional FRPM machine and PS-FRPM machines with basic topology and developed topologies

Fig. 5.16 show the average torque compasion for the 12/10-pole conventional single stator FRPM machine having surface-mounted PMs and non-overlapping armature windings, PS-FRPM machines having surface-mounted PMs and non-overlapping armature windings referred to Appendix B, consequent-pole PMs and non-overlapping armature windings (CPM) analysed in Chapter 4, and surface-mounted PMs and overlapping armature windings analysed in Chapter 5. As shown in Fig. 5.16 and listed in Table 4.4, all the PS-FRPM machines with the basic topology and the developed topology have more than 84.5% higher torque density when they have the same PM volume 13414.6 mm^3 . As for the three PS-FRPM machines, their torque densities are similar, even in the whole copper loss range as shown in Fig. 7.2. However, it is worth noting that compared with the basic topology, the PM volume can be saved by $\sim 1/3$ in the consequent-pole PM counterpart. As for the ovaerlapping counterpart, it has more sinsoidal armature excitation MMF and hence smaller losses and higher efficiency, higher self/mutual-inductance ratio and better capability to restrict the short-circuit current, higher flux-weakening capability.

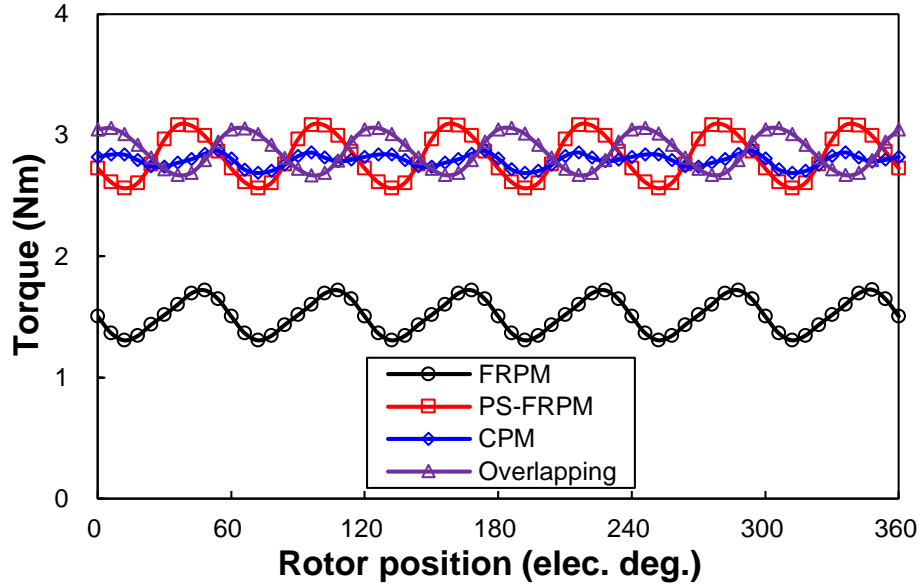


Fig. 7.1. Comparison of average torque for the 12/10-pole conventional single stator FRPM machine having surface-mounted PMs and non-overlapping armature windings (FRPM), PS-FRPM machines having surface-mounted PMs and non-overlapping armature windings (PS-FRPM), consequent-pole PMs and non-overlapping armature windings (CPM), and surface-mounted PMs and overlapping armature windings (overlapping) having same PM volume ($p_{cu}=20W$, BLAC, phase current and phase back-EMF have the same phase angle).

Table 7.1 Comparison of Torque Characteristics for the Four Machines in Fig. 5.16

Item	Unit	FRPM	PS-FRPM	CPM	Overlapping
Average Torque, T_{avg}	Nm	1.51	2.83	2.79	2.87
Maximum Torque, T_{max}	Nm	1.72	3.10	2.87	3.06
Minimum Torque, T_{min}	Nm	1.31	2.56	2.69	2.67
Torque ripple, T_r	%	27.65	18.95	6.62	13.71

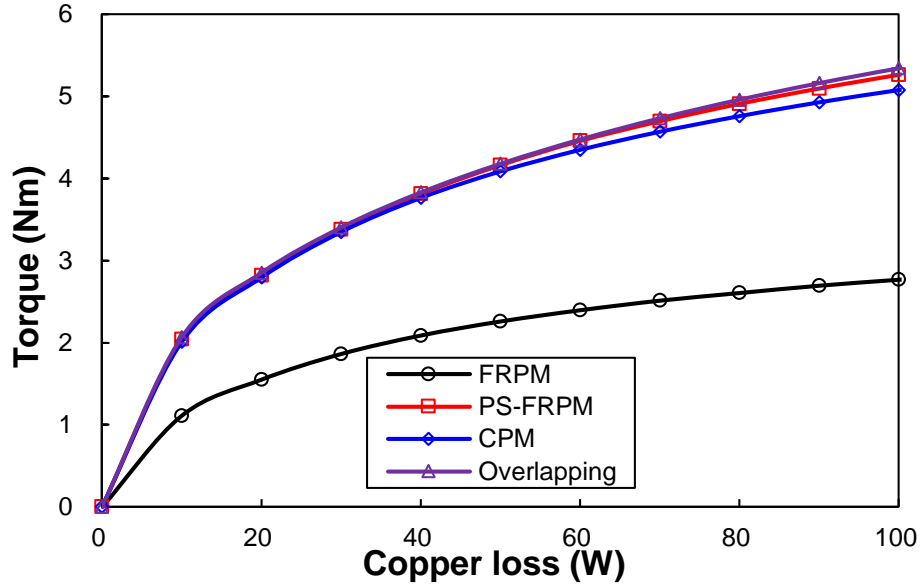


Fig. 7.2. Comparison of torque versus copper loss for the 12/10-pole conventional single stator FRPM machine having surface-mounted PMs and non-overlapping armature windings (FRPM), PS-FRPM machines having surface-mounted PMs and non-overlapping armature windings (PS-FRPM), consequent-pole PMs and non-overlapping armature windings (CPM), and surface-mounted PMs and overlapping armature windings (overlapping) having same PM volume (BLAC, phase current and phase back-EMF have the same phase angle).

7.4 Future Work

As for the stator-PM machines including both the single-stator-PM and partitioned-stator-PM machines, based on the analysed magnetic gearing effect, the proposed future research includes:

- The parasitic effect contribution of the air-gap field harmonics;
- Influence of gear ratio on the electromagnetic performance;
- Investigation of new machine topologies based on magnetic gearing effect.

Specifically, the partitioned-stator-PM machines suffer from the high manufacturing cost due to the two air-gaps and the cup rotor. Further research on reducing the manufacturing cost of the partitioned-stator-PM machines can be conducted. More importantly, the research on stress analysis of the rotor iron pieces and the effort to reduce the force can be conducted, which is also beneficial for manufacturing.

References

- [ABB10a] M. Abbasian, M. Moallem, and B. Fahimi, "Double-stator switched reluctance machines (DSSRM): fundamentals and magnetic force analysis," *IEEE Trans. Energy Convers.*, vol. 25, no. 3, pp. 589-597, Sep. 2010.
- [ABD14a] S. E. Abdollahi, and S. Vaez-ZAdeh, "Back EMF analysis of a novel linear flux switching motor with segmented secondary," *IEEE Trans. Magn.*, vol. 50, no. 4, Apr. 2014, Art. ID 8200809.
- [ACH13a] V. M. Acharya, J. Z. Bird, and M. Calvin, "A flux focusing axial magnetic gear," *IEEE Trans. Magn.*, vol.49, no. 7, pp. 4092-4095, Jul. 2013.
- [ATA93a] K. Atallah, and D. Howe, "Calculation of the rotational power loss in electrical steel laminations from measured H and B"," *IEEE Trans. Magn.*, vol. 29, no. 6, pp. 3547-3549, Nov. 1993.
- [ATA01a] K. Atallah, and D. Howe, "A novel high-performance magnetic gear," *IEEE Trans. Magn.*, vol. 37, no. 4, pp. 2844-2846, Jul. 2001.
- [ATA04a] K. Atallah, S. D. Calverley, and D. Howe, "Design, analysis and realisation of a high-performance magnetic gear," *IEE Proc. Electric Power Appl.*, vol. 151, no. 2, pp. 135-143, Mar. 2004.
- [ATA08a] K. Atallah, J. Rens, S. Mezani, and D. Howe, "A novel "Pseudo" direct-drive brushless permanent magnet machine," *IEEE Trans. Magn.*, vol. 44, no. 11, pp. 4349-4352, Nov. 2008.
- [BAI15a] J. Bai, P. Zheng, C. Tong, Z. Song and Q. Zhao, "Characteristic analysis and verification of the magnetic-field-modulated brushless double-rotor machine," *IEEE Trans. Ind. Electron.*, vol. 62, no. 7, pp. 4023-4033, Jul. 2015.
- [BAS11a] M. L. Bash, and S. D. Pekarek, "Modeling of salient-pole wound-rotor synchronous machines for population-based design," *IEEE Trans. Energy Convers.*, vol. 26, no. 2, pp. 381-392, Jun. 2011.

- [BIA06a] N. Bianchi, S. Bolognani, M. D. Pr e, and G. Grezzani, "Design considerations for fractional-slot winding configurations of synchronous machines," *IEEE Trans. Ind. Appl.*, vol. 42, no. 4, pp. 997-1006, Jul.-Aug. 2006.
- [BIA08a] N. Bianchi, S. Bolognani, and M. Dai Pr e, "Magnetic loading of fractional-slot three-phase PM motors with non-overlapped coils," *IEEE Trans. Ind. Appl.*, vol. 44, no. 5, pp. 1513-1521, Sep./Oct. 2008.
- [BOI16a] J. Boisson, F. Louf, J. Ojeda, X. Mininger, M. Gabsi, "Low computational-cost determination of vibrational behavior: application to five-phase flux-switching permanent-magnet motor," *IEEE Trans. Magn.*, in press.
- [BOL14a] I. Boldea, L. N. Tutelea, L. Parsa, and D. Dorrell, "Automotive electric propulsion systems with reduced or no permanent magnets: an overview," *IEEE Trans. Ind. Electron.*, vol. 61, no. 10, pp. 5696-5711, Oct. 2014.
- [BOM14a] W. Bomela, J. Bird, and V. Acharya, "The performance of a transverse flux magnetic gear," *IEEE Trans. Magn.*, vol. 50, no. 1, Jan 2014, Art. ID 4000104.
- [BOU13a] K. Boughrara, T. Lubin, and R. Ibtouen, "General subdomain model for predicting magnetic field in internal and external rotor multiphase flux-switching machines topologies," *IEEE Trans. Magn.*, vol. 49, no. 10, pp. 5310-5325, Oct. 2013.
- [BOU15a] M. Bouheraoua, J. Wang, and K. Atallah, "Slip recovery and prevention in pseudo direct drive permanent-magnet machines," *IEEE Trans. Ind. Appl.*, vol. 51, no. 3, pp. 2291-2299, May-Jun. 2015.
- [BOU14a] M. Bouheraoua, J. Wang, and K. Atallah, "Speed control for a pseudo direct drive permanent-magnet machine with one position sensor on low-speed rotor," *IEEE Trans. Ind. Appl.*, vol. 50, no. 6, pp. 3825-3833, Nov.-Dec. 2014.
- [CAO11a] R. W. Cao, M. Cheng, C. Mi, W. Hua, and W. X. Zhao, "A linear doubly salient permanent-magnet motor with modular and complementary structure," *IEEE Trans. Magn.*, vol. 47, no. 12, pp. 4809-4821, Dec. 2011.

- [CAO12a] R. Cao, C. Mi, and M. Cheng, "Quantitative comparison of flux-switching permanent-magnet motors with interior permanent magnet motor for EV, HEV and PHEV applications," *IEEE Trans. Magn.*, vol. 48, no. 8, pp. 2374-2384, Aug. 2012.
- [CHA05a] F. Chai, S. Cui, and S. Cheng, "Performance analysis of double-stator starter generator for the hybrid electric vehicle," *IEEE Trans. Magn.*, vol. 41, no. 1, pp. 484-487, Jan. 2005.
- [CHA08a] K. T. Chau, C. C. Chan, and C. H. Liu, "Overview of permanent-magnet brushless drives for electric and hybrid electric vehicles," *IEEE Trans. Indus. Electron.*, vol. 55, no. 6, pp. 2246-2257, Jun. 2008.
- [CHA09a] F. Chai, J. Xia, B. Guo, S. Cheng, and J. Zhang, "Double-stator permanent magnet synchronous in-wheel motor for hybrid electric drive system," *IEEE Trans. Magn.*, vol. 45, no. 1, pp. 278-281, Jan. 2009.
- [CHE00a] M. Cheng, K. T. Chau, C. C. Chan, E. Zhou, and X. Huang, "Nonlinear varying-network magnetic circuit analysis for doubly salient permanent-magnet motors," *IEEE Trans. Magn.*, vol. 36, no. 1, pp. 339-348, Jan. 2000.
- [CHE01a] M. Cheng, K. T. Chau, and C. C. Chan, "Static characteristics of a new doubly salient permanent magnet motor," *IEEE Trans. Energy Convers.*, vol. 16, no. 1, pp. 20-25, Mar. 2001.
- [CHE03a] M. Cheng, K. T. Chau, C. C. Chan, and Q. Sun, "Control and operation of a new 8/6-pole doubly salient permanent-magnet motor drive," *IEEE Trans. Ind. Appl.*, vol. 39, no. 5, pp. 1363-1371, Sep./Oct. 2003.
- [CHE06a] Y. Chen, S. Chen, Z. Q. Zhu, D. Howe, and Y. Y. Ye, "Starting torque of single-phase flux-switching permanent magnet motors," *IEEE Trans. Magn.*, vol. 42, no. 10, pp. 3416-3418, Oct. 2006.
- [CHE08a] Y. Chen, Z. Q. Zhu, and D. Howe, "Three-dimensional lumped-parameter magnetic circuit analysis of single-phase flux-switching permanent-magnet motor," *IEEE Trans. Ind. Appl.*, vol. 44, no. 6, pp. 1701-1710, Nov.-Dec. 2008.

- [CHE10a] J. T. Chen, and Z. Q. Zhu, "Winding configurations and optimal stator and rotor pole combination of flux-switching PM brushless AC machines," *IEEE Trans. Energy Convers.*, vol. 25, no. 2, pp. 293-302, Jun. 2010.
- [CHE10b] J. T. Chen, and Z. Q. Zhu, "Influence of the rotor pole number on optimal parameters in flux-switching PM brushless ac machines by the lumped-parameter magnetic circuit model," *IEEE Trans. Ind. Appl.*, vol. 46, no. 4, pp. 1381-1388, Jul.-Aug. 2010.
- [CHE10c] J. T. Chen, Z. Q. Zhu, S. Iwasaki, and R. Deodhar, "Low cost flux-switching brushless ac machines," *Proc. Conf. Veh. Pow. Prop.*, Lille, France, 2010, pp. 1-6.
- [CHE10d] J. T. Chen, and Z. Q. Zhu, "Comparison of all- and alternate-poles-wound flux-switching PM machines having different stator and rotor pole numbers," *IEEE Trans. Appl.*, vol. 46, no. 4, pp. 1406-1415, Jul.-Aug. 2010.
- [CHE11a] M. Cheng, W. Hua, J. Zhang, and W. Zhao, "Overview of stator-permanent magnet brushless machines," *IEEE Trans. Ind. Electron.*, vol. 58, no. 11, pp. 5087-5101, Nov. 2011.
- [CHE11b] J. T. Chen, Z. Q. Zhu, S. Iwasaki, and R. P. Deodhar, "Influence of slot opening on optimal stator and rotor pole combination and electromagnetic performance of switched-flux PM brushless AC machines," *IEEE Trans. Appl.*, vol. 47, no. 4, pp. 1681-1691, Jul./Aug. 2011.
- [CHE11c] J. T. Chen, Z. Q. Zhu, S. Iwasaki, and R. P. Deodhar, "A novel E-core switched-flux PM brushless AC machine," *IEEE Trans. Ind. Appl.*, vol. 47, no. 3, pp. 1273-1282, May-Jun. 2011.
- [CHE14a] Q. Chen, G. Liu, W. Zhao, L. Sun, M. Shao, and Z. Liu, "Design and comparison of two fault-tolerant interior-permanent-magnet motors," *IEEE Trans. Ind. Electron.*, vol. 61, no. 12, pp. 6615-6623, Dec. 2014.
- [CHE16a] M. Cheng, F. Yu, K. T. Chau, and W. Hua, "Dynamic performance evaluation of a nine-phase flux-switching permanent-magnet motor drive with model

predictive control,” *IEEE Trans. Ind. Electron.*, vol. 63, no. 7, pp. 4539-4549, Jul. 2016.

- [CHE90a] S. Chen, *Electrical machine design*, Beijing, China: MI press, 1990.
- [CHU08a] S. U. Chung, H. J. Lee, and S. M. Hwang, “A novel design of linear synchronous motor using FRM topology,” *IEEE Trans. Magn.*, vol. 44, no. 6, pp. 1514-1517, Jun. 2008.
- [CHU11a] S. U. Chung, J. W. Kim, B. C. Woo, D. K. Hong, J. Y. Lee, and D. H. Koo, “A novel design of modular three-phase permanent magnet vernier machine with consequent pole rotor,” *IEEE Trans. Magn.*, vol. 47, no. 1, pp. 7021704, Orc. 2011.
- [CHU12a] S. U. Chung, J. M. Kim, D. H. Koo, B. C. Woo, D. K. Hong, and J. Y. Lee, “Fractional slot concentrated winding permanent magnet synchronous machine with consequent pole rotor for low speed direct drive,” *IEEE Trans. Magn.*, vol. 48, no. 11, pp. 2965-2968, Nov. 2012.
- [CHU14a] W. Q. Chu, Z. Q. Zhu, and J. T. Chen, “Simplified analytical optimization and comparison of torque densities between electrically excited and permanent-magnet machines,” *IEEE Trans. Ind. Electron.*, vol. 61, no. 9, pp. 5000-5011, Sep. 2014.
- [CHU15a] S. U. Chung, J. W. Kim, Y. D. Chun, B. C. Woo, and D. K. Hong, “Fractional slot concentrated winding PMSM with consequent pole rotor for a low-speed direct drive: reduction of rare earth permanent magnet,” *IEEE Trans. Energy Convers.*, vol. 30, no. 1, pp. 103-109, Mar. 2015.
- [CHU16a] S. Chung, S. Moon, D. Kim, and J. Kim, “Development of a 20-pole–24-slot SPMSM with consequent pole rotor for in-wheel direct drive,” *IEEE Trans. Ind. Elec.*, vol. 63, no. 1, pp. 302-309, Jan. 2016.
- [COS14a] E. Cosoroaba, W. Wang, and B. Fahimi, “Comparative study of two winding configurations for a double stator switched reluctance machine,” in *Proc. Inter. Conf. Elec. Mach.*, Berlin, German, 2014, pp. 1013-1017.

- [CRI15a] J. M. Crider, and S. D. Sudhoff, "An inner rotor flux-modulated permanent magnet synchronous machine for low-speed high-torque applications," *IEEE Trans. Energy Convers.*, vol. 30, no. 3, pp. 1247-1254, Sep. 2015.
- [CRO02a] J. Cros, and P. Viarouge, "Synthesis of high performance PM motors with concentrated windings," *IEEE Trans. Energy Convers.*, vol. 17, no.2, pp. 248-253, Jun. 2002.
- [DAJ12a] G. Dajaku, and D. Gerling, "Air-gap flux density characteristics of salient pole synchronous permanent-magnet machines," *IEEE Trans. Magn.*, vol. 48, no. 7, pp. 2196-2204, Jul. 2012.
- [DEO14a] R. Deodhar, A. Pride, S. Iwasaki, and J. J. Bremner, "Performance improvement in flux-switching pm machines using flux diverters," *IEEE Trans. Ind. Appl.*, vol. 50, no. 2, pp. 973-978, Mar.-Apr. 2014.
- [DEO97a] R. Deodhar, S. Anderson, I. Boldea, and T. J. E. Miller, "The flux-reversal machine: A new brushless doubly-salient permanent magnet machine," *IEEE Trans. Ind. Appl.*, vol. 33, no. 4, pp. 925-934, Jul./Aug. 1997.
- [DOR10a] D. G. Dorrell, M. Popescu, and D. M. Ionel, "Unbalanced magnetic pull due to asymmetry and low-level static rotor eccentricity in fractional-slot brushless permanent-magnet motors with surface-magnet and consequent-pole rotors," *IEEE Trans. Magn.*, vol. 46, no. 7, pp. 2675-2685, Jul. 2010.
- [DU16a] Y. Du, F. Xiao, W. Hua, X. Zhu, M. Cheng, L. Quan, and K. T. Chau, "Comparison of flux-switching PM motors with different winding configurations using magnetic gearing principle," *IEEE Trans. Magn.*, vol. 52, no. 5, May 2016, Art. ID 8201908.
- [DU16b] Y. Du, C. Zou, X. Zhu, C. Zhang, and F. Xiao, "A full-pitched flux-switching permanent magnet motor," *IEEE Trans. Trans. Appl. Supercond.*, vol. 26, no. 4, Jun. 2016, Art. ID 0604505.
- [ELR06a] A. M. EL-Refaie, T. M. Jahns, and D. W. Novotny, "Analysis of surface permanent magnet machines with fractional-slot concentrated windings," *IEEE Trans. Energy Convers.*, vol. 21, no. 1, pp. 34-43, Mar. 2006.

- [ELR10a] A. M. EL-Refaei., “Fractional-slot concentrated-windings synchronous permanent magnet machines: opportunities and challenges,” *IEEE Trans. Ind. Electron.*, vol. 57, no. 1, pp. 107-121, Jan. 2010.
- [EVA15a] D. J. Evans, and Z. Q. Zhu, “Novel partitioned stator switched flux permanent magnet machines,” *IEEE Trans. Magn.*, vol. 51, no. 1, Jan. 2015, Art. ID 8100114.
- [FAN06a] Y. Fan, K. T. Chau, and M. Cheng, “A new three-phase doubly salient permanent magnet machine for wind power generation,” *IEEE Trans. Ind. Appl.*, vol. 42, no. 1, pp. 53-60, Jan.-Feb. 2006.
- [FAN14a] Y. Fan, L. Zhang, J. Huang, and X. Han, “Design, analysis, and sensorless control of a self-decelerating permanent-magnet in-wheel motor,” *IEEE Trans. Ind. Electron.*, vol. 61, no. 10, pp. 5788-5797, Oct. 2014.
- [FAS14a] A. Fasolo, L. Alberti, and N. Bianchi, “Performance comparison between switching-flux and IPM machines with rare-earth and ferrite PMs,” *IEEE Trans. Ind. Appl.*, vol. 50, no.6, pp.3708-3716, Nov.-Dec. 2014.
- [FEI11a] W. Z. Fei, P. C. K. Luk, J. X. Shen, B. Xia, and Y. Wang, “Permanent-magnet flux-switching integrated starter generator with different rotor configurations for cogging torque and torque ripple mitigations,” *IEEE Trans. Ind. Appl.*, vol. 47, no.3, pp.1247-1256, May/Jun. 2011.
- [FEI12a] W. Z. Fei, P. C. K. Kuk, and J. X. Shen, “Torque analysis of permanent-magnet flux switching machines with rotor step skewing,” *IEEE Trans. Magn.*, vol. 48, no. 0, pp. 2664-2673, Oct. 2012.
- [FRA11a] N. W. Frank, and H. A. Toliyat, “Analysis of the concentric planetary magnetic gear with strengthened stator and interior permanent magnet inner rotor,” *IEEE Trans. Ind. Appl.*, vol. 47, no. 4, pp. 1652-1660, July-Aug. 2011.
- [FRE07a] M. Freddy and L. Heinz, “Parasitic effects in PM machines with concentrated windings,” *IEEE Trans. Ind. Appl.*, vol. 43, no. 5, pp. 1223-1232, Sep./Oct. 2007.
- [FUK10a] T. Fukami, Y. Matsuura, K. Shima, M. Momiyama, and M. Kawamura, “Development of a low-speed multi-pole synchronous machine with a field

winding on the stator side,” in *Proc. Int. Conf. Elec. Mach.*, Rome, Italy, 2010, pp. 1-6.

- [FUK12a] T. Fukami, Y. Matsuura, K. Shima, M. Momiyama, and M. Kawamura, “A multi-pole synchronous machine with nonoverlapping concentrated armature and field winding on the stator,” *IEEE Trans. Ind. Electron.*, vol. 59, no. 6, pp. 2583-2591, Jun. 2012.
- [FUK12b] T. Fukami, K. Shima, T. Tsuda, and M. Kawamura, “Prediction of field currents in flux-modulating synchronous machines under loaded conditions,” in *Proc. Int. Conf. Elec. Mach.*, Marseille, France, 2012, pp. 441-446.
- [FUK12c] T. Fukami, H. Aoki, K. Shima, M. Momiyama, and M. Kawamura, “Assessment of core losses in a flux-modulating synchronous machine,” *IEEE Trans. Ind. Appl.*, vol. 48, no. 2, pp. 603-611, Mar.-Apr. 2012.
- [GAO16a] Y. Gao, R. Qu, D. Li, J. Li, and G. Zhou, “Consequent-pole flux reversal permanent magnet machine for electric vehicle propulsion”, *IEEE Trans. Appl. Supercond.*, vol. 26, no. 4, Jun. 2016, Art. ID 5200105.
- [GAO16b] Y. Gao; R. Qu; D. Li; J. Li; L. Wu, “Design of three-phase flux reversal machines with fractional-slot windings,” *IEEE Trans. Ind. Appl.*, vol. 52, no. 4, pp. 2856-2864, Jul.-Aug. 2016.
- [GAP14a] F. G. Capponi, G. De Donato, G. Borocci, and F. Caricchi, “Axial-flux hybrid-excitation synchronous machine: analysis, design, and experimental evaluation,” *IEEE Trans. Ind. Appl.*, vol. 50, no. 5, pp. 3173-3184, Sep.-Oct. 2014.
- [GAS12a] B. Gaussens, E. Hoang, O. de la Barriere, J. Saint-Michel, M. Lecrivain, and M. Gabsi, “Analytical approach for air-gap modeling of field-excited flux-switching machine: no-load operation,” *IEEE Trans. Magn.*, vol. 48, no. 9, pp. 2505-2517, Sep. 2012.
- [GAU14a] B. Gaussens, E. Hoang, M. Lecrivain, P. Manfe, and M. Gabsi, “A hybrid-excited flux-switching machine for high-speed dc-alternator applications,” *IEEE Trans. Ind. Electron.*, vol. 61, no. 6, pp. 2976-2989, Jun. 2014.

- [GER15a] S. Gerber, and R. J. Wang, "Design and evaluation of a MG pm machine," *IEEE Trans. Magn.*, vol. 51, no. 8, Aug. 2015, Art. ID 8107010.
- [HOA97a] E. Hoang, A. H. Ben Ahmed, and J. Lucidarme, "Switching flux permanent magnet polyphased synchronous machines," in *Proc. Eur. Power Electron. Conf.*, Trondheim, Norway, 1997, vol. 3, pp. 903-908.
- [HUA08a] W. Hua, M. Cheng, Z. Q. Zhu, and D. Howe, "Analysis and optimization of back-EMF waveform of a novel flux-switching PM motor," *IEEE Trans. Energy Convers.*, vol. 23, no. 3, pp. 727-733, Sep. 2008.
- [HUA09a] W. Hua, M. Cheng, and G. Zhang, "A novel hybrid excitation flux-switching motor for hybrid vehicles," *IEEE Trans. Magn.*, vol. 45, no. 10, pp. 4728-4731, Oct. 2009.
- [ILH10a] E. Ilhan, B. L. J. Gysen, J. J. H. Paulides, and E. A. Lomonova, "Analytical hybrid model for flux switching permanent magnet machines," *IEEE Trans. Magn.*, vol. 46, no. 6, pp. 1762-1765, Nov. 2010.
- [ILH14a] E. Ilhan, T. L. Balyovski, J. J. H. Paulides, and E. A. Lomonova, "Servo flux switching PM machines", in *Proc. of Inter. Conf. on Eelec. Mach.*, Berlin, Germany, 2014, pp. 634-640.
- [ISF14a] A. H. Isfahani, and B. Fahimi, "Comparison of mechanical vibration between a double-stator switched reluctance machine and a conventional switched reluctance machine," *IEEE Trans. Magn.*, vol. 50, no. 2, pp. 293-296, Feb. 2014.
- [ISH05a] D. Ishak, Z. Q. Zhu, and D. Howe, "Eddy-current loss in the rotor magnets of permanent-magnet brushless machines having a fractional number of slots per pole," *IEEE Trans. Magn.*, vol. 41, no. 9, pp. 2462-2469, Sep. 2005.
- [JAH04a] T. M. Jahns, N. Bianchi, S. Bolognani, A. Consoli, A. Vagati, E. Lovelace, S. Morimoto, and Robert Lorenz, *Design, analysis, and control of interior PM synchronous machines*. Padova, Italy: CLEUP, 2004.

- [JAH86a] T. M. Jahns, G. B. Kliman, and Thomas W. Neumann, "Interior permanent-magnet synchronous motors for adjustable-speed drives," *IEEE Trans. Ind. Appl.*, vol. IA-22, no. 4, pp. 738-747, Jul. 1986.
- [JAH87a] T. M. Jahns, "Flux-weakening regime operation of an interior permanent-magnet synchronous motor drive," *IEEE Trans. Ind. Appl.*, vol. IA-23, no. 4, pp. 681-689, Jul. 1987.
- [JIA09a] L. Jian, K. T. Chau, Y. Gong, J. Z. Jiang, C. Yu and W. Li, "Comparison of coaxial magnetic gears with different topologies," *IEEE Trans. Magn.*, vol. 45, no. 10, pp. 4526-4529, Oct. 2009.
- [JIA09b] L. Jian, K. T. Chau, and J. Z. Jiang, "A magnetic-gearing outer-rotor permanent-magnet brushless machine for wind power generation," *IEEE Trans. Ind. Appl.*, vol. 45, no. 3, pp. 954-962, May/June. 2009.
- [JIA10a] L. N. Jian, and K. T. Chau, "A coaxial magnetic gear with Halbach permanent-magnet arrays," *IEEE Trans. Energy Convers.*, vol. 25, no. 2, pp. 319-328, Jun. 2010.
- [KAS12a] Y. Kashitani, and S. Shimomura, "Novel slipring-less winding-excited synchronous machine," in *Int. Conf. Elect. Mach. and Syst.*, Sept. 2012, pp. 1-6.
- [KIM16a] D. Kim, H. Hwang, S. Bae, and C. Lee, "Analysis and design of a double-stator flux-switching permanent magnet machine using ferrite magnet in hybrid electric vehicles," *IEEE Trans. Magn.*, vol. 52, no. 7, Art. ID 8106604.
- [LAB13a] A. Labak, and N. C. Kar, "Designing and prototyping a novel five-phase pancake-shaped axial-flux SRM for electric vehicle application through dynamic fea incorporating flux-tube modeling," *IEEE Trans. Ind. Appl.*, vol. 51, no. 3, pp. 1276-1288, May-June. 2013.
- [LEE15a] C. H. T. Lee, K. T. Chau, and C. Liu, "Design and analysis of a cost-effective magnetless multiphase flux-reversal DC-field machine for wind power generation," *IEEE Trans. Energy Convers.*, vol. 30, no. 4, pp. 1565-1573, Dec. 2015.

- [LI07a] Y. Li, and C. C. Mi, “Doubly salient permanent-magnet machine with skewed rotor and six-state commutating mode,” *IEEE Trans. Magn.*, vol. 43, no. 9, pp. 3623–3629, Sep. 2007.
- [LI10a] J. Li, K. T. Chau, J. Z. Jiang, C. Liu, and W. Li, “A new efficient permanent-magnet vernier machine for wind power generation,” *IEEE Trans. Magn.*, vol. 46, no. 6, pp. 1475-1478, Jun. 2010.
- [LI11a] Y. Li, J. Xing, Y. Lu, and Z. Yin, “Torque analysis of a novel non-contact permanent variable transmission,” *IEEE Trans. Magn.*, vol. 47, no. 10, pp. 4465-4468, Oct. 2011.
- [LI11b] J. Li, K. T. Chau, and W. Li, “Harmonic analysis and comparison of permanent magnet vernier and magnetic-g geared machines,” *IEEE Trans. Magn.*, 47, no. 10, pp. 3649-3652, Oct. 2011.
- [LI13a] D. Li, and R. H. Qu, “High power factor vernier permanent magnet machines,” *Proc. IEEE Eng. Con. Congr. Exp.*, Denver, USA, 2013, pp. 1534-1540.
- [LI14a] D. Li, R. Qu, and T. A. Lipo, “High-power-factor vernier permanent-magnet machines,” *IEEE Trans. Ind. Appl.*, vol. 50, no. 6, pp. 3664-3674, Nov.-Dec. 2014.
- [LI14b] F. Li, W. Hua, M. Cheng, and G. Zhang, “Analysis of fault tolerant control for a nine-phase flux-switching permanent magnet machine,” *IEEE Trans. Magn.*, vol. 50, no. 11, Nov. 2014, Art. ID 8206004.
- [LI15a] F. Li, W. Hua, M. Tong, G. Zhao, and M. Cheng, “Nine-phase flux-switching permanent magnet brushless machine for low-speed and high-torque applications,” *IEEE Trans. Magn.*, vol. 51, no. 3, Mar. 2015, Art. ID 8700204.
- [LI16a] D. Li, R. Qu, J. Li, W. Xu, and L. Wu, “Synthesis of flux switching permanent magnet machines,” *IEEE Trans. Energy Convers.*, vol. 31, no. 1, pp. 106-117, Mar. 2016.

- [LI16b] Y. Li, D. Bobba, and B. Sarlioglu, "A novel 6/4 flux-switching permanent magnet machine designed for high-speed operations," *IEEE Trans. Magn.*, vol. 52, no. 8, Aug. 2016, Art. ID 8107109.
- [LI16c] Y. Li, D. Bobba, and B. Sarlioglu, "Design and performance characterization of a novel low-pole dual-stator flux-switching permanent magnet machine for traction application," *IEEE Trans. Ind. Appl.*, vol. 52, no. 5, pp. 4304-4314, Sep.-Oct. 2016.
- [LIN04a] D. Lin, P. Zhou, W. N. Fu, Z. Badics, and Z. J. Cendes, "A dynamic core loss model for soft ferromagnetic and power ferrite materials in transient finite element analysis," *IEEE Trans. Magn.*, vol. 40, no. 2, pp. 1318-1341, Mar. 2004.
- [LIA95a] Y. Liao, F. Liang, and T. A. Lipo, "A novel permanent magnet motor with doubly salient structure," *IEEE Trans. Ind. Appl.*, vol. 31, pp. 1069-1078, Sep./Oct. 1995.
- [LIU09a] X. H. Liu, K. T. Chau, J. Z. Jiang, and C. Yu, "Design and analysis of interior-magnet outer-rotor concentric magnetic gears," *J. Appl. Phys.*, vol. 105, no. 7, pp. 07F101, Jun. 2009.
- [LIU12a] X. Liu, Z. Q. Zhu, and Z. P. Pan, "Analysis of electromagnetic torque in sinusoidal excited switched reluctance machines having DC bias in excitation," in *Proc. of ICEM2012*, Marseille, 2012, pp. 2882-2888.
- [LIU13a] X. Liu, and Z. Q. Zhu, "Comparative study of novel variable flux reluctance machines with doubly fed doubly salient machines," *IEEE Trans. Magn.*, vol. 49, no. 7, pp. 3838-3841, Jul. 2013.
- [LIU14a] X. Liu, and Z. Q. Zhu, "Stator/rotor pole combinations and winding configurations of variable flux reluctance machines", *IEEE Trans. Ind. Appl.*, vol.50, no.6, pp.3675-3684, Nov. 2014.
- [LIU14b] C. T. Liu, H. Y. Chung, and C. C. Hwang, "Design assessments of a magnetic-gear double-rotor permanent magnet generator," *IEEE Trans. Magn.*, vol. 50, no. 1, Jan. 2014, Art. ID 4001004.

- [LUB10a] T. Lubin, S. Mezani, and A. Rezzoug, "Analytical computation of the magnetic field distribution in a magnetic gear," *IEEE Trans. Magn.*, vol. 46, no. 7, pp. 2611-2621, Jul. 2010.
- [LUB13a] T. Lubin, S. Mezani, and A. Rezzoug, "Development of a 2D analytical model for the electromagnetic computation of axial-field magnetic gears," *IEEE Trans. Magn.*, vol. 49, no. 11, pp. 5507-5521, Nov 2013.
- [LUO00a] X. Luo, and T. A. Lipo, "A synchronous/permanent magnet hybrid AC machine," *IEEE Trans. Energy Convers.*, vol. 15, no. 2, pp. 203-210, Jun. 2000.
- [MCF14a] J. D. McFarland, T. M. Jahns, and A. M. EL-Refaie, "Analysis of the torque production mechanism for flux-switching permanent magnet machines," in *Proc. IEEE Eng. Con. Congr. Exp.*, Pittsburgh, USA, 2014, pp. 310-317.
- [MCF14b] J. D. McFarland, T. M. Jahns, and A. M. El-Refaie, "Demagnetization performance characteristics of flux switching permanent magnet machines," *Proc. of Int. Conf. on Electrical Machines (ICEM)*, Berlin, Germany, pp. 2001-2007, 2014.
- [MCF15a] J. D. McFarland, T. M. Jahns, and A. M. El-Refaie, "Analysis of the torque production mechanism for flux-switching permanent-magnet machines," *IEEE Trans. Ind. Appl.*, vol. 51, no. 4, pp. 3041-3049, Jul.-Aug. 2015.
- [MEZ06a] S. Mezani, K. Atallah, and D. Howe, "A high-performance axial-field magnetic gear," *Journal of Appl. Phys.*, vol. 99, no. 8, 2006, Art. ID pp. 08R303.
- [MOR10a] D. S. More, and B. G. Fernandes, "Analysis of flux-reversal machine based on fictitious electrical gear," *IEEE Trans. Energy Convers.*, vol. 25, no. 4, pp. 940-947, Dec. 2010.
- [MOR13a] D. S. More, and B. G. Fernandes, "Modelling and performance of three-phase 6/14 pole flux reversal machine," *IET Elect. Power Appl.*, vol. 7, no. 2, pp. 131-139, Feb. 2013.

- [NIU08a] S. X. Niu, K. T. Chau, and J. Z. Jiang, "Analysis of eddy-current loss in a double-stator cup-rotor PM machine," *IEEE Trans. Magn.*, vol. 44, no. 11, pp. 4401-4404, Nov. 2008.
- [NIU09a] S. X. Niu, K. T. Chau, and C. Yu, "Quantitative comparison of double-stator and traditional permanent magnet brushless machines," *J. Appl. Phys.*, vol. 105, no. 7, pp. 07F105, Apr. 2009.
- [QI09a] G. Qi, J. T. Chen, Z. Q. Zhu, D. Howe, L. B. Zhou, and C. L. Gu, "Influence of skew and cross-coupling on flux-weakening performance of permanent-magnet brushless AC machines," *IEEE Trans. Magn.*, vol. 45, no. 5, pp. 2110-2117, May 2009.
- [QU11a] R. Qu, D. Li, and J. Wang, "Relationship between magnetic gears and vernier machines," in *Proc. Int. Conf. Electr. Mach. Syst.*, Beijing, China, 2011, pp. 1-6.
- [RAS05a] P. O. Rasmussen, T. O. Andersen, F. T. Jorgensen, and O. Nielsen, "Development of a high-performance magnetic gear," *IEEE Trans. Ind. Appl.*, vol. 41, no. 3, pp. 764-770, May-Jun. 2005.
- [RAU55a] S. E. Rauch, and L. J. Johnson, "Design principles of the flux-switch alternators," *AIEE Trans.*, vol. 74, no. 3, pp. 1261-1268, Jan. 1955.
- [SED15a] E. B. Sedrine, J. Ojeda, M. Gabsi, and I. Slama-Belkhodja, "Fault-tolerant control using the GA optimization considering the reluctance torque of a five-phase flux switching machine," *IEEE Trans. Energy Convers.*, vol. 30, no. 3, pp. 927-938, Sep. 2015.
- [SHA15a] L. Shao, W. Hua, and M. Cheng, "A new 12/11-pole dual three-phase flux-switching permanent magnet machine," in *Proc. of Inter. Conf. Elec. Mach. and Sys.*, Pattaya, 2015, pp. 1502-1507.
- [SHI16a] Y. Shi, L. Jian, J. Wei, Z. Shao, W. Li, and C. C. Chan, "A new perspective on the operating principle of flux-switching permanent magnet machines," *IEEE Trans. Ind. Electron.*, vol. 63, no. 3, pp. 1425-1437, Mar. 2016.

- [SIK15a] C. Sikder, I. Husain, and O. Wang, "Cogging torque reduction in flux-switching permanent-magnet machines by rotor pole shaping," *IEEE Trans. Ind. Appl.*, vol. 51, no. 5, pp. 3609-3619, Sep./Oct. 2015.
- [SPO87a] M. I. Spong, R. Marino, S. Peresada, and D. Taylor, "Feedback linearizing control of switched reluctance motors," *IEEE Trans. Auto. Cont.*, vol. 32, no. 5, pp. 371-379, May 1987.
- [SRI11a] M. Sridharbabu, T. Kosaka, and N. Matsui, "Design reconsiderations of high speed permanent magnet hybrid excitation motor for main spindle drive in machine tools based on experimental results of prototype machine," *IEEE Trans. Magn.*, 47, no. 10, pp. 4469-4472, Oct. 2011.
- [SUL11a] E. Sulaiman, T. Kosaka, and N. Matsui, "A new structure of 12 slot-10 pole field-excitation flux switching synchronous machine for hybrid electric vehicles," *Proc. 14th Eur. Conf. Pow. Electron. Appli.*, Birmingham, UK, 2011, pp. 1-10.
- [SUN09a] X. Sun, M. Cheng, W. Hua, and L. Xu, "Optimal design of double-layer permanent magnet dual mechanical port machine for wind power application," *IEEE Trans. Magn.*, vol. 45, no. 10, pp. 4613-4616, Oct. 2009.
- [SUN13a] X. Sun, M. Cheng, Y. Zhu, and L. Xu, "Application of electrical variable transmission in wind power generation system," *IEEE Trans. Ind. Appl.*, vol. 49, no. 3, pp. 1299-1307, May-Jun. 2013.
- [TAI14a] W. Tai, M. Tsai, Z. Gaing, P. Huang, and Y. Hsu, "Novel stator design of double salient permanent magnet motor," *IEEE Trans. Magn.*, vol. 50, no. 4, Apr. 2014, Art. ID 8100504.
- [TAN13a] Y. Tang, J. J. H. Paulides, and E. A. Lomonova, "Winding topologies of flux-switching motors for in-wheel traction," *COMPEL: The International Journal for Computation and Mathematics in Electrical and Electronic Engineering*, vol. 34, no. 1, pp. 32-45, 2013.
- [TAR15a] P. Taras, G. J. Li, and Z. Q. Zhu, "Comparative study of alternative modular switched flux permanent magnet machines," in *Proc. of IEEE Inter. Conf.*

Indus. Tech., Seville, 2015, pp. 658-663.

- [THO12a] A. S. Thomas, Z. Q. Zhu, and L. J. Wu, "Novel modular-rotor switched-flux permanent magnet machines," *IEEE Trans. Ind. Appl.*, vol. 48, no. 6, pp. 2249-2258, Nov.-Dec. 2012.
- [TIA15a] Y. Tian, G. Liu, W. Zhao, and J. Ji, "Design and analysis of coaxial magnetic gears considering rotor losses," *IEEE Trans. Magn.*, vol. 51, no. 11, Nov. 2015, Art. ID 8108304.
- [TOB99a] A. Toba, and T. A. Lipo, "Novel dual-excitation permanent magnet vernier machine," in *Proc. IEEE IAS Annu. Conf.*, Phoenix, USA, 1999, vol. 4, pp. 2539-2544.
- [TON16a] M. Tong, W. Hua, P. Su, M. Cheng, and J. Meng, "Investigation of a vector-controlled five-phase flux-switching permanent-magnet machine drive system," *IEEE Trans. Magn.*, vol. 52, no. 7, Jul. 2016, Art. ID 8600105.
- [WAN01a] C. X. Wang, I. Boldea, and S. A. Nasar, "Characterization of three phase flux reversal machine as an automotive generator," *IEEE Trans. Energy Convers.*, vol. 16, no. 1, pp. 74-80, Mar. 2001.
- [WAN08a] L. L. Wang, J. X. Shen, Y. Wang, and K. Wang, "A novel magnetic-gear outer-rotor permanent-magnet brushless motor," in *Proc. of Power Electro. Mach. and Dri.*, Yoke, UK, 2008. pp. 33-36.
- [WAN09a] L. L. Wang, J. X. Shen, P. C.-K. Luk, W. Z. Fei, C. F. Wang, and H. Hao, "Development of a magnetic-gear permanent-magnet brushless motor," *IEEE Trans. Magn.*, vol. 45, no. 10, pp. 4578-4581, Oct. 2009.
- [WAN09b] Y. Wang, M. J. Jin, W. Z. Fei, and J. X. Shen, "Cogging torque reduction in permanent magnet flux-switching machines by rotor teeth axial pairing", *IET Electr. Power Appl.*, vol. 4, no. 7, pp. 500-506, 2010.
- [WAN11a] Y. Wang, M. Cheng, Y. Du, and K. T. Chau, "Design of high-torque-density double-stator permanent magnet brushless motors," *IET Electr. Power Appl.*, vol. 5, no. 3, pp. 317-323, Mar. 2011.

- [WAN11b] Y. Wang, M. Cheng, Y. Du, and K. T. Chau, "Design of high-torque-density double-stator permanent magnet brushless motors," *IET Electr. Power Appl.*, vol. 5, no. 3, pp. 317-323, Mar. 2011.
- [WAN11c] J. Wang, K. Atallah, and S. D. Carvley, "A magnetic continuously variable transmission device," *IEEE Trans. Magn.*, vol. 47, no. 10, pp. 2815-2818, Oct. 2011.
- [WAN12a] Y. Wang, and Z. Deng, "Comparison of hybrid excitation topologies for flux-switching machines," *IEEE Trans. Magn.*, vol. 48, no. 9, pp. 2518-2527, Sep. 2012.
- [WAN12b] Y. Wang, and Z. Deng, "An integration algorithm for stator flux estimation of a direct-torque-controlled electrical excitation flux-switching generator," *IEEE Trans. Energy Convers.*, vol. 27, no. 2, pp. 411-420, Jun. 2012.
- [WAN14a] K. Wang, Z. Q. Zhu, G. Ombach, M. Koch, S. Zhang, and J. Xu, "Electromagnetic performance of an 18-slot/10-pole fractional-slot surface-mounted permanent-magnet machine," *IEEE Trans. Ind. Appl.*, vol. 50, no. 6, pp. 3685-3696, Nov.-Dec. 2014.
- [WAN14b] K. Wang, Z. Q. Zhu, and G. Ombach, "Synthesis of high performance fractional-slot permanent-magnet machines with coil-pitch of two slot-pitches," *IEEE Trans. Energy Convers.*, vol. 29, no. 3, pp. 758-770, Sep. 2014.
- [WIE97a] S. Wiesember, A. Proca, and A. Keyhani, "Estimation of permanent magnet motor parameters," in *Rec. of IEEE-IAS Annu. Meeting*, New Orleans, US, 1997, vol. 1, pp. 29-34.
- [WU14a] D. Wu, J. T. Shi, Z. Q. Zhu, and X. Liu, "Electromagnetic performance of novel synchronous machines with permanent magnets in stator yoke," *IEEE Trans. Magn.*, vol. 50, no. 9, Sep. 2014, Art. ID 8102009.
- [WU15a] Z. Z. Wu, and Z. Q. Zhu, "Analysis of air-gap field modulation and magnetic gearing effects in switched flux permanent magnet machines," *IEEE Trans. Magn.*, vol. 51, no. 5, pp. 1-12, May 2015, Art. ID 8105012.

- [WU15b] Z. Z. Wu, Z. Q. Zhu, and J. T. Shi, "Novel doubly salient permanent magnet machines with partitioned stator and iron pieces rotor," *IEEE Trans. Magn.*, vol. 51, no. 5, May 2015, Art. ID 8105212.
- [WU16b] Z. Z. Wu, and Z. Q. Zhu, "Partitioned stator flux reversal machine with consequent-pole PM stator," *IEEE Trans. on Energy Convers.*, vol. 30, no. 4, pp. 1472 - 1482, Dec. 2015.
- [XUE13a] X. Xue, W. Zhao, J. Zhu, G. Liu, X. Zhu, and M. Cheng, "Design of five-phase modular flux-switching permanent-magnet machines for high reliability applications," *IEEE Trans. Magn.*, vol. 49, no. 7, pp. 3941-3944, Jul. 2013.
- [YIN15a] X. Yin, P. D. Pfister, and Y. Fang, "A novel magnetic gear: toward a higher torque density," *IEEE Trans. Magn.*, vol. 51, no. 11, Nov. 2015, Art. ID 8002804.
- [YU15a] C. Yu, and S. Niu, "Development of a magnetless flux switching machine for rooftop wind power generation," *IEEE Trans. Energy Convers.*, vol. 30, no. 4, pp. 1703-1711, Dec. 2012.
- [YU16a] F. Yu, M. Cheng, and K. T. Chau, "Controllability and performance of a nine-phase fspm motor under severe five open-phase fault conditions," *IEEE Trans. Energy Convers.*, vol. 31, no. 1, pp. 323-332, Mar. 2016.
- [ZHA09a] J. Zhang, M. Cheng, Z. Chen, and W. Hua, "Comparison of stator-mounted permanent-magnet machines based on a general power equation," *IEEE Trans. Energy Convers.*, vol. 24, no. 4, pp. 826–834, Dec. 2009.
- [ZHA10a] W. Zhao, K. T. Chau, M. Cheng, J. Ji, and X. Zhu, "Remedial brushless AC operation of fault-tolerant doubly salient permanent magnet motor drives," *IEEE Trans. Ind. Electron.*, vol. 57, no. 6, pp.2134–2141, Jun. 2010.
- [ZHA11a] W. Zhao, M. Cheng, W Hua, H. Jia, and R. Cao, "Back-EMF harmonic analysis and fault-tolerant control of flux-switching permanent-magnet machine with redundancy," *IEEE Trans. Ind. Electron.*, vol. 58, no. 5, pp. 1926-1935, May 2011.

- [ZHA12a] Z. Zhang, Y. Yan, and Y. Tao, "A new topology of low speed doubly salient brushless dc generator for wind power generation," *IEEE Trans. Magn.*, vol. 48, no. 3, pp. 1227-1233, Mar. 2012.
- [ZHA12b] Y. Zhang, M. Zhang, W. Ma, J. Xu, J. Lu, and Z. Sun, "Modeling of a double-stator linear induction motor," *IEEE Trans. Energy Convers.*, vol. 27, no. 3, pp. 572-579, Sep. 2012.
- [ZHA15a] X. Zhang, X. Liu, J. Liu, and Z. Chen, "Analytical investigation on the power factor of a flux-modulated permanent-magnet synchronous machine," *IEEE Trans. Magn.*, vol. 51, no. 11, pp. 1-4, May 2015, Art. ID 8110704.
- [ZHU05a] Z. Q. Zhu, Y. Pang, D. Howe, S. Iwasaki, R. Deodhar, and A. Pride, "Analysis of electromagnetic performance of switched flux switching permanent magnet machines by non-linear adaptive lumped parameter magnetic circuit model," *IEEE Trans. Magn.*, vol. 41, no. 11, pp. 4277-4287, Nov. 2005.
- [ZHU07a] Z. Q. Zhu, and D. Howe, "Electrical machines and drives for electric, hybrid and fuel cell vehicles," *Proc. IEEE*, vol. 95, no. 4, pp. 746-765, Apr. 2007.
- [ZHU07b] X. Zhu, M. Cheng, W. Zhao, C. Liu, and K. T. Chau, "A transient cosimulation approach to performance analysis of hybrid excited doubly salient machine considering indirect field-circuit coupling," *IEEE Trans. Magn.*, vol. 43, no. 6, pp. 2558-2560, Jun. 2007.
- [ZHU09a] L. Zhu, S. Z. Jiang, Z. Q. Zhu, and C. C. Chan, "Analytical methods for minimizing cogging torque in permanent-magnet machines," *IEEE Trans. Magn.*, vol. 45, no. 4, pp. 2023-2031, Apr. 2009.
- [ZHU09b] Z. Q. Zhu, A. S. Thomas, J. T. Chen, and G. W. Jewell, "Cogging torque in flux-switching permanent magnet machines," *IEEE Trans. Magn.*, vol. 45, no. 10, pp. 4708-4711, Oct. 2009.
- [ZHU10a] Z. Q. Zhu, and J. T. Chen, "Advanced flux-switching permanent magnet brushless machines," *IEEE Trans. Magn.*, vol. 46, no. 6, pp. 1447-1453, Jun. 2010.

- [ZHU10b] Z. Q. Zhu, L. J. Wu, and Z. P. Xia, "An accurate subdomain model for magnetic field computation in slotted surface-mounted permanent-magnet machines," *IEEE Trans. Magn.*, vol. 46, no. 4, pp. 1100-1115, Apr. 2010.
- [ZHU11a] Z. Q. Zhu, "Fractional-slot permanent magnet brushless machines and drives for electric and hybrid propulsion systems," *COMPEL: Int. J. Comput. Math. Electr. Electron. Eng.*, vol. 30, no. 1, pp. 9-31, 2011.
- [ZHU11b] Z. Q. Zhu, "Switched flux permanent magnet machines – innovation continues", *Keynote Speech, Proc. of Int. Conf. on Electrical Machines and Systems (ICEMS2011)*, 2011, Beijing, chapter Keynote Speech-06, pp. 1-10.
- [ZHU11c] X. Zhu, L. Quan, D. Chen, M. Cheng, W. Hua, and X. Sun, "Electromagnetic performance analysis of a new stator-permanent-magnet doubly salient flux memory motor using a piecewise-linear hysteresis model," *IEEE Trans. Magn.*, vol. 47, no. 5, pp. 1106-1109, May 2011.
- [ZHU12a] X. Zhu, L. Chen, L. Quan, Y. Sun, W. Hua, and Z. Wang, "A new magnetic-planetary-gear permanent magnet brushless machine for hybrid electric vehicle," *IEEE Trans. Magn.*, vol. 48, no. 11, pp. 4642-4645, Nov. 2012.
- [ZHU13a] Z. Q. Zhu, L. J. Wu, M. L. Mohd Jamil, "Distortion of back-EMF and torque of PM brushless machines due to eccentricity," *IEEE Trans. Magn.*, vol. 49, no. 8, pp. 4927-4936, Aug. 2013.
- [ZHU14a] Z. Q. Zhu, and D. J. Evans, "Overview of recent advances in innovative electrical machines, with particular reference to MG switched flux machines," Keynote Speech, *Int. Conf. Electrical Machines and Systems (ICEMS2014)*, Hangzhou, China, 2014, pp. 1-10.
- [ZHU14b] Z. Q. Zhu, M. Al-Ani, B. Lee, and X. Liu, "Comparative study of the electromagnetic performance of switched flux permanent magnet machines," *IET Electr. Power Appl.*, vol. 9, no. 4, pp. 297-306, Apr. 2015.
- [ZHU15a] Z. Q. Zhu, Z. Z. Wu, D. J. Evans, and W. Q. Chu, "Novel electrical machine having separate PM excitation stator," *IEEE Trans. Magn.*, vol. 51, no. 4, Apr. 2015, Art. ID 8104109.

- [ZHU15b] Z. Q. Zhu, Z. Z. Wu, D. J. Evans, and W. Q. Chu, "A wound field switched flux machine with field and armature windings separately wound in double stators," *IEEE Trans. Energy Convers.*, vol. 30, no. 2, pp. 772-783, Jun. 2015.
- [ZHU15c] S. Zhu, M. Cheng, W. Hua, X. Cai, and M. Tong, "Finite element analysis of flux-switching PM machine considering oversaturation and irreversible demagnetization", *IEEE Trans. Magn.*, vol. 51, no. 11, Nov. 2015, Art. ID 7403404.
- [ZHU15d] Z. Q. Zhu, and X. Liu, "Novel stator electrically field excited synchronous machines without rare-earth magnet", *IEEE Trans. Magn.*, vol. 51, no. 4, pp. 1-9, Apr. 2015.
- [ZHU15e] Z. Q. Zhu, M. M. J. Al-Ani, X. Liu, and B. Lee, "A mechanical flux weakening method for switched flux permanent magnet machines," *IEEE Trans. Energy Convers.*, vol. 30, no. 2, pp. 806-815, Jun. 2015.
- [ZHU16a] D. Zhu, F. Yang, Y. Du, F. Xiao, and Z. Ling, "An axial-field flux modulation magnetic gear," *IEEE Trans. Trans. Appl. Supercond.*, vol. 26, no. 4, Jun. 2016, Art. ID 0604405.
- [ZHU16b] Z. Q. Zhu, B. Lee and X. Liu, "Integrated field and armature current control strategy for variable flux reluctance machine using open winding," *IEEE Trans. Ind. Appl.*, vol. 52, no. 2, pp. 1519-1529, Mar./Apr. 2016.
- [ZHU93a] Z. Q. Zhu, D. Howe, E. Bolte, and B. Ackermann, "Instantaneous magnetic field distribution in brushless permanent magnet DC motors. I. Open-circuit field," *IEEE Trans. Magn.*, vol. 29, no. 1, pp. 124-135, Jan. 1993.
- [ZHU93b] Z. Q. Zhu, and D. Howe, "Instantaneous magnetic field distribution in brushless permanent magnet DC motors. II. Armature reaction field," *IEEE Trans. Magn.*, vol. 29, no. 1, pp. 136-142, Jan. 1993.
- [ZHU93c] Z. Q. Zhu, and D. Howe, "Instantaneous magnetic field distribution in brushless permanent magnet DC motors. III. Effect of stator slotting," *IEEE Trans. Magn.*, vol. 29, no. 1, pp. 143-151, Jan. 1993.

- [ZHU93D] Z. Q. Zhu, and D. Howe, "Instantaneous magnetic field distribution in brushless permanent magnet DC motors. IV. Magnetic field on load," *IEEE Trans. Magn.*, vol. 29, no. 1, pp. 152-158, Jan. 1993.
- [ZON14a] Z. Y. Zong, L. Quan, and Y. M. Ge, "A new double-stator flux-switching permanent magnet machine for electric vehicle application," in *Rec. of IEEE Inter. Magn. Conf.*, Dresden, Germany, 2014, pp. GP-5.
- [ZUL10a] A. Zulu, B. C. Mecrow, and M. Armstrong, "A wound-field three-phase flux-switching synchronous motor with all excitation sources on the stator," *IEEE Trans. Ind. Appl.*, vol. 46, no. 6, pp. 2363-2371, Nov./Dec. 2010.

Appendix A Air-Gap MMF and Field Harmonics of Armature Excitation in 12-Stator-Pole SFPM Machines Having 11-, 13- And 14-Rotor-Pole Rotors

Fig. A.1 illustrates the air-gap MMF of armature excitation in 12/11-pole SFPM machine accounting for the stator saliency. For 12/13- and 12/14-pole SFPM machines, the air-gap magnetomotive forces (MMFs) of armature excitation waveforms are similar to those of 12/11- and 12/10-pole SFPM machines, except the exchanging of B- and C-phase MMFs.

The Fourier series expansion of the air-gap MMF in 12/11-, 12/13- and 12/14-pole SFPM machines are given by (A.1)-(A.3).

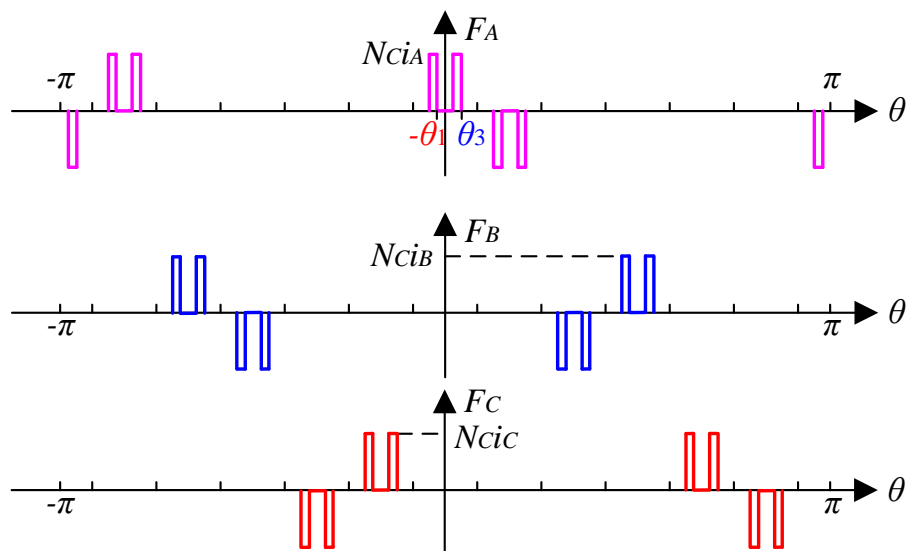


Fig. A.1 Air-gap MMF of armature excitation in 12/11-pole SFPM machine accounting for the stator saliency.

$$\left\{ \begin{array}{l}
F_{ABC}(\theta, t) = \sum_{q=1}^{\infty} \left[\frac{3S_{ABC}}{2} M_{ABCq} \sin(\xi) \right] \\
S_{ABC} = \frac{8\sqrt{2}N_c I_{rms}}{\pi} \\
M_{ABCq} = \frac{1}{q} \sin\left(\frac{q\pi}{2}\right) \sin\left(\frac{q\pi}{12}\right) [\sin(q\theta_3) - \sin(q\theta_1)] \\
\xi = \begin{cases} q\left(\theta + \frac{5\pi}{12}\right) + N_r \Omega_r t, q = 6r - 5 \\ -q\left(\theta + \frac{5\pi}{12}\right) + N_r \Omega_r t, q = 6r - 1 \\ 0, q = \text{else} \end{cases}
\end{array} \right. \quad (\text{A.1})$$

$$\left\{ \begin{array}{l}
F_{ABC}(\theta, t) = \sum_{q=1}^{\infty} \left[\frac{3S_{ABC}}{2} M_{ABCq} \sin(\xi) \right] \\
S_{ABC} = \frac{8\sqrt{2}N_c I_{rms}}{\pi} \\
M_{ABCq} = \frac{1}{q} \sin\left(\frac{q\pi}{2}\right) \sin\left(\frac{q\pi}{12}\right) [\sin(q\theta_3) - \sin(q\theta_1)] \\
\xi = \begin{cases} -q\left(\theta + \frac{5\pi}{12}\right) + N_r \Omega_r t, q = 6r - 5 \\ q\left(\theta + \frac{5\pi}{12}\right) + N_r \Omega_r t, q = 6r - 1 \\ 0, q = \text{else} \end{cases}
\end{array} \right. \quad (\text{A.2})$$

$$\left\{ \begin{array}{l}
F_{ABC}(\theta, t) = \frac{3S_{ABC}}{2} \sum_{q=1}^{\infty} [M_{ABCq} \sin(\xi)] \\
S_{ABC} = \frac{2\sqrt{2}N_c I_{rms}}{\pi} \\
M_{ABCq} = \frac{1}{q} [\sin(4q\theta_3) - \sin(4q\theta_1)] \\
\xi = \begin{cases} 4q\theta + N_r \Omega_r t, q = 3r - 2 \\ -4q\theta + N_r \Omega_r t, q = 3r - 1 \\ 0, q = 3r \end{cases}
\end{array} \right. \quad (\text{A.3})$$

For the 11-rotor-pole one, when $q=6r-5$ ($q=1, 7, 13, \dots$) B_{ABC} is given by (A.4) and (A.5). When $q=6r-1$ ($q=5, 11, 17, \dots$), B_{ABC} can also be expressed by (A.4) and (A.5) with the coefficient of q multiplied by “-1”.

$$\begin{aligned}
 & B_{ABC}(\theta, t) \\
 &= \frac{3P_0 S_{ABC}}{2} \sum_{q=1}^{\infty} \left\{ M_{ABCq} \cos \left[q\theta + N_r \Omega_r t + \frac{(5q-6)\pi}{12} \right] \right\} \\
 &+ \frac{3S_{ABC} S_2}{4} \sum_{q=1}^{\infty} \sum_{k=1}^{\infty} [M_{ABCq} M_{2k} (\cos \gamma_1 + \cos \gamma_2)]
 \end{aligned} \tag{A.4}$$

$$\begin{cases}
 \gamma_1 = (kN_r + q) \left[\theta - \frac{(k-1)N_r \Omega_r t + kN_r \theta_0 - \frac{(5q-6)\pi}{12}}{kN_r + q} \right] \\
 \gamma_2 = (kN_r - q) \left[\theta - \frac{(k+1)N_r \Omega_r t + kN_r \theta_0 + \frac{(5q-6)\pi}{12}}{kN_r - q} \right]
 \end{cases} \tag{A.5}$$

Table A.1 Characteristics of Armature Excitation Air-Gap Flux Density Elements in 12/11-Pole SFPM Machines

q	Pole-Pairs	Rotating Speed/ $N_r \Omega_r$
$q=6r-5$	q	$-\frac{1}{q}$
	$kN_r + q$	$\frac{k-1}{kN_r + q}$
	$ kN_r - q $	$\frac{k+1}{kN_r - q}$
$q=6r-1$	q	$\frac{1}{q}$
	$ kn_r - q $	$\frac{k-1}{kN_r - q}$
	$kN_r + q$	$\frac{k+1}{kN_r + q}$

For the 13-rotor-pole one, when $q=6r-5$ ($q=1, 7, 13, \dots$) B_{ABC} is given by (A.6) and (A.7). When $q=6r-1$ ($q=5, 11, 17, \dots$), B_{ABC} can also be expressed by (A.6) and (A.7) with the coefficient of q multiplied by “-1”.

$$\begin{aligned}
 & B_{ABC}(\theta, t) \\
 &= \frac{3P_0 S_{ABC}}{2} \sum_{q=1}^{\infty} \left\{ M_{ABCq} \cos \left[q\theta - N_r \Omega_r t + \frac{(5q+6)\pi}{12} \right] \right\} \\
 &+ \frac{3S_{ABC} S_2}{4} \sum_{q=1}^{\infty} \sum_{k=1}^{\infty} [M_{ABCq} M_{2k} (\cos \xi_1 + \cos \xi_2)]
 \end{aligned} \tag{A.6}$$

$$\begin{cases}
 \xi_1 = (kN_r - q) \left[\theta - \frac{(k-1)N_r \Omega_r t + kN_r \theta_0 + \frac{(5q+6)\pi}{12}}{kN_r - q} \right] \\
 \xi_2 = (kN_r + q) \left[\theta - \frac{(k+1)N_r \Omega_r t + kN_r \theta_0 - \frac{(5q+6)\pi}{12}}{kN_r + q} \right]
 \end{cases} \tag{A.7}$$

Table A.2 Characteristics of Armature Excitation Air-Gap Flux Density Elements in 12/13-Pole SFPM Machines

q	Pole-Pairs	Rotating Speed/ $N_r \Omega_r$
$q=6r-5$	q	$\frac{1}{q}$
	$ kN_r - q $	$\frac{k-1}{kN_r - q}$
	$kN_r + q$	$\frac{k+1}{kN_r + q}$
$q=6r-1$	q	$-\frac{1}{q}$
	$kN_r + q$	$\frac{k-1}{kN_r + q}$
	$ kN_r - q $	$\frac{k+1}{kN_r - q}$

For the 14-rotor-pole one, when $q=3r-2$ ($q=1, 4, 7, \dots$), B_{ABC} is given by (A.8) and (A.9). When $q=3r-1$ ($q=2, 5, 8, \dots$), B_{ABC} can also be expressed by (A.8) and (A.9) with the coefficient of q multiplied by “-1”.

$$\begin{aligned}
 & B_{ABC}(\theta, t) \\
 &= \frac{3P_0 S_{ABC}}{2} \sum_{q=1}^{\infty} \left\{ M_{ABCq} \cos \left[4q\theta + N_r \Omega_r t - \frac{\pi}{2} \right] \right\} \\
 &+ \frac{3S_{ABC} S_2}{4} \sum_{q=1}^{\infty} \sum_{k=1}^{\infty} [M_{ABCq} M_{2k} (\cos \sigma_1 + \cos \sigma_2)]
 \end{aligned} \tag{A.8}$$

$$\begin{cases}
 \sigma_1 = (kN_r + 4q) \left[\theta - \frac{(k-1)N_r \Omega_r t + kN_r \theta_0 + \frac{\pi}{2}}{kN_r + 4q} \right] \\
 \sigma_2 = (kN_r - 4q) \left[\theta - \frac{(k+1)N_r \Omega_r t + kN_r \theta_0 - \frac{\pi}{2}}{kN_r - 4q} \right]
 \end{cases} \tag{A.9}$$

Table A.3 Characteristics of Armature Excitation Air-Gap Flux Density Elements in 12/14-Pole SFPM Machines

q	Pole-Pairs	Rotating Speed/ $N_r \Omega_r$
$q=3r-2$	$4q$	$-\frac{1}{4q}$
	$kN_r + 4q$	$\frac{k-1}{kN_r + 4q}$
	$ kN_r - 4q $	$\frac{k+1}{kN_r - 4q}$
$q=3r-1$	$4q$	$\frac{1}{4q}$
	$ kN_r - 4q $	$\frac{k-1}{kN_r - 4q}$
	$kN_r + 4q$	$\frac{k+1}{kN_r + 4q}$

Appendix B Partitioned Stator Flux Reversal Permanent Magnet Machine

B.1 Introduction

In this appendix, for increasing the torque density of flux reversal permanent magnet (PM) (FRPM) machines shown in Fig. B.1(a), a partitioned stator FRPM (PS-FRPM) machine is introduced, as shown in Fig. B.1(b), based on the concept of a novel electrical machine having a separate PM excitation stator proposed in [EVA15a]. The PS-FRPM machine has two stators, *i.e.* one stator having the armature windings and another stator having the PMs. In Fig. B.1(b), the armature windings are on the outer stator, while the PMs are on the inner stator. Compared with the conventional double-stator configuration, the PMs and the armature windings in PS-FRPM machines are geometrically separated. The inner stator of PS-FRPM machine becomes a typical surface-mounted PM configuration and is much easier to make and cool since the PMs are physically separately from the armature windings but remain stationary.

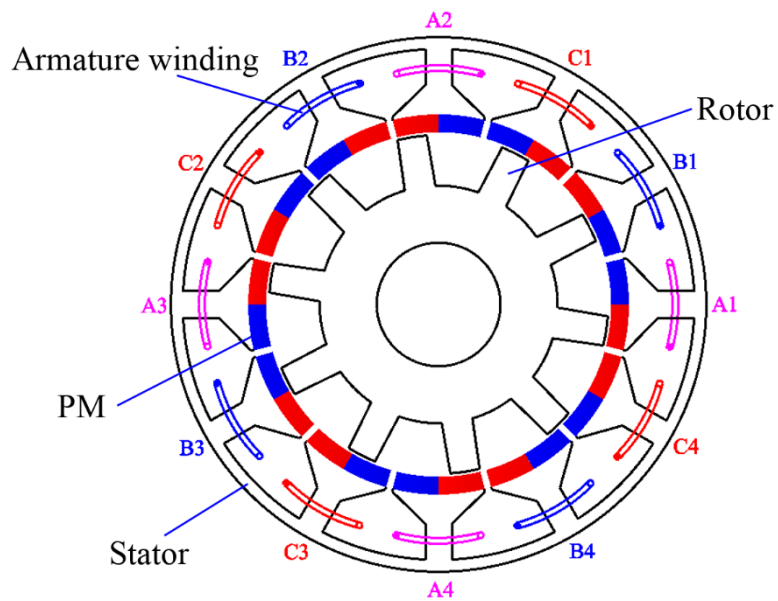
This appendix is organized as follows. The operation principle of the PS-FRPM machine will be introduced in section B.2. In section B.3, different stator/rotor pole combinations of PS-FRPM machines are investigated in terms of quantitatively compared. In section B.5, the influence of PM thickness on average electromagnetic torque is investigated in both the PS-FRPM and conventional FRPM machines when both types of machines are optimized. The experimental validation based on two prototype machines is presented in section B.6 followed by the conclusions.

B.2 Operation Principle

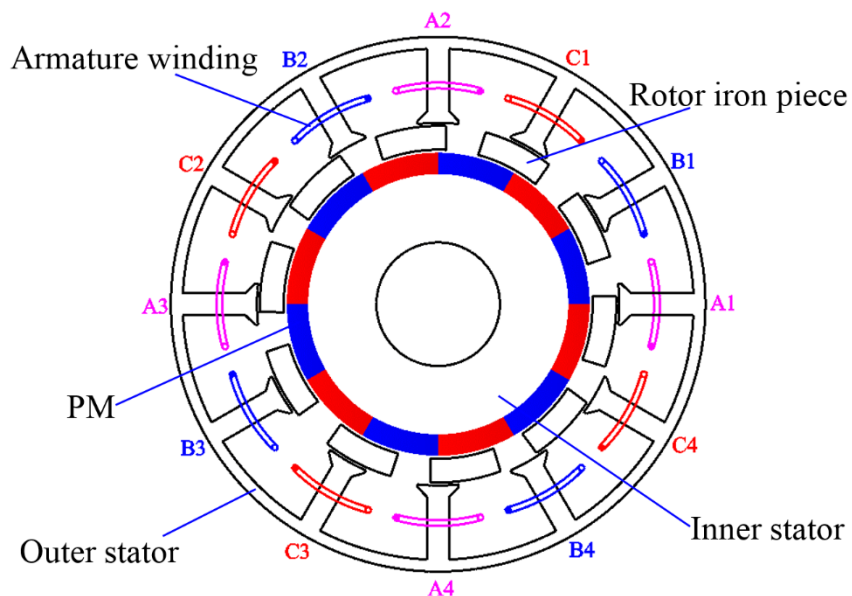
The 12/10-stator/rotor-pole PS-FRPM machine is illustrated in Fig. B.1(b), where PMs and armature windings are physically separated. The inner stator with surface-mounted PMs is similar to the rotor of a conventional surface-mounted PM machine [1]. Therefore, it is easy to mount the PMs in the PS-FRPM machine. Furthermore, the number of magnets in the PS-FRPM machine is half of the magnet number in conventional FRPM machines, since the adjacent two PMs having the same polarity become one single piece. This further eases the manufacturing. Between the outer stator and the inner stator, the rotor iron pieces are sandwiched.

Despite various differences between the PS-FRPM and conventional FRPM machines, they still share the same operation principle. In PS-FRPM machine, the rotor position θ_e in electric degrees can be given by (B.1), where N_r is rotor pole number and θ_m is rotor position in mechanical degrees.

$$\theta_e = N_r \theta_m \quad (\text{B.1})$$



(a) FRPM machine



(b) PS-FRPM machine

Fig. B.1. Cross-sections of 12/10-pole FRPM and PS-FRPM machines.

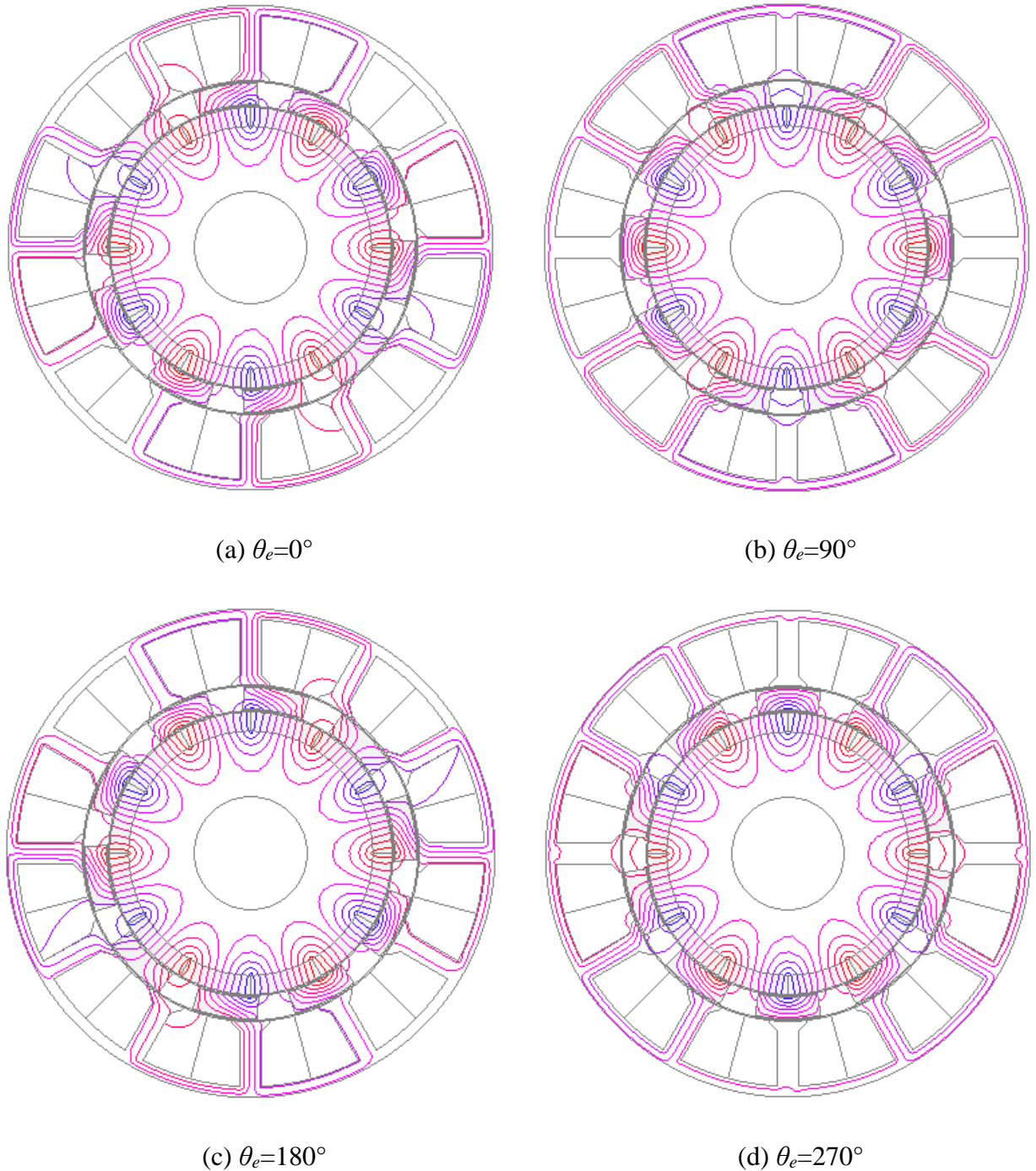
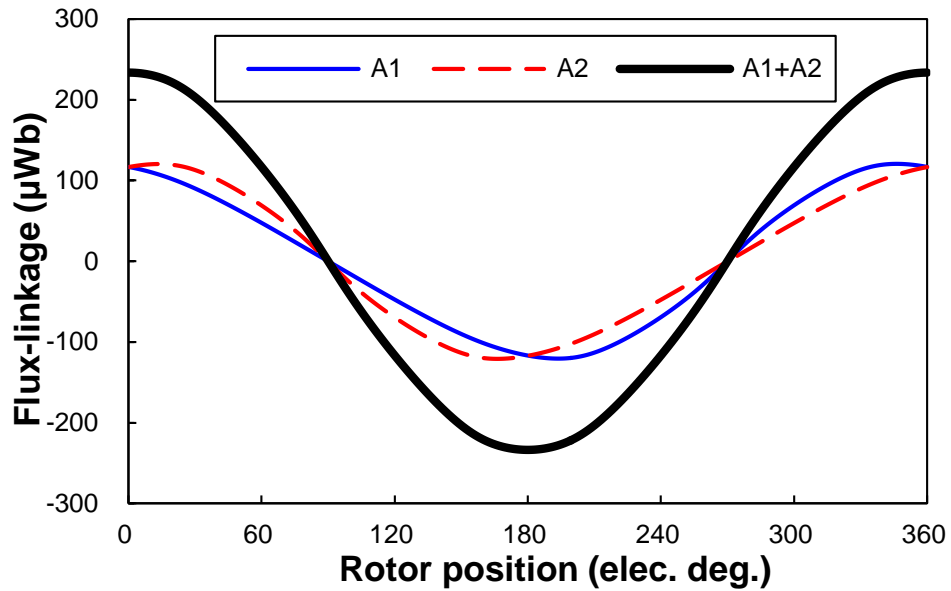


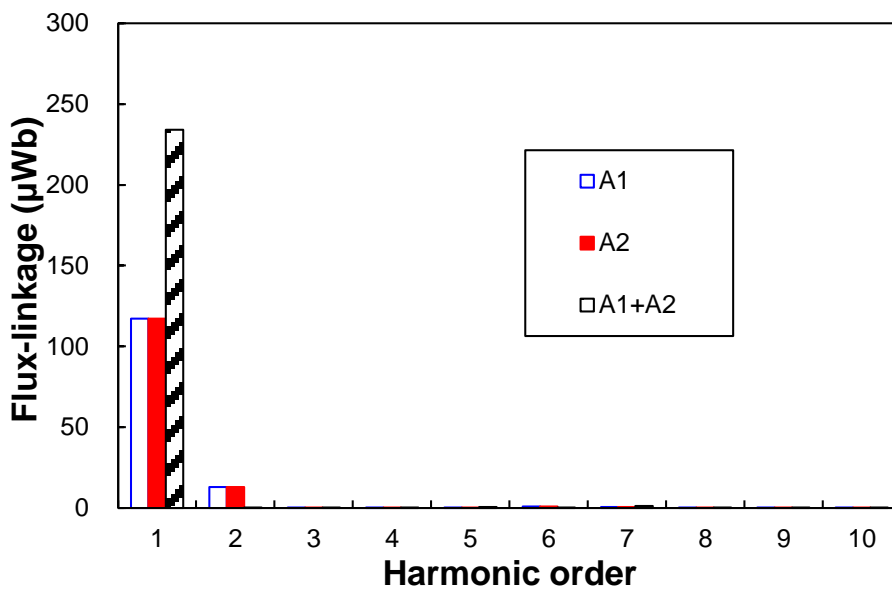
Fig. B.2. Open-circuit flux distributions of 12/10 stator/rotor-pole PS-FRPM machine at four typical rotor positions.

For a 12/10 stator/rotor pole PS-FRPM machine, as shown in Fig. B.2(a), when $\theta_e=0$, the phase A flux-linkage of Φ_A reaches positive maximum. After the rotor rotates to 90° electric degrees, Fig. B.2(b), the PM flux is short-circuited and $\Phi_A=0$. When $\theta_e=180^\circ$, Fig. B.2(c), Φ_A becomes negative maximum. Φ_A is 0 again when $\theta_e=270^\circ$, Fig. B.2(d). Therefore, a bipolar phase flux-linkage can be obtained in a PS-FRPM machine.

The flux-linkage waveforms and spectra of coils A1, A2 and their sum (half of phase A) of the 12/10-pole PS-FRPM machine are shown in Fig. B.9. N_c is the number of turns in each armature coil. Although there are even flux-linkage harmonics in coils A1 and A2, they will be cancelled when A1 and A2 are connected in series.



(a) Waveforms



(b) Spectra

Fig. B.3. Flux-linkages of coils A1, A2 and their sum (half of phase A) in 12/10-pole PS-FRPM machine, $N_c=1$.

B.3 Stator and Rotor Pole Combinations

The influence of stator and rotor pole number combinations on electromagnetic performance is investigated based on 12-stator-pole PS-FRPM machines. Theoretically, for a 3-phase machine, there are a lot of feasible combinations of stator and rotor pole numbers in PS-FRPM machines. For N_s/N_r -stator/rotor-pole PS-FRPM machine, the pitch factor of each coil can be given by (B.2), in which the fundamental pitch factor k_{pv} increases when the stator and rotor pole numbers differ less. Therefore, to obtain a larger fundamental pitch factor, 12-stator-pole PS-FRPM machines having 10-, 11-, 13- and 14-rotor-pole are selected for analysis in this section.

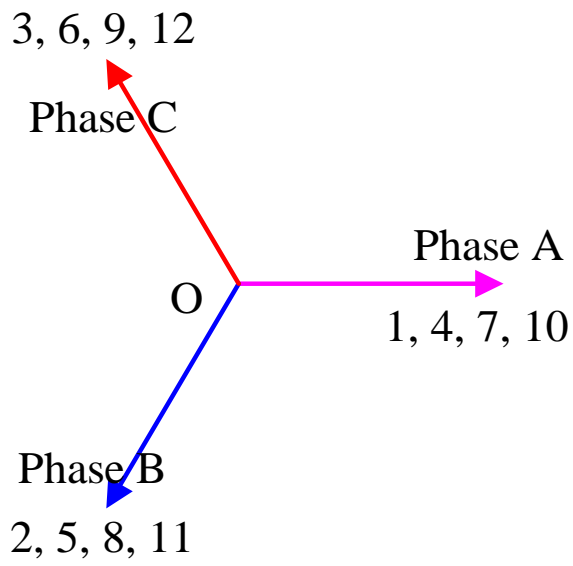
$$k_{pv} = \cos[v\pi(\frac{N_r}{N_s} - 1)] \quad (\text{B.2})$$

where v is the harmonic order. N_s is the stator pole number.

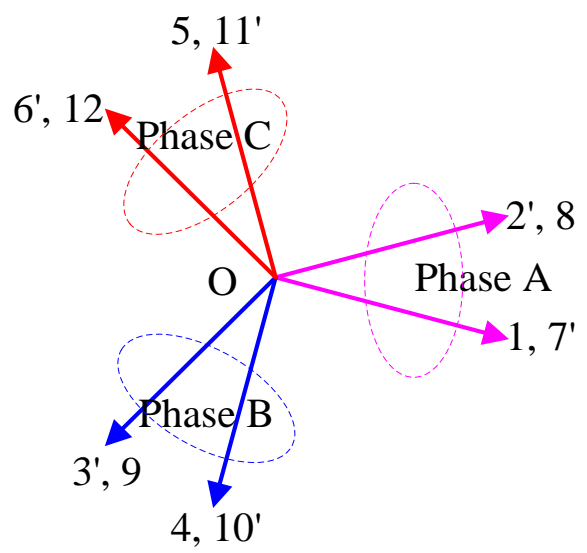
In order to connect the armature coils belong to the same phase appropriately, coil back-EMF vectors of these four PS-FRPM machines are obtained and shown in Fig. B.4. The open-circuit flux distributions of these optimal designs are given in Fig. B.5.

All these four 12-stator-pole PS-FRPM machines are optimized for the maximum torque when having 45mm outer radius, 10.4mm inner radius, 25mm effective axial length, 20W rated copper loss. It should be noted that for a fair comparison, the PM volume of PS-SPM machines are set to be the same with the conventional 12/10-pole FRPM machine. The parameters of the conventional 12/10-pole FRPM machine will be given later.

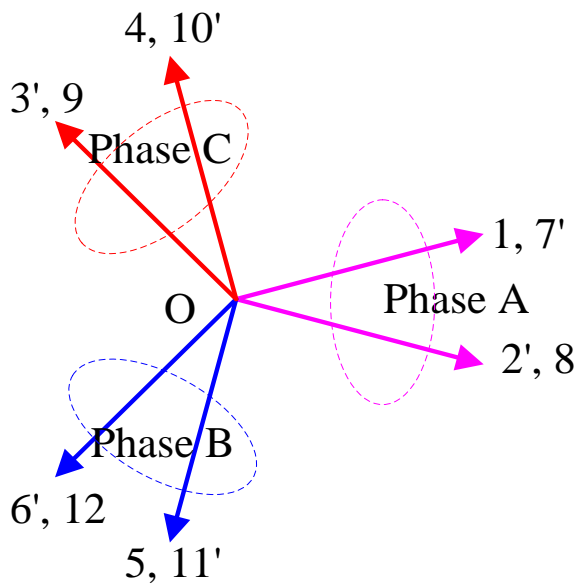
The design parameters of the PS-FRPM machines are illustrated in Fig. B.6 while their optimal values are listed in Table B.1. In Table B.1, the parameters from L_s to l_{otb} are fixed, as well as $\theta_{PM}=30^\circ$, whilst those from R_{osy} to θ_{ri} are optimized parameters. The influence of leading design parameters, such as air-gap radius, rotor pole radial thickness and pole arcs, on the electromagnetic torques in 12-stator-pole PS-FRPM machines with 10-, 11-, 13- and 14-rotor-poles are illustrated and analysed as follows.



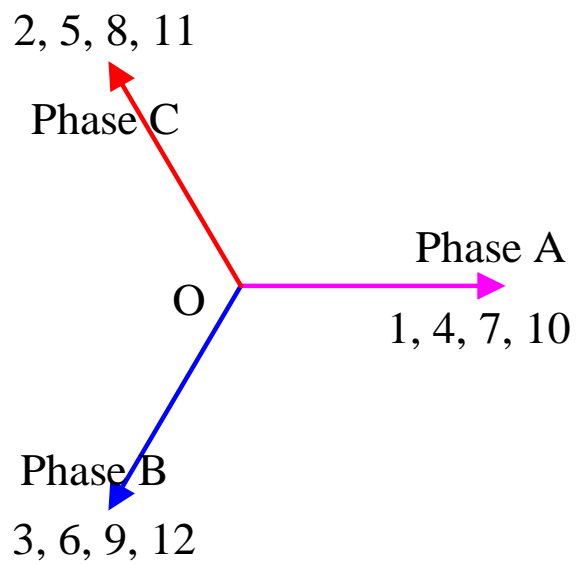
(a) 10-rotor-pole rotor



(b) 11-rotor-pole rotor

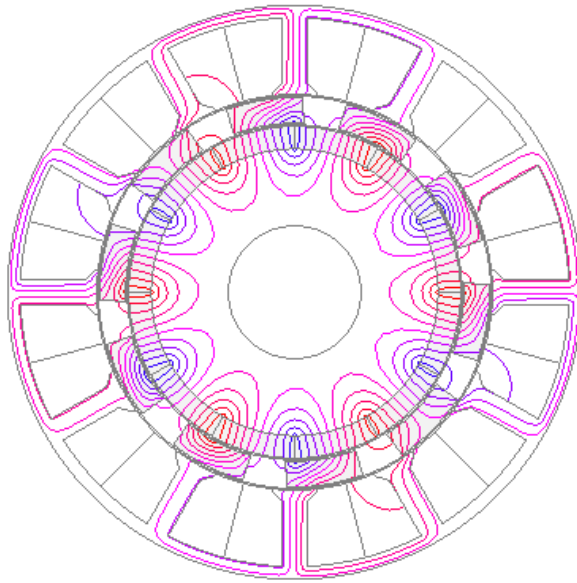


(c) 13-rotor-pole rotor

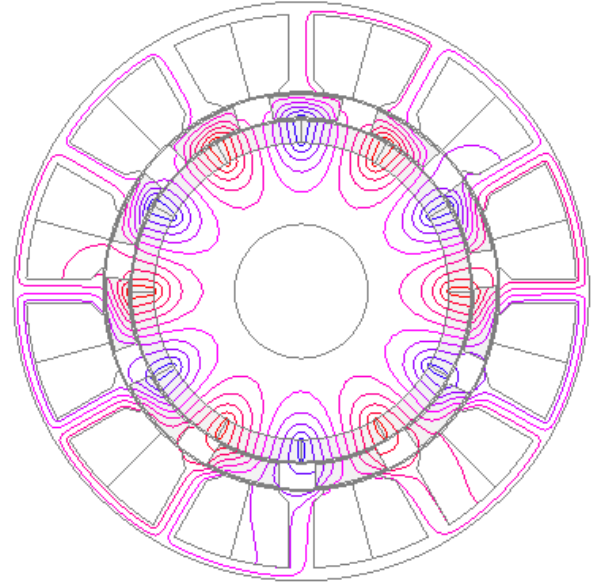


(d) 14-rotor-pole rotor

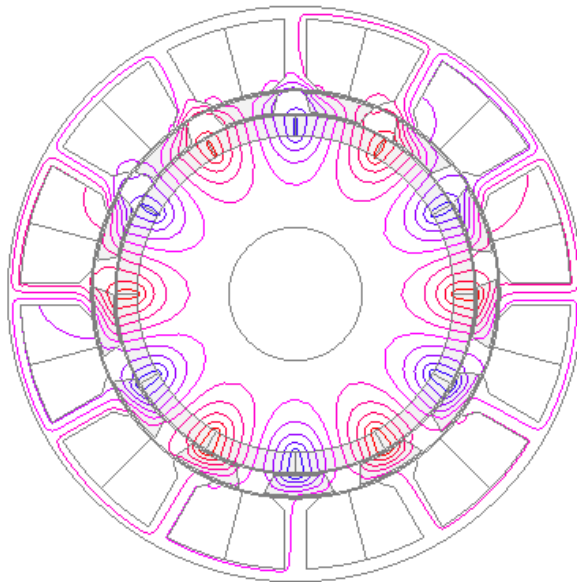
Fig. B.4. Coil back-EMF vectors for 12-stator-pole PS-FRPM machines with different rotor pole numbers.



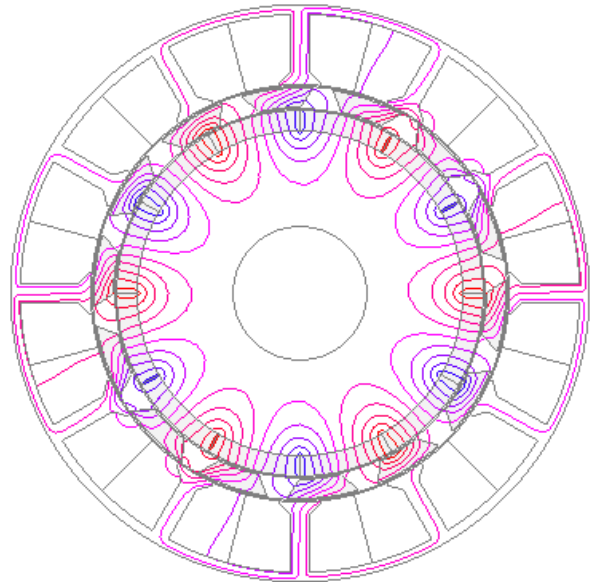
(a) 10-rotor-pole rotor



(b) 11-rotor-pole rotor



(c) 13-rotor-pole rotor



(b) 14-rotor-pole rotor

Fig. B.5. Open-circuit flux distributions of 12-stator-pole PS-FRPM machines with different rotor pole numbers ($\theta_e=0^\circ$).

Table B.1 Design Parameters of 12-Stator-Pole PS-FRPM Machines

Parameters	Unit	Value			
Rotor pole number, N_r	-	10	11	13	14
Stack length, L_s	mm	25			
Outer stator outer radius, R_{oso}	mm	45			
Inner stator inner radius, R_{isi}	mm	10.4			
Outer air-gap width, g_o	mm	0.5			
Inner air-gap width, g_i	mm	0.5			
Outer stator tip top length, l_{ott}	mm	0.5			
Outer stator tip bottom length, l_{otb}	mm	2			
PM arc, θ_{PM}	°	30			
Outer stator yoke radius, R_{osy}	mm	43	43	43	43.5
Outer stator inner radius, R_{osi}	mm	31	31	32	32.5
Rotor inner edge radius, R_{ri}	mm	26.5	27	28.5	29
Outer stator tooth arc, θ_{ost}	°	7	7	6	5
Outer stator tip arc, θ_{ot}	°	3	3	3	3
Rotor piece outer edge arc, θ_{ro}	°	23	22	20	20
Rotor piece inner edge arc, θ_{ri}	°	24	21	16	13

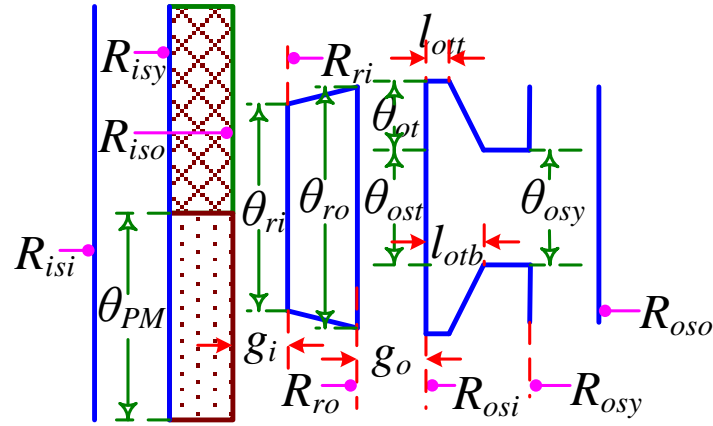
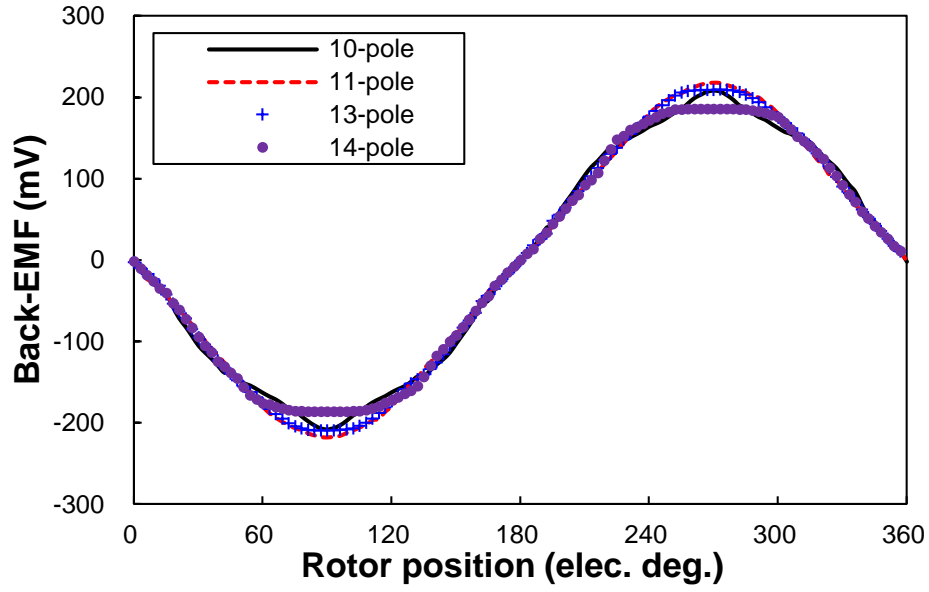


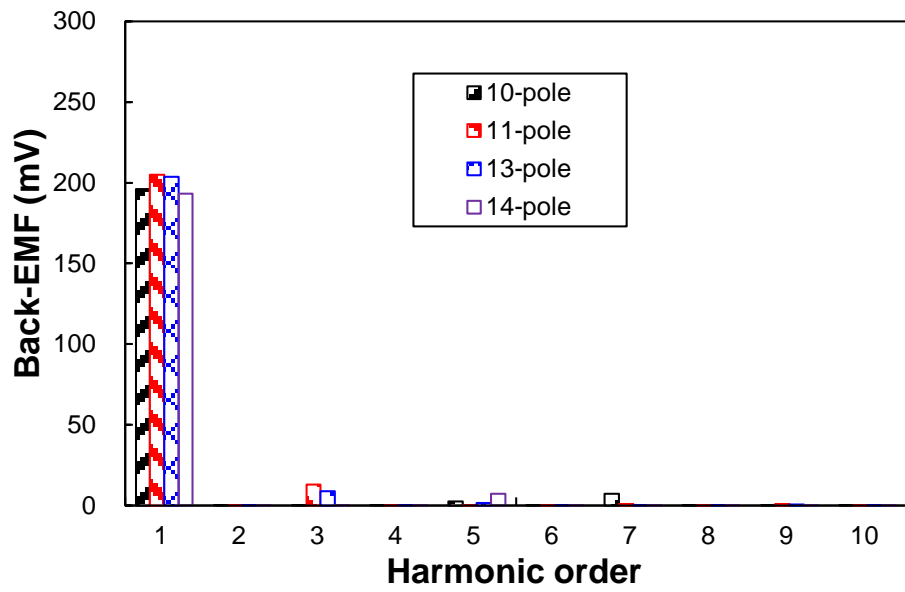
Fig. B.6. Illustration of design parameters in PS-FRPM machine.

B.4 Electromagnetic Performance

With all the PS-FRPM machines optimized, Fig. B.7 and Fig. B.8 show the phase back-EMF and cogging torque of the optimal designs. As shown in Fig. B.7(b), the 12/11-pole and 12/13-pole PS-FRPM machines exhibit larger fundamental back EMF, which implies that the 12/11- and 12/13-pole machines will potentially generate larger torque since as in the conventional FRPM machines the reluctance torque is negligible in PS-FRPM machines. Although 12/11- and 12/13-pole PS-FRPM machines have a 3rd harmonic in the phase back-EMFs, it will be eliminated in the line back-EMFs when Y-type winding connection is employed. For the 12/10- and 12/14-pole PS-FRPM machines, they have larger 5th and 7th harmonics, which implies larger torque ripples than 11- and 13-pole machines. The PMs in PS-FRPM machines result in cogging torque which will cause torque ripple, acoustic noise and vibration. As shown in Fig. B.8, the cogging torques in 10- and 14-pole machines are larger than those of 11- and 13-rotor-pole PS-FRPM machines. The reason is the larger ‘goodness’ factor, which is defined as the greatest common divisor of the stator slot number N_s and the rotor pole number N_r [ZHU00a], in 10- and 14-pole machines.

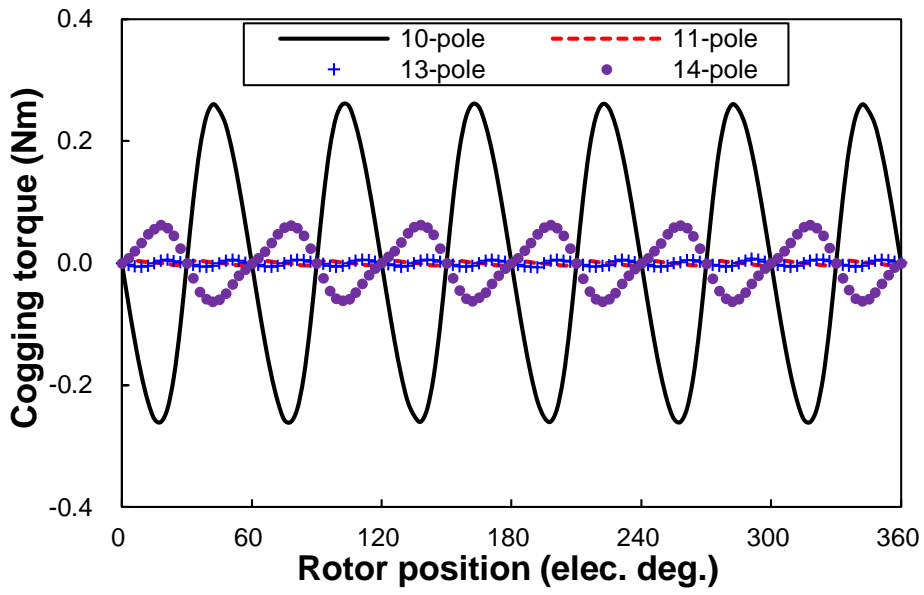


(a) Waveforms

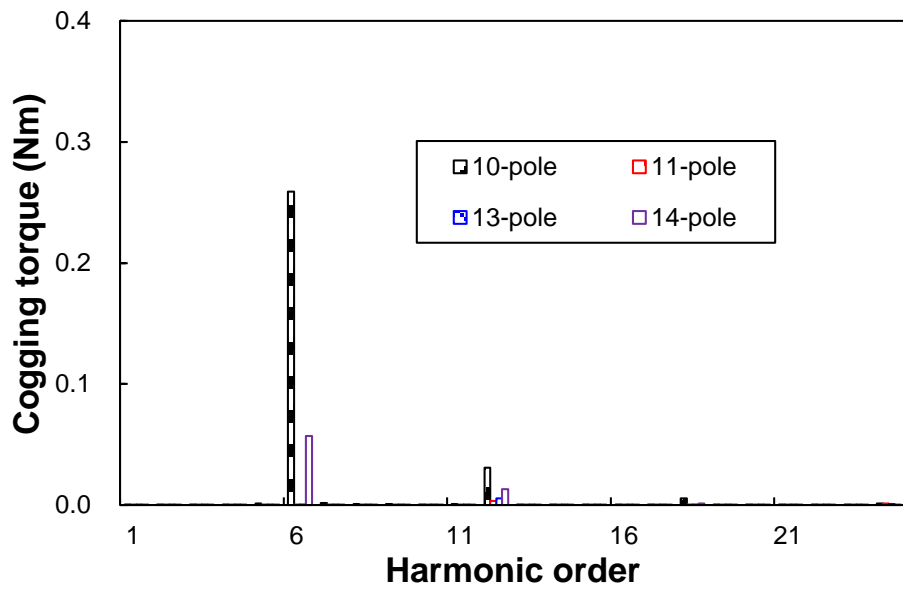


(b) Spectra

Fig. B.7. Phase back-EMF of PS-FRPM machines, $N_c=1$ @400rpm.

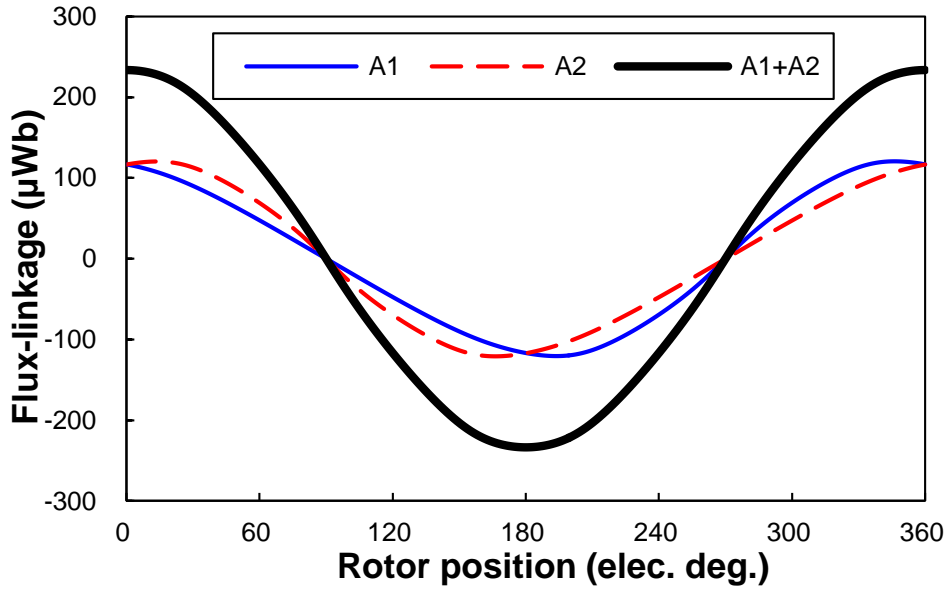


(a) Waveforms

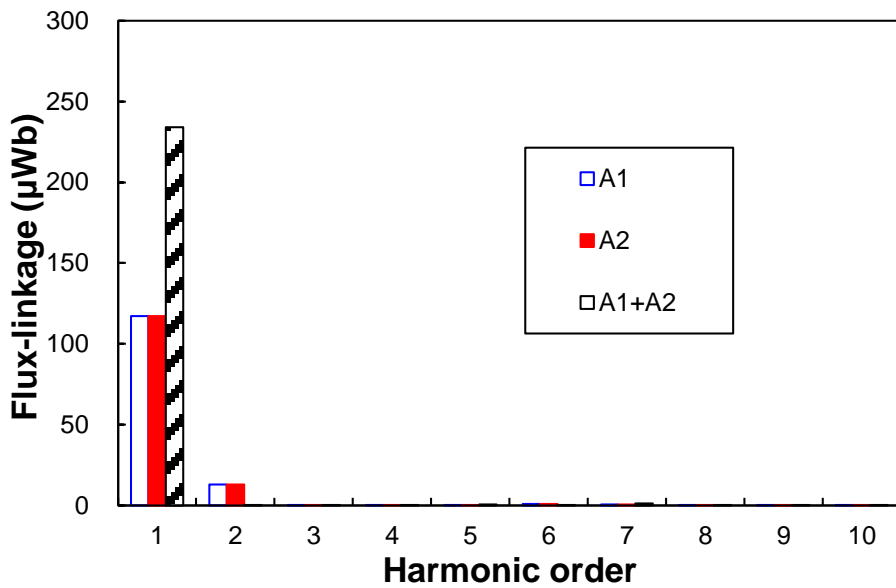


(b) Spectra

Fig. B.8. Cogging torque of PS-FRPM machines.



(a) Waveforms



(b) Spectra

Fig. B.9. Flux-linkages of coils A1, A2 and their sum (half of phase A) in 12/10-pole PS-FRPM machine, $N_c=1$.

In this section, the torque characteristics of the 12-stator-pole PS-FRPM machines having 10-, 11-, 13-, and 14-rotor-pole rotors will be comprehensively compared. In order to compare the torque ripple of the four analysed PS-FRPM machines and the conventional FRPM machine, the torque ripple coefficient T_r is given by,

$$T_r = \frac{T_{max} - T_{min}}{T_{avg}} \times 100\% \quad (\text{B.3})$$

where T_{max} , T_{min} and T_{avg} are maximum, minimum and average electromagnetic torques, respectively.

In Fig. B.10 and Table B.2, 11- and 13-rotor-pole PS-FRPM machines exhibit larger torque density, due to the larger fundamental back-EMF values as aforementioned in Fig. B.7(a). The 10- and 14-pole PS-FRPM machines have larger torque ripple than 11- and 13-pole PS-FRPM machines since the 10- and 14-pole machines have larger 5th and 7th back-EMF harmonics, Fig. B.7(b), as well as higher cogging torque, Fig. B.8(a). As shown in Fig. B.11, all PS-FRPM and FRPM machines in this chapter reach the maximum torque when the current angle is approximately 90 degrees, *i.e.* zero d -axis current due to negligible reluctance torque. Hence, all the machines are optimized when phase current and phase back-EMF have the same phase angle. The variation of average electromagnetic torque with the copper loss is shown in Fig. B.12. Over the whole investigated copper loss range, the 11- and 13-rotor pole PS-FRPM machines always exhibit larger electromagnetic torque than the 10- and 14-rotor pole PS-FRPM machines.

More importantly, all the PS-FRPM machines exhibit much larger torque density than the conventional 12/10-pole FRPM machine having single stator and the same PM volume. It is worth noting that the 12/10-pole FRPM machine is also optimized for the largest average torque with the same outer radius 45mm, inner radius 10.4mm, effective axial length 25mm and rated copper loss 20W as PS-FRPM machines. More importantly, for the 12/10-pole conventional FRPM machine, the optimal PM thickness should be 1.5mm and the average torque is 1.89Nm if the design parameters are optimized, which will be shown later. However, the 1.5mm thick PMs will be irreversibly demagnetized and also are mechanically too fragile. In order to avoid these, the PM thickness is chosen to be 3mm (13414.6 mm³ PM volume) to avoid these problems while other parameters are optimized. The optimised parameters based on 3mm PM thickness are stator yoke radius R_{sy} =43mm, stator inner radius R_{si} =32mm, stator tooth arc θ_{st} =8°, stator tip arc θ_{stip} =10°, and rotor pole arc θ_{rp} =10°.

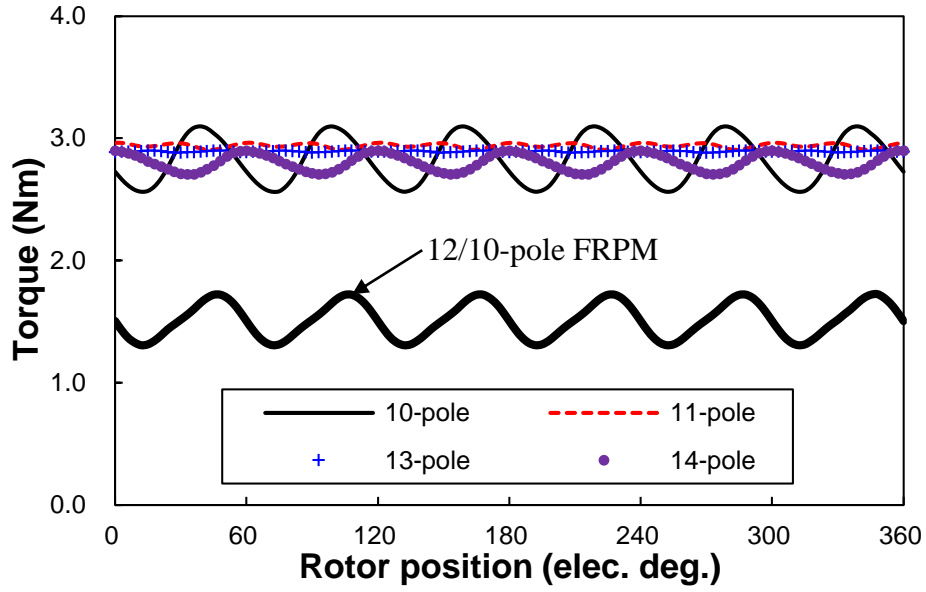


Fig. B.10. Rated electromagnetic torque waveforms.

Table B.2 Torque Characteristics of 12-Stator-Pole PS-FRPM and 12/10-Pole FRPM Machines

Item	12-stator-pole PS-FRPM				FRPM
	10	11	13	14	
N_r	10	11	13	14	10
T_{max} (Nm)	3.10	2.96	2.90	2.90	1.72
T_{min} (Nm)	2.56	2.91	2.88	2.71	1.31
T_{avg} (Nm)	2.83	2.94	2.89	2.81	1.51
T_r (%)	18.95	1.87	0.62	6.96	27.65

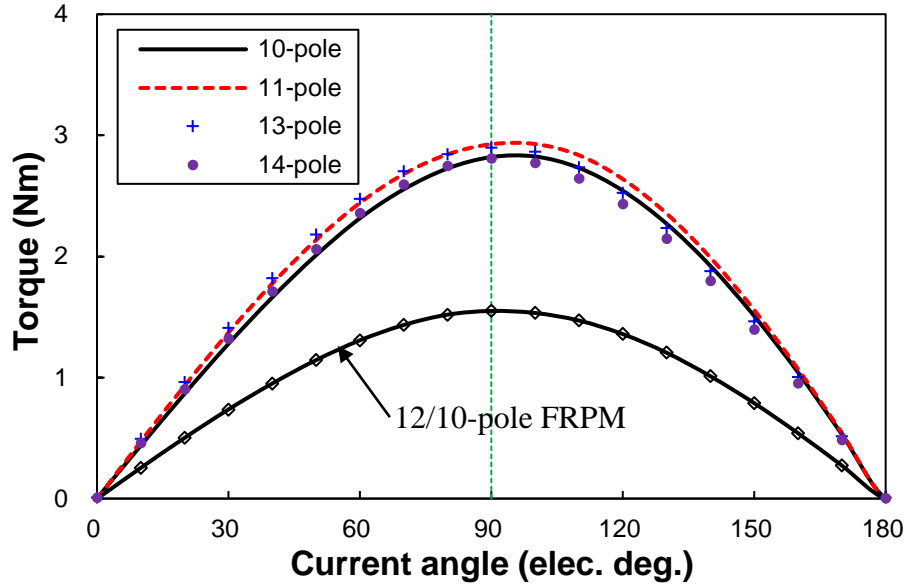


Fig. B.11. Variation of average electromagnetic torque against current angle in 12-stator-pole PS-FRPM machines with different rotor pole numbers and 12/10-pole FRPM machine.

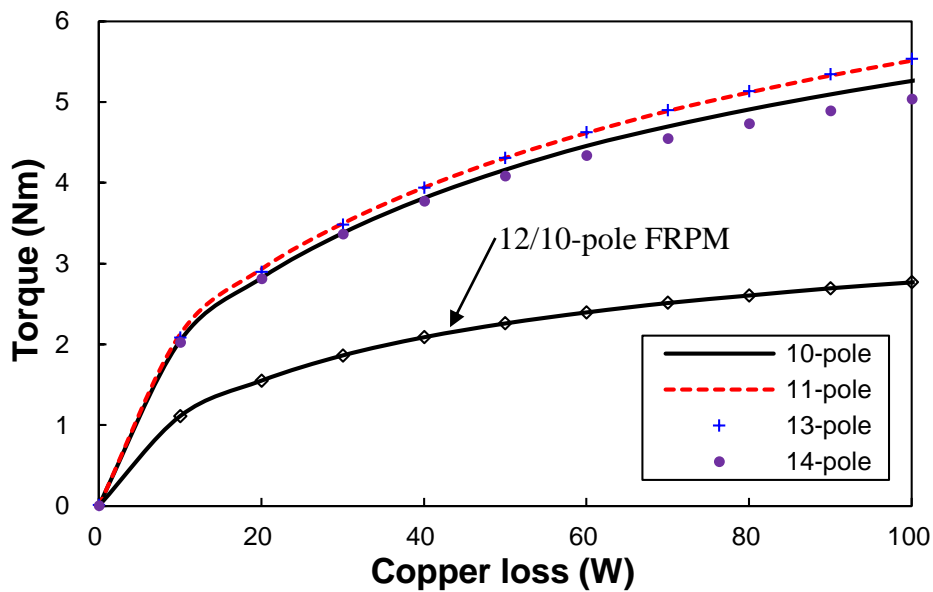


Fig. B.12. Variation of electromagnetic torque against copper loss in 12-stator-pole PS-FRPM machines with different rotor pole numbers and 12/10-pole FRPM machine.

B.5 Influence of Leading Design Parameters

The influence of split ratio, which is defined in (B.4), on the torque of PS-FRPM machines is shown in Fig. B.13.

$$\gamma_{sp} = \frac{R_{out}}{R_{oso}} \quad (\text{B.4})$$

where R_{out} is the radius of outer air-gap.

A larger split ratio will reduce the armature slot area and hence the electrical load but increase the air-gap diameter and PM flux. Hence, for all the combinations, the torque increases first and then decreases with the split ratio, as shown in Fig. B.13. The optimal split ratio increases slightly with the rotor pole number. However, for all the four machines, the optimal split ratios are close to 0.7.

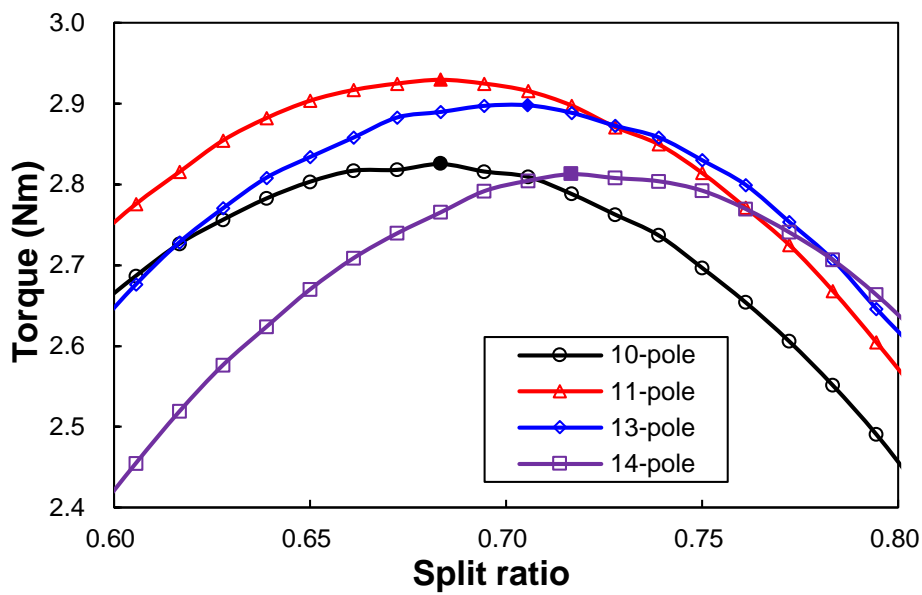


Fig. B.13. Average electromagnetic torque variation with split ratio.

Fig. B.14 shows the relationship between the average electromagnetic torque and the rotor radial thickness in PS-FRPM machines. It can be observed that the optimal rotor radial thickness is smaller when the rotor pole number is higher. The optimal rotor radial thickness is 4 mm for the 10-pole machine, 3.5 mm for the 11-pole machine, and 3 mm for the 13- and 14-pole machines.

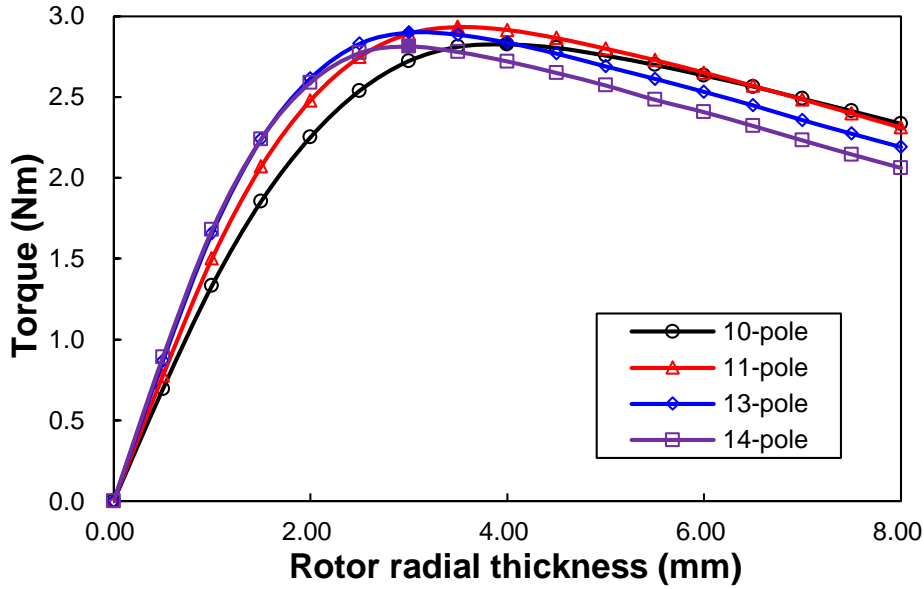


Fig. B.14. Average electromagnetic torque variation and rotor radial thickness.

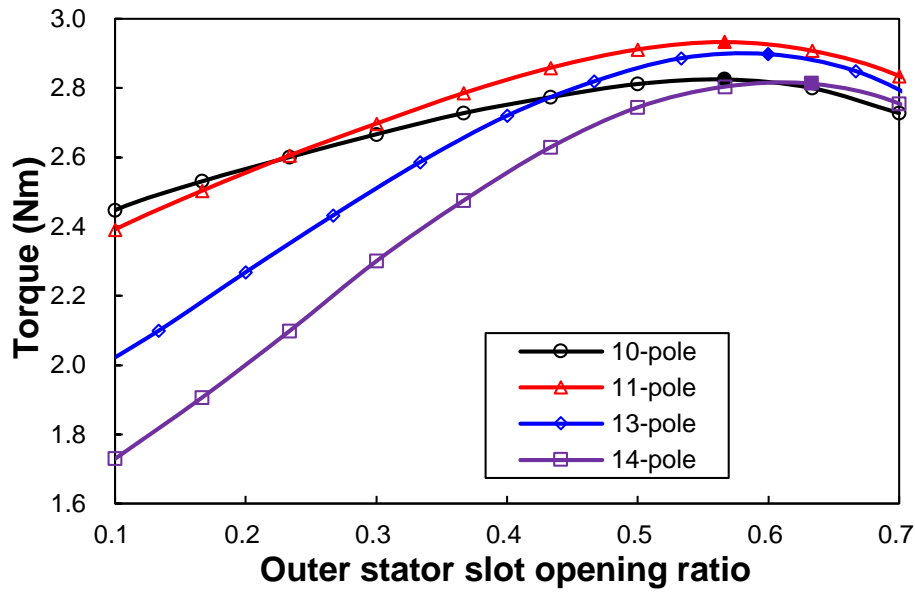


Fig. B.15. Average electromagnetic torque against slot opening in outer stator.

In PS-FRPM machines, the flux leakage between outer stator teeth is higher if the slot opening is smaller. However, the flux focusing effect will be less if the slot opening is bigger. As shown in Fig. B.15, for 12-stator-pole with 10-, 11-, 13- and 14-rotor-pole PS-FRPM machines, the optimal outer stator slot opening ratio, which is defined as the ratio of the slot opening to the stator pitch of the outer stator, is ~ 0.6 . This optimal slot opening in PS-FRPM machines are significantly larger than the optimal slot opening in the conventional 12/10-pole FRPM machine shown in Fig. B.1(a) since the PM width in conventional FRPM machine is

linked to the slot opening whilst it is independent in PS-FRPM machine.

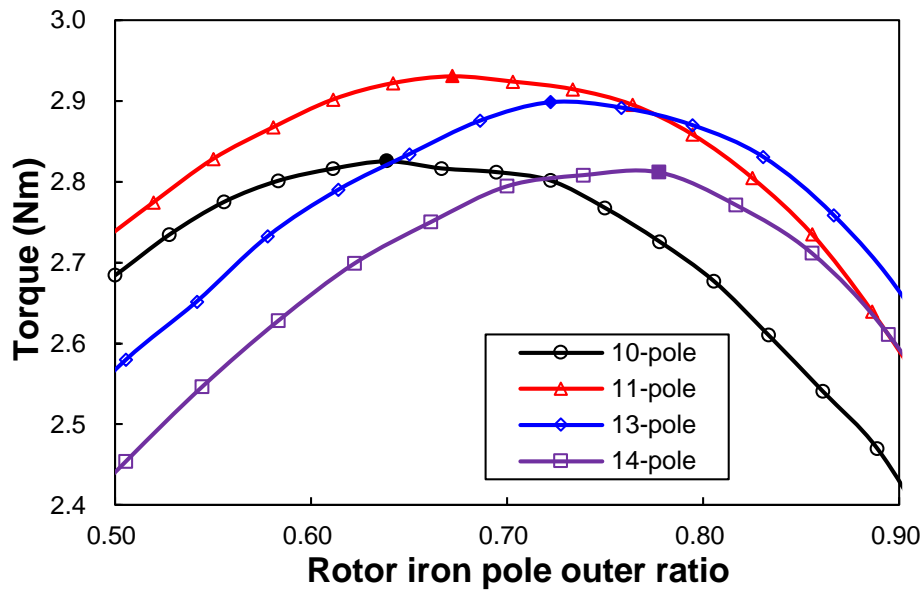


Fig. B.16. Average electromagnetic torque variation with rotor outer iron pole arc ratio.

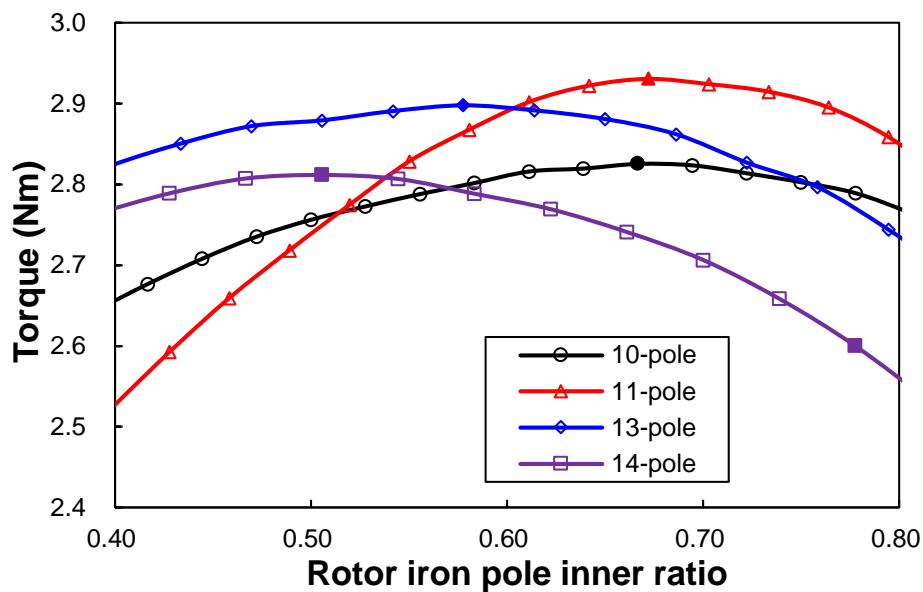


Fig. B.17. Average electromagnetic torque variation with rotor inner iron pole arc ratio.

Fig. B.16 and Fig. B.17 show the relationships between the electromagnetic torque and the rotor outer and inner iron pole arc ratios which are defined as the ratio of rotor pole arc to the rotor pitch, respectively. Obviously, flux focusing effect will be less with smaller iron pole arc ratios, whilst larger iron pole arc ratios will result in more flux leakage between rotor iron pieces. As shown in Fig. B.16, the optimal rotor outer iron pole arc ratio increases with the rotor pole number, viz. 0.64, 0.67, 0.72, and 0.78 for 10-, 11-, 13- and 14-rotor pole machines,

respectively. For the rotor inner iron pole arc ratios, they are 0.67, 0.67, 0.57 and 0.51, respectively.

As aforementioned, in the conventional 12/10-pole FRPM machine, the PM thickness is not the optimal value in terms of the torque density. Here, the influence of PM thickness on average electromagnetic torque is investigated in both the PS-FRPM and conventional FRPM machines when all the other parameters remain the same as the optimal values listed in Table B.1. The variation of the average torque with the PM thickness is shown in Fig. B.18. It shows that the average electromagnetic torque in PS-FRPM machines increases and then saturates with the PM thickness. However, for the conventional FRPM machine, the torque first increases and then decreases when the PM thickness is higher since the PMs will directly affect the stator slot area and the rotor outer diameter. These have been overcome in the PS-FRPM machines due to partitioned stator and physical separation of armature windings and PMs.

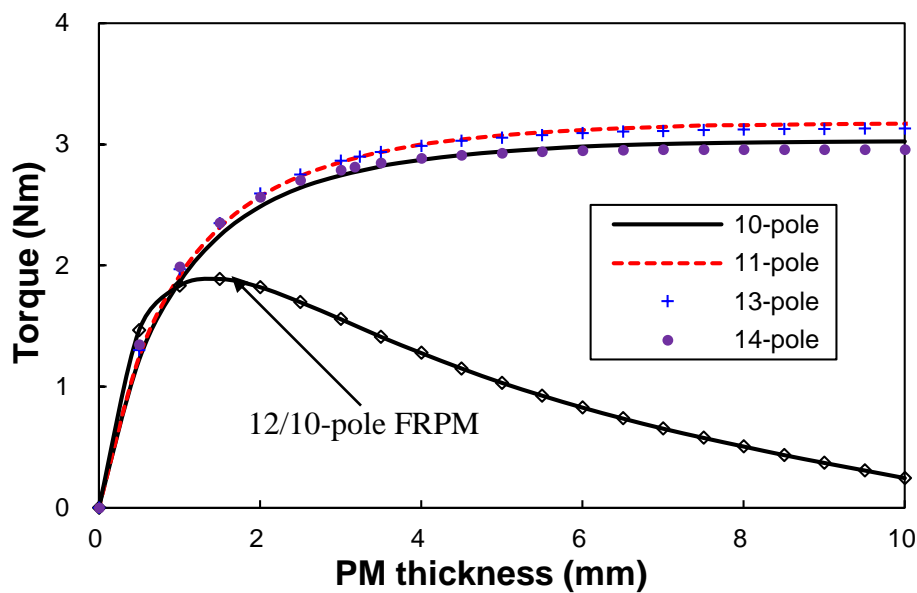


Fig. B.18. Electromagnetic torque against PM thickness in 12-stator-pole PS-FRPM machines with different rotor pole numbers and 12/10-pole FRPM machine.

In order to further numerically explain these phenomena, the flux density variation on the outer stator tooth surface of the 12/10-pole conventional FRPM and PS-FRPM machines are obtained and analysed when the rotor is at the position for the maximum A-phase flux linkage. As shown in Fig. B.19, in order to illustrate the variation more clearly, the two tooth edges are designated as -1 and 1, respectively. For the conventional FRPM machine, both positive and negative parts of the radial flux density increase with the PM thickness. However, the negative

part rises more quickly than positive part when the PM thickness is larger than 1mm. Therefore, the phase flux-linkage and hence the back-EMF fundamental magnitude will exhibit a maximum when the PM thickness varies. As shown in Fig. B.18, when the PM thickness is 1.5mm, the conventional 12/10-pole FRPM machine exhibits the largest torque. However, taking mechanical strength and irreversible demagnetisation into consideration, the PM thickness is designed to be 3mm as aforementioned. Different from the conventional FRPM machine with opposite polarity PMs mounted on teeth surface, the PMs in PS-FRPM machines are moved onto the inner stator. The radial flux density of the teeth surface and hence the torque always increase with PM thickness, as shown in Fig. B.19 and Fig. B.21.

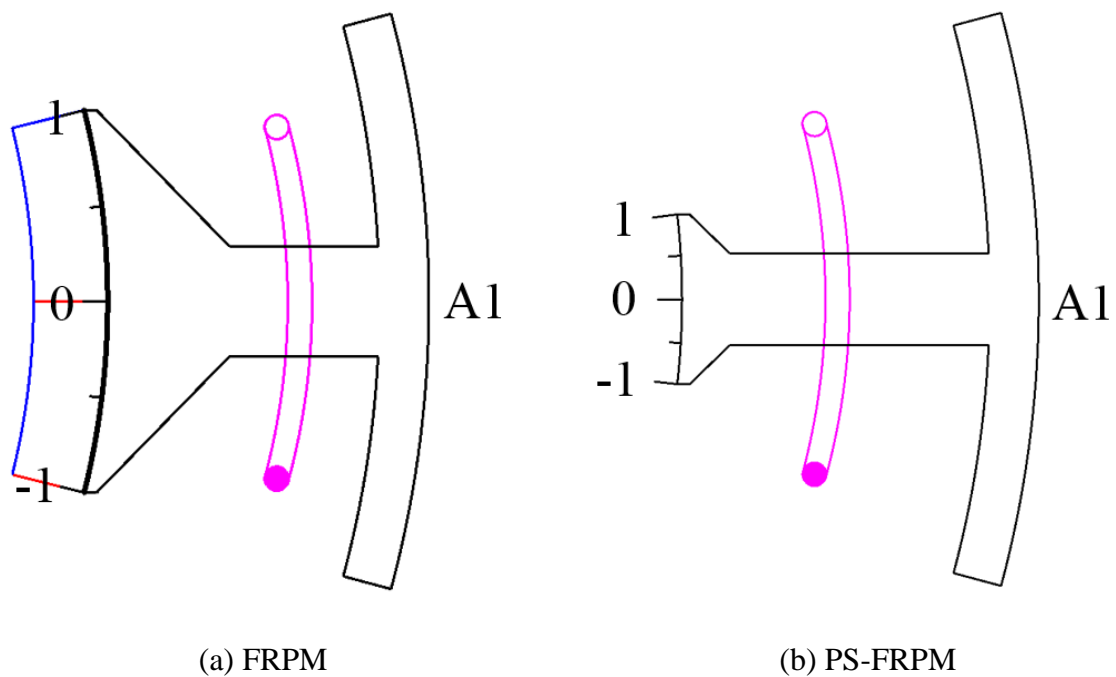


Fig. B.19. Illustration of the radial flux density paths in 12/10-pole FRPM and PS-FRPM machines.

Since PMs in PS-FRPM machines have smaller radius than the one of the FRPM machine, PM thickness in PS-FRPM machines is larger than 3mm as shown in TABLE I when the PM volume is the same. As given in Fig. B.18, the conventional 12/10-pole FRPM machine having 3mm thick PMs produces 1.55Nm torque. However, the PS-FRPM machines having the same PM volume can produce more than 2.81Nm torque, which is ~181% of that in the conventional 12/10-pole FRPM machine. Without considering the mechanical stress and demagnetisation, as shown in Fig. B.18, the conventional 12/10-pole FRPM machine has the largest torque 1.89Nm when the PM thickness is 1.5mm. However, the 12/10-pole PS-FRPM machines can

produce more than 2.95Nm as shown in Fig. B.18. Therefore, it can also be concluded the torque density of PS-FRPM machine can be 56% higher than that of the conventional FRPM machine.

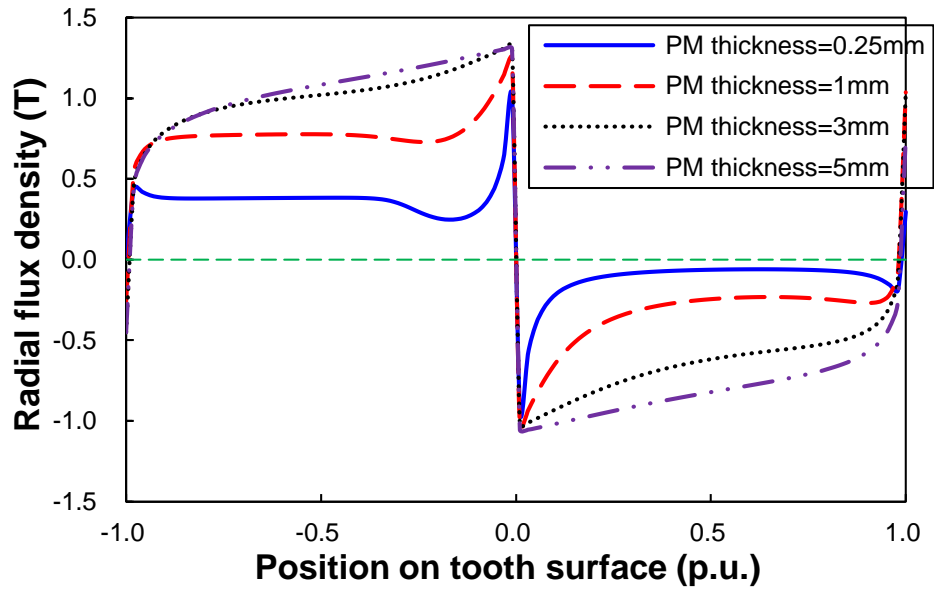


Fig. B.20. Radial flux density waveforms on the surface of tooth corresponding to coil A1 in 12/10-pole FRPM machine ($\theta_e=0^\circ$).

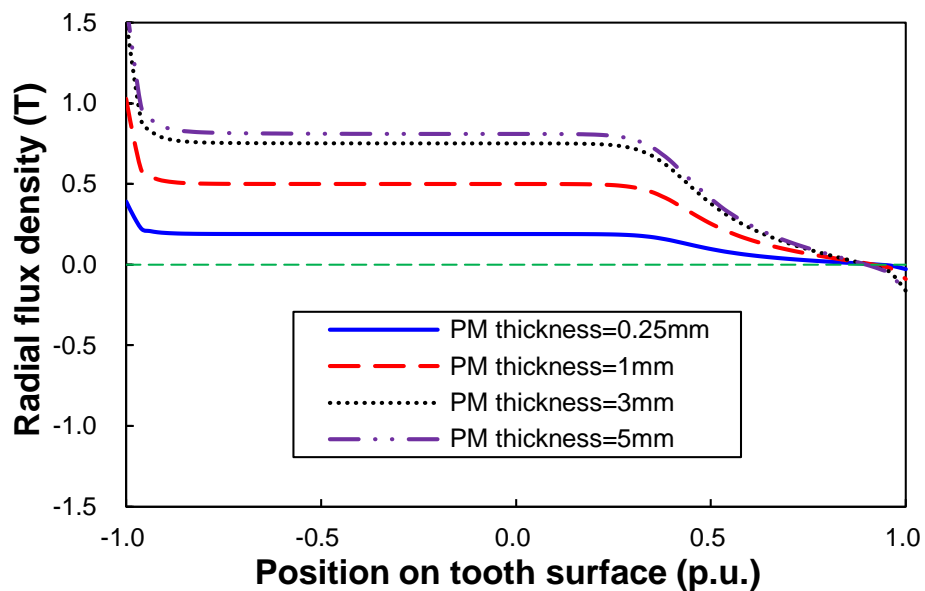
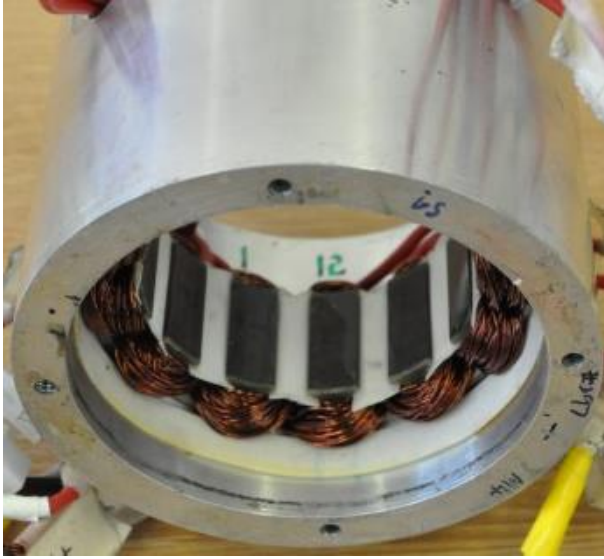


Fig. B.21. Radial flux density waveforms on the surface of tooth corresponding of coil A1 in 12/10-pole PS-FRPM machine ($\theta_e=0^\circ$).

B.6 Experimental Validation

Two PS-FRPM prototype machines are manufactured to verify the above analyses and shown in Fig. B.22. Both prototype machines share the same partitioned stators, *i.e.* outer and inner stators. The dimensions of the prototype machines are listed in Table B.3. In order to ease the prototyping, additional lamination bridges between rotor poles are employed adjacent to the inner surface. T_{bri} in Table B.3 is the thickness of the lamination bridges between rotor iron pieces. Thus, all the rotor poles are mechanically connected to obtain enough mechanical strength and relieve the tolerance requirement. The PM thickness is also rounded to 4mm. Electromagnetic performance of the prototype machines are predicted by 2D FE analysis and compared with the measures results including the back-EMFs, the static torques, the inductances, and the torque-speed curves.

As shown in Fig. B.23, although the phase back-EMFs calculated by 2D FE are slightly higher than those of measurements due to the end effect, good agreements are achieved. The variation of static torque with the rotor position for PS-FRPM prototype machines is shown in Fig. B.24. In 12/10-pole PS-FRPM prototype machine, good agreements between the 2D FE predicted and measured static torques under $I_a=5A$ can be achieved. The difference slight increases when $I_a=10A$ and $I_a=15A$ due to stronger end effects. For the 12/11-pole PS-FRPM prototype machine, there is a 3rd torque harmonic in measured static torque, which is caused by the imperfect manufacturing. Fig. B.25 shows the variation of 2D FE predicted and measured peak torques with the armature current. Again, good agreements are obtained despite of slightly difference due to the end effect in the 12/10-pole PS-FRPM machine. For the 12/11-pole PS-FRPM machine, the measured and 2D FE predicted peak torques are nearly the same. Although the end effect may lead to a slightly smaller measured peak torque than the 2D FE predicted one. However, the measured 3rd torque harmonic which is caused by imperfect manufacturing of the 11-pole rotor causes a higher measured peak torque, as shown in Fig. 23. Consequently, the measured and 2D FE predicted peak torques are approximately the same as in the 12/11-pole PS-FRPM machine. It should be noted that as shown in Fig. B.25, 2D FE predicted peak torque in the 10-pole PS-FRPM prototype machine is higher than the 11-pole one. This is because the values of design parameters of the prototype machine are not the same as the optimized ones, for easing the prototyping.



(a) 12-pole outer stator



(b) 12-pole inner stator



(c) 10-pole rotor



(d) 11-pole rotor

Fig. B.22. 12/10-pole and 12/11-pole prototype PS-FRPM machines.

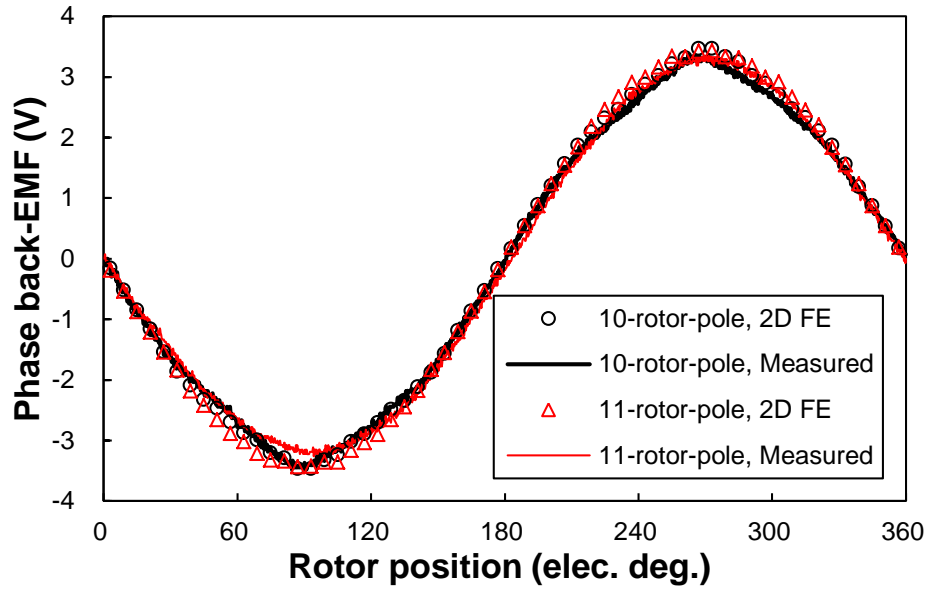
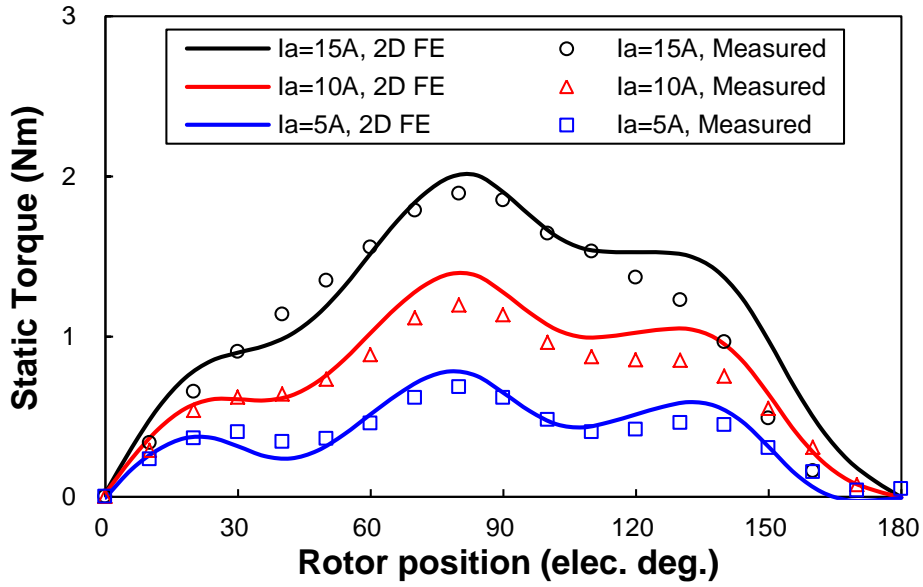
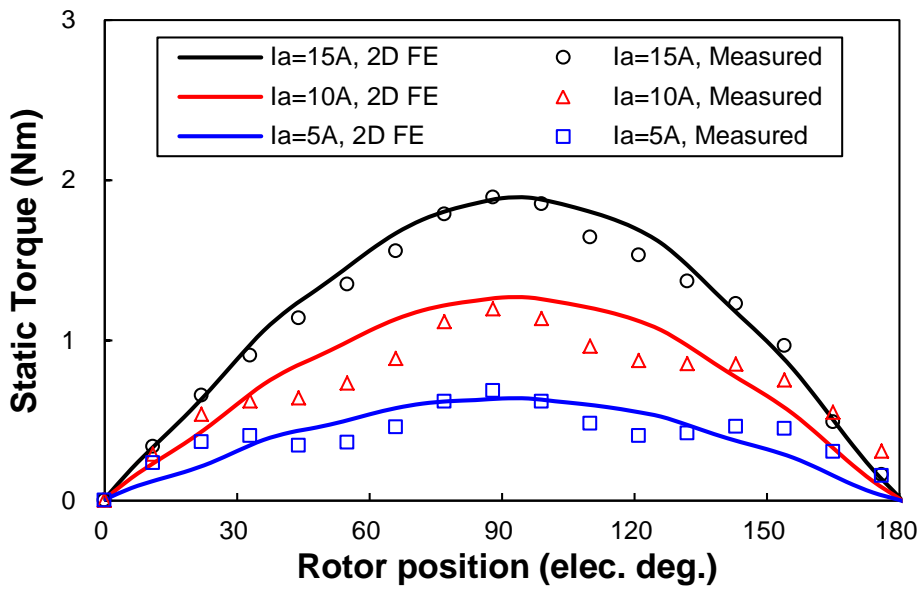


Fig. B.23. Variation of 2D FE predicted and measured phase back-EMFs with rotor position in the prototype machines.



(a) 10-rotor-pole rotor



(b) 11-rotor-pole rotor

Fig. B.24. Variation of 2D FE predicted and measured static torque with rotor position

$$(I_a = -2I_b = -2I_c).$$

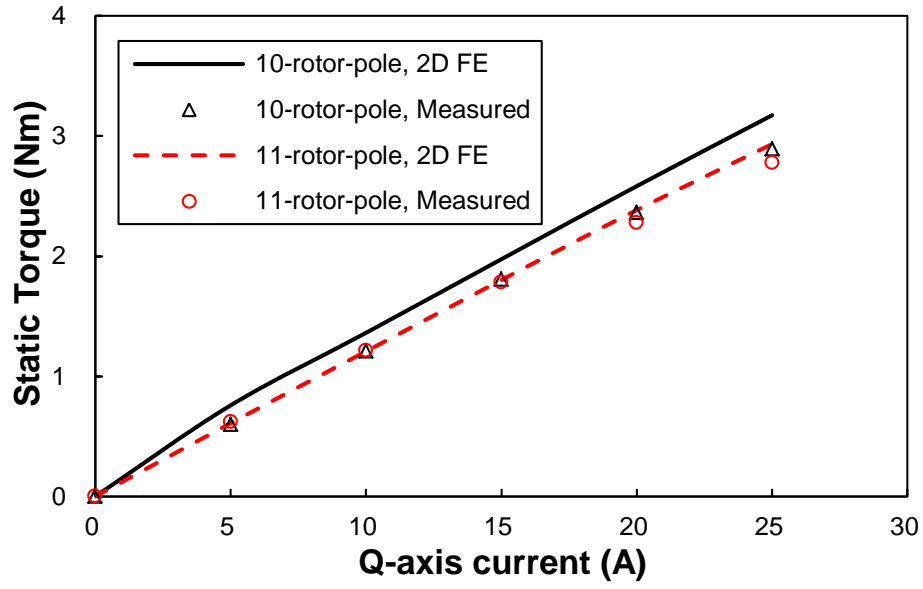


Fig. B.25. Variation of FE predicted and measured peak torques of the prototype machines.

Table B.3 Design Parameters of 12-Stator-Pole PS-FRPM Prototype Machines

Parameters	Prototype Machines		Parameters	Prototype Machines	
N_r	10	11	N_r	10	11
L_a (mm)	25		g_o (mm)	0.5	
R_{oso} (mm)	45		g_i (mm)	0.5	
R_{osy} (mm)	42		θ_{ost} (°)	8.12	
R_{osi} (mm)	31.75		θ_{osy} (°)	6.14	
R_{ro} (mm)	31.25		θ_{ot} (°)	4.94	
R_{ri} (mm)	26.15		l_{ott} (mm)	1	
R_{iso} (mm)	25.75		l_{otb} (mm)	3	
R_{isy} (mm)	21.75		θ_{ro} (°)	18	20
R_{isi} (mm)	10.4		θ_{ri} (°)	24	22.7
T_{PM} (mm)	4		θ_{PM} (°)	30	
T_{bri} (mm)	0.5				

Fig. B.26 compares the measured and 2D FE predicted self- and mutual inductances of the 12/10-stator/rotor-pole PS-FRPM prototype. The self-inductance is measured directly by LCR meter, whilst the mutual inductance is calculated by,

$$M_{BA} = \frac{L_{A+B} - L_{AA} - L_{BB}}{2} \quad (\text{B.5})$$

where M_{BA} is the calculated mutual inductance between phase A and phase B. L_{A+B} is the measured self-inductance of the serially connected windings of phase A and phase B. L_{AA} and L_{BB} are the measured self-inductance of phase A and phase B, respectively.

As shown in Fig. B.26, as the 2D FE analysis cannot account for the end winding inductance, the measured self-inductances are slightly higher than the 2D FE predicted values. However, this influence can be eliminated in the calculated mutual inductance based on (B.5), resulting

in good agreement between the measured and 2D FE predicted mutual inductances, as shown in Fig. B.26.

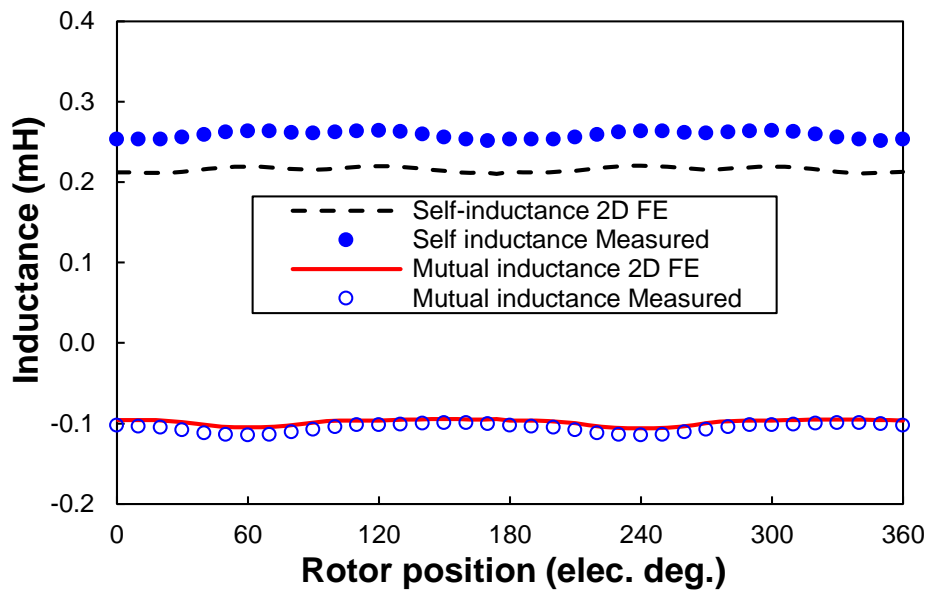


Fig. B.26. Variation of 2D FE predicted and measured inductances of the 12/10-stator/rotor-pole prototype machine.

Based on the test rig shown in Fig. B.27, the torque-speed curve of the 12/10-stator/rotor-pole PS-FRPM prototype is tested. The DC bus voltage and current are $U_{dc}=18V$ and $I_{dc}=7.5A$, respectively. The comparison of the FE predicted and measured torque-speed curves are shown in Fig. B.28. In the constant-torque region, 2D FE predicted torque-speed curves have slightly higher torque, due to end effect again. Also, 2D FE predicted characteristic speed is higher than that measured one, since that the end winding inductance cannot be accounted for in the 2D FE analysis, as aforementioned.

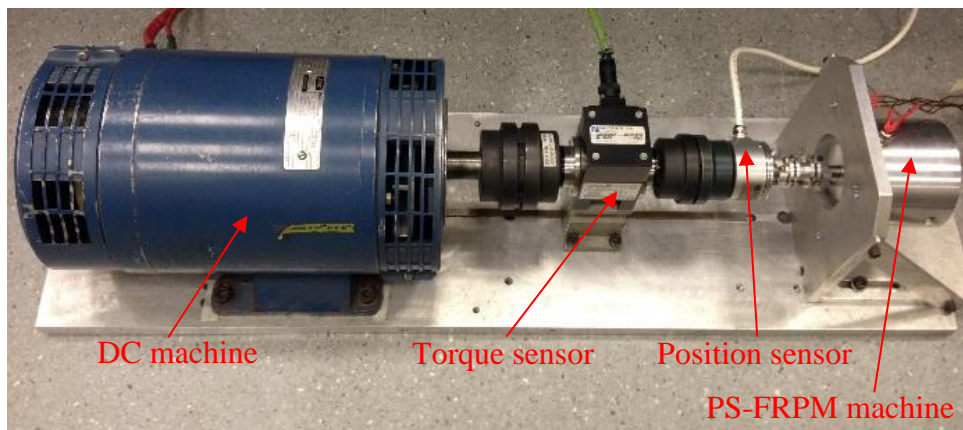


Fig. B.27. Test rig configuration ($U_{dc}=18V$, $I_{dc}=7.5A$).

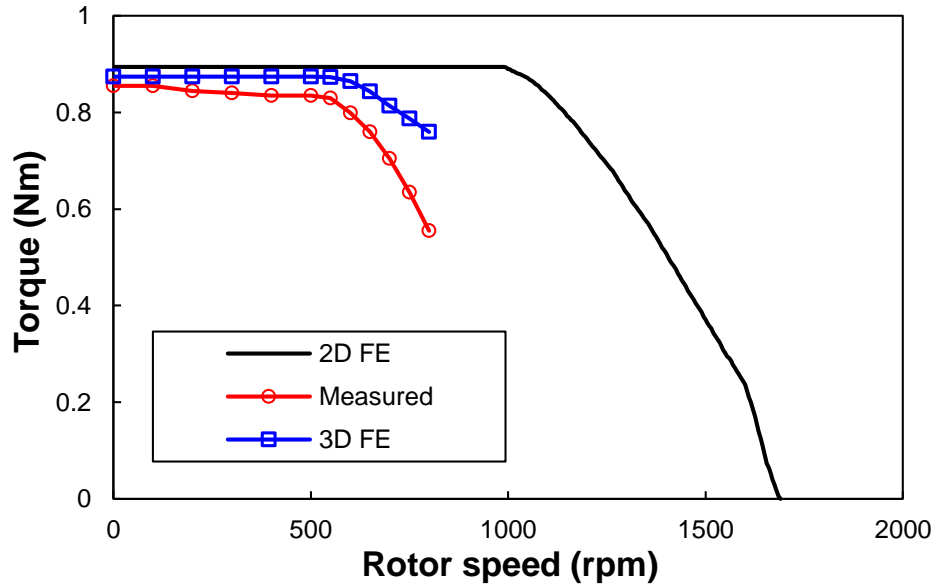


Fig. B.28. Variation of FE predicted and measured torque-speed curves of the 12/10-stator/rotor-pole prototype machine.

B.7 Conclusions

In this appendix, a novel type of PS-FRPM machine with partitioned stator is described, in which PMs and armature windings are separately located in the inner and outer stators, respectively. Compared with the conventional FRPM machine having single stator, the PS-FRPM machines can exhibit ~56% higher torque capability. The influence of rotor pole numbers in a 12-stator-pole PS-FRPM machine is investigated. It shows that amongst 12/10, 12/11, 12/13 and 12/14 stator/rotor-pole PS-FRPM machines, 11-pole and 13-pole machines exhibit larger back-EMF and hence electromagnetic torque as well as lower cogging torque and torque ripple, albeit with potentially higher unbalanced magnetic force due to odd rotor pole numbers. In addition, the influence of leading design parameters is also investigated. It shows that in PS-FRPM machines electromagnetic torque increases and saturates with the PM thickness, whilst for the conventional FRPM machines, there will be an optimal PM thickness for maximum torque.

Appendix C Comparative Analysis of End Effect in Partitioned Stator Flux Reversal Machines Having Surface-Mounted and Consequent Pole Permanent Magnets

C.1 Introduction

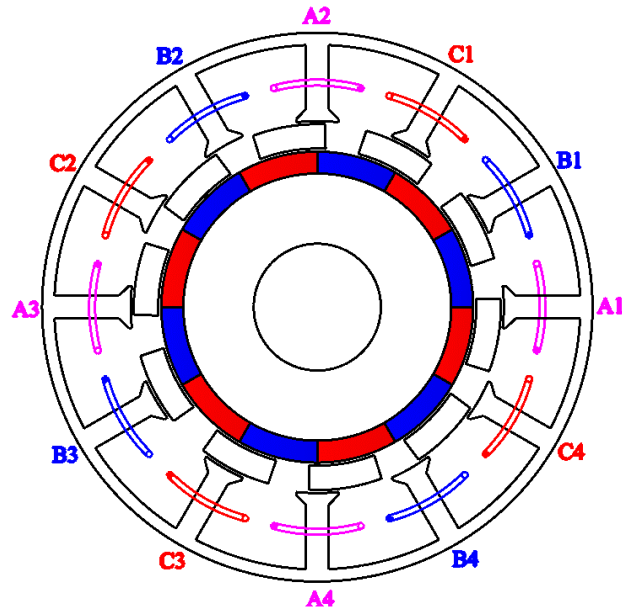
Although the torque density in PS-FRPM machine which can be referred to Appendix B shown in Fig. C.1(a) is higher, it suffers from an apparent demerit of high cost due to the rare earth PMs. For reducing the PM cost in the PS-FRPM machine, a modified PS-FRPM machine having consequent pole inner stator shown in Fig. C.1(b) is studied in [WU15b], as presented in Chapter 5. PS-FRPM machine having a consequent pole PM (CPM) inner stator can exhibit > 95% torque density of that having surface-mounted PM (SPM) inner stator, whilst the PM volume can be saved by ~30%. However, in this appendix it is found that the PS-FRPM machine having CPM inner stator suffers from higher end effect than that having SPM inner stator, due to the higher saturation. The influence of armature excitation and aspect ratio on the end effect in both SPM and CPM machines will also be investigated by the finite element (FE) method in this appendix, together with the influence of PM arc in the CPM machine.

C.2 Machine Topology and Operation Principle

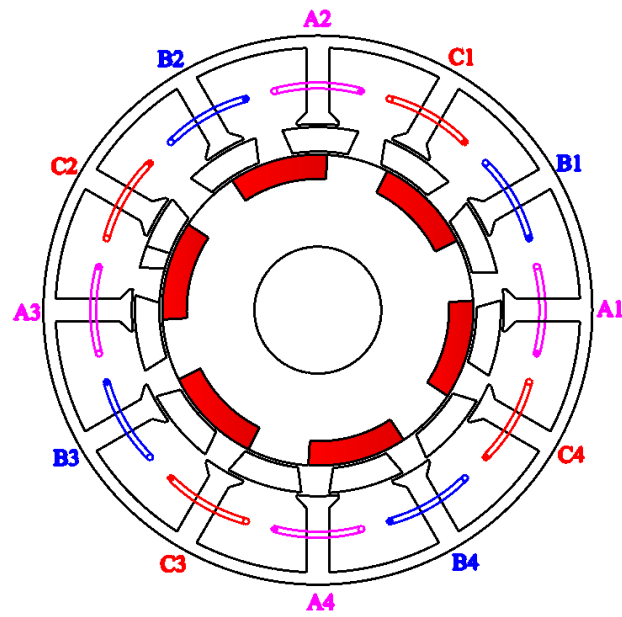
As analysed in [WU15a], similar to the magnetically geared (MG) machine [WAN09a] and magnetic gear [ATA01a], in PS-FRPM machines armature winding pole-pair p_{ea} , rotor pole number N_r , and PM pole-pair p_{PM} matches,

$$N_r = p_{PM} + p_{ea} \quad (C.1)$$

As shown in (C.1), the modulation of the rotor iron pieces on the open-circuit PM and armature excitation fields make them synchronous with each other in the air-gaps, generating electromagnetic torque. Specifically, in the 12/10-pole PS-FRPM machine having SPM machine shown in Fig. C.1(a), $p_{ea}=4$, $N_r=10$, and $p_{PM}=6$. Although the PM numbers is only half of that having SPM inner stator, $p_{PM}=6$ in the PS-FRPM machine having CPM inner stator, due to alternate PMs and iron poles, Fig. 1(b). The design parameters of the 12/10-pole PS-FRPM machines having SPM and CPM inner stators are given in [ZHU15a] and [WU15b], respectively. The machine stack length and outer diameter are $l_s=25\text{mm}$ and $D_o=90\text{mm}$, respectively.



(a) SPM



(b) CPM

Fig. C.1. Cross-sections of 12/10-pole PS-FRPM machines having SPM and CPM inner stators. (a) SPM. (b) CPM.

C.3 End Effect

C.3.1 Open-circuit

As shown in Fig. C.2(a), both the 2D and 3D FE predicted phase flux-linkages of the CPM

machine are smaller than those of the SPM machine. Moreover, the gap between the 2D and 3D FE predicted results in the CPM machine is apparently higher than that of the SPM machine. This indicates that the CPM machine suffers from larger end effect, as evidenced by the phase back-EMFs shown in Fig. C.3 and Table C.1. In Fig. C.2 and Fig. C.3, N_{ac} is the armature coil turns. As listed in Table C.1, 2D FE predicted CPM machine fundamental back-EMF is 95.66% of the SPM machine, however the 3D FE predicted percentage is 2.31% smaller, *i.e.* 93.45%. This is due to the larger end effect in the CPM machine. In Table C.1, the open-circuit end effect coefficient E_{open} is defined as the ratio of the 3D FE predicted phase fundamental back-EMF E_{3D} to the 2D value E_{2D} ,

$$E_{open} = \frac{E_{3D}}{E_{2D}} * 100\% \quad (C.2)$$

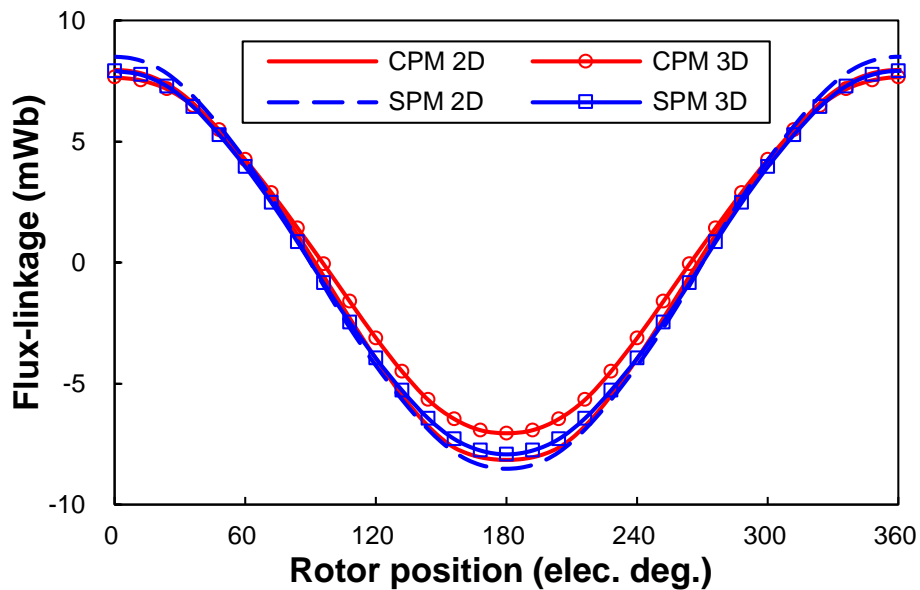


Fig. C.2. Open-circuit phase flux-linkage waveforms, $N_{ac}=18$.

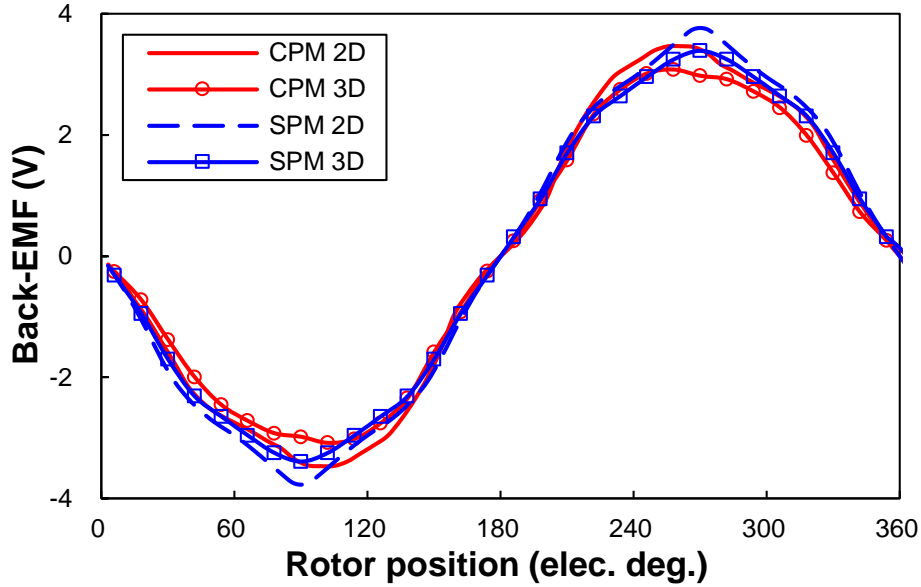


Fig. C.3. Open-circuit phase back-EMF waveforms, $N_{ac}=18$, 400rpm.

Table C.1 2D and 3D FE Predicted Fundamental Back-EMFs, $N_{ac}=18$, 400rpm

Item	2D FE	3D FE	E_{eopen}
CPM	3.41V	3.10V	90.88%
SPM	3.57V	3.32V	93.03%
Ratio	95.66%	93.45%	97.69%

The higher end effect in the CPM machine is due to the more severe axial flux leakage, as shown in Fig. C.4. This can be explained by the higher saturation in the inner stator, as shown in Fig. C.5 for the open-circuit inner stator flux density. Due to higher saturation, the relative permeability of the inner stator pole steel is smaller in the CPM machine, as shown in Fig. C.6. Therefore, the radial magnetic circuit reluctance is higher in the CPM machine, resulting in more axial flux-leakage and hence higher end effect [LAB13a].

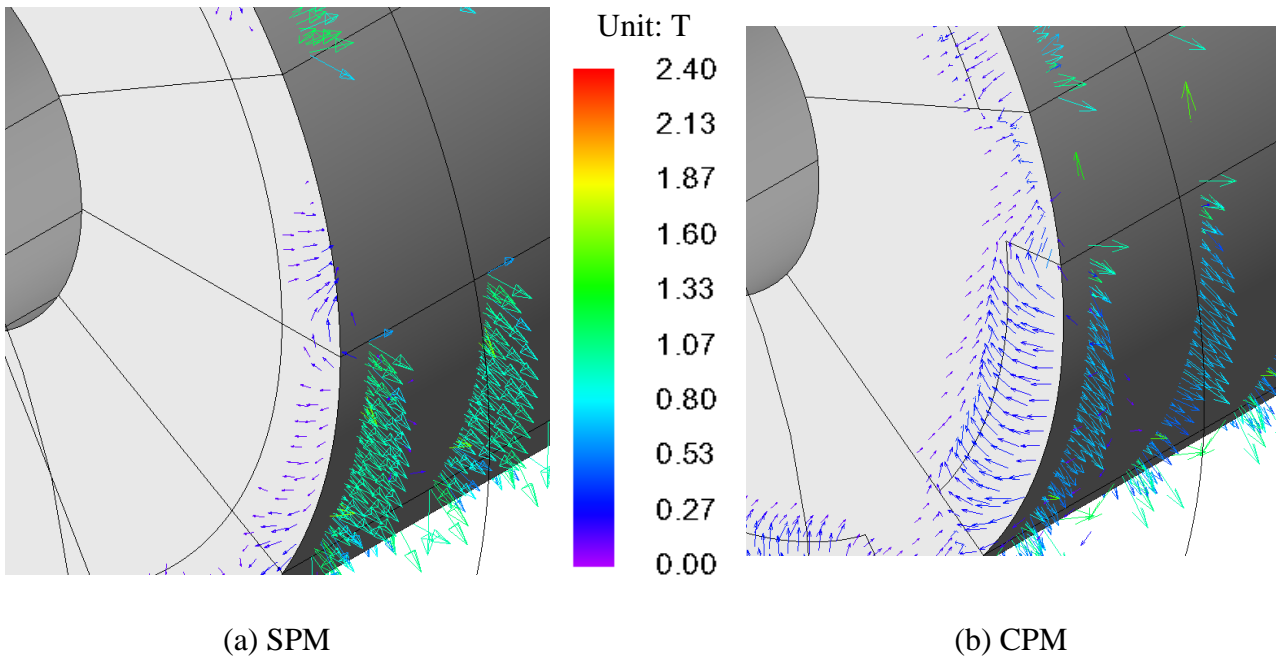


Fig. C.4. Open-circuit inner stator end region flux density vectors at d -axis rotor position (0-2.4T).

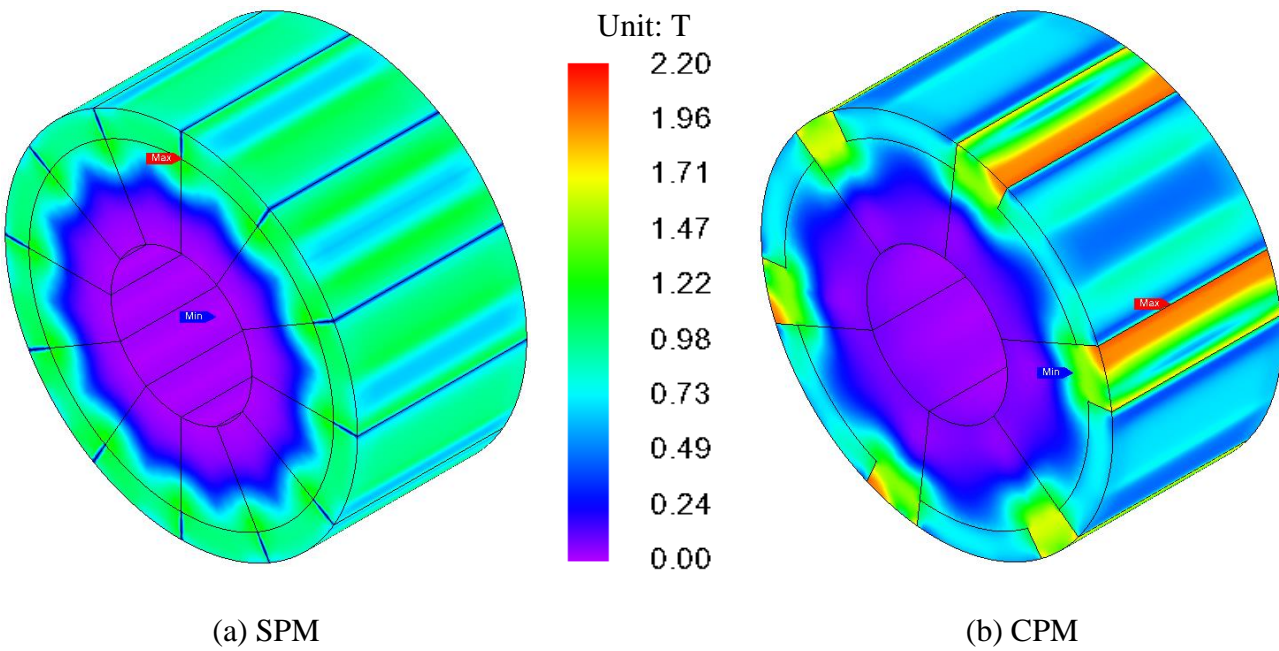


Fig. C.5. Open-circuit inner stator flux density at d -axis rotor position (0-2.2T).

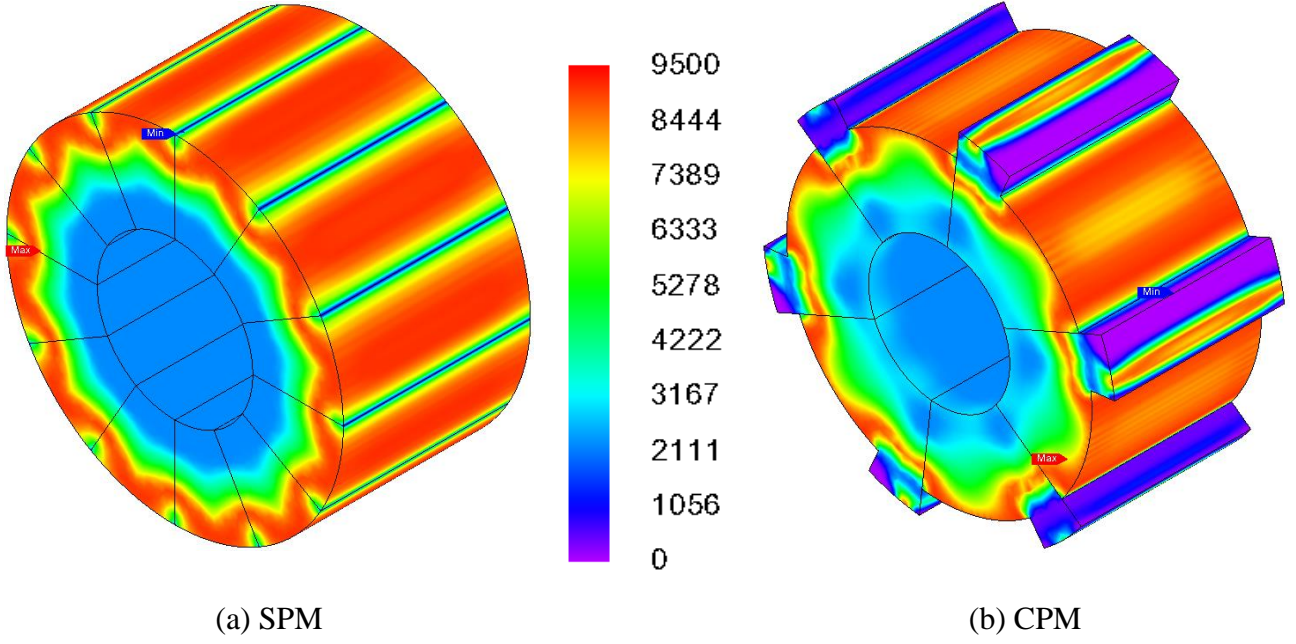


Fig. C.6. Open-circuit inner stator steel relative permeability at d -axis rotor position (0-9500).

C.3.2 On-load

In this appendix, both the two machines operate at brushless AC (BLAC) model under zero d -axis current control, *i.e.* phase current and phase back-EMF have the same phase angle, due to the similar d - and q -axis inductances and hence the negligible reluctance torque [ZHU15a] [WU15b]. As shown in Fig. C.7 and Table C.2, when the copper loss $p_{cu}=20\text{W}$, the 2D FE predicted average electromagnetic torque of the CPM machine is only 4.64% smaller than the SPM machine. However, when the end effect is accounted for, the 3D FE predicted average electromagnetic torque of the CPM machine will be 10.48% smaller than that of the SPM machine. This is also due to the larger end effect caused by more axial flux-leakage in the CPM machine, as shown in Fig. C.8. In Fig. C.8, the on-load end effect coefficient E_{load} is defined as the ratio of the 3D FE predicted average electromagnetic torque T_{avg3D} to the 2D value T_{avg2D} ,

$$E_{load} = \frac{T_{avg3D}}{T_{avg2D}} * 100\% \quad (\text{C.3})$$

Table C.2 2D and 3D FE Predicted Average Torques (BLAC, phase current and phase back-EMF have the same phase angle, $p_{cu}=20W$)

Item	2D FE	3D FE	E_{load}
CPM	2.73Nm	2.46Nm	90.15%
SPM	2.86Nm	2.75Nm	96.03%
Ratio	95.36%	89.52%	93.88%

As shown in Fig. C.9, the end effect coefficient E_{load} is smaller with higher copper loss p_{cu} for both these two analysed machines. This means the end effect is larger with higher load as expected due to higher saturation. With accounting for the different end effects, the 3D FE predicted average torque ratio of the CPM machine to the SPM machine achieves the peak value when $p_{cu}=30W$, whilst that for the 2D FE predicted curves is $p_{cu}=20W$, as shown in Fig. C.10.

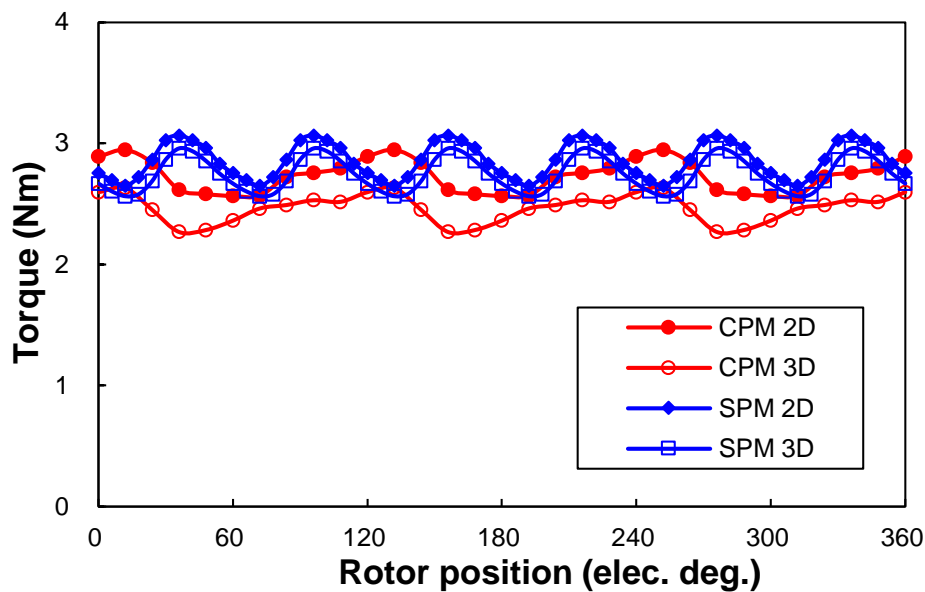


Fig. C.7. 2D and 3D FE predicted torque waveforms (BLAC, phase current and phase back-EMF have the same phase angle, $p_{cu}=20W$).

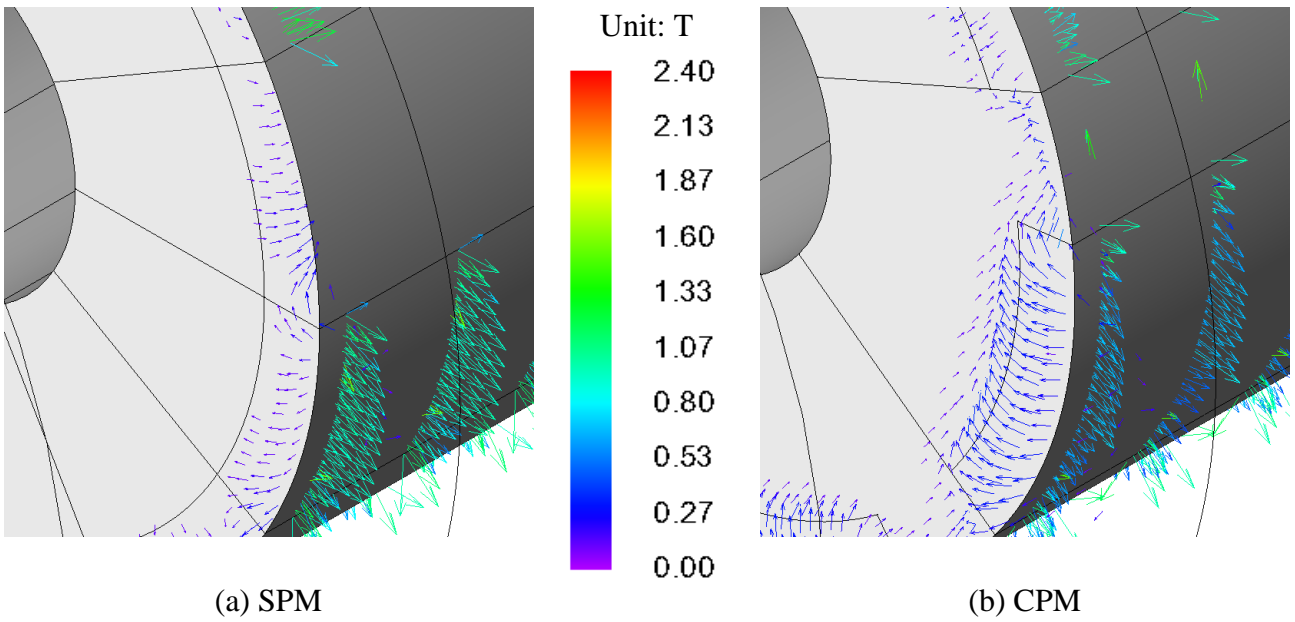


Fig. C.8. On-load inner stator end region flux density vectors at d -axis rotor position (BLAC, phase current and phase back-EMF have the same phase angle, $p_{cu}=20\text{W}$, $0-2.4\text{T}$).

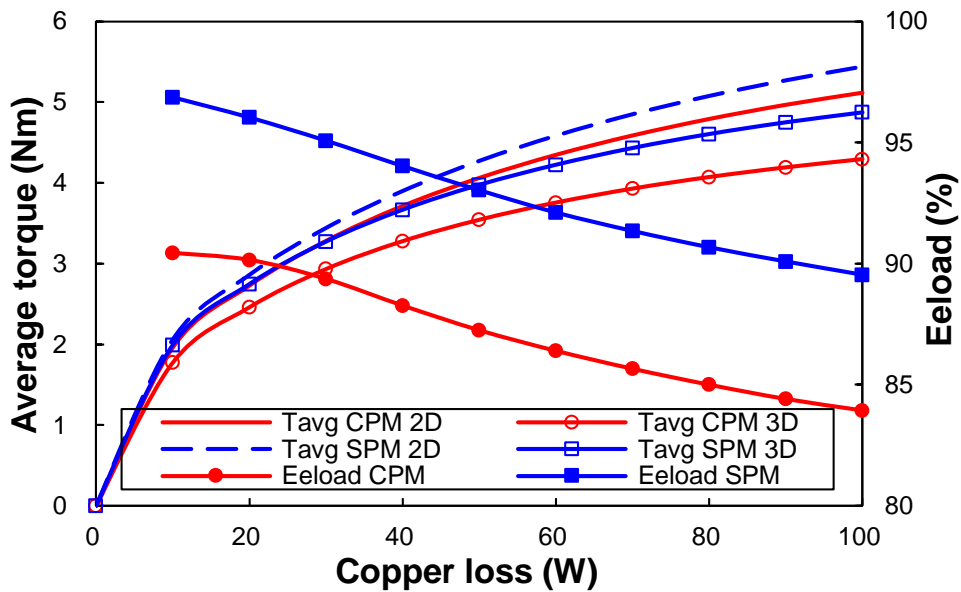


Fig. C.9. 2D and 3D FE predicted average torques and end effects of the CPM machine to the SPM machine for different copper loss (BLAC, phase current and phase back-EMF have the same phase angle).

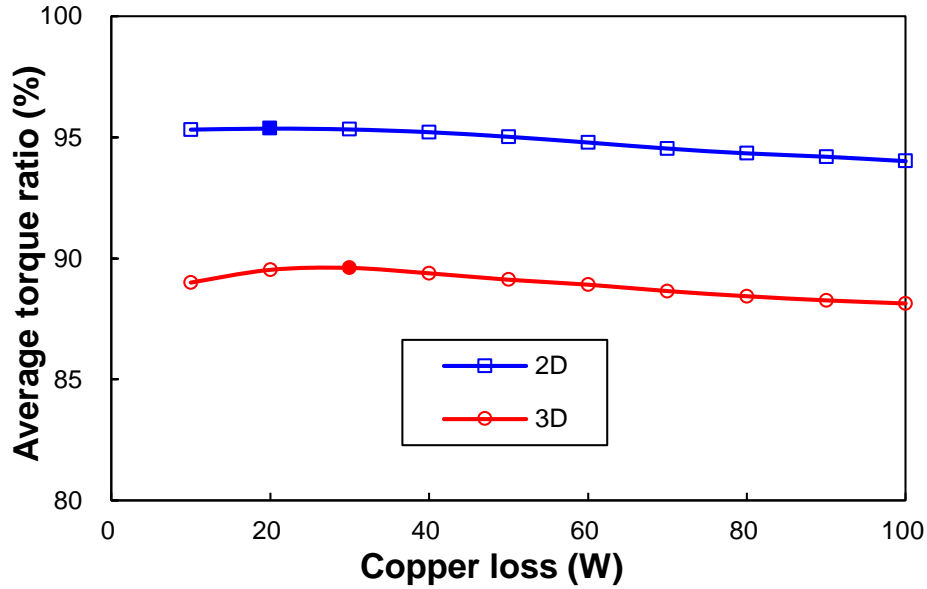


Fig. C.10. 2D and 3D FE predicted average torque ratio of the CPM machine to the SPM machine for different copper loss (BLAC, phase current and phase back-EMF have the same phase angle).

Obviously, the best way to achieve the highest T_{avg} is 3D FE optimization. However, it is very time-consuming. Alternatively, 2D FE optimization is always preferred for saving time. However, only T_{avg2D} can be obtained whilst the end effect cannot be accounted for in 2D FE optimization. By designing the PS-FRPM machine based on the flow chart illustrated in Fig. C.11, the highest T_{avg3D} can be achieved by 2D FE optimization. In Fig. C.11, parameters with superscript 0 are from 2D FE optimization, whilst those with superscript $j=1$ or -1 are related to one dimension parameter variation. However, it should be noted that when T_{avg3D} is maximum, the on-load end effect may not be minimum. As well known, the aspect ratio has a significant influence on end effect. Therefore, the end effect can be reduced by enlarging the aspect ratio in an electrical machine, *i.e.* increasing the ratio of the stack length to the machine outer diameter. Also, in the CPM machine, PM arc θ_{PM} will influence the end effect. They are analysed as follows.

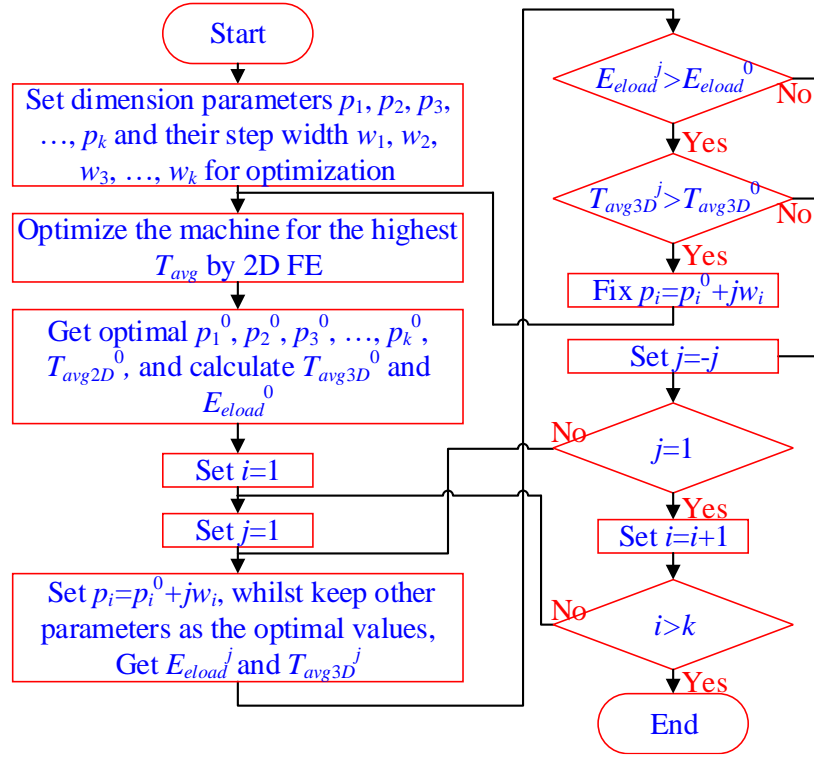


Fig. C.11. Flow chart of 2D FE optimization for the highest T_{avg3D} .

C.3.3 Influence of aspect ratio

As shown in Fig. C.12, in both CPM and SPM machines, end effect coefficient E_{load} can be effectively enlarged by increasing the stack length, resulting in smaller end effect, when D_o is fixed as 90mm. As shown in Fig. C.12, E_{load} can be improved from 90.15% to 97.11% when the stack length l_s is extended from 25mm to 100mm, as shown in Fig. C.12. As for the SPM machine, $E_{load} \geq 99.24\%$ when the stack length $l_s \geq 50\text{mm}$. Overall, as shown in Fig. C.13, the average torque ratio of the CPM machine to the SPM machine accounting for the end effect can be enlarged from 89.53% to 92.85% for $l_s=25\text{mm}$ and $l_s=100\text{mm}$, respectively. As may be expected, this average torque ratio will get closer to the ideal 2D FE predicted value, *i.e.* 95.36%. It is worth noting that in the machine with $l_s=25\text{mm}$, when the q -axis current $i_q=23.19\text{A}$ and phase current and phase back-EMF have the same phase angle, the copper loss p_{cu} is 20W.

When $D_o=90\text{mm}$, for generating the same average electromagnetic torque as the SPM machine with $l_s=25\text{mm}$, l_s in the CPM machine needs to be designed as 27.5mm, *i.e.* 10% higher, as shown in Fig. C.13. Consequently, the cost of iron and PM will be increased by 10%, whilst that of copper is smaller than 10% since the end winding length is remained the same. However, compared with the SPM machine of which the PM volume is 13414.6 mm^3 , the PM

volume in the CPM machine with $l_s=27.5\text{mm}$ is still 21.17% smaller, *i.e.* 10575.18mm^3 . Since the price of rare-earth NdFeB PM is much higher than those of iron and copper [FAS14a], the cost of CPM machine with $l_s=27.5\text{mm}$ is still lower than the SPM machine with $l_s=25\text{mm}$.

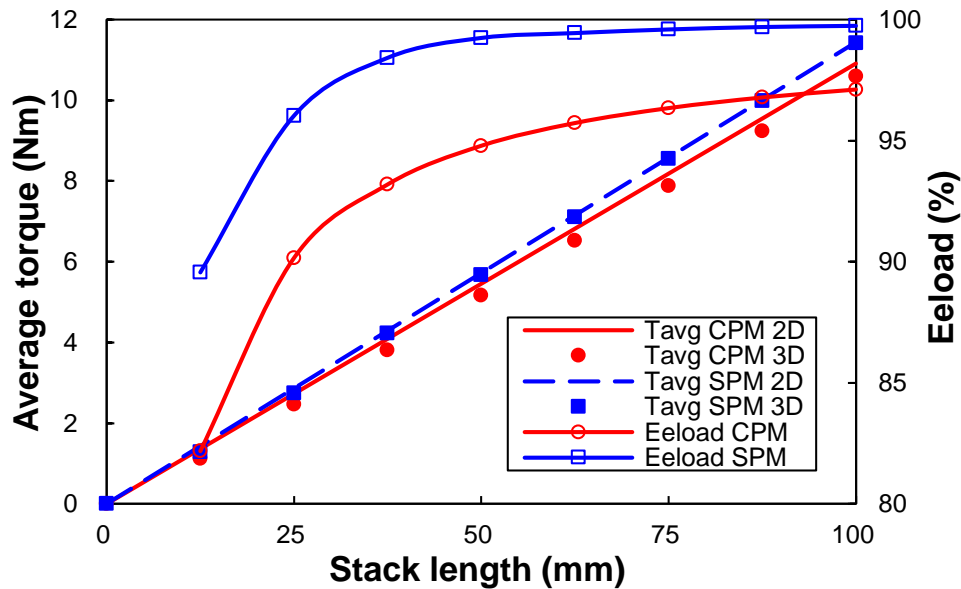


Fig. C.12. 2D and 3D FE predicted average torques and end effects of the CPM machine to the SPM machine for different stack length with $D_o=90\text{mm}$ (BLAC, phase current and phase back-EMF have the same phase angle, $i_q=23.19\text{A}$).

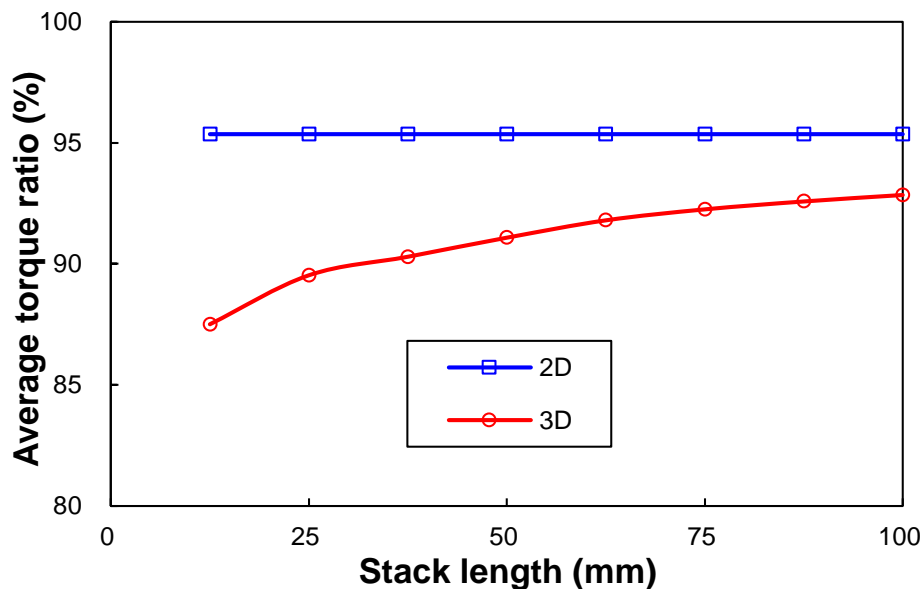


Fig. C.13. 2D and 3D FE predicted average torque ratio of the CPM machine to the SPM machine for different stack length with $D_o=90\text{mm}$ (BLAC, phase current and phase back-EMF have the same phase angle, $i_q=23.19\text{A}$).

C.3.4 Influence of PM arc in CPM machine

In the foregoing analysis, the PM arc θ_{PM} in the CPM machine is 43 mechanical degrees [WU15b], whilst that in the SPM machine is 30 mechanical degrees [ZHU15a]. Although a larger θ_{PM} can lead to a higher PM magnetomotive force (MMF), it will also cause a thinner lamination steel between PMs and hence higher saturation in the inner stator pole steel, which will increase the radial magnetic circuit reluctance. Therefore, there is a balance between PM MMF and saturation in the inner stator pole steel to achieve the highest average electromagnetic torque. This can be evidenced by the 2D FE predicted peak average electromagnetic torque point when $\theta_{PM}=41$ mechanical degrees, as shown in Fig. C.14.

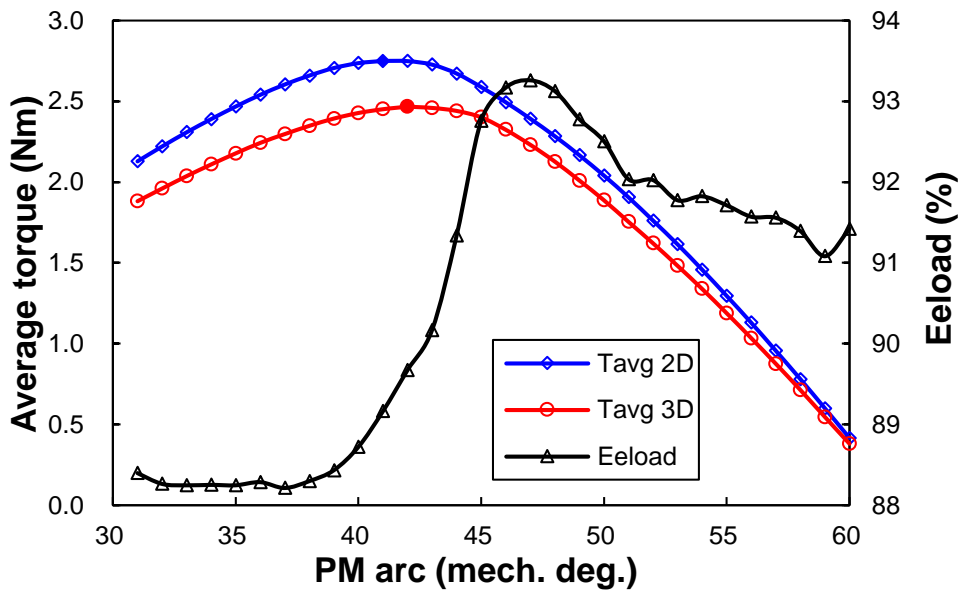


Fig. C.14. 2D and 3D FE predicted average electromagnetic torques and end effects under different PM arc θ_{PM} (BLAC, phase current and phase back-EMF have the same phase angle, $i_q=23.19A$).

However, as shown in Fig. C.14, the peak points are different for 2D and 3D FE results, *i.e.* 41 mechanical degrees and 42 mechanical degrees, respectively. This is due to different end effect coefficients for various PM arc θ_{PM} , as shown in Fig. C.14. The end effect coefficient E_{eload} remains stable firstly and then increases from $\theta_{PM}=38$ mechanical degrees, then falls after reaching the peak value at $\theta_{PM}=47$ mechanical degrees.

C.4 Experimental Validation

To verify the foregoing FE analysis, the 12/10-pole PS-FRPM prototype machines having SPM and CPM inner stators are built, as shown in Fig. C.15. These two machines use the same outer stator and rotor, whilst the inner stators are different. Although PS-FRPM machines have higher torque density than the conventional FRPM machine, the dual air-gaps design and separated rotor iron pieces make it a challenge for the fabrication of the rotor. For easing manufacturing, the rotor iron pieces are connected by introducing a 0.5mm thick iron bridge adjacent to the inner air-gap. The cup rotor is fixed between the rotating shaft and the bottom bearing by nonmagnetic aluminum bars and an epoxy resin, as shown in Fig. C.15(b).



(a) Outer stator



(b) Rotor



(c) SPM inner stator



(d) CPM inner stator

Fig. C.15. Photos of 12/10-pole PS-FRPM prototype machines. (a) Outer stator. (b) Rotor. (c) SPM inner stator. (d) CPM inner stator.

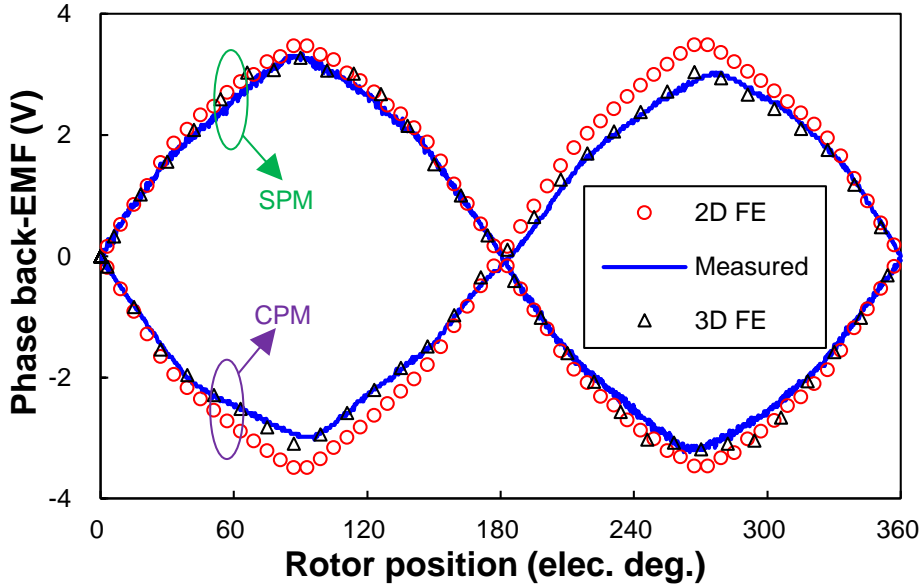


Fig. C.16. Comparison of FE predicted and measured back-EMFs at 400rpm.

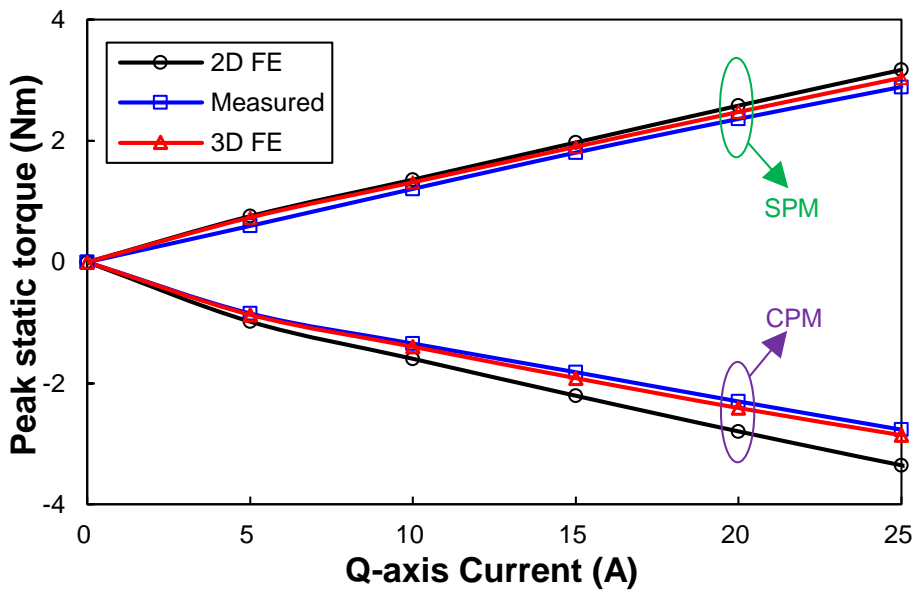


Fig. C.17. Comparison of FE predicted and measured peak static torques.

C.5 Conclusions

In this appendix, the end effect in PS-FRPM machines having SPM and CPM inner stators respectively are comparatively analysed. It is found that the CPM machine suffers from higher end effect, due to higher saturation. FE results show that the end effect increases with armature excitation due to more severe saturation, but can be effectively reduced by increasing the aspect ratio. Specifically, in the CPM machine the optimal PM arc for the highest average

electromagnetic torque predicted by 2D and 3D FE are different due to the various end effect with PM arc.

Publications

SCI Journal papers:

- [1] Chapter 2 **Z. Z. Wu**, and Z. Q. Zhu, “Analysis of air-gap field modulation and magnetic gearing effects in switched flux permanent magnet machines,” *IEEE Transactions on Magnetics*, vol. 51, no. 5, pp. 1-12, May 2015, Art. ID 8105012.
- [2] Chapter 3 **Z. Z. Wu**, and Z. Q. Zhu, “Analysis of magnetic gearing effect in partitioned stator switched flux PM machines,” *IEEE Transactions on Energy Conversion*, vol. 31, no. 4, pp. 1239-1249, Dec. 2016.
- [3] Chapter 4 **Z. Z. Wu**, and Z. Q. Zhu, “Partitioned stator flux reversal machine with consequent-pole PM stator,” *IEEE Transactions on Energy Conversion*, vol. 30, no. 4, pp. 1472-1482, Dec. 2015.
- [4] Chapter 5 **Z. Z. Wu**, Z. Q. Zhu, and H. L. Zhan, “Comparative analysis of partitioned stator flux reversal PM machines having fractional-slot non-overlapping and integer-slot overlapping windings,” *IEEE Transactions on Energy Conversion*, vol. 31, no. 2, pp. 776-788, Jun. 2016.
- [5] Chapter 6 **Z. Z. Wu**, and Z. Q. Zhu, “Comparison of partitioned stator flux reversal PM machine and magnetically geared machine operating at stator-PM and rotor-PM modes,” submitted to *IEEE Transactions on Energy Conversion* in 2016, under 2nd round review.
- [6] Z. Q. Zhu, **Z. Z. Wu**, D. J. Evans, and W. Q. Chu, “Novel electrical machines having separate PM excitation stator,” *IEEE Transactions on Magnetics*, vol. 51, no. 4, pp. 1-9, Apr. 2015, Art. ID 8104109.
- [7] Z. Q. Zhu, **Z. Z. Wu**, D. J. Evans, and W. Q. Chu, “A wound field switched flux machine with field and armature windings separately wound in double stators,” *IEEE Transactions on Energy Conversion*, vol. 30, no. 2, pp. 772-783, Jun. 2015.
- [8] Z. Q. Zhu, **Z. Z. Wu**, and X. Liu, “A partitioned stator variable flux

reluctance machine,” *IEEE Transactions on Energy Conversion*, vol. 31, no. 1, pp. 78-92, Mar. 2016.

- [9] **Z. Z. Wu**, Z. Q. Zhu, and J. T. Shi, “Novel doubly salient permanent magnet machines with partitioned stator and iron pieces rotor,” *IEEE Transactions on Magnetics*, vol. 51, no. 5, pp. 1-12, May 2015, Art. ID 8105212.
- [10] **Z. Z. Wu**, and Z. Q. Zhu, “Comparative analysis of end effect in partitioned stator flux reversal machines having surface-mounted and consequent pole permanent magnets,” *IEEE Transactions on Magnetics*, vol. 52, no. 7, pp. 1-4, July 2016, Art. ID 8103904. (From *Intermag* 2016)
- [11] M. Zheng, **Z. Z. Wu**, and Z. Q. Zhu, “Partitioned stator flux reversal machines having Halbach array PMs,” *COMPEL: The International Journal for Computation and Mathematics in Electrical and Electronic Engineering*, vol. 35, no. 2, pp. 396-406, 2016.
- [12] C. C. Awah, Z. Q. Zhu, **Z. Z. Wu**, H. L. Zhan, J. T. Shi, D. Wu, and X. Ge, “Comparison of partitioned stator switched flux permanent magnet machines having single- or double-layer windings,” *IEEE Transactions on Magnetics*, vol. 52, no. 1, pp. 1-10, Jan. 2016, Art. ID 9500310.
- [13] C. C. Awah, Z. Q. Zhu, **Z. Z. Wu**, D. Wu, and X. Ge, “Electromagnetic performance of switched flux PM machines with two separate stators,” *COMPEL: The International Journal for Computation and Mathematics in Electrical and Electronic Engineering*, vol. 35, no. 2, pp. 376–395, 2016.
- [14] D. J. Evans, Z. Q. Zhu, H. L. Zhan, **Z. Z. Wu**, and X. Ge, “Flux-weakening control performance of partitioned stator-switched flux PM machines,” *IEEE Transactions on Industrial Applications*, vol. 52, no. 3, pp. 2350-2359, May/Jun. 2016.
- [15] Z. Q. Zhu, H. Hua, D. Wu, J. T. Shi, and **Z. Z. Wu**, “Comparison of partitioned stator machines with different PM excitation stator topologies,” *IEEE Transactions on Industrial Applications*, vol. 52, no. 1, pp. 199-208,

Jan./Feb. 2016.

- [16] Lingyun Shao, Wei Hua, Z. Q. Zhu, Xiaofeng Zhu, Ming Cheng, and **Zhongze Wu**, “A novel flux-switching permanent magnet machine with overlapping windings,” *IEEE Transactions on Energy Conversion*, accepted.
- [17] K. Wang, Z. Q. Zhu, Z. Y. Gu, and **Z. Z. Wu**, “Optimum injected harmonics into magnet shape in multi-phase surface-mounted PM machine for maximum output torque,” *IEEE Transactions on Industrial Electronics*, accepted.
- [18] H. Hua, Z.Q. Zhu, C. Wang, M. Zheng, **Z. Z. Wu**, D. Wu, and X. Ge, “Partitioned stator machines with NdFeB and ferrite magnets,” *IEEE Transactions on Industrial Applications*, accepted.

International Conference papers:

- [19] **Z. Z. Wu**, Z. Q. Zhu, J. C. Mipo, and P. Farah, “Design and analysis of a partitioned stator wound field switched flux machine for electric vehicle,” *International Conference on Electrical Machines and Systems*, Chiba, Japan, 2016, accepted.
- [20] **Z. Z. Wu**, and Z. Q. Zhu, “Comparative analysis of end effect in partitioned stator flux reversal machines having surface mounted and consequent pole permanent magnets,” in *Proc. of Joint Magnetism and Magnetic Materials - International Magnetics Conference*, San Diego, US, 2016, Art. ID FX-12.
- [21] **Z. Z. Wu**, Z. Q. Zhu, and D. J. Evans, “Comparison of globally optimized partitioned stator SFPM machines with different stator/rotor pole combinations,” in *Proc. of International Magnetics Conference*, Beijing, China, 2015, Art. ID FX-02.
- [22] M. Zheng, **Z. Z. Wu**, and Z. Q. Zhu, “Partitioned stator flux reversal machines having halbach array PMs,” in *Proc. of International Magnetics Conference*, Beijing, China, 2015, Art. ID FY-03.

- [23] H. L. Zhan, Z. Q. Zhu, and **Z. Z. Wu**, “Active voltage regulation of partitioned stator switched flux permanent magnet generator supplying isolated passive load,” in *Proc. of IEEE Energy Conversion Conference and Exposition*, Milwaukee, US, 2016, pp. 1-7.
- [24] D. J. Evans, Z. Q. Zhu, **Z. Z. Wu**, H. L. Zhan, and X. Ge, “Comparative analysis of parasitic losses in partitioned stator switched flux PM machines with double- and single-layer windings,” in *Proc. of IEEE International Electrical Machines and Drives Conference*, Coeur d'Alene, US, 2015, pp. 167-173.
- [25] C. C. Awah, Z. Q. Zhu, **Z. Z. Wu**, J. T. Shi, and D. Wu, “Comparison of partitioned stator switched flux permanent magnet machines having single- and double-layer windings,” in *Proc. of International Conference on Ecological Vehicles and Renewable Energies*, Monaco, Monaco, 2015, pp. 1-5.
- [26] C. C. Awah, Z. Q. Zhu, **Z. Wu**, and D. Wu, “High torque density magnetically-g geared switched flux permanent magnet machines,” in *Proc. of International Conference on Ecological Vehicles and Renewable Energies*, Monaco, Monaco, 2015, pp. 1-6.
- [27] D. J. Evans, Z. Q. Zhu, H. L. Zhan, **Z. Z. Wu**, and X. Ge, “Flux-weakening control performance of partitioned stator switched flux PM machines,” in *Proc. of IEEE International Electrical Machines and Drives Conference*, Coeur d'Alene, US, 2015, pp. 391-397.
- [28] H. Hua, Z. Q. Zhu, M. Zheng, **Z. Z. Wu**, D. Wu, and X. Ge, “Performance comparison of partitioned stator machines with NdFeB and ferrite magnets,” in *Proc. of IEEE International Electrical Machines and Drives Conference*, Coeur d'Alene, US, 2015, pp. 461-467.
- [29] Lingyun Shao, Wei Hua, Z. Q. Zhu, **Zhongze Wu**, and Ming Cheng, “Influence of rotor-pole number on electromagnetic performance in twelve-phase redundant SFPM machines for wind power generation,” in

Proc. of International Conference on Electrical Machines, Lausanne, Switzerland, 2016, Art. ID LD-007838.

- [30] Z. Q. Zhu, H. Hua, D. Wu, J. T. Shi, and **Z. Z. Wu**, “Comparison of partitioned stator machines with different PM excitation stator topologies,” in *Proc. of International Conference on Ecological Vehicles and Renewable Energies*, Monaco, Monaco, 2015, pp. 1-7.